Title
Synthesis, Structure, and Properties of Refractory Hard-Metal Borides

Author
Lech, Andrew Thomas

Publication Date
2014

Peer reviewed|Thesis/dissertation

UNIVERSITY OF CALIFORNIA

Los Angeles

Synthesis, Structure, and Properties of Refractory Hard-Metal Borides

A dissertation submitted in partial satisfaction of

the requirements for the degree of Doctor of

Philosophy in Chemistry

by

Andrew Thomas Lech

2014

ABSTRACT OF THE DISSERTATION

Synthesis, Structure, and Properties of Refractory Hard-Metal Borides

by

Andrew Thomas Lech

Doctor of Philosophy in Chemistry

University of California, Los Angeles, 2014

Professor Richard B. Kaner, Chair

As the limits of what can be achieved with conventional hard compounds, such as tungsten carbide, are nearing reach, super-hard materials are an area of increasing industrial interest. The refractory hard metal borides, such as ReB_2 and WB_4, offer an increasingly attractive alternative to diamond and cubic boron nitride as a next-generation tool material. In this Thesis, a thorough discussion is made of the progress achieved by our laboratory towards understanding the synthesis, structure, and properties of these extremely hard compounds. Particular emphasis is placed on structural manipulation, solid solution formation, and the unique crystallographic manifestations of what might also be called “super-hard metals”.

The dissertation of Andrew Thomas Lech is approved.

_____

Sarah Tolbert

_____

Vijay Gupta

_____

Richard B. Kaner, Committee Chair

University of California, Los Angeles

2014

TABLE OF CONTENTS

LIST OF FIGURES

LIST OF TABLES

DEDICATION

My First Wife, of ten years, Lisa Dudek, was instrumental in providing me with the grounding, motivation, and support I needed in the early part of my graduate career. Without her instrumental, if tacit, guidance, much that I have accomplished would have been impossible. As this work is all that remains of those years, I dedicate it to her.

I also wish to gratefully thank my advisor and mentor, Professor Richard B. Kaner for the influence he has had on my thinking and for his kind-hearted patience. In many ways, he is very much of a second father to me. When this is all over, I owe him a Coke Zero.

ACKNOWLEDGEMENTS

Chapter 3 is largely adapted from the work: Mohammadi, R.; Lech, A. T.; Xie, M.; Weaver, B. E.; Yeung, M. T.; Tolbert, S. H.; Kaner, R. B. Tungsten Tetraboride, an Inexpensive Super-hard Material. *Proc. Natl. Acad. Sci. U. S. A.* **2011**, *108*, 10958–10962.

Chapter 4 is largely adapted from the work: Mohammadi, R.; Xie, M.; Lech, A. T.; Turner, C. L.; Kavner, A.; Tolbert, S. H.; Kaner, R. B. Toward Inexpensive Super-hard Materials: Tungsten Tetraboride-Based Solid Solutions. *J. Am. Chem. Soc.* **2012**, *134*, 20660–20668.

In addition to incorporating parts of the above two works, Chapter 5 is also largely adapted from the work: Xie, M.; Mohammadi, R.; Mao, Z.; Armentrout, M. M.; Kavner, A.; Kaner, R. B.; Tolbert, S. H. Exploring the High-Pressure Behavior of Super-hard Tungsten Tetraboride. *Phys. Rev. B* **2012**, *85*, 64118.

I would like to thank Drs. Sven Vogel and Luke Deamon as well as Mr. Helmut Reike at the Lujan Center of the Los Alamos National Laboratory for their help with neutron diffraction experiments. Furthermore, I wish to thank Ceradyne for their generous material's support through their provision of isotopically refined ^{11}B. Financial support for this research from the National Science Foundation under grant 1106364 and the Department of Energy under LANSCE grant number 20112198 is gratefully acknowledged.

VITA

Education

B.S. Chemistry	The Pennsylvania State University 2006
B.S. Biochemistry and Molecular Biology	The Pennsylvania State University 2006
M.S. Chemistry	The University of California Los Angeles 2010
Ph. D Candidate in Chemistry	The University of California Los Angeles 2010 –

Research

Post-Baccalaureate

Research Fellow, UCLA, Kaner Group
Focus 1: Synthesis of new super-hard, ultra-incompressible materials.
Focus 2: Structural/property studies of hard metal borides and their solid solutions.

Undergraduate Research

Fall 2003-Summer 2005	Research for credit, PSU, Bollinger Group, Department of Chem./Biochem./Molec. Biol.
Summer 2003	NSF-REU, WSU, Jones Group Department of Chemistry/Biochemistry
Fall 2002-Spring 2003	Research for credit, PSU, Guiltinan Group Department of Horticulture/Plant Biology

Skills

- High temperature synthesis
- Solvothermal synthesis
- Powder Metallurgy
- Scanning Electron Microscopy (SEM)
- Energy-dispersive spectrometry (EDS)
- X-Ray powder diffraction (XRD)
- TOF-neutron diffraction
- Micro-Indentation
- Nano-Indentation
- Rietveld refinement
- Inductively Coupled Plasma spectrometry(ICP)
- X-ray photoelectron spectroscopy (XPS)
- Atomic Force Microscopy (AFM)
- 13 quarters teaching experience
- NSF Grant application authoring
- Television Consulting
- Repair and maintenance of various common types of laboratory equipment

Awards

Fall 2005 – Spring 2006	Charles R. Gerth Scholarship in Biochemistry
Fall 2004 – Spring 2005	Atlas Scholarship in Biochemistry
Fall 2004 – Spring 2005	Bright Scholarship in Chemistry
Summer 2003	NSF-REU at Washington State University
Fall 2002 – Spring 2006	Schreyer Honors Scholar
Spring 2002	American Chemistry Society Award (in HS)

Publications and Presentations

(1) Kaner, R. B.; Levine, J. B.; Lech, A. T.; Weaver, B. E.; Mohammadi, R.; Tolbert, S. H. Preparation and Properties of Super-hard, Ultra-Incompressible Borides. In *Abstracts of Papers of the American Chemical Society*; 2009; Vol. 238.

(2) Kalantar-zadeh, K.; Tang, J.; Wang, M.; Wang, K. L.; Shailos, A.; Galatsis, K.; Kojima, R.; Strong, V.; Lech, A.; Wlodarski, W.; Kaner, R. B. Synthesis of Nanometre-Thick MoO3 Sheets. *Nanoscale* **2010**, *2*, 429–433.

(3) Mohammadi, R.; Lech, A. T.; Weaver, B. E.; Xie, M.; Yeung, M. T.; Turner, C. L.; Levine, J. B.; Tolbert, S. H.; Kaner, R. B. Ambient-Pressure Synthesis and Characterization of Super-hard Intermetallic and Solid-Solution Borides. In *Abstracts of Papers of the American Chemical Society*; 2011; Vol. 241.

(4) Mohammadi, R.; Lech, A. T.; Xie, M.; Weaver, B. E.; Yeung, M. T.; Tolbert, S. H.; Kaner, R. B. Tungsten Tetraboride, an Inexpensive Super-hard Material. *Proc. Natl. Acad. Sci. U. S. A.* **2011**, *108*, 10958–10962.

(5) Lech, A. T.; Mohammadi, R.; Turner, C. L.; Tolbert, S. H.; Kaner, R. B. Structural Considerations in Refractory Hard Metal Borides. In *Abstracts of Papers of the American Chemical Society*; 2012; Vol. 243.

(6) Mohammadi, R.; Xie, M.; Lech, A. T.; Turner, C. L.; Kavner, A.; Tolbert, S. H.; Kaner, R. B. Toward Inexpensive Super-hard Materials: Tungsten Tetraboride-Based Solid Solutions. *J. Am. Chem. Soc.* **2012**, *134*, 20660–20668.

(7) Strong, V.; Dubin, S.; El-Kady, M. F.; Lech, A.; Wang, Y.; Weiller, B. H.; Kaner, R. B. Patterning and Electronic Tuning of Laser Scribed Graphene for Flexible All-Carbon Devices. *ACS Nano* **2012**, *6*, 1395–1403.

(8) Mariani, G.; Wang, Y.; Wong, P.-S.; Lech, A.; Hung, C.-H.; Shapiro, J.; Prikhodko, S.; El-Kady, M.; Kaner, R. B.; Huffaker, D. L. Three-Dimensional Core-Shell Hybrid Solar Cells via Controlled in Situ Materials Engineering. *Nano Lett.* **2012**, *12*, 3581–3586.

(9) Kaner, R. B.; Tolbert, S. H.; Mohammadi, R.; Lech, A. T.; Xie, M.; others. Compositional Variations of Tungsten Tetraboride With Transition Metals and Light Elements. WO2013022503, 2013.

(10) D'Arcy, J. M.; El-Kady, M. F.; Khine, P. P.; Zhang, L.; Lee, S. H.; Davis, N. R.; Liu, D. S.; Yeung, M. T.; Kim, S. Y.; Turner, C. L.; Lech, A. T.; Hammond, P. T.; Kaner, R. B. Vapor-Phase Polymerization of Nanofibrillar poly(3,4-Ethylenedioxythiophene) for Supercapacitors. *ACS Nano* **2014**, *8*, 1500–1510.

Chapter 1

Introduction

Motivation

The creation or discovery of (and subsequent mastery over) new tools and tool materials is an endeavor at least as old as man himself. The importance of *hard* materials to tools, technology, and the societies they sustain is so self-evident that it was once common archaeological practice to name pre-historic human eras by the tooling resources employed (i.e. Stone Age[1], Bronze Age[2], Iron Age[3], etc.) – an established succession of ever stronger, more versatile, more *chemically-tailored* materials.[4]

As new engineering materials are developed for increasingly demanding tasks, the tools used to machine them must advance as well. The availability of new structural steels in the 19th century played no small part in accelerating the industrial revolution.[5,6] Some have even referred to this time period as "The Steel Age"[7] (marking the introduction of steels with controlled carbon content) or "The Alloy Age"[8] (demarked by the introduction of high-speed too steels). However, the properties that made these steels desirable also made them difficult to work. Thus, by chemical modification and engineering treatments, new iron alloys and high-speed steels were developed to work them into useful forms.[9] Likewise, the introduction of cemented tungsten carbide (WC) tooling (known industrially as "hard metals") in the 20th century again revolutionized the world of machining and forming.[10] Tools made of these compounds may be used to "turn" (cut by lathing) high-performance super-alloys[11] for aerospace, or new metal-matrix ceramic composites for advanced engine designs.[12] It would seem that no sooner has a newer, more efficient tool material been developed than new applications for it are immediately tested and more industrial progress is made.

In modernity, the compounds useful for tooling under demanding conditions have been dominated by metal carbides of tungsten and titanium.[12] Newer grades of cemented carbides are superior to older ones due to enhancements such as grain refining[13–16] (including nano-structuring[17]), solid-solution hardening[18–20], multi-phase dispersions[21], and the addition of protective coatings[22]. Through these enhancements, we have learned much about the science of materials; but, by comparison against an entirely new generation of compounds, they have been largely incremental feats of engineering.[23] Additionally, and most frustratingly, most such knowledge is obfuscated by vague patents or trade secrets.[24] Meanwhile, high performance and difficult to machine materials have continued to proliferate.[25] There is, therefore, great demand for new, harder compounds.[26]

In order to bring about another revolutionize of the machining industry, it seems apparent that the next generation of tool materials must be based on so-called "super-hard" compounds, *i.e*. those demonstrating indentation hardness values in excess of ≈40 GPa[27]. The most obvious place to look for these materials might then be in the direction of diamond and it's extremely hard, hetero-atom analogue, cubic boron nitride (*c*-BN). However, while there are indeed tools available[28–31] based on these compounds, their application is surprisingly limited as cutting and forming tools.

While diamond possesses superlative hardness, is a poor choice for cutting steels and other alloys containing Group VIII transition metals (Fe, Ni, Co), as these metals cause its catalytic degradation to graphite and subsequent dissolution to form brittle carbides.[32] Thus, edges of diamond tools are rapidly dulled and yield inferior results on a variety of common substrates. Cubic boron nitride, another extremely hard material, largely circumvents this issue, but is exceptionally difficult to produce in large quantities as it requires high pressure – high temperature conditions to synthesize, which leads to it being even more expensive than diamond. The application of both materials is further complicated by

the difficulty of grinding, sintering, or otherwise shaping them, either into their final geometry, or for re-sharpening.[33]

Metals, alloys, and metallic compounds do not suffer this limitation because they may be shaped using techniques that take advantage of their electrical conductivity. Thus, while insulators such as diamond, *c*-BN, and most ceramics can be sintered by furnaces and cut only mechanically, metals can be synthesized by electric arc melting, fused by radio-frequency induction and cut by electric discharge machining (EDM).[34] These, less 'conventional', processes are inherently independent of the hardness of the compound being manipulated, are much less limited by the melting point of containment vessels, and are often significantly more time and energy efficient than prolonged powder metallurgy or grinding.

Our approach to the creation of new hard materials has not been to make well-known compounds more workable, but rather to introduce and characterize new ones with desirable properties. Therefore, our goal is to lay the foundation for this next advancement through the continued development of materials we refer to as *super-hard metals* or *refractory hard-metal borides*. To achieve this goal, we have operated under the hypothesis that, by introducing short, covalent bonds to metals with a large number of valence electrons, such as osmium, rhenium and tungsten, a system of delocalized, conductive electrons can be maintained while the metal atoms themselves are rigidly locked in place (**Figure 1.1**).[35–37] NSF funding has allowed us to demonstrate this concept in compounds such as OsB_2, ReB_2, and WB_4.[38–40] In fact, these materials, particularly ReB_2 and WB_4, are among the hardest metallic species known.[41,42]

Borides

Most metals of Group 7 and earlier, including the rare earths, form at least one diboride (see **Figure 1.1**). For the most part, these borides are nearly universally of the AlB_2 structure-type (**Figure 1.1a**). The crystallographic properties of these borides are extremely uniform, with a few notable exceptions such as MgB_2, as well as the non-stoichiometric compounds $Nb_{1-x}B_{2+y}$, $Ta_{1-x}B_{2+y}$, and $Al_{1-x}B_2$. In fact, a nearly perfectly linear trend line (**Figure 1.3**) may be fit to a plot *c* versus a for their unit cell axes, which shows a generally smooth increase in the size of both parameters as the size of the metal atom is also increased, with the *c*-axis increasing approximately $\sqrt{2} * \sqrt{3}$ faster than the *a*-axis. This behavior is followed quite well for solid solutions between these borides (when the size ratio of the metal atoms permit), indicating generally good adherence to Vegard's Law (**Table 1.2** and **Figure 1.3**).[43]

Many of these borides are very hard, as summarized in **Table 1.3**, but none of them are super-hard (having hardness greater than 40 GPa, at any load). They are, however, nearly as a rule, harder than the corresponding carbides, as the indentation hardness values for a selection of which are available in **Table 1.4**. The hardness of TiB_2 is approximately 13% higher, for instance, than the corresponding carbide TiC, which is already one of the hardest carbides known and at the forefront of some of the most advanced carbide-based cutting tools.[12] That TiB_2 should be harder than TiC should, however, be expected. Both carbon and boron are members of the p-block in the period table, and are therefore elements that strongly favor the formation of covalent bonds. As TiB_2 contains a higher concentration of a covalent bond forming element, the entire compound is thus more covalent and therefore harder.[44,45]

There is also, however, a strong correlation between the hardness of a compound and its incompressibility.[27,46] Our initial forays into the world of hard metals where motivated by this principle. Thus, we took the metal with the highest room temperature incompressibility (osmium, 395 – 462

GPa[47–49], c.f. diamond 442 GPa[50]) and added enough excess boron to form OsB_2. The hardness data of the resulting compound are presented in **Figure 1.4**, where it is apparent that OsB_2 is extremely hard, but not super-hard. Somewhat to our surprise, the lattice in OsB_2 is greatly expanded versus that of pure osmium and no longer contains any close-packed layers. In fact, OsB_2 takes a unique structure type among the borides, shared only with RuB_2 and a few solid solutions, and nearly totally un-related to that of the AlB_2 structure-type (see **Figure 1.1b**). However, OsB_2 still has an extremely high incompressibility (365 – 395 GPa)[51], and we were thus encouraged by these results.

It was on our second attempt at synthesizing a super-hard boride that we succeeded, resulting in our discovery of the extremely high hardness and incompressibility of rhenium diboride (ReB_2).[52] While ReB_2 also takes a unique structure (**Figure 1.1c**), the unit cell of the parent HCP metal is not nearly so disturbed as it is in the case of OsB_2 and, in fact, the layer of metal in the *a* – *b* plane is nearly close-packed, with a linear expansion of only ≈5% (2.90 Å versus 2.76 Å). With this less grossly distorted structure, ReB_2 obtains an extremely high 40.5 GPa micro-indentation hardness (**Figure 1.5**) and has a bulk modulus (incompressibility) of 360 GPa. In fact, given rhenium diboride's metallic conductivity[53], we consider ReB_2 to be the first super-hard metal identified.

In addition to its high hardness, high bulk modulus, and high conductivity, rhenium diboride is also extremely crystalline. In fact, ReB_2 solidifies with multiple, visible facets directly from the molten mass produced by arc-melting elemental powders of rhenium and boron. An image of such an as-prepared ReB_2 ingot is shown in **Figure 1.6**, and **Figure 1.7** shows an SEM image of the surface of one of these facets. The clearly hexagonal pattern visible on all of the crystalline faces is a strong indicator that ReB_2 demonstrates a preferential growth direction in the *a* – *b* plane, yielding the *c*-plane as the largest surface. This hypothesis is confirmed by X-ray diffraction (**Figure 1.8**), as well as from the morphology of crystals of rhenium diboride grown from an aluminum flux.[53] This high crystallinity can be taken as a

qualitative indicator of the unusual position that super-hard metals hold between that of a “metal” in the sense of being lustrous and highly conductive, and that of a “ceramic” in the sense of being highly crystalline and hard. Some interesting properties of solid solutions based on ReB_2 will be discussed in Chapter 2.

Finally, moving yet one element further to the left on the Periodic Table, we aimed our attention at the tungsten borides. Indeed, tungsten is one of the few main-group transition metals to form a boride with a B : M ratio greater than 2 : 1. In this case the compound is “tungsten tetraboride” (WB_4), although the composition of the compound is actually closer to $WB_{4.25}$ (see Chapter 6). WB_4 takes yet another interesting structure (**Figure 1.1d**) which we have recently solved by powder X-ray and time-of-flight neutron diffraction (Chapter 6). The micro-indentation hardness of WB_4 is given in **Figure 1.9**, and again demonstrates super-hardness. Solid solutions based on WB_4 with the nearby metals tantalum and chromium, as discussed in Chapter 4, have the current distinction (as of 2014) of being the hardest metals known.

What follow in the remaining chapters of this Thesis are a series of detailed discussions of borides based on the above parent compounds, with particular emphasis on ReB_2-type solid-solutions and WB_4. Given the proclivity of these compounds to take unique crystal structures, a strong emphasis is put on crystallography and crystallochemistry. It has been the aim of this Thesis Candidate to further explore, understand, and harness the structure-property relationships in these borides, as it is hoped the following might demonstrate.

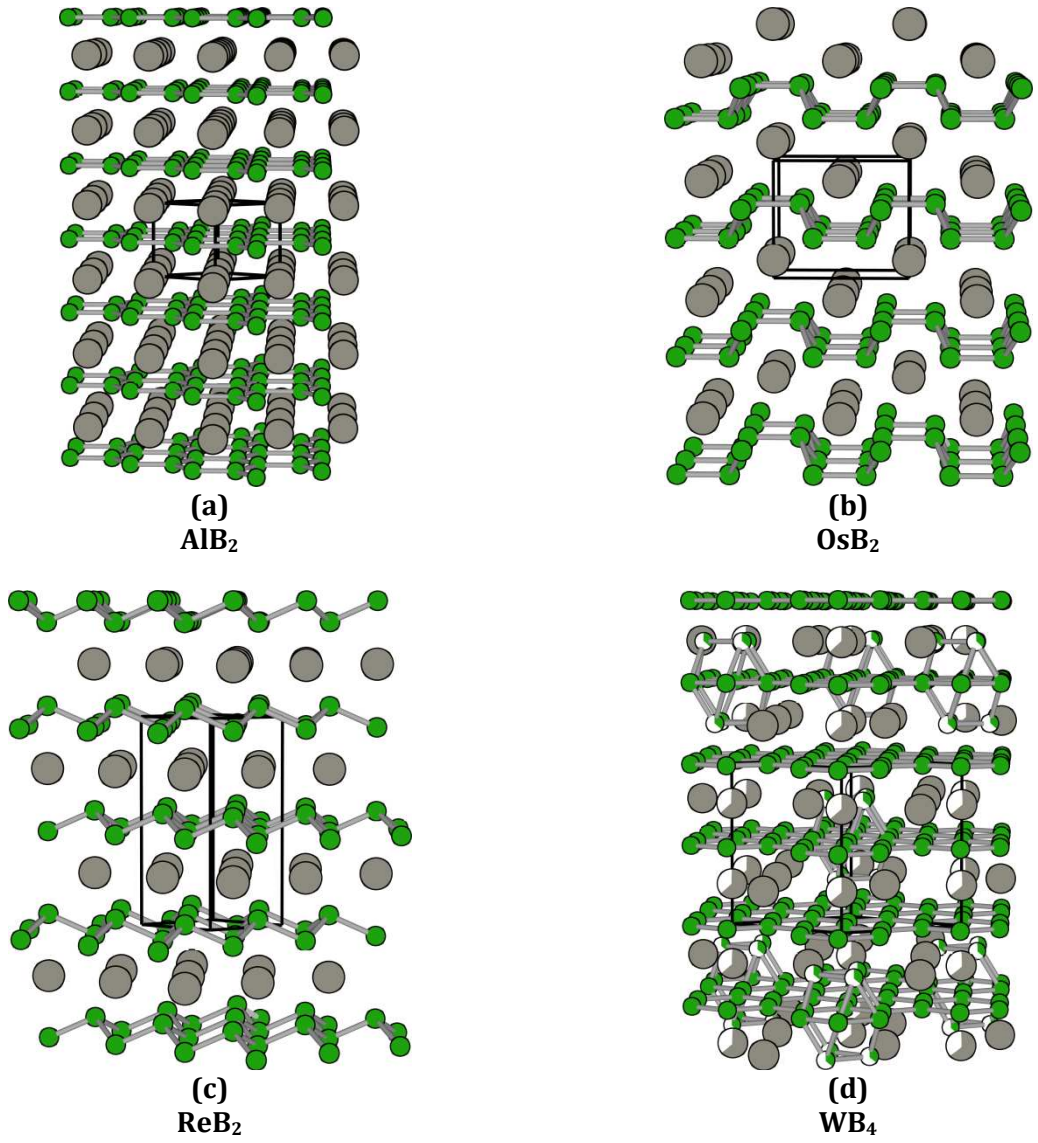

Figure 1.1: The structures of a few of the most relevant borides discussed in this Thesis.

Table 1.1: Lattice Parameters, Unit Cell Volumes, and Axial Ratios for a Selection of Diborides

Composition	*a* Parameter (Å)	*c* Parameter (Å)	Volume (Å^3)	*c*/*a* Ratio
AlB_2[54,55]	3.0045	3.2524	25.4257	1.0825
CrB_2[56–60]	2.9718	3.0690	23.4729	1.0327
DyB_2[61,62]	3.2872	3.8422	35.9548	1.1688
ErB_2[61,63,64]	3.2706	3.7837	35.0519	1.1569
GdB_2[65]	3.3150	3.9360	37.4587	1.1873
HfB_2[66–69]	3.1433	3.4743	29.7269	1.1053
HoB_2[61,63,65]	3.2812	3.8142	35.5624	1.1625
LuB_2[61,70]	3.2431	3.7116	33.8070	1.1444
MnB_2[71,72]	3.0083	3.0377	23.8069	1.0098
MoB_2[73–76]	3.0119	3.1402	24.6691	1.0426
NbB_2[69,77,78]	3.0830	3.3030	27.1886	1.0714
ScB_2[61,79]	3.1480	3.5159	30.1740	1.1169
TaB_2[77,80,81]	3.3185	4.0275	38.4112	1.2137
TbB_2[62,63]	3.0712	3.2760	26.7601	1.0667
TiB_2[82,83]	3.2919	3.8820	36.4318	1.1793
TmB_2[61,64,65]	3.0302	3.2282	25.6701	1.0653
VB_2[84,85]	3.2588	3.7491	34.4798	1.1505
YbB_2[86,87]	2.9994	3.0585	23.8291	1.0197
YB_2[61,88]	3.2503	3.7315	34.1400	1.1480
ZrB_2[89,90]	3.3011	3.8448	36.2841	1.1647
SmB_2[65,91]	3.1691	3.5299	30.7019	1.1138

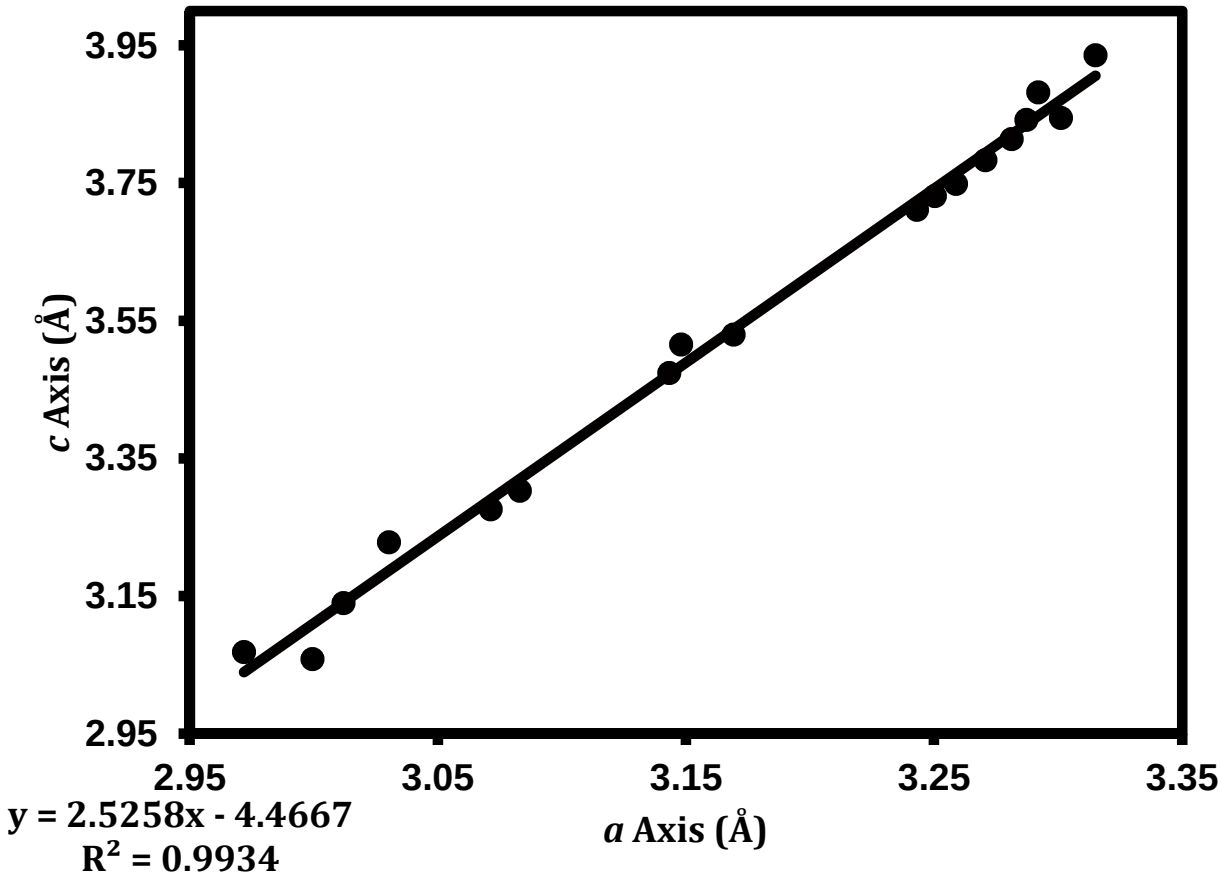

Figure 1.2: A plot of *c versus a* axes for the borides presented in **Figure 1.1**. The trend is fit well by a linear regression curve (lower left corner).

Table 1.2: Lattice Parameters, Unit Cell Volumes, and Axial Ratios for a Selection of Solid-Solutions Among the Diborides

Composition	*a* Parameter (Å)	*c* Parameter (Å)	Volume (Å^3)	*c/a* Ratio
$Cr_{0.5}V_{0.5}B_2$[68]	2.99	3.045	23.5755	1.0184
$Cr_{0.6}V_{0.4}B_2$[92]	2.979	3.063	23.5407	1.0282
$Al_{0.23}Ta_{0.77}B_2$[93]	3.06	3.294	26.7114	1.0765
$Al_{0.333}Nb_{0.667}B_2$[93]	3.068	3.334	27.1773	1.0867
$Cr_{0.5}Mo_{0.5}B_2$[68]	3.01	3.12	24.4804	1.0365
$Cr_{0.5}Ti_{0.5}B_2$[68]	2.99	3.14	24.3110	1.0502
$Cr_{0.5}Ta_{0.5}B_2$[68]	3.025	3.21	25.4382	1.0612
$Hf_{0.5}Ti_{0.5}B_2$[68]	3.085	3.368	27.7596	1.0917
$Hf_{0.5}Ta_{0.5}B_2$[69]	3.11	3.37	28.2281	1.0836
$Hf_{0.5}Nb_{0.5}B_2$[69]	3.12	3.4	28.6628	1.0897
$Hf_{0.5}Zr_{0.5}B_2$[68]	3.155	3.497	30.1457	1.1084
$Mo_{0.5}Ti_{0.5}B_2$[68]	3.035	3.206	25.5748	1.0563
$Ti_{0.5}Mo_{0.5}B_2$[75]	3.044	3.207	25.7347	1.0535
$Mo_{0.5}Zr_{0.5}B_2$[68]	3.085	3.4	28.0233	1.1021
$Nb_{0.5}V_{0.5}B_2$[69]	3.03	3.2	25.4429	1.0561
$Nb_{0.5}Ti_{0.5}B_2$[68]	3.06	3.264	26.4682	1.0667
$Nb_{0.5}Zr_{0.5}B_2$[68]	3.128	3.42	28.9795	1.0934
$Ta_{0.5}V_{0.5}B_2$[69]	3.04	3.16	25.2909	1.0395
$Ta_{0.5}Ti_{0.5}B_2$[68]	3.05	3.246	26.1504	1.0643
$Ta_{0.5}Zr_{0.5}B_2$[68]	3.12	3.4	28.6628	1.0897
$Ti_{0.5}V_{0.5}B_2$[68]	3.01	3.15	24.7158	1.0465
$Ti_{0.5}Zr_{0.5}B_2$[68]	3.098	3.39	28.1769	1.0943
$Ti_{0.39}Zr_{0.61}B_2$[94]	3.12	3.42	28.8314	1.0962

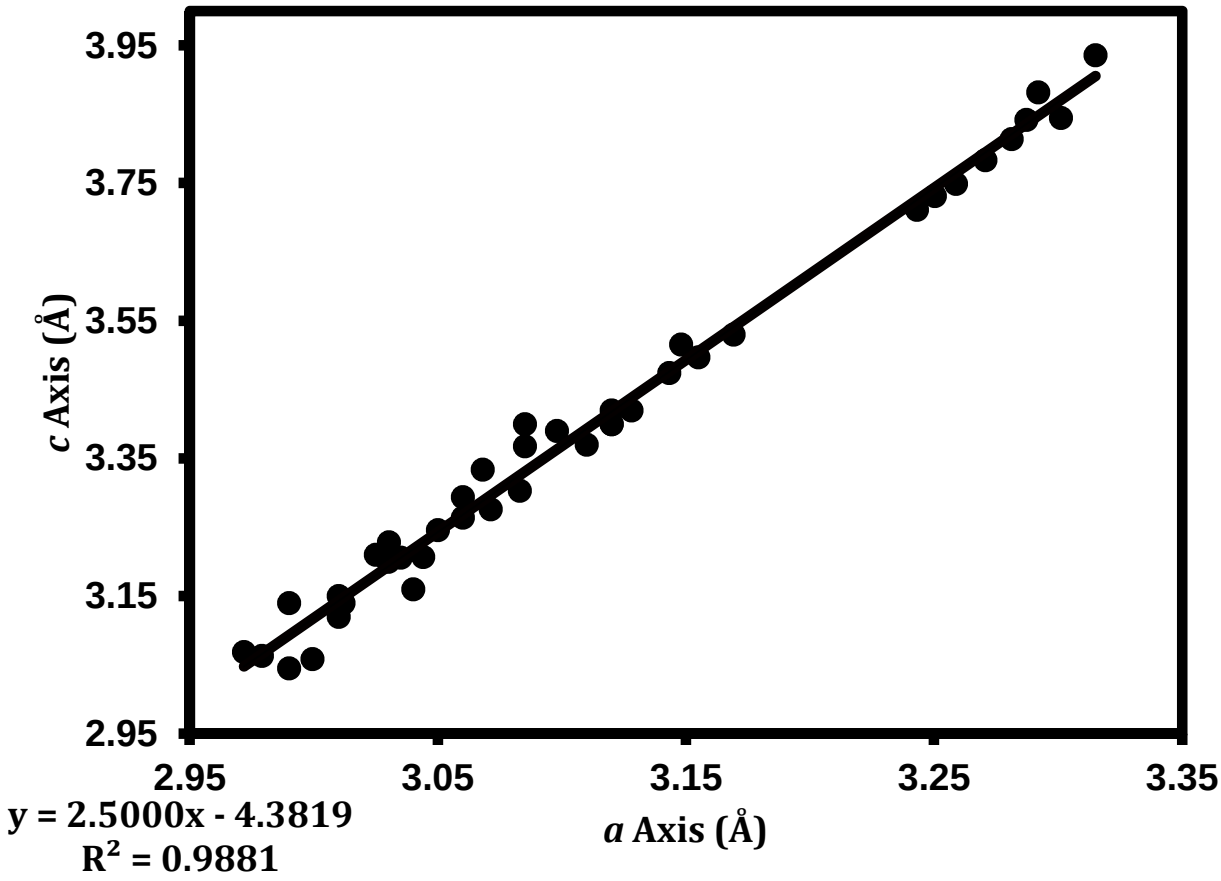

Figure 1.3: A plot of *c versus a* axes for the borides presented in **Table 1.2**. The trend is fit nearly as well by a linear regression curve (lower left corner) as the presentation in **Figure 1.2** and would likely be further improved by additional certainty through averaging replications of the solid solutions.

Table 1.3: Hardness Data for a Selection of AlB_2-Type Diborides

Compound	Row	Group	Type	H_v (GPa)	Load (grams)
ScB_2	4	3b	Single crystal	17.8[79]	--
TiB_2	4	4b	Polycrystalline	33.04[95]	--
ZrB_2	5	4b	Polycrystalline	29.40[90]	50
			{100}	19.51[77]	200
			{001}	22.26[77]	200
HfB_2	6	4b	Polycrystalline	31.50[90]	50
			{100}	24.52[77]	200
			{001}	17.85[77]	200
VB_2	4	5b	Polycrystalline	25.40[95]	--
			{100}	30.59[84]	200
			{001}	30.18[84]	200
			{101}	27.12[84]	200
NbB_2	5	5b	{100}	19.12[77]	200
			{001}	21.67[77]	200
TaB_2	6	5b	{100}	22.26[77]	200
			{001}	29.22[77]	200
			{001}	27.26-29.03[80]	200
			Polycrystalline	20.89-21.97[56]	50
CrB_2	4	6b	Polycrystalline	20.59[96]	50
			{100}	21.4[60]	100-200
			{001}	22.6[60]	100-200
Mo_2B_4	5	6b	Polycrystalline	15.2[97]	500
MnB_2	4	7b	Polycrystalline	12.40[72]	50

Table 1.4: The Hardness Under Low-Load (50 gram-force, 0.49 N), adapted from Samsonov *et al.*[98], of a Selection of Common Carbides

Compound	Hardness (GPA)
TiC	29.27
ZrC	28.68
HfC	28.57
VC	20.54
NbC	19.23
TaC	15.69
WC	17.45

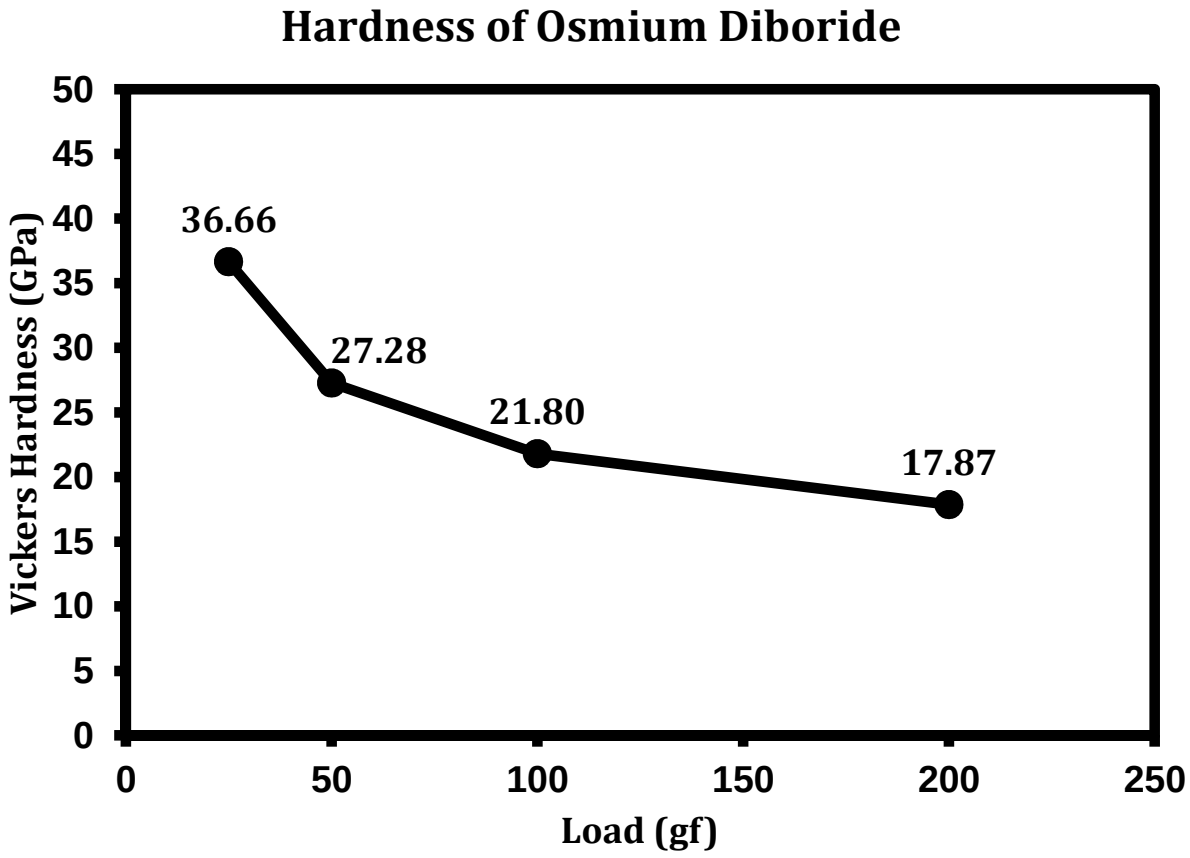

Figure 1.4: A plot of the hardness of osmium diboride. While very hard, OsB_2 never breaks the 40 GPa cut-off for super-hard materials.

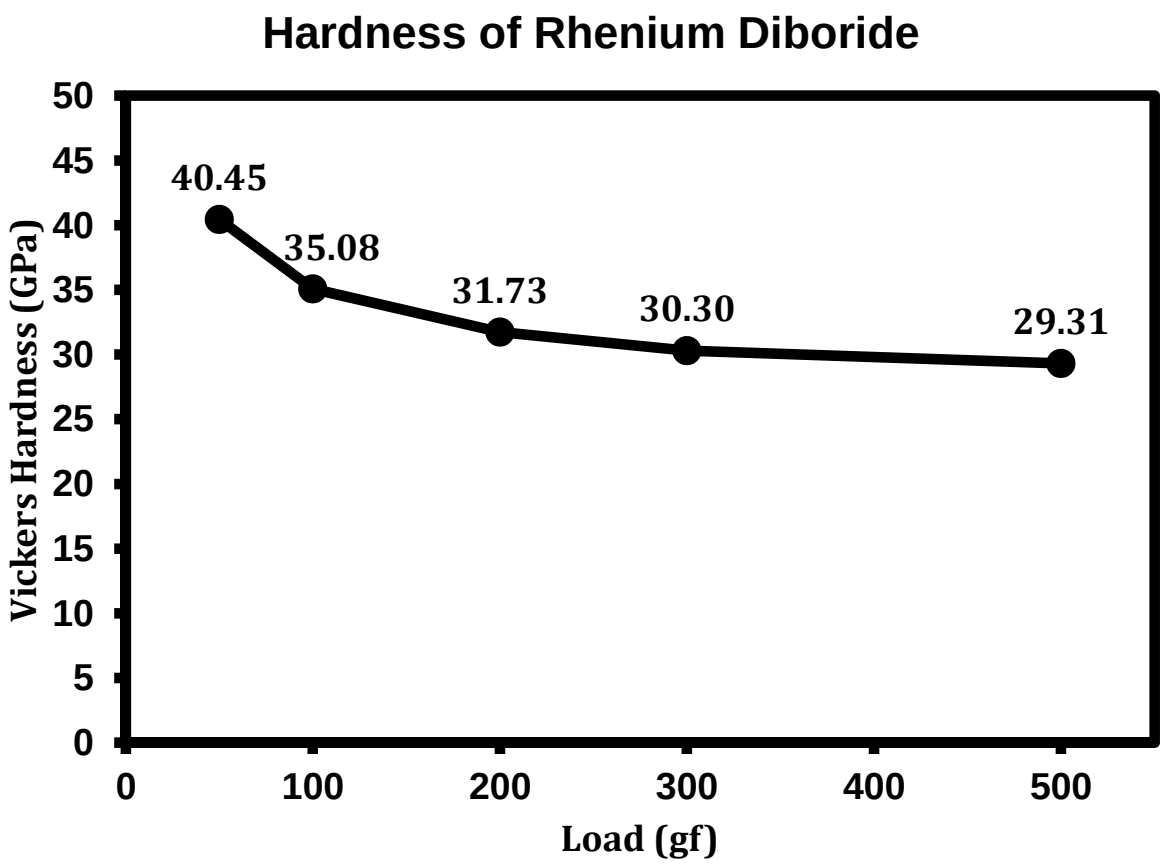

Figure 1.5: A plot of the hardness of rhenium diboride. ReB_2 is much harder than OsB_2, reaching over 40 GPa of hardness at low load. The fall-off in hardness at higher loads is also significantly decreased as compared to OsB_2.

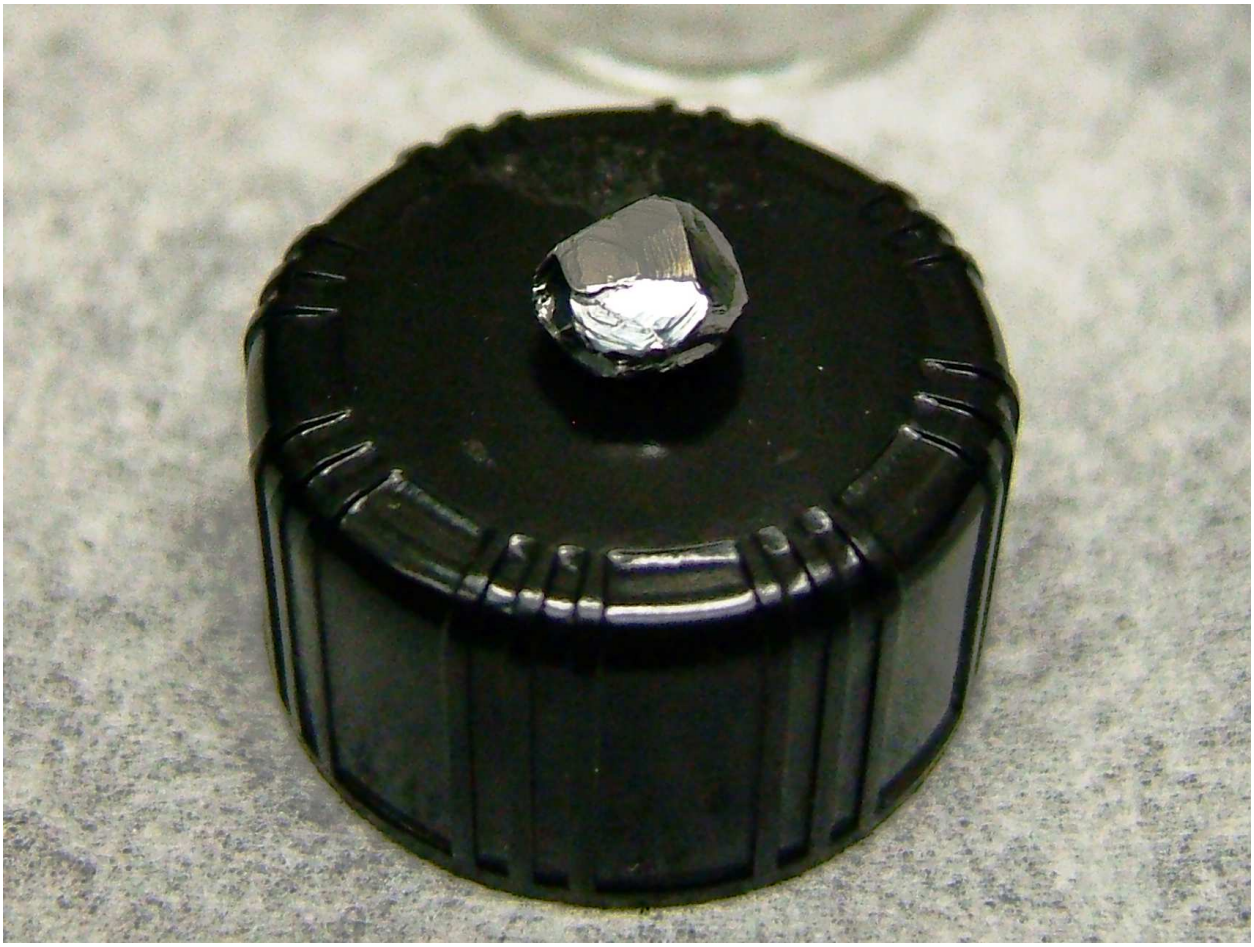

Figure 1.6: An ingot of ReB_2 formed directly from the molten compound during arc-melting. Note the highly crystalline nature of this compound, as evidenced by the large facets.

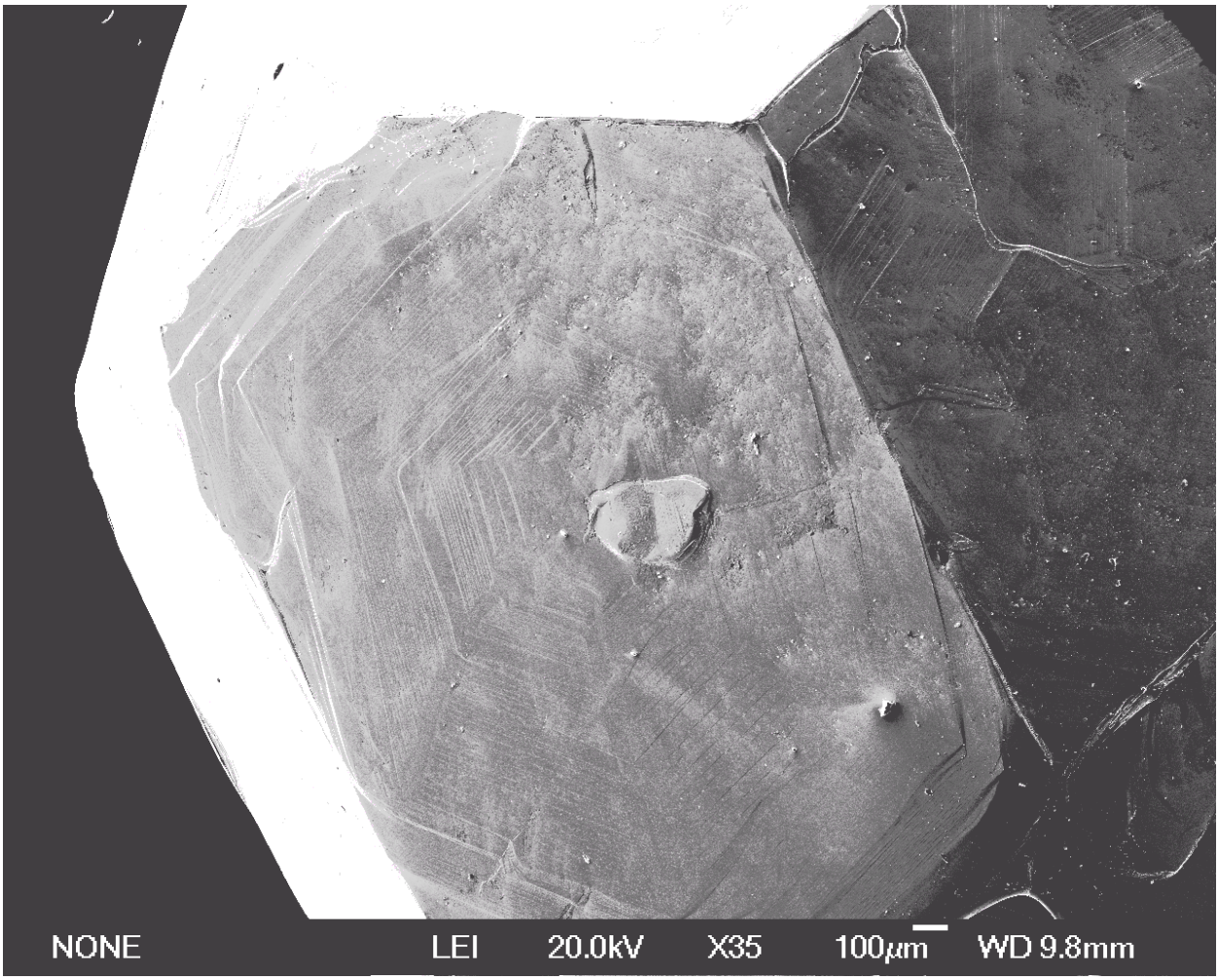

Figure 1.7: An SEM image of an ReB_2 ingot, similar to **Figure 1.6** above. A regular hexagonal pattern is obvious from the striations. The crystalline facets are highly oriented along the *c*-axis.

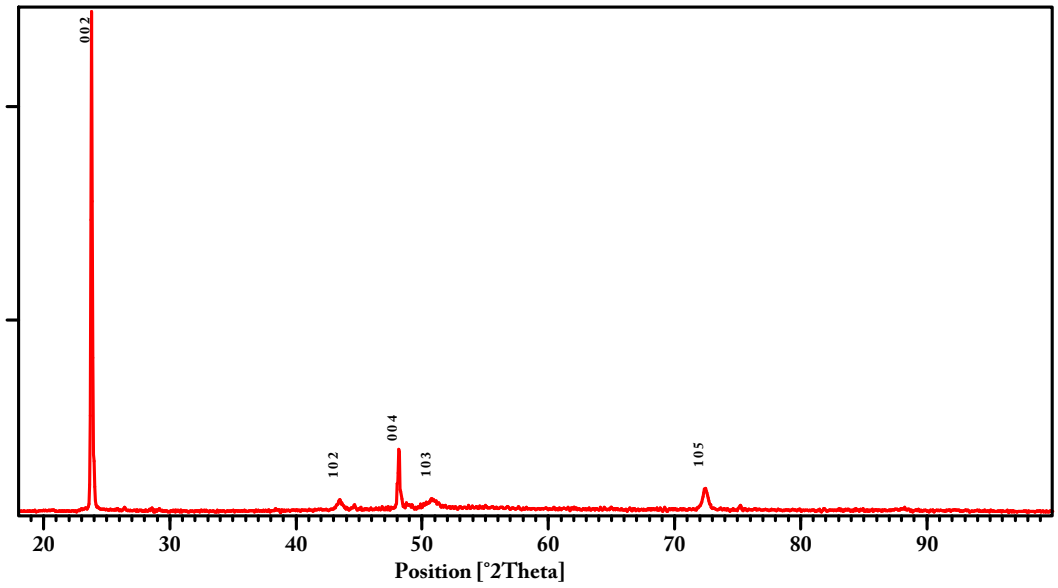

Figure 1.8: X-ray diffraction pattern of the ReB_2 ingot shown above in **Figure 1.6**, showing that the facets on the surface are, indeed, the [002] *c*-axis growth plates.

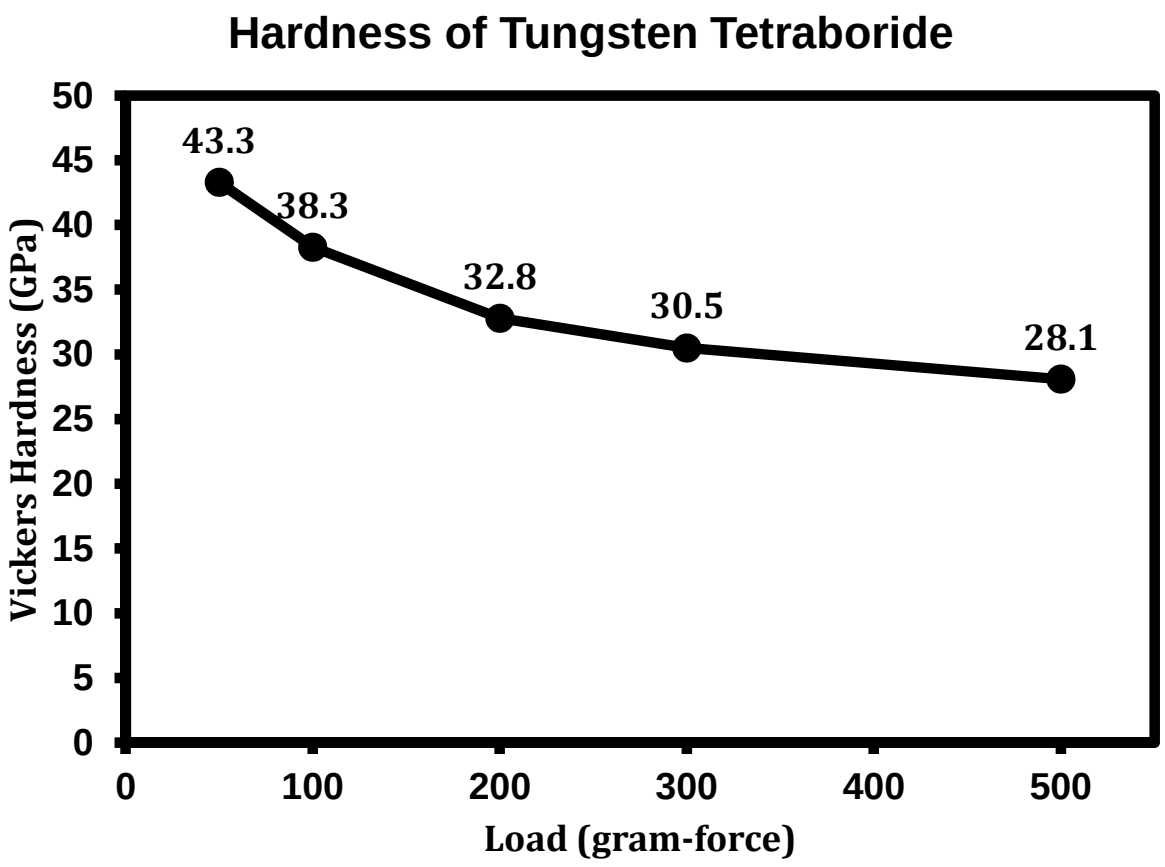

Figure 1.9: A plot of the hardness of tungsten tetraboride. WB_4 is at least as hard as ReB_2 and much harder than OsB_2, reaching over 40 GPa of hardness at low load. The fall-off in hardness at higher loads is also significantly decreased as compared to OsB_2, and comparable to that of ReB_2.

Chapter 2

Super-Hard Solid-Solutions of Tungsten in Rhenium Diboride

Introduction

The transition metal borides have attracted attention amongst materials researchers for many years due to their combination of outstanding physical properties such as metallic conductivity, high incompressibility, high shear strength, and exceptionally high hardness.[99] All of these attributes are desirable in materials for structural and engineering compounds and could positively indicated that diborides may be suitable replacements for current metal carbides in next-generation cutting tools.[100] These properties are also, generally, highly correlated, with a high bulk modulus (incompressibility), for example, appearing to be a necessary[27], if not sufficient[46], predictor of high hardness. [101] It has been the design philosophy of our laboratory to take advantage of this correlation by attempting to force highly incompressible metals to also become resistant to shear through the introduction of additional covalent bonds.[102,103] As boron is a small, highly covalent[104] element that is capable of forming bonds to metals[105], our attention was drawn to transition metal borides as well.

As such, we have previously shown that rhenium diboride (ReB_2) is one of the hardest metallic compounds yet discovered, with a hardness under low loads (0.49 N) reaching as high as 40.5 GPa.[53] This value is above the arbitrary threshold[27] of 40 GPa commonly accepted for super-hard compounds, and gives ReB_2 the distinction of being one of the first super-hard metals identified.[52] We have since moved our attention to even higher borides, such as WB_4, which we have shown has the potential to be even harder, achieving a Vickers hardness of up to 57.3 GPa under a 0.49 N load.[106] However, it was in the course of our work with tungsten tetraboride that we first noticed a peculiarity in the interaction of

rhenium and tungsten in the presence of excess boron.[107] While the addition of rhenium was found to slightly increase the hardness of WB_4, this effect was due most apparently to a fine dispersion of ReB_2 found in the arc melted ingots. Intriguingly, the lattice parameters of the ReB_2 dispersion were found to be somewhat larger than those of pure ReB_2, implying the formation of a solid solution between rhenium diboride and a boride of tungsten.

Tungsten diboride is not known to take the ReB_2 structure. Indeed, the structure of WB_2 (previously referred to as "W_2B_5", a name that will be used here to refer to its unique structure type) is somewhat unique among the borides in that it equally incorporates structural elements found in two parent structure types: AlB_2 (*P6/mmm*) and ReB_2 (*$P6_3$/mmc*) (**Figure 2.1**). Given the hybrid nature of the structure of WB_2, it seems intuitive that that tungsten might show some ability to form mixed-metal ternaries and solid solutions with *either* the ReB_2 *or* the AlB_2 structure-types. Indeed, solid solutions of tungsten with other borides taking the AlB_2 structure type (e.g. TiB_2) have been noted.[108] Furthermore, it is known that some tungsten-containing ternaries, such as $W_{0.5}Ru_{0.5}B_2$ and $W_{0.5}Os_{0.5}B_2$ may take the ReB_2 structure-type, as first identified by Rogl *et al.*[109–111] and recently revisited by Zelringer and Rogl *et alia*[112]. Unfortunately, little is known about the solid solubility of tungsten in ReB_2 itself, save for a lone mention by Kuz'ma *et al.* in a Soviet-era phase-diagram[89].

Additionally, since the our original identification of super-hardness in ReB_2, an increasingly large number of theoretical works have appeared in the literature purporting to calculate the hardness "from first-principles" of metal borides of this type. [113–129] Several of these works have made claims to "predict" the already measured and reported properties of previously synthesized materials. Therefore, it is as-yet unclear to what extent the experimentalist might find these sorts of calculations to be a useful guidance for the creation of new compounds with reliably pre-determined properties, and to what extent these works represent *post-hoc* rationalization of properties that have already been determined. A few of

these works, however, have gone so far as to make predictions for the properties of solid solutions that are hypothetically synthesizable using ordinary techniques, but the properties for which have not yet been reported. Included among these are several works making predictions for the ReB_2-structured WB_2 and tungsten/rhenium diboride solid solutions. [113,116,124,125,129–131]

For the above to reasons, solid solutions employing WB_2 as either the host or guest component are a worthy system of study for the hard-materials researcher. From a crystallochemical perspective, WB_2's hybrid structure should lend it to relatively straight-forward transformations to other structure types with, presumably, 'tunable' lattice parameters and properties. From the perspective of the experimentalist wary of the reliability of guidance taken from "theory", it makes an interesting test for the accuracy that can be expected from predictions of this kind.

Here, we report the successful synthesis of solid solutions of tungsten diboride – rhenium diboride based on the super-hard ReB_2 structure-type, the hardness of these solid solutions, and the structural evolution occurring in the ReB_2 lattice as a result of the dissolution of tungsten. The work presented here would appear to be the only extant, detailed, experimental study of properties of solid solutions of tungsten and rhenium diborides. Surprisingly, we have found that, while tungsten causes a monotonic increase in the lattice parameters of ReB_2, all of the solutions maintain super-hardness under low loads, and, for small additions of tungsten metal, the hardness is significantly increased by *c.a.* ≈17%. Comparisons of these properties to selected theoretical prediction from the literature are also made, from which we conclude that "first-principles" hardness modeling does, indeed, have some merit to the experimentalist.

Materials and Methods

Powders of tungsten (99.9994%, JMC Puratronic, U.S.A.), rhenium (99.99%, CERAC Inc., U.S.A), and amorphous boron (99+%, Strem Chemicals, U.S.A) were uniformly mixed in the ratio M : B = 1 : 2.25 using an agate mortar and pestle. A slight excess of boron is required to counter-act the evaporation of boron during the process of arc-melting, and to prevent the formation of lower borides of tungsten. Tungsten was substituted for rhenium at concentrations in the range of 0.5 – 50.0 at.%. Each mixture was pressed into a 12 mm, ≈350 mg pellet by means of a hydraulic (Model 3851, Carver, USA) press under 10 000 pounds of force. The pellets were then placed in an arc melting furnace consisting of a non-consumable tungsten electrode and water cooled copper hearth and purged 4 times under high-purity argon. After eliminating the last traces of oxygen from the system by melting several small chips of titanium, an AC current of ≥70 amps was applied to the samples at ambient pressure. The fused ingots were then flipped and re-subjected to the electric arc a total of three times to ensure homogeneity.

After cooling, the ingots were bisected using a sinter-bonded diamond lapidary sectioning saw (South Bay Technology Inc., USA). One-half of each ingot was crushed to a fine (-625 mesh) powder using a hardened-steel mortar. The powdered samples were washed 3 times with 1 M HCl to remove impurities introduced from the steel grinding equipment and mounted in a flat-stage samples holder for X-ray diffraction (XRD) employing an X'Pert Pro™ X-ray powder diffraction system (PANalytical, Netherlands). The X-ray diffraction data (λ: $K_{\alpha 1}$ = 1.540598 Å $K_{\alpha 2}$ = 1.544260 Å)[132] were subjected to least-squares refinement using the EXPGUI[133] and GSAS[134] Rietveld refinement software packages, from which the lattice parameters were extracted.

To further verify the results obtained from X-ray diffraction, check for possible substitutional ordering, and to assess what effect, if any, was had on the position of the boron atom in the ReB_2 structure samples of ReB_2 and $W_{0.48}Re_{0.52}B_2$ enriched in 98.5% ^{11}B (Ceradyne, 3M USA) were also subjected to neutron time-of-flight powder diffraction at the HIPPO Beamline at LANSCE, Los Alamos New Mexico. The samples had each been annealed at 1300 K for 24 hours prior to their coarse grinding (-220 mesh) and subsequent washing with 1 M HCl. The powders were placed in sealed vanadium "cans" and subjected to thermal neutron irradiation for total time of 1 h each whilst their diffraction pattern was collected by an array of 3He scintillation-counter panels arranged at 144° and 90° degrees about the sample. The neutron diffraction data were refined from the high-resolution 144° back-scattering panel using the EXPGUI[133] and GSAS[134] Rietveld refinement software packages.

The other half of the ingot was cold mounted in epoxy, using a resin/hardener set (Allied High Tech Products Inc.) and polished to an optically flat surface for hardness testing. Polishing was performed with a tripod polisher (South Bay Technology Inc., USA) using SiC polishing papers (120 – 1,200 grit, Allied High Tech Products Inc., USA) followed by diamond films (30 – 0.5 µm, South Bay Technology Inc., USA). Micro-indentation and nano-indentation were performed to test the hardness of these samples.

Vickers micro-indentation was executed using a MicroMet® 2103 micro-hardness tester (Buehler GmBH, Germany) with a pyramid diamond tip. Indentations were made by applying five loads ranging from 0.49 N to 4.9 N with a dwell time of 15 s. To ensure accuracy, at least 15 randomly chosen spots separated by over 100 micrometers where chosen for indentation. The results reported here represent the average of these points. The lengths of the diagonals of the indents were then measured with a high-resolution Zeiss Axiotech® 100HD optical microscope (Carl Zeiss Vision GmbH, Germany) and **Equation (2.1)** was used to obtain Vickers micro-indentation hardness values (H_v):

$$H_v = \frac{1854.4P}{d^2} \qquad \textbf{Equation (2.1)}$$

where *P* is the applied load (in N) and *d* is the arithmetic mean of the diagonals of the indent (in micrometers).

To corroborate the results of micro-indentation, nano-indentation was also performed using an MTS Nano Indenter XP (MTS, USA) with a Berkovich diamond tip. After calibration of the indenter with a standard silica block, the samples were indented automatically over-night to a depth of 950 nm at 20 randomly pre-determined points and the resulting load versus displacement plots were averaged. The nano-indentation hardness of the material may be found based on the shape of the loading and un-loading curves by the method of Oliver and Pharr[135] using **Equation (2.2)**:

$$H = \frac{P_{max}}{A} \qquad \textbf{Equation (2.2)}$$

where *H*, P_{max}, and *A* are nano-indentation hardness, peak indentation load, and projected area of the hardness impression, respectively.

Thermal stability of the powder samples (-325 mesh) was studied in air using a Pyris Diamond thermogravimetric/differential thermal analyzer module (TG-DTA, Perkin Elmer Instruments, USA). Samples were heated up to 200°C at a rate of 20°C/min and soaked at this temperature for 10 min to remove water vapor. They were then heated up to a 1,000°C at a rate of 2°C⁄min and held at this temperature for 120 min. The samples were then air cooled at a rate of 5°C⁄min. X-ray diffraction was carried out on the powders after cooling to determine the resulting phases.

To assess the phase stability of the solid solutions, several samples were thermally annealed over a period of 24 h at a temperature of 1300 K under flowing high-purity argon in a Lindberg/Blue M Mini Mite™ laboratory tube furnace. The samples were crushed and analyzed by X-ray diffraction using the above procedure. The lattice parameters differed trivially from samples subjected only to arc melting, though the FWHM for the peaks was somewhat reduced indicating the elimination of some lattice strain.

Results

As one might predict on the basis of the WB_2 structure consisting of one-half ReB_2-type HCP layers and one-half AlB_2-type simple hexagonal layers, the maximum solubility of tungsten in ReB_2 is nearly 50%. A sample powder X-ray diffraction pattern for the highest concentration used in this study (48 at.% W) is given in **Figure 2.2**. The lattice parameters, unit cell volume, and *c*/*a* axial ratios for a selection of solid solutions synthesized for this study are listed in **Table 2.1**. Both the *a*- and *c*-axes are expanded by incorporation of tungsten into the ReB_2 structure and monotonically increase in absolute value as a function of tungsten concentration. The nearly perfectly linear trend observed (**Figure 2.3** and **Figure 2.4**) is exactly what would be expected from perfect adherence to Vegard's law if a hypothetical ReB_2-type tungsten diboride existed. By extrapolating the curves in **Figure 2.3** and **Figure 2.4**, the lattice parameters for such a compound may be estimated as a = 2.9159 Å and c = 7.7486 Å (c.f. 2.9002 Å and 7.4759 Å, respectively, for pure ReB_2) for a total volume increase of approximately 4.64%.

Micro-hardness data are presented in **Figure 2.6** and **Figure 2.7**. Small additions of tungsten in the range of 0.5 – 2 at.% have a relatively large and immediate impact on the hardness of ReB_2, which increases from 40.5 ± 2.8 GPa to 47.8 ± 3.5 GPa at low (0.49 N) load and from 29.3 ± 0.8 GPa to 33.9 ± 0.7 GPa at high (4.9 N) load for 1% and 0.5% additions, respectively. The addition of larger amounts of

tungsten produces a much less dramatic effect, though all of the solid solutions are at least slightly harder than pure ReB_2. The hardness values are given in tabular form with their corresponding estimated standard errors in **Table 2.2**.

The nano-indentation data largely corroborate the Vickers micro-hardness data and are shown plotted as hardness versus load in **Figure 2.9**. As the curves heavily overlap for the samples of various concentrations (again emphasizing their similarity in hardness), the inset shows an expanded view of the region of low load where, again, small concentrations of tungsten are found to have a disproportionately large impact on the hardness of ReB_2, though all concentrations are at least as hard as pure ReB_2. A maximum hardness of 48.12 GPa was found for 0.5% W in ReB_2 at a load of 2.629 mN (55.4 nm displacement) compared to 43.99 GPa at 3.165 mN (64.0 nm displacement) for pure ReB_2. Likewise, **Figure 2.10** depicts the curves for hardness versus displacement as calculated from nano-indentation. All of the tungsten containing solid solutions synthesized maintained values greater than 40 GPa until well over 200 nm of penetration depth. **Table 2.3** summarizes the hardness values obtained at various penetration depths as well as the average value of hardness over the range from 60 nm to 900 nm penetration for the various compositions tested. All of the compositions tested were super-hard.

To examine any crystallographic effects the dissolution of tungsten has on ReB_2, time-of-flight (TOF) neutron powder diffraction data were obtained for the highest composition obtained (48 at.% W) as well as for pure ReB_2. The background-subtracted, Rietveld-refined powder diffraction patterns are depicted in **Figure 2.11** and **Figure 2.12** for ReB_2 and $W_{0.48}Re_{0.52}B_2$, respectively. Relevant crystallographic data may be found in **Table 2.4** and **Table 2.5**. The neutron diffraction data for ReB_2 are in excellent agreement with those observed by Frotscher *et al.* (c.f. a = 2.90059 Å c = 7.47745 Å *versus* our a = 2.900468 Å and c = 7.47734 Å).[136] There is no evidence for preferential site orientation or

secondary phases. The fit for the solid solution sample is nearly as good as that for pure ReB_2 ($\chi 2 = 1.731$ versus 2.023), and may have been improved toward parity if the thermal parameters were separately refinable for the Re and W atoms without serial correlation. The discrepancy in lattice parameters between the neutron diffraction and X-ray diffraction samples is most likely due to a slight difference in zero-point calibration between the two machines. The overall trend in parameters, however, is still maintained, as can be seen from the c/a axial ratios shown in **Table 2.1**, where the error is less than might be anticipated from a 0.25% change in tungsten composition following the trend in **Figure 2.5**

Thermogravimetric analysis data are presented in **Figure 2.13**, **Figure 2.14**, and **Figure 2.15**. These data show little difference in thermal stability of the solid solutions versus data previously published for ReB_2, where oxidation of samples was observed to begin at approximately the same temperature (≈500°C).[53] The qualitative difference between the tungsten-containing samples and pure ReB_2 (i.e. an initial rise in mass before a steep drop), may be ascribed to the formation of WO_3 or a mixed oxide of W/ReO_3 before the temperature is sufficiently hot enough for the sublimation of Re_2O_7. X-ray diffraction of the end product (a yellow, glassy, microcrystalline mass) corroborates this hypothesis by confirming the presence of WO_3. From **Figure 2.15** it may be inferred that the formation of the boron oxidation product (B_2O_3 glass) offers relatively little protection against high-temperature oxidation, as the samples continue to decompose nearly linearly at 1000°C, implying steady-state oxidation has already been reached by this point.

Discussion

Whereas AlB_2-type borides are based on boron filling the interstices of a primitive hexagonal arrangement of metal atoms, ReB_2-type borides are based on an expanded hexagonal-close-packed metal lattice. Glancing at **Figure 2.1**, it is clear that one consequence of this atomic arrangement is a

greater volumetric increase for the formation of ReB_2 from HCP rhenium than for forming an AlB_2 structured compound from a native HCP metal. The relative increase in lattice parameters between the two structure types, however, is uneven. For example, from Ti to TiB_2, the lattice parameters increase from a = 2.951 Å and c = 4.684 Å[137] to a = 3.024 Å and c = 3.154 Å[138], whereas for Re to ReB_2, the parameter increase is from a = 2.76 Å and c = 4.458 Å[139] to a = 2.90 Å and c = 7.747 Å. These values correspond to a 2.47 % increase in the metal-metal contact distance in *a* and a 8.90 % increase in contact distance in *c* for the case of titanium and 5.07 % and 49.5 % increases along *a* and *c*, respectively, for the case of rhenium. Therefore, one may conclude that the borides of the AlB_2 type can be thought of as relatively true interstitial compounds, obeying the Hume-Rothery[140] rules for their formation, whereas borides of the ReB_2 type represent a distinctly layered structure, with the insertion of 'puckered' boron nets behaving nearly as though an additional layer of metal had been added. Taken another way, in accordance with the qualitative interpretation offered by Pauling[141], the *small* increase in metal-metal distance for the AlB_2 structure type indicates a *large* degree of metal-metal bonding, whereas the much larger increases in compounds of the ReB_2 structure type indicate that metal-metal bonding is virtually eliminated in the *c*-direction and replaced with metal-boron covalent bonds. This interpretation is further corroborated by the fact that the boron-boron bond distances increase from 1.75 Å in TiB_2 to 1.83 Å in ReB_2, indicating a decrease in B-B bond order going from planar boron 'sheets' to 'puckered' boron nets, and therefore a concomitant increase in bond order from boron to metal (assuming valance is maintained).[142] Indeed, electronic calculations on ReB_2 have shown exactly this effect, with significant electron density localized between boron and rhenium, which has also been used to explain the extremely high hardness of this compound.[116,129,143] The extreme change in packing density between the two boride types is not detrimental to the hardness of the larger-volume ReB_2-type compounds, but rather a consequence of the covalency that gives rise to this hardness. That the lattice

parameters for W/ReB_2 solid solutions should increase with increasing tungsten content should not, necessarily, be an indication of lowered hardness, as our results bear out.

One may hypothesize, based on the above, that other compounds with the ReB_2 structure type might also be super-hard. This does indeed appear to be the case as, for example, Gu *et al.* have studied the mechanical properties of $W_{0.5}Os_{0.5}B_2$ (a = 2.913 Å c = 7.566 Å), a ternary taking the ReB_2-structure, and measured a low load (0.49 N) hardness of 40.4 ± 1.3 GPa. Additionally, recent work by Tao et al. has demonstrated that in the MoB_2 system, where there are two structure types available (depending on synthetic conditions), the structure with more 'puckering' in the boron sheets, as opposed to the lower-volume AlB_2-type structure, is harder. The reported high load (9.8 N) hardness values for AlB_2-type MoB_2 and "Mo_2B_5"-type MoB_2 are 15.2 GPa and 22.0 GPa, respectively; a relatively drastic difference of 44.7%.[97] As the reported hardness of "W_2B_5"-type WB_2 is 26.1 GPa (0.98 N)[144] to , a similar 44.7% increase of hardness would result in a compound having a hardness of approximately 37.8 GPa, which is nearly super-hard.

Indeed, ReB_2-structured WB_2 has previously been proposed as candidate hard or super-hard compound.[116,124] Chen *et al.* have predicted from *ab initio* calculations that ReB_2-structured WB_2 should be stable *versus* the AlB_2-structured form under ambient conditions.[129] The calculated shear modulus reported for this structural form is 273 to 294 GPa based on GGA and LDA approximations, respectively (c.f. 271.6 to 302 GPa for ReB_2, as determined experimentally[145–147]). Assuming the correlation between shear modulus and indentation hardness holds,[148] this may be interpreted as a prediction that the hardness of ReB_2-structured WB_2 should have comparable hardness to native ReB_2. This hypothesis was later partially corroborated by Zhong *et al.*, who used the Voigt-Reuss-Hill (VRH) approximation to calculate shear moduli of 253 GPa and 291 GPa and a semi-empirical method to estimated hardness values of 35.7 GPa and 39.1 GPa, for ReB_2-structured WB_2 and native ReB_2, respectively.[124]

Unfortunately, WB_2 takes the "W_2B_5" structure type under ambient conditions, and an ReB_2-like phase has never been isolated. However, some speculation has been offered from theoretical calculations about the properties of W/ReB_2 solid solutions, where these compounds were anticipated to also be super-hard.[113,125,130] The estimated values for the hardness of $W_{0.5}Re_{0.5}B_2$ from these works is 40.1 GPa according to Du *et al.*[130] and 40.9 GPa according to Ivanovskii[149]. Remarkably, our results completely corroborate these claims, as our experimentally determined values for the hardness of $W_{0.48}Re_{0.52}B_2$ are 41.7 ± 0.7 GPa (0.98 N) from micro-indentation and 39.96 GPa (average) from nano-indentation. While there are some discrepancies in the lattice parameters between the predicted values of a = 2.88 Å c = 7.57 Å according to Du[130] and a = 2.8702 Å c = 7.5224 Å according to Tu *et al.* and our experimentally determined values of a = 2.9076 Å and c = 7.6076 Å for 50 at. % W, the qualitatively excellent agreement between the sets of results would seem to indicate that computational methods have quite some value in relation to the prediction of the properties of hard materials.

Tu *et al.* further predicted peaks in the hardness of tungsten/rhenium diboride solid solutions at both 10 at. % W and 60 at. % tungsten, predictions that agree well with our experimental results, especially if 40 % is taken to correspond to our data at 48 at. %. The slight variations in hardness that we observe in the range from 10 at. % – 50 at. % W can likely be ascribed to subtle electronic effects. However, none of the previously described theoretical works predict the relatively large increase in hardness that we observe for small amounts of additional tungsten, in the range of 0.5 to 1 at. %. The most likely cause of this discrepancy is that the theoretical calculation take for granted the perfect stoichiometric ratio, atomic regularity, and homogeneity that may only exist in an 'ideal' compound. All 'real' samples should be expected to have some slight deviations from perfect conformance to the 'ideal' compound, many of which will manifest as slight strains on the lattice. A strained crystalline lattice should be expected to contribute to the hardness of the compound. The addition of very small amounts of tungsten many

enter the crystalline structure of ReB_2 in such a way to compensate for these strains an therefore exert a disproportionately large effect on the measured hardness of the compound. One would not expect this sort of extrinsic factor to be readily anticipated from the assumption made during theoretical calculations.

As far as we are aware, the only other experimental work on these solid solutions was executed as part of a phase-diagrammatic study by Kuz'ma *et al.*, who reported a maximum solubility limit of $W_{0.19}Re_{0.81}B_2$ with lattice parameters a = 2.910 Å and c = 7.590 Å.[89] On the basis of the axial ratio (2.6082), these values correspond well for values along our curve for a boride of formula $W_{0.35}Re_{0.65}B_2$. The discrepancy in the atomic fraction is likely due to poor optimization of the compositions for the samples in the Kuz'ma study, given that most samples prepared in that work were multi-phase ingots (making it much more difficult to estimate the atomic ratios in each phase of the sample). A further likely contribution to the difference between our estimates for maximum tungsten solubility is a slight boron deficiency in the compounds synthesized in previous work. In the course of optimizing our own synthetic procedure, we have found that a slight excess of boron is necessary to ensure the complete formation of the ReB_2 structured compound. Ratios of boron less than approximately 2.2 : 1 (B : M) appear to encourage the formation of the "W_2B_5" phase.

Conclusions

We have successfully synthesized solid solutions of tungsten in rhenium diboride using an electric-arc furnace. The solubility limit for tungsten in ReB_2 is very nearly 50 at. % (maximum composition reported here is 48%), indicating a very high degree of solubility. The lattice parameters for the solid solutions vary linearly along both the *a* and *c* axes with increasing tungsten content. The solid solutions are statistically random up to and including the limiting composition according to both X-ray and neutron

diffraction. All of the compositions tested within the range from 0 – 48 at.% W are super-hard according to analyses of both micro-indentation and nano-indentation data. These results further indicate that ReB_2 structured compounds are super-hard, and may warrant further studies into additional solid solutions or ternary compounds taking this structure type.

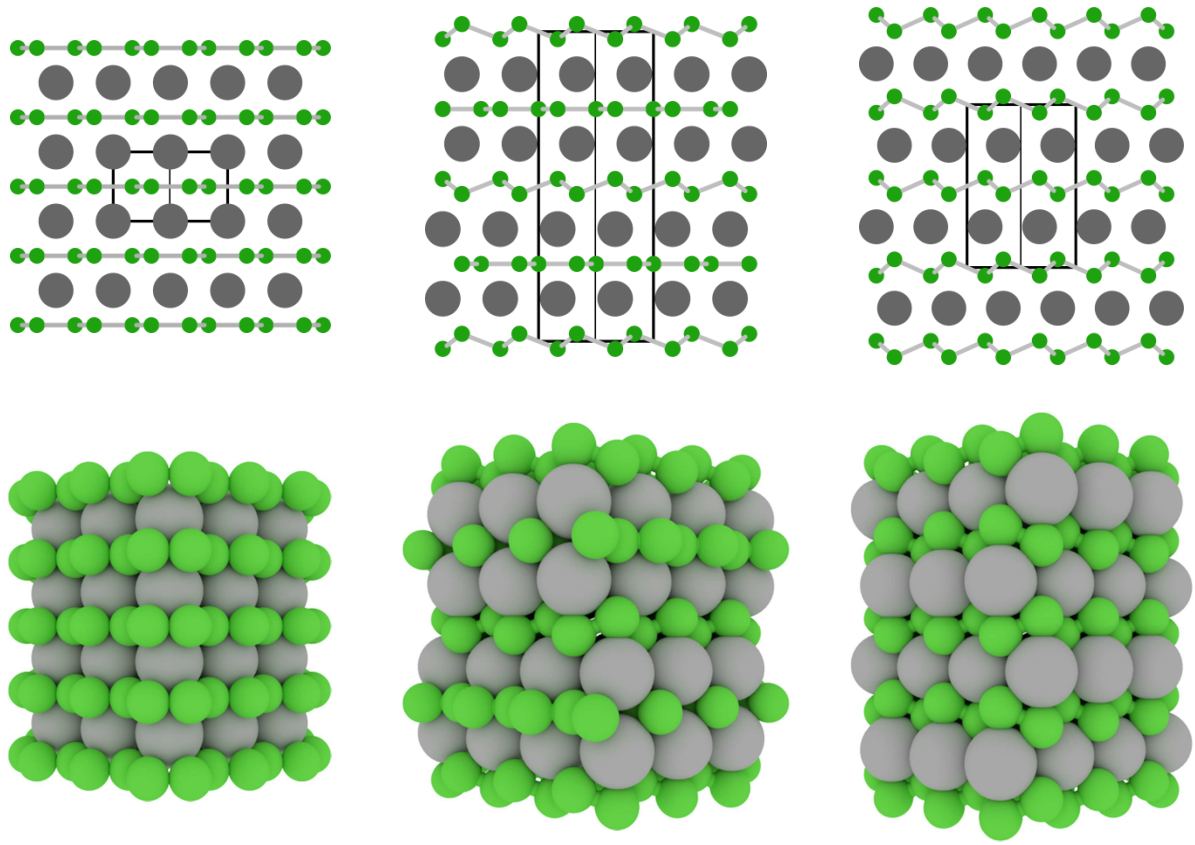

(a) **(b)** **(c)**

AlB_2-type WB_2 **"W_2B_5"-type WB_2** **ReB_2**

Figure 2.1: A comparison of the structures of several diborides structure types. **Top:** A schematic representation of the borides, normal to the [111] crystallographic plane, emphasizing the stacking sequence of the metal atoms. The unit cell for each structure is bounded by the black box. **Bottom:** space filling atomic models of the above structures shown along the same viewing direction, emphasizing the interstitial nature of the boron atomic filling. All structures are drawn to scale.

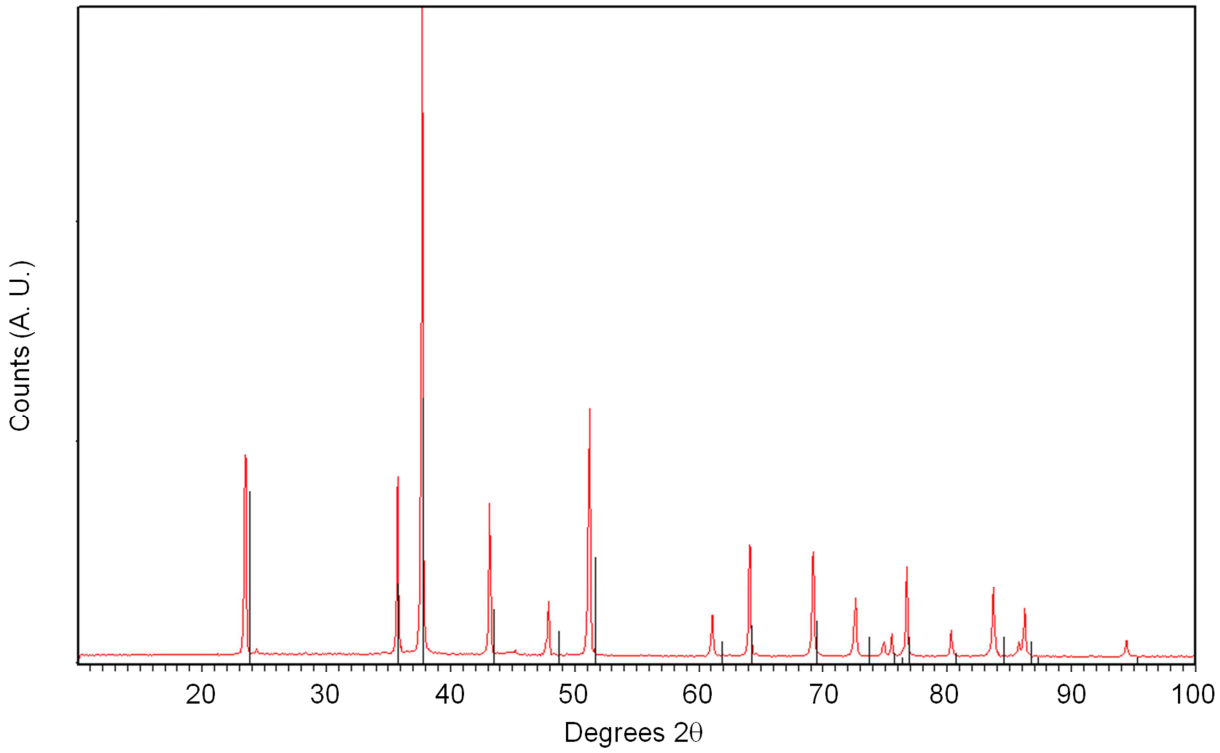

Figure 2.2: Sample X-ray diffraction pattern of a specimen containing 48% at.% tungsten in ReB_2 showing the full pattern shifting of peaks. Those peaks having greater {00*l*} character are shifted to a larger degree. The black stick pattern represents where the diffraction peaks appear for native ReB_2.

Table 2.1: Lattice Parameters and Calculated Unit Cell Volume and Axial Ratio for the Series of Solid Solutions Presented in this Work

Composition	*a* Parameter (Å)	*c* Parameter (Å)	Volume (Å^3)	*c/a* Ratio
ReB_2 (X-Ray)	2.90016(1)	7.47591(8)	54.455	2.5778
ReB_2 (Neutron)	2.900468(24)	7.47734(10)	54.477	2.5780
$Re_{0.995}W_{0.005}B_2$	2.9006(7)	7.4799(2)	54.504	2.5787
$Re_{0.95}W_{0.05}B_2$	2.9014(5)	7.4917(2)	54.618	2.5821
$Re_{0.90}W_{0.10}B_2$	2.9019(3)	7.5056(5)	54.738	2.5864
$Re_{0.80}W_{0.2}B_2$	2.9033(8)	7.5315(6)	54.981	2.5941
$Re_{0.70}W_{0.30}B_2$	2.9046(7)	7.5573(2)	55.220	2.6018
$Re_{0.60}W_{0.40}B_2$	2.9065(7)	7.5884(1)	55.519	2.6108
$Re_{0.52}W_{0.48}B_2$ (X-ray)	2.9076(9)	7.6076(8)	55.701	2.6164
$Re_{0.52}W_{0.48}B_2$ (Neutron)	2.909085(21)	7.61009(10)	55.774	2.6160

(The number in the parentheses represents the uncertainty of the preceding least-significant digit)

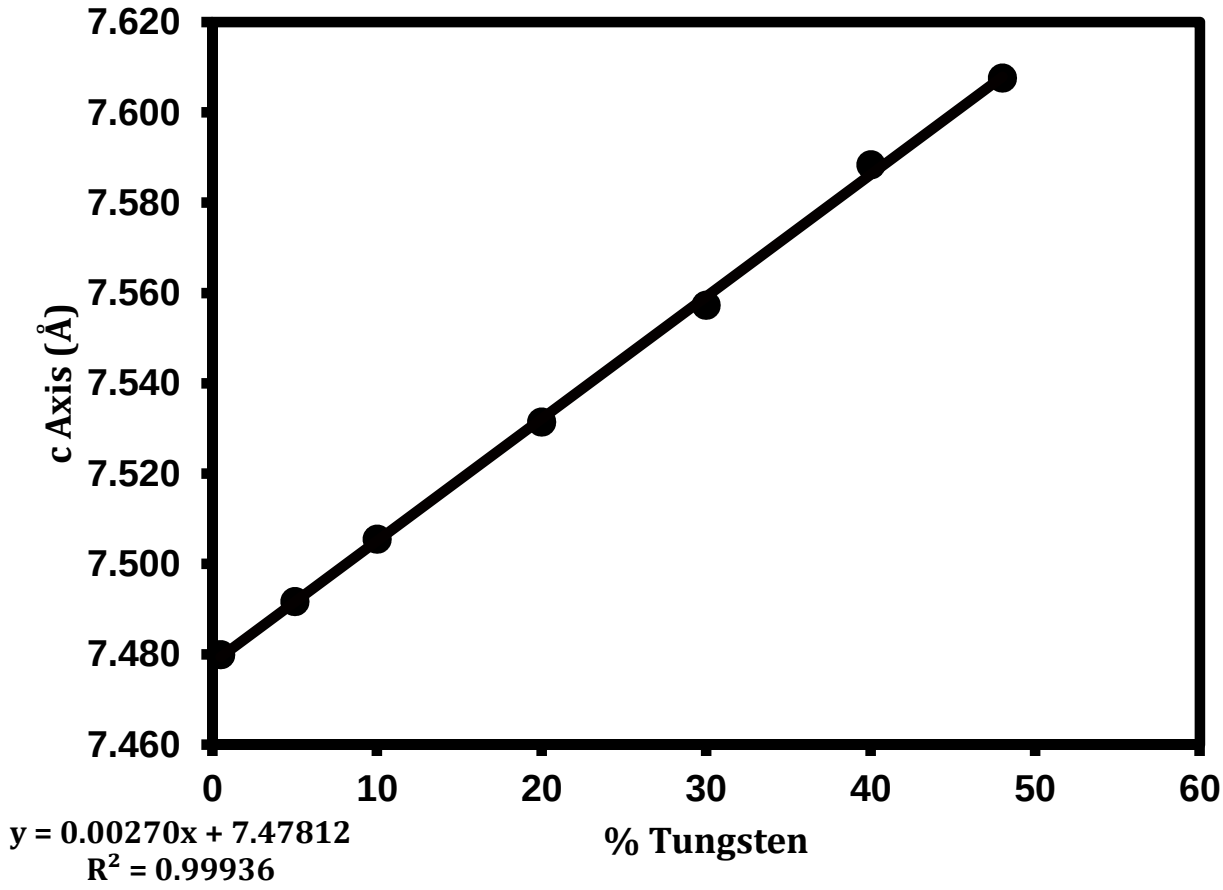

Figure 2.3: A plot of the measured *c*-axis for the ReB_2 structured solid solutions versus tungsten content in atomic percentage. The increase is virtually monotonic. The linear best-fit equation is shown in the lower left corner. The extrapolated value at zero agrees well with the measured parameter for pure ReB_2.

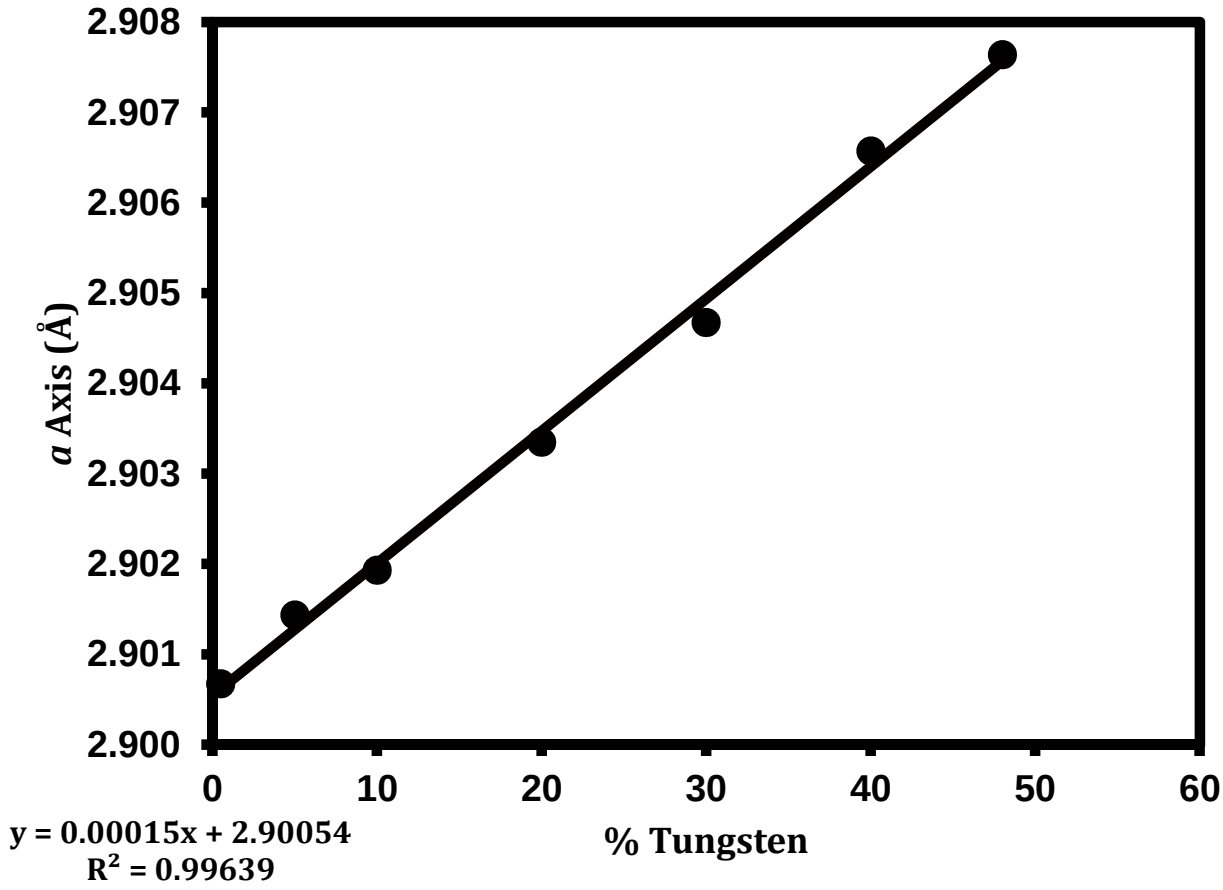

Figure 2.4: A plot of the measured *a*-axis for the ReB_2 structured solid solutions versus tungsten content in atomic percentage. The increase is virtually monotonic, but significantly less than seen for the *c*-axis. The linear best-fit is shown in the lower left corner. The extrapolated value at zero agrees well with the measured parameter for pure ReB_2.

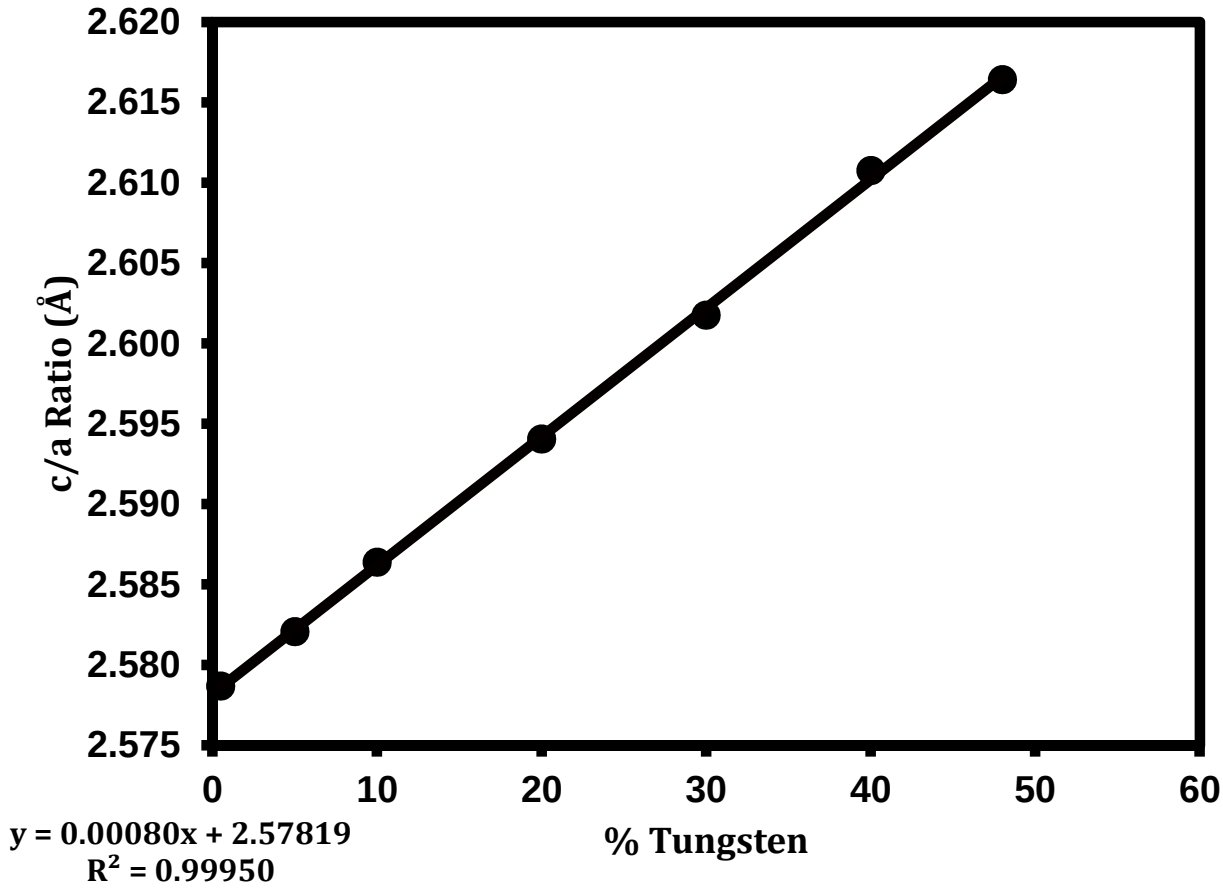

Figure 2.5: A plot of the calculated axial ratio for the ReB_2 structured solid solutions versus tungsten content in atomic percentage. As both values increase monotonically, the axial ratio increases monotonically as well.

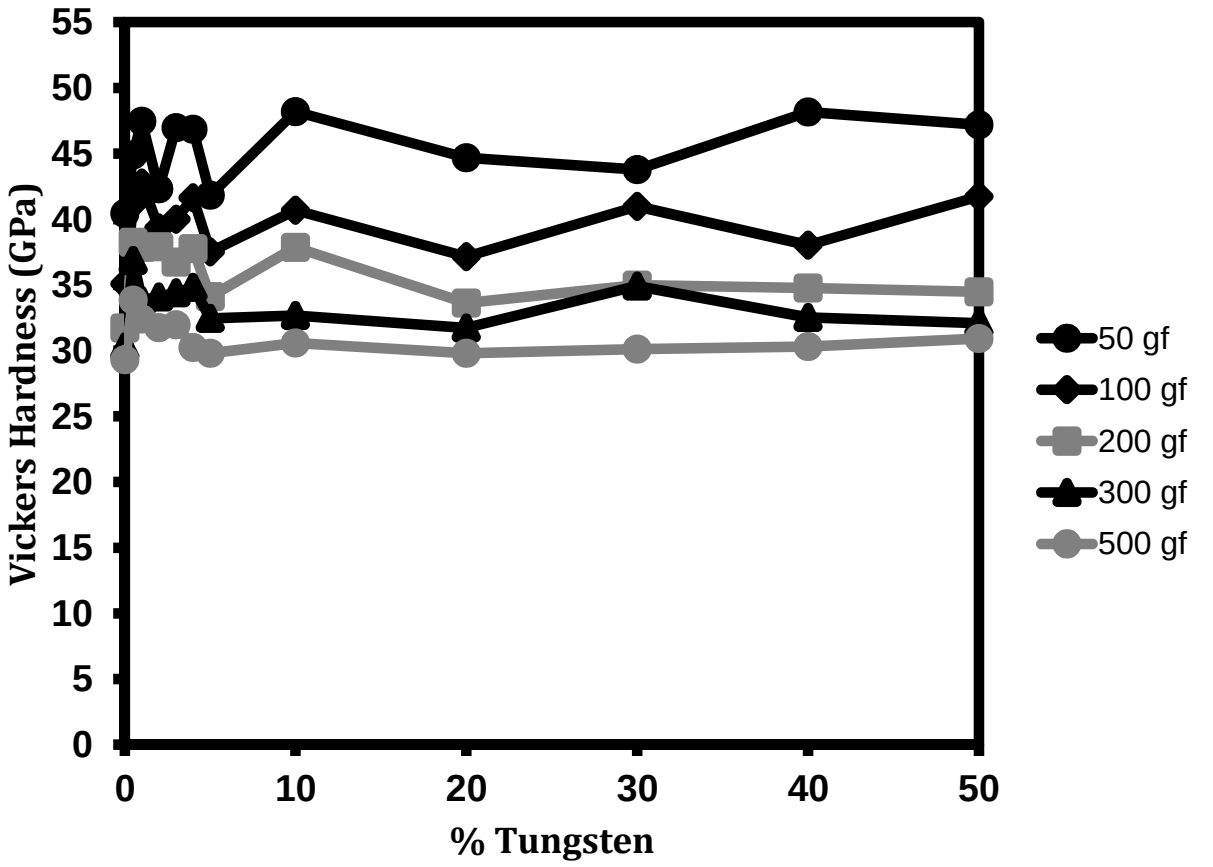

Figure 2.6: Vickers micro-indentation hardness versus metal-basis atomic composition of tungsten for various ReB_2-based solid solutions. Each indentation load is represented from a separate line in the plot. The hardness is dramatically increased with small additions of tungsten atoms, the effect rapidly falling off as higher solid-solubility is reached.

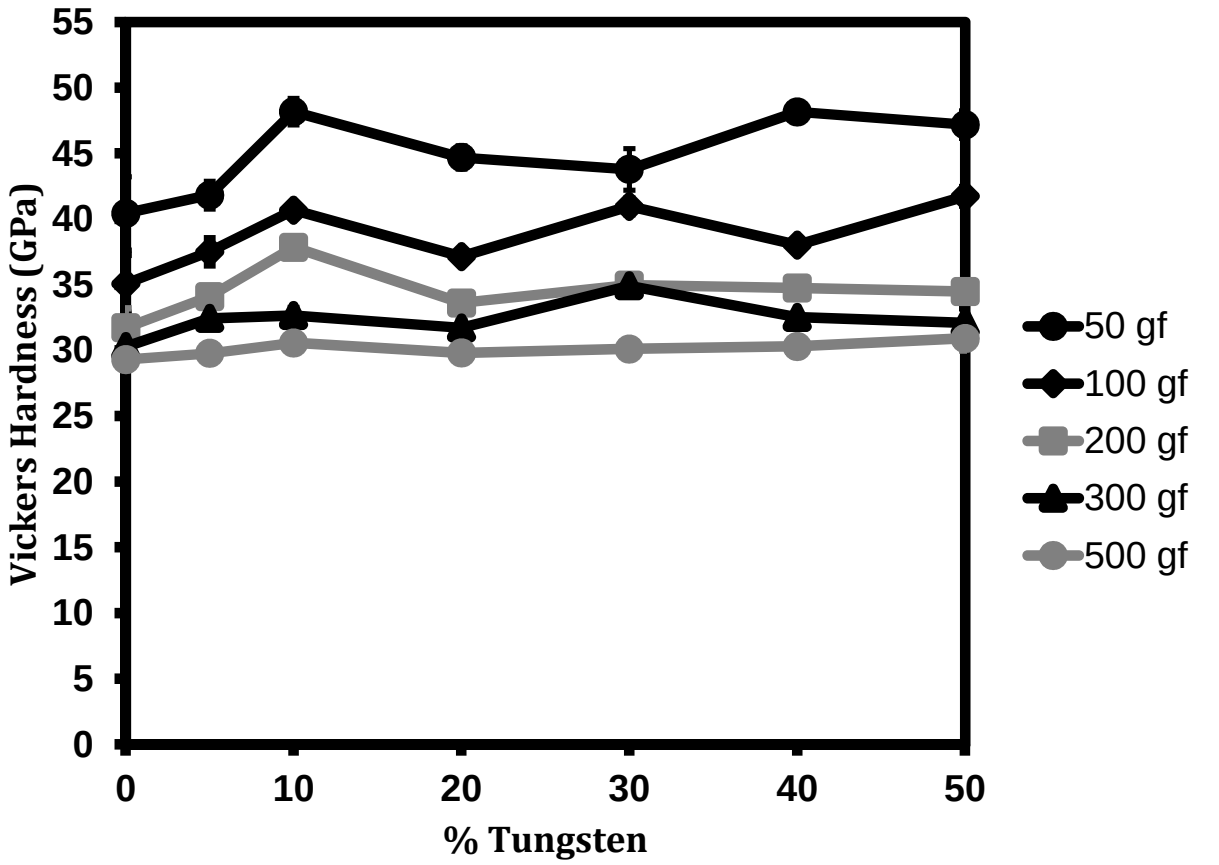

Figure 2.7: A plot of hardness for various concentrations of tungsten dissolved in ReB_2 with the lower atomic percentages removed for clarity. This plot emphasizes the near-flatness in hardness values for every load and nearly every concentration of tungsten from 10 at.% to 48 at.%.

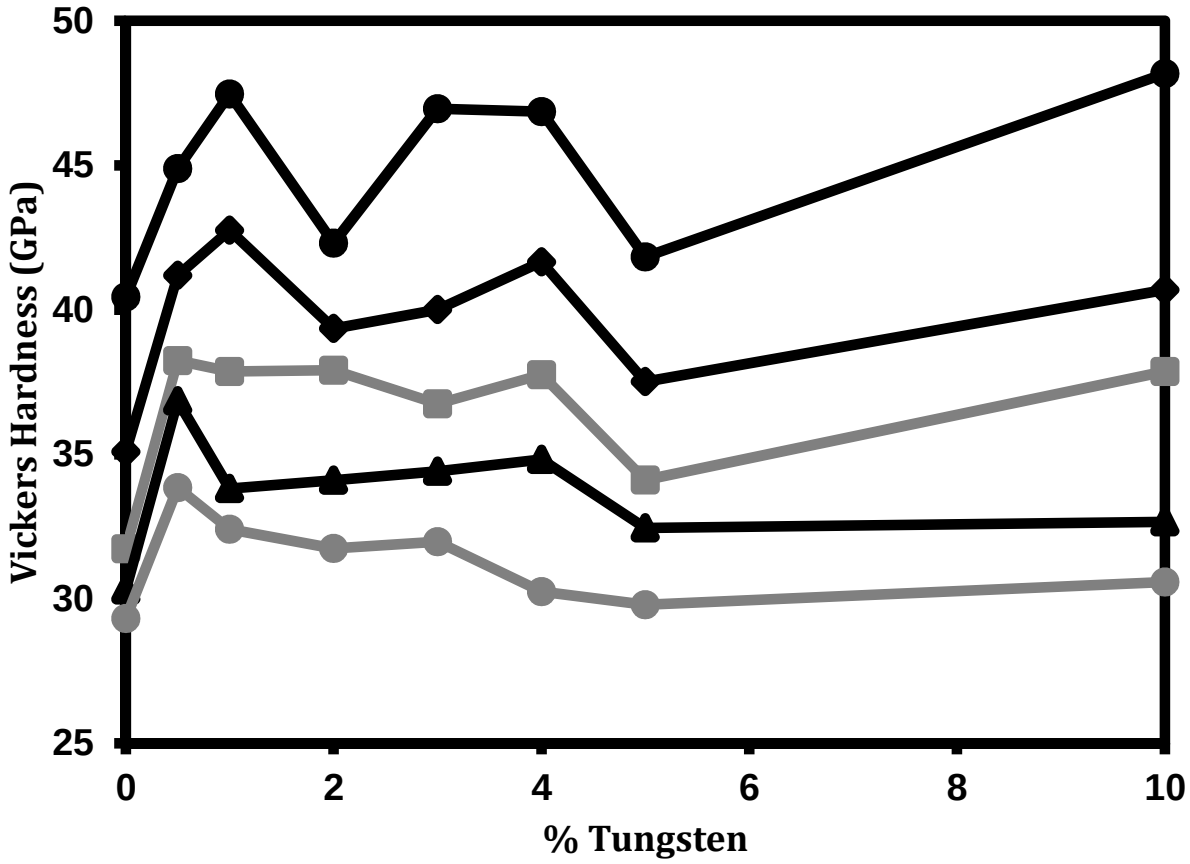

Figure 2.8: A plot of hardness for the lower concentrations of tungsten dissolved in ReB_2. This plot highlights the early increase in hardness at every load for tungsten concentration below 5 at. %.

Table 2.2: Summary of Vickers Micro-Hardness Data Presented in **Figure 2.6** and **Figure 2.7**

	Vickers Hardness (GPa)				
Composition	**0.49 N**	**0.98 N**	**1.96 N**	**2.94 N**	**4.90 N**
ReB_2	40.45 ± 2.79	35.08 ± 2.21	31.73 ± 1.49	30.30 ± 0.74	29.31 ± 0.77
0.5% W	44.89 ± 1.94	41.19 ± 1.56	38.24 ± 1.21	36.85 ± 1.13	33.85 ± 0.69
1% W	47.47 ± 3.49	42.75 ± 2.39	37.86 ± 2.50	33.81 ± 1.07	32.40 ± 0.92
2% W	42.31 ± 2.38	39.35 ± 1.32	37.91 ± 1.31	34.10 ± 0.77	31.74 ± 0.57
3% W	46.96 ± 1.77	40.00 ± 1.17	36.75 ± 1.28	34.41 ± 0.83	31.97 ± 0.82
4% W	46.86 ± 1.71	41.65 ± 2.01	37.75 ± 1.28	34.82 ± 1.02	30.24 ± 0.66
5% W	41.83 ± 1.06	37.51 ± 1.03	34.11 ± 0.56	32.45 ± 0.38	29.79 ± 0.20
10% W	48.18 ± 1.01	40.69 ± 0.47	37.87 ± 0.25	32.66 ± 0.59	30.58 ± 0.34
20% W	44.69 ± 0.89	37.15 ± 0.37	33.62 ± 0.32	31.72 ± 0.54	29.81 ± 0.09
30% W	43.79 ± 1.58	40.98 ± 0.60	34.99 ± 0.35	34.92 ± 0.48	30.12 ± 0.31
40% W	48.17 ± 0.53	38.03 ± 0.53	34.76 ± 0.71	32.52 ± 0.28	30.31 ± 0.59
48% W	47.20 ± 1.06	41.74 ± 0.70	34.49 ± 0.21	32.10 ± 1.11	30.92 ± 0.92

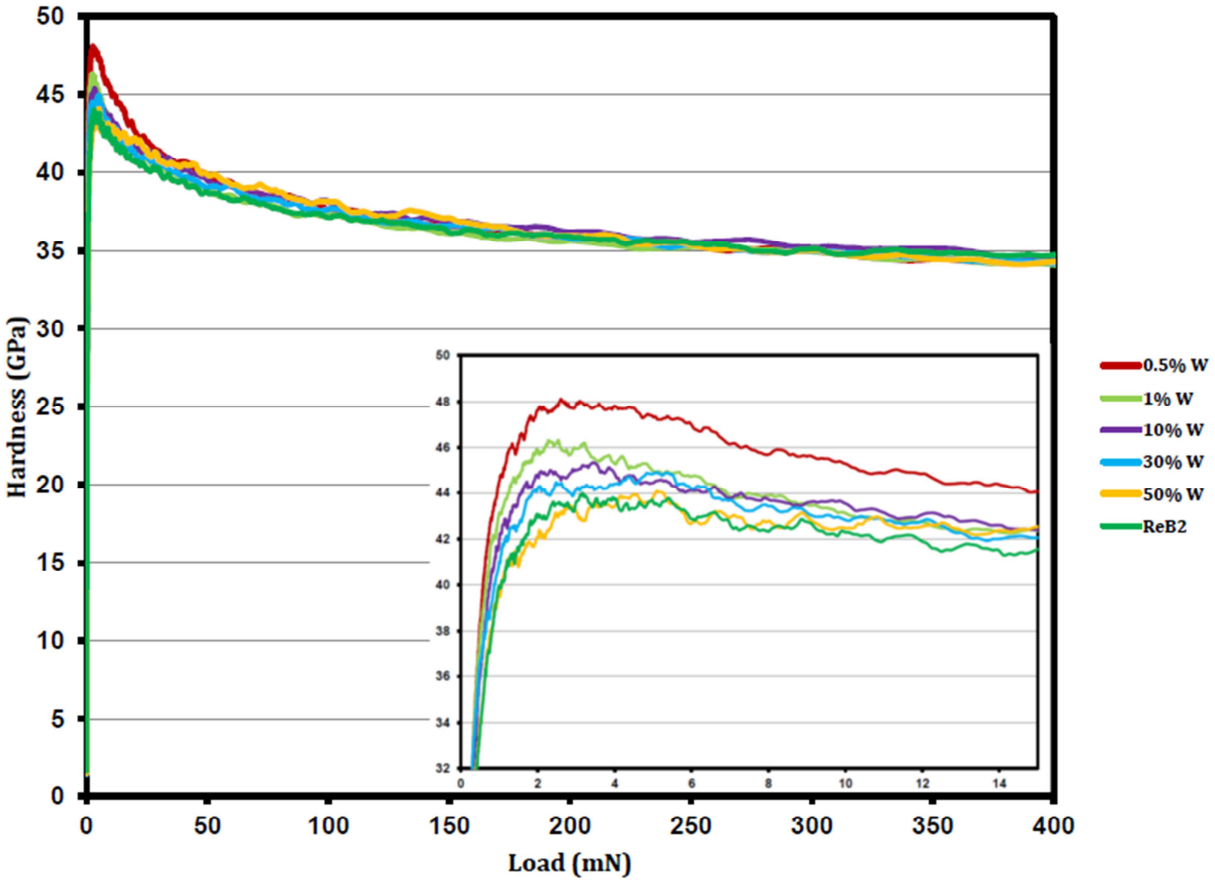

Figure 2.9: Nano-indentation hardness *versus* load curves for several concentrations of tungsten dissolved in rhenium diboride. The hardness values shown here agree well with those calculated from micro-indentation. **Inset:** cropped view of the early part of the hardness vs. load curve showing the significantly enhanced hardness of ReB_2 containing small amounts of tungsten.

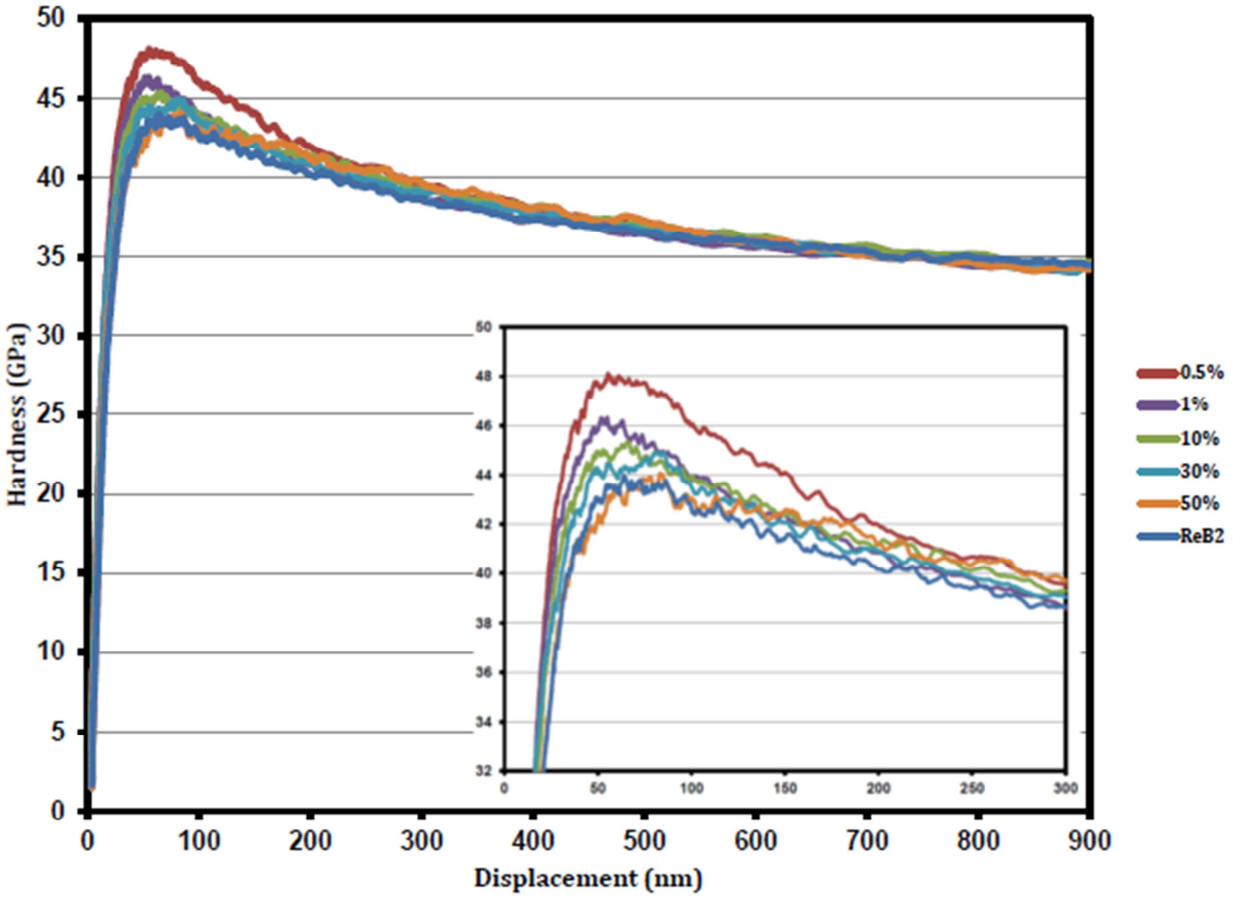

Figure 2.10: Nano-indentation hardness *versus* displacement curves for several concentrations of tungsten dissolved in rhenium diboride. **Inset:** cropped view of the first 300 nm of indentation into the sample surface. All of the solid solutions tested maintained hardness values greater than 40 GPa until at least nm of penetration depth, further indicating super-hardness.

Table 2.3: Nano-Indentation Hardness at Selected Penetration Depths and the Average over the Range from 60 nm to 900 nm

	Nano-Indentation Hardness (GPa)			
Composition	**at 60 nm**	**at 250 nm**	**at 900 nm**	**Avg(60-900)**
ReB_2	43.39	39.43	34.48	39.44
0.5% W	47.81	40.66	34.25	41.14
1% W	45.88	39.76	34.16	40.00
10% W	44.97	40.17	34.64	40.23
30% W	43.97	39.86	34.11	39.94
48% W	43.37	40.42	34.29	39.96

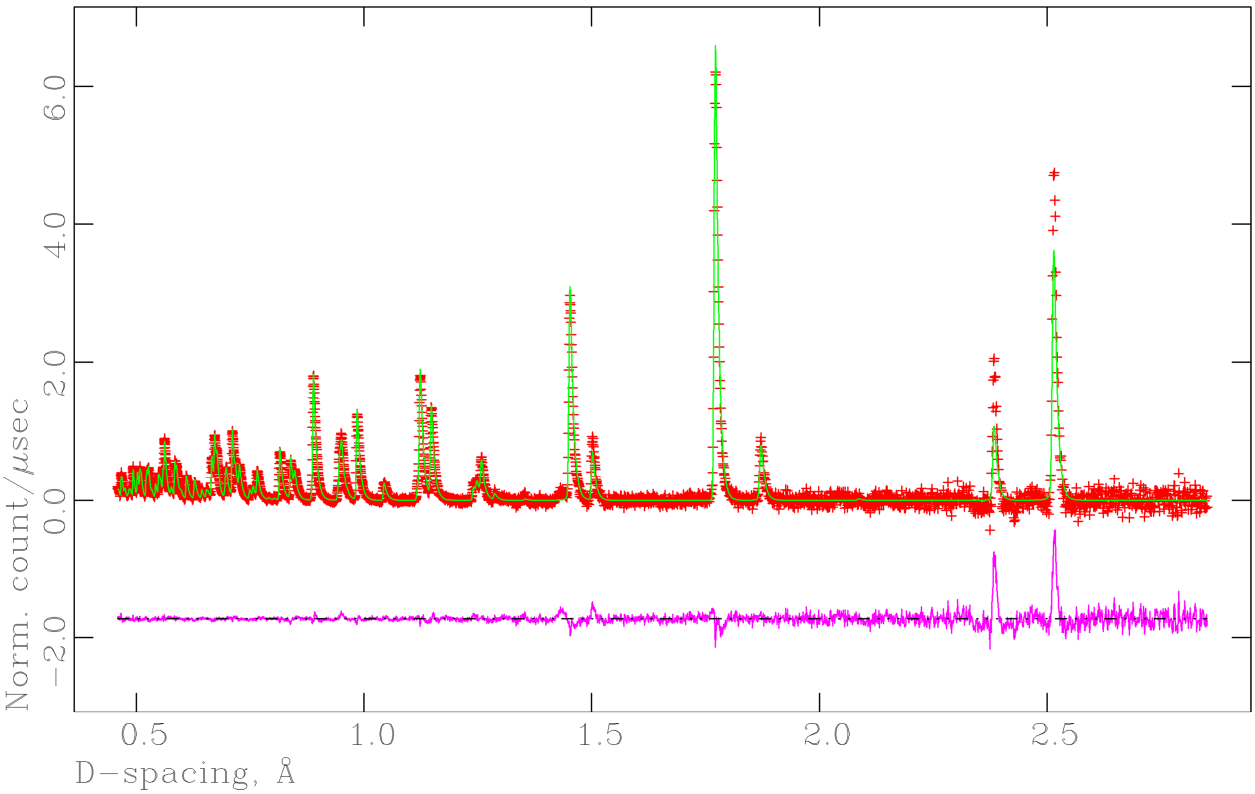

Figure 2.11: TOF-neutron powder diffraction refinement fit for ReB_2. Red (+): observed Green (–): calculated Magenta (–): difference. The background is subtracted for clarity. [Statistics: R_{wp} = 1.40%, R_{wp}(background subtracted) = 1.91%, R^2_{free} = 3.41%, χ^2 = 1.731]

Table 2.4: Crystallographic Date for ReB_2 from TOF-Neutron Diffraction

ReB_2	
Crystal System	Hexagonal
Space Group	*$P6_3/mmc$*
Lattice Parameters	
$a = b$ (Å)	2.900468(24)
c (Å)	7.47734(10)
V (Å^3)	54.4771(10)
Calculated Density (g/cm^3)	
$R_{wp\text{-}b}$	1.91%
χ^2	1.731

ReB_2	Mult.	Symm.	x	y	z	Frac.	$U_{11=22}$	U_{33}	U_{12}
Re	2	-6m2	1/3	2/3	1/4	1.00	0.00249(3)	0.00309(7)	0.00124(2)
B	4	3m	1/3	2/3	0.54805(5)	1.00	0.00559(5)	0.00630(8)	0.00100(2)

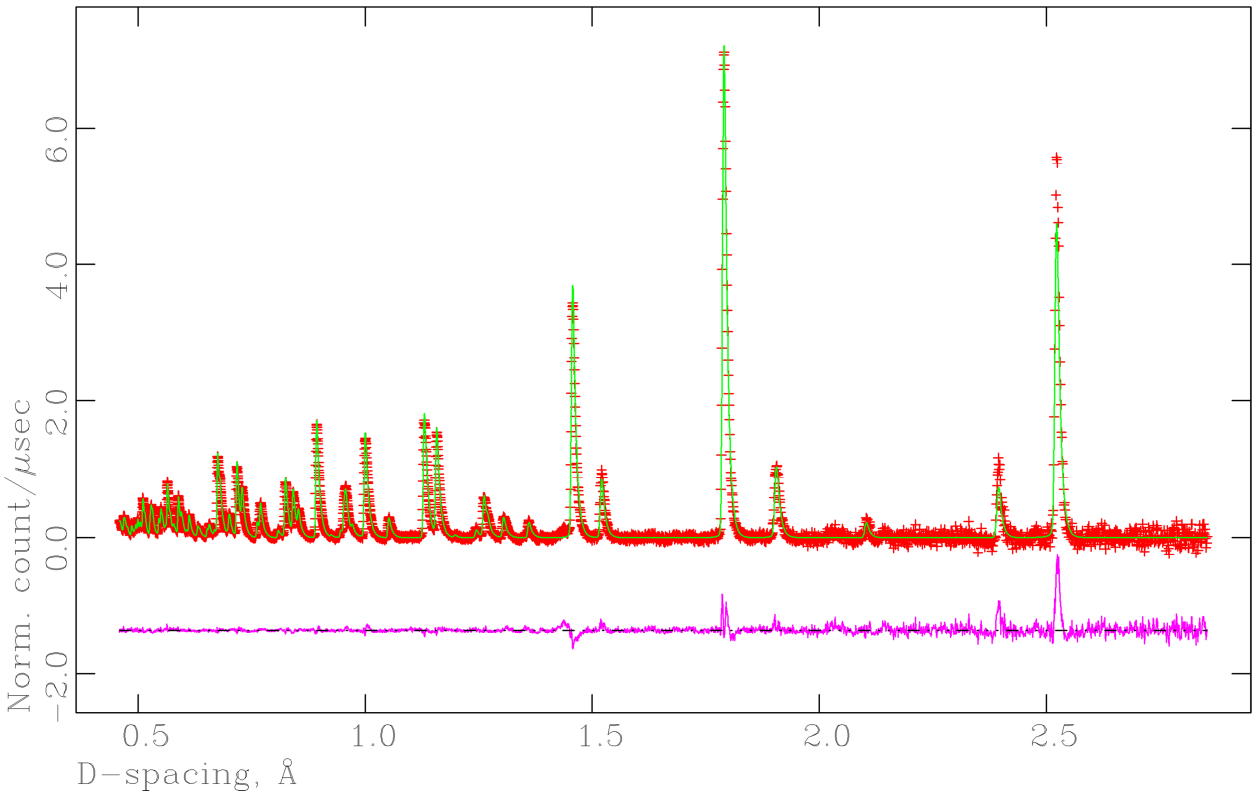

Figure 2.12: TOF-neutron powder diffraction refinement fit for $W_{0.48}Re_{0.52}B_2$. Red (+): observed Green (–): calculated Magenta (–): difference. The background is subtracted for clarity. [Statistics: R_{wp} = 1.77%, R_{wp}(background subtracted) = 2.41%, R^2_{free} = 2.44%, χ^2 = 2.023]

Table 2.5 Crystallographic Data for $W_{0.48}Re_{0.52}B_2$ from TOF-Neutron Diffraction

$W_{0.48}Re_{0.52}B_2$	
Crystal System	Hexagonal
Space Group	*$P6_3/mmc$*
Lattice Parameters	
$a = b$ (Å)	2.909085(21)
c (Å)	7.61009(10)
V (Å^3)	55.7742(9)
Calculated Density (g/cm^3)	
$R_{wp\text{-}b}$	2.41%
χ^2	2.023

$W_{0.48}Re_{0.52}B_2$	Mult.	Symm.	x	y	z	Frac.	$U_{11=22}$	U_{33}	U_{12}
Re	2	-6m2	1/3	2/3	1/4	0.52	0.00088(4)	0.00084(7)	0.00044(2)
B	4	3m	1/3	2/3	0.54403(4)	1.00	0.00439(3)	0.00356(6)	0.00219(2)
W	2	-6m2	1/3	2/3	1/4	0.48	0.00088(4)	0.00084(7)	0.00044(2)

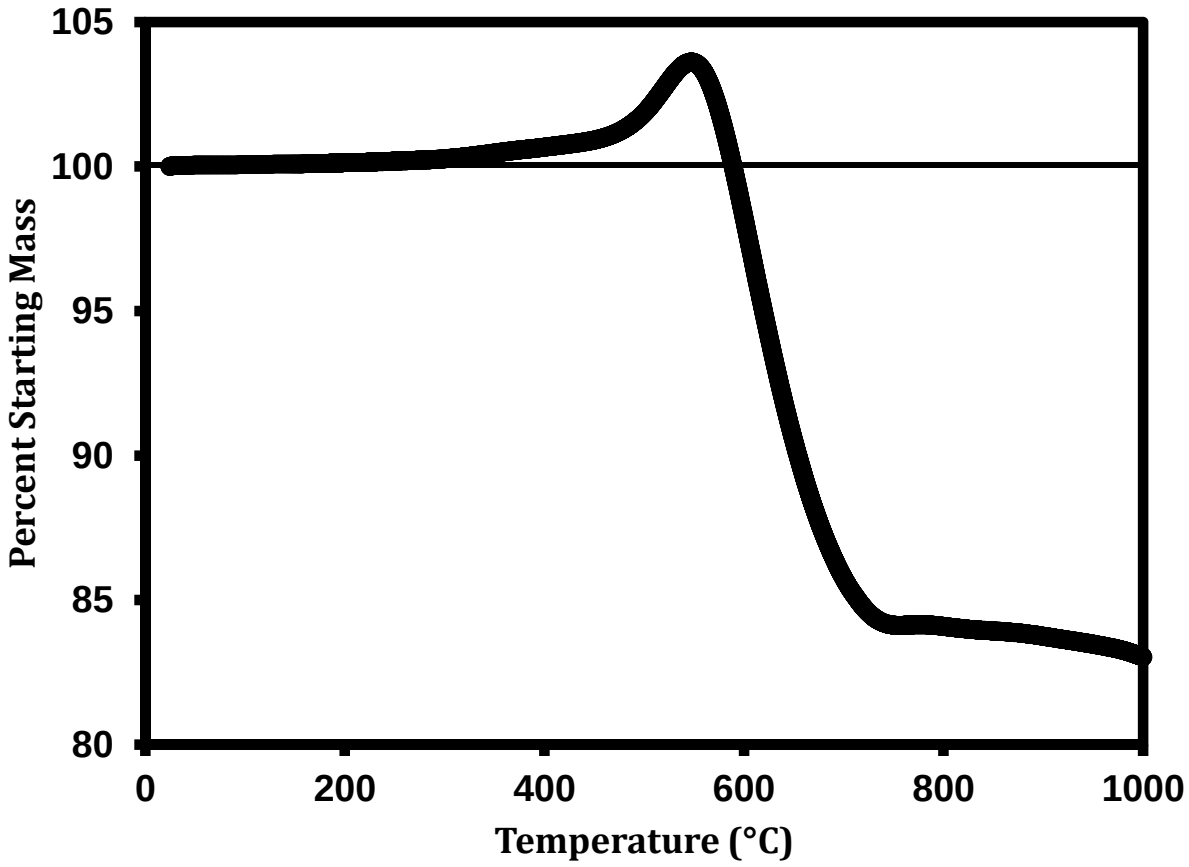

Figure 2.13: Percent mass versus temperature plot from the data obtained by thermogravimetric analysis (TGA) of a powdered sample containing 25 at.% tungsten under ambient air. The sample is stable up to ≈500°C before first gaining mass (due to the formation of WO_3/B_2O_3) and then rapidly losing mass at ≈600°C (due to the volatilization of Re_2O_7). There does not appear to be any thermal stability enhancement from the addition of tungsten to ReB_2 (c.f. Levine *et al.*[53]).

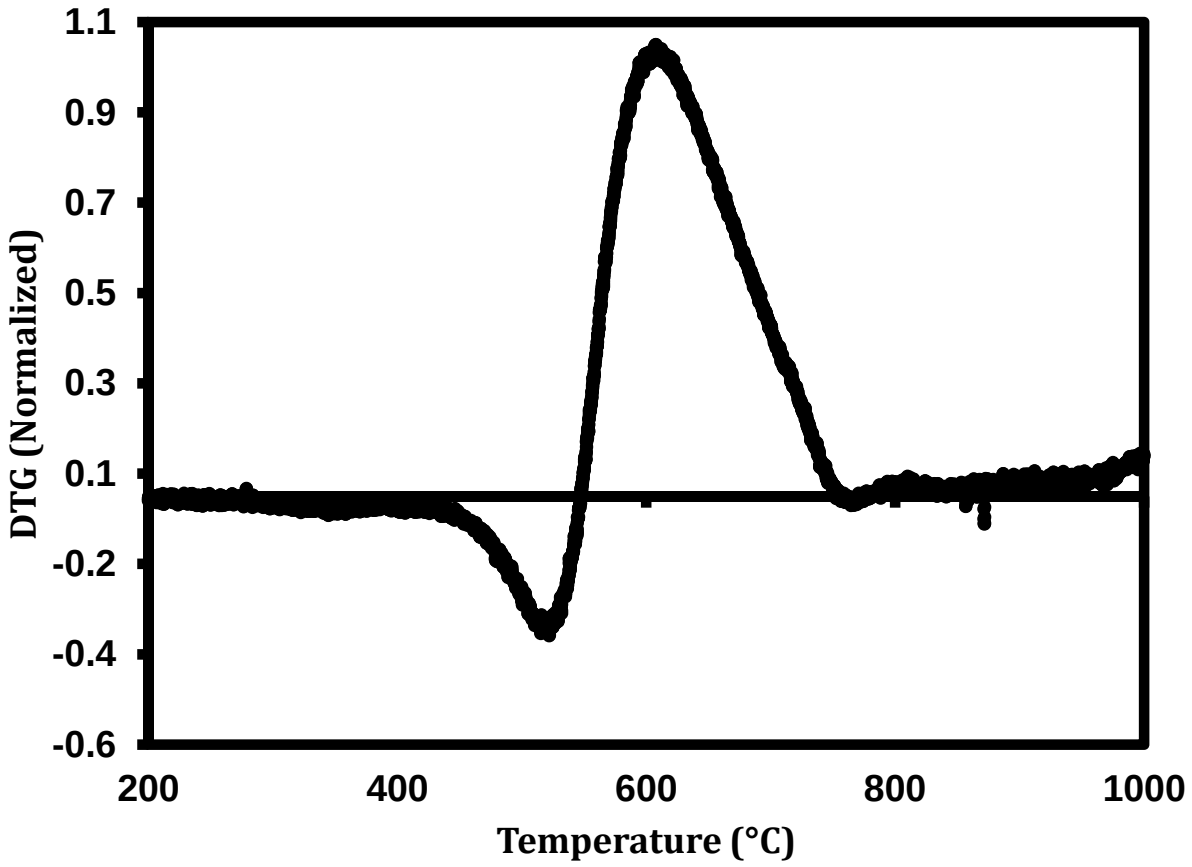

Figure 2.14: The normalized differential thermo-gravimetric (derivative) of the above data versus temperature showing mass gain (peaking at ≈520°C) and mass loss (peaking at ≈610°C).

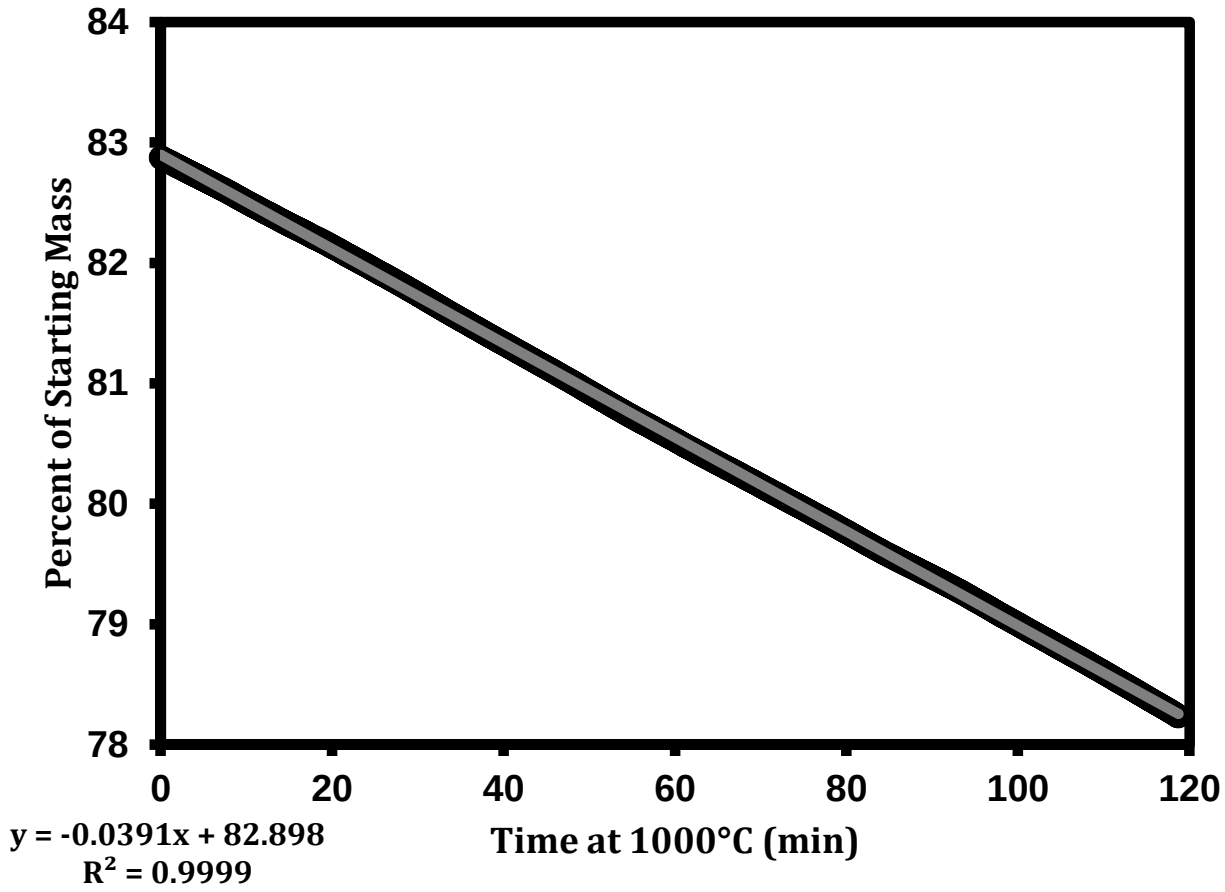

Figure 2.15: The rate of mass loss for a sample of -325 mesh particle size and 25 at.% tungsten is nearly linear with time at 1000°C, showing that the sample rapidly reaches a steady-state of oxidation. It is likely that B_2O_3 acts as a flux for Re_2O_7, rather than as an oxygen barrier. The rate law equation is shown in the lower left corner.

Chapter 3

"Tungsten Tetraboride"

Introduction

Arc melting and metathesis reactions have been used to synthesize the transition metal diborides OsB_2[51,150], RuB_2[147], and ReB_2[52,53,145,146,151] (Chapter 2). Among these, rhenium diboride (ReB_2) with a hardness of approximately 48 GPa under a load of 0.49 N has proven to be the hardest[52,115]. As mentioned in chapters above, the boron atoms in metal borides facilitate the building of the strong, covalent metal – boron and boron – boron bonds that are responsible for the high hardness of these materials[103]. Thus, one may expect that by increasing the concentration of boron in the metal/covalent lattice even harder borides may be formed.

Unfortunately, most transition metals form compounds with relatively low boron content. Tungsten, however, is one of only a few transition metals known to form borides of with metal : boron ratios greater than 1 : 2. In addition to tungsten diboride (WB_2), which is not super-hard[152,153], tungsten forms "tungsten tetraboride" (nominally WB_4), the highest boride of tungsten that exists under equilibrium conditions[154–156]. The advantage of this material over other borides are: (i) Both tungsten and boron are relatively inexpensive, (ii) the lower metal content in the higher borides reduces the overall cost of production because the more costly transition metal is being replaced by less expensive boron thus reducing the cost per unit volume, and (iii) the higher boron content lowers the overall density of the structure, which could be beneficial in applications where lighter weight is an asset.

Tungsten tetraboride was originally synthesized in 1966[154] and its structure assigned to an hexagonal lattice (space group: $P6_3/mmc$). The possibility of high hardness in this material was first suggested by

Brazhkin *et alia*[46], and we discussed its potential applications as a super-hard material in a Science Perspective in 2005[103]. Recently, Gu *et alia*[157] reported hardness values of 46 and 31.8 GPa under applied loads of 0.49 and 4.9 N, respectively, and a bulk modulus of 200 – 304 GPa, though no synthetic details or X-ray diffraction patterns where given.

Because super-hard materials have shown a large load-dependent hardness,[51,52] commonly referred to as the "indentation size effect," reporting a single hardness value for these materials is insufficient and suggests that a more detailed study is needed. Therefore, we have examined the hardness of tungsten tetraboride thoroughly using micro- and nano-indentation. Additionally, since a boride of nominal composition "WB4" may be calculated to possess a valence electron density of 0.485 $e^- Å^{-3}$,[158] comparable to that of ReB_2 (0.477 $e^- Å^{-3}$), the bulk modulus of 200 – 304 GPa reported by Gu *et alia* for this material seems low compared to other super-hard transition metal borides such as ReB_2, with a bulk modulus of 360 GPa[52], and therefore required further investigation. Because the purity of super-hard materials directly influences their mechanical properties,[159] the existence of other borides of tungsten in the samples might explain the anomalously low bulk modulus. Making solid ingots of phase pure WB_4 is especially challenging because the tungsten – boron phase diagram indicates that WB_2 is thermodynamically favorable with any W : B molar ratio below 1 : 12.[160]

Beyond producing data on well characterized phase pure materials, a second goal of this work was to develop ways to further enhance the hardness of this economically interesting hard material. It is well known that the hardness of a material can be increased using several different kinds of dislocation-locking mechanisms, such as solid solution hardening, dispersion hardening and grain boundary strengthening.[161] The possibility of enhancing the mechanical properties of transition metal borides specifically by introducing a third element into their structure has shown some promise due to solid solution hardening.[101] Therefore, adding a third element with a size close to W (such as Re) into WB_4 to

test the formation of either substitutional solid solutions or dispersed phases leading to an increased hardness could be of considerable interest. By taking this approach and an appropriate design of microstructure, switching from an intrinsic super-hard material to an extrinsic super-hard material, with enhanced mechanical properties, is an intriguing possibility. While diamond, *c*-BN, BC_2N, and some other nitrides are well known as intrinsic super-hard materials, polycrystalline heterostructures and nanocomposites are good examples of extrinsic super-hard materials.[162]

This chapter details the synthesis and characterization of tungsten tetraboride, with an emphasis on estimating its hardness. Further, exploration of the possibility for improving the hardness of this compound by dispersion hardening with another hard phase (ReB_2) was also examined.

Materials and Methods

Powders of pure tungsten (99.9994%, JMC Puratronic, U.S.A.) and amorphous boron (99+%, Strem Chemicals, U.S.A) were ground together in the ratio 1 **:** 12 using an agate mortar and pestle until a uniform mixture was achieved. The excess boron is needed to ensure the thermodynamic stability of the WB_4 structure based on the binary phase diagram of the tungsten–boron system.[154,156] To test the possibility of increasing the hardness, rhenium (99.99%, CERAC Inc., U.S.A) was substituted for tungsten at different concentrations of 0.5 – 50.0 at.%. Each mixture was pressed into a 12 mm, ≈350 mg pellet by means of an hydraulic (Model 3851, Carver, USA) press under 10 000 pounds of force. The pellets were then placed in an arc melting furnace and an AC current of ≥70 amps was applied under high-purity argon at ambient pressure. The synthesized ingots were bisected using a sinter-bonded diamond lapidary sectioning saw (South Bay Technology Inc.). One-half of each ingot was crushed to form a fine powder using a hardened-steel mortar. The powder was used for X-ray powder diffraction as well as high-pressure and thermal stability studies. The other half of the ingot was cold mounted in epoxy, using

a resin/hardener set (Allied High Tech Products Inc.) and polished to an optically flat surface for hardness testing. Polishing was performed with a tripod polisher (South Bay Technology Inc.) using polishing papers (120 – 1,200 grit, Allied High Tech Products Inc.) followed by diamond films (30 – 0.5 μm, South Bay Technology Inc.).

The purity and composition of the samples were examined using X-ray powder diffraction (XRD) and energy-dispersive X-ray spectroscopy (EDX). Powder samples from crushing the ingots were tested for phase purity by employing an X'Pert Pro™ X-ray powder diffraction system (PANalytical, Netherlands). This test is critical as it determines the existence of other common low-hardness impurities, such as WB_2, in the synthesized samples. Because X-ray diffraction only gives information about the phase purity of the sample and does not provide elemental analysis, energy-dispersive X-ray spectroscopy (EDX) was used to check the composition of the synthesized materials. This was accomplished by scanning the flat, polished samples using an EDAX detector installed on a JEOL JSM 6700 F scanning electron microscope (SEM).

The mechanical properties of the samples were investigated using micro-indentation, nano-indentation, and high-pressure X-ray diffraction. To measure the Vickers micro-indentation hardness of the compounds, the optically flat polished samples were indented using a MicroMet® 2103 micro-hardness tester (Buehler Ltd.) with a pyramid diamond tip. With a dwell time of 15 s, the indentation was carried out with the application of five different loads ranging from 4.9 N (high load) to 0.49 N (low load). Under each load, the surface was indented at 15 randomly chosen spots to ensure very accurate hardness measurements. The lengths of the diagonals of the indents were then measured with a high-resolution Zeiss Axiotech® 100HD optical microscope (Carl Zeiss Vision GmbH) and **Equation (3.1)** was used to obtain Vickers micro-indentation hardness values ($\boldsymbol{H_v}$):

$$H_v = \frac{1854.4P}{d^2}$$ **Equation (3.1)**

where *P* is the applied load (in N) and *d* is the arithmetic mean of the diagonals of the indent (in micrometers).

Nano-indentation hardness testing was also performed on the polished samples by employing an MTS Nano Indenter XP instrument (MTS) with a Berkovich diamond tip. After calibration of the indenter with a standard silica block, the samples were carefully indented at 20 randomly chosen points. The indenter was set to indent the surface to a depth of 1,000 nm and then retract. From the load-displacement curves for loading and unloading, both nano-indentation hardness of the material and an estimate of its Young's (elastic) modulus are achieved based on the method originally developed by Oliver and Pharr[135] using **Equation (3.2)** and **Equation (3.3)**:

$$H = \frac{P_{max}}{A}$$ **Equation (3.2)**

where *H*, P_{max}, and *A* are nano-indentation hardness, peak indentation load, and projected area of the hardness impression, respectively, and

$$\frac{1}{E_r} = \frac{\frac{(1-v^2)}{E + (1-v_i^2)}}{E_i}$$ **Equation (3.3)**

where *E* and *v* are the elastic modulus and Poisson's ratio of the material and E_i and v_i are the elastic modulus and Poisson's ratio of the indenter, respectively. The reduced modulus (E_r) can be calculated from the elastic stiffness (*S*), as follows:

$$S = \frac{dp}{dh} = \frac{2}{\sqrt{\pi}} E_r \sqrt{A} \qquad \textbf{Equation (3.4)}$$

where *p* and *h* are load and depth of penetration, respectively, and *dp⁄dh* is the tangent to the unloading curve at the maximum (peak) load. Because the Poisson's ratio of WB_4 with and without Re is not yet known, an approximate value of 0.18 (calculated for ReB_2) was used to determine the Young's modulus.[147] The reported modulus values are, therefore, estimates.

Thermal stability of the powder samples was studied in air using a Pyris Diamond thermogravimetric/differential thermal analyzer module (TG-DTA, Perkin Elmer Instruments). Samples were heated up to 200°C at a rate of 20°C⁄min and soaked at this temperature for 10 min to remove water vapor. They were then heated up to a 1,000°C at a rate of 2°C⁄min and held at this temperature for 120 min. The samples were then air cooled at a rate of 5°C⁄min. X-ray diffraction was carried out on the powders after cooling to determine the resulting phases.

Results and Discussion

A representative X-ray powder diffraction (XRD) pattern for tungsten tetraboride synthesized by arc melting of the eutectic composition is displayed in **Figure 3.1**. The XRD pattern demonstrates excellent agreement with patterns published for previously reported syntheses of this compound and may be fully indexed against the reference data available in the Joint Committee on Powder Diffraction Standards (JCPDS) database[163]. The WB_4 pattern shows no signs of lower-boride impurity phases such as tungsten diboride (WB_2 with major peaks at 2ϑ = 25.683°, 34.680° and 35.275°). The purity of the boride phase was further confirmed using energy-dispersive X-ray spectroscopy (EDX), showing no signs of contamination with arcing (copper) or grinding (iron, nickel) materials. Peaks for crystalline b-boron are, however, barely identifiable at lower angles in the XRD pattern and the secondary boron phase is clearly

identifiable in backscattered scanning electron micrographs (SEM). The presence of a boron phase was anticipated, given the large excess of elemental boron required to reach the eutectic composition.

Vickers micro-indentation hardness testing of tungsten tetraboride was carried out on optically flat samples obtained after cutting and polishing the arc melted ingots. Great care was taken to indent only the boride phase, with the results depicted in **Figure 3.2**. Hardness values of 43.3 ± 2.9 GPa under an applied load of 0.49 N (low load) and 28.1 ± 1.4 GPa under an applied load of 4.9 N (high load) were measured, representing the aggregated values from several such samples. While there are no theoretical or experimental data in the literature for medium loads (2.94, 1.96, and 0.98 N), the low-load hardness value of 43.3 GPa is very close to a theoretical prediction of 41.1 – 42.2 GPa[164], and both low-load and high-load hardness values are lower than the experimental values of 46.2 GPa and 31.8 GPa, respectively, reported by Gu *et alia*[157]. Moreover, the load-dependent hardness, commonly known as the indentation size effect[165] as seen in **Figure 3.2**, has been observed with several other super-hard materials as well.[52,150] This behavior has been attributed to the role of friction in indentation[166] and the recovery of the elastic component of deformation after unloading, which is prevalent in smaller indents, as well as the material's intrinsic response to different loads[167,168].

In addition, nano-indentation hardness values of 40.4 ± 1.2 GPa (at a penetration depth of 250 nm) and 36.1 ± 0.6 GPa (at a penetration depth of 1,000 nm) were measured for WB_4 from the load-displacement curves, a representative example of which is presented in **Figure 3.3**. The small pop-in events, observed in this figure, may be due to a burst of dislocations, elastic-plastic deformation transitions, or initiation and propagation of subsurface cracks.[147] From this test, we estimate an elastic (Young's) modulus of 553 ± 14 GPa for WB_4. The discrepancy between the hardness data obtained from micro-indentation and nano-indentation can be attributed to the differences in the geometry and shape of the indenters, depth of penetration of the indenters, and hardness measurement methods.[158] These high

hardness values, regardless of the method of measurement, indicate that WB_4, within experimental errors, is similar in hardness to rhenium diboride, which possesses micro-indentation and nano-indentation hardness values of 48.0 ± 5.6 GPa and 39.5 ± 2.5 GPa, respectively.[52,145] These results are encouraging, considering that tungsten is much less expensive than rhenium. Note also that the hardness of WB_4 is considerably higher than that of OsB_2 and RuB_2[147] and at least 1.5 times that of the traditional material used for machine tools, tungsten carbide[14,169,170]. The high hardness of WB_4 may be associated with its unique crystal structure consisting of a three-dimensional network of boron (see Chapter 8).

Once the properties of WB_4 were well characterized, the possibility of increasing its hardness was investigated by adding rhenium to WB_4 in an attempt to make solid solutions. Compositions of the samples were confirmed with EDX. The micro-indentation hardness data for these compounds are plotted in **Figure 3.4**. The hardness under low load (0.49 N) increases from 43.3 GPa for WB_4 to a maximum of 49.8 GPa for 1 at.% Re addition. It then decreases to about 29 GPa for 20 at.% Re and increases again to 34 GPa for 50 at. % Re. Similar trends are seen for loads of 0.98, 1.96, 2.9 and 4.9 N.

The XRD patterns for all these compounds are presented in **Figure 3.5** in order to follow the structural evolution of the samples. In this figure, the top pattern belongs to WB_4 with no Re addition, while the bottom pattern with a W **:** Re ratio of 1 **:** 1 matches the ReB_2 pattern (JCPDS ref. code 00-011-0581). However, because the peaks of the pattern of this compound are shifted with respect to those of pure ReB_2, this material appears to be a solid solution of ReB_2 with W, i.e. $Re_{1-x}W_xB_2$ (see Chapter 4), which is likely saturated with tungsten. On the other hand, no shifts are observed in the peaks of WB_4 with the addition of Re, indicating that $W_xRe_{1-x}B_4$ solid solutions do not form under these synthetic conditions. By following the major peak of the $Re_{1-x}W_xB_2$ solid solution (*101*) from top to bottom, as highlighted inside

the dotted rectangle, it is clear that this peak begins to appear at 0.5 at.% Re addition and increases substantially at 10 at.% Re.

Based on the rhenium – boron binary phase diagram, it appears that the $Re_{1-x}W_xB_2$ phase should precipitate from the melt first. If this is the case, it could serve as nucleation sites for WB_4 formation, resulting in $Re_{1-x}W_xB_2$ grains dispersed in a WB_4 majority phase. At low Re concentration, these $Re_{1-x}W_xB_2$ grains could prevent dislocations slip and make a harder material. This trend is indeed observed with the compound containing 1 at.% Re being the hardest (approximately 50 GPa). Therefore, it is deduced that by adding small amounts of Re to WB_4 an intrinsically super-hard material (WB_4) may be further hardened by means of an extrinsic component.[162] The overall decrease in hardness at Re concentrations larger than 10 at.% can be attributed to the development of bulk $Re_{1-x}W_xB_2$ domains, leading to a decrease in the overall concentration of WB_4 and a large increase in the proportion of amorphous boron. The slight increase in hardness for 40 and 50 at.% Re may be attributed to a change in stoichiometry of the $Re_{1-x}W_xB_2$ phase toward a more Re-rich composition with a higher intrinsic hardness.

While the precise mechanism for the increased hardness by the addition of Re is not yet understood in detail, it is important to note that the measured nano-indentation hardness values for the compound of 1 at.% Re in WB_4 are 42.5 ± 1.0 GPa and 37.3 ± 0.4 GPa at penetration depths of 250 and 1,000 nm, respectively, demonstrating that this extrinsic super-hard material is harder than pure WB_4 (40.4 and 36.1 GPa) or ReB_2 (39.5 and 37.0 GPa) at the same penetration depths[52,145]. The elastic modulus of WB_4 containing 1 at.% Re is estimated to be 597 ± 33 GPa using **Equation (3.3)** and **Equation (3.4)**. This value is higher than those of RuB_2 (366 GPa), OsB_2 (410 GPa) and WB_4 (553 GPa), but lower than the value of 712 GPa[147] determined for ReB_2.

In addition to mechanical properties, the thermal stability at high temperatures is important if these materials are to be considered for applications such as high-speed machining or cutting. Thermal stability curves on heating both tungsten tetraboride and tungsten tetraboride with 1 at.% Re are shown in **Figure 3.6**. Both compounds are stable in air up to approximately 400 °C. The weight gain above 400 °C in both compounds can be attributed to the formation of WO_3, as confirmed by powder X-ray diffraction.

Conclusions

Tungsten tetraboride is an interesting candidate as a less expensive member of the growing group of super-hard transition metal borides. As with other transition metal borides, tungsten tetraboride was successfully synthesized by arc melting from the elements. Characterization using powder X-ray diffraction (XRD) and energy-dispersive X-ray spectroscopy (EDX) indicates that the as-synthesized material contains only a single boride phase. Mechanical testing using micro-indentation gives a Vickers hardness of 43.3 ± 2.9 GPa under an applied load of 0.49 N. Using nano-indentation, a Young's modulus of 553 ± 14 GPa may be calculated for this material. Various ratios of rhenium may be added to WB_4 to further increase hardness. With the addition of 1 at.% Re, the Vickers hardness increases to approximately 50 GPa at 0.49 N. Powders of tungsten tetraboride with and without 1 at.% Re addition are thermally stable up to approximately 400 °C in air as measured by thermal gravimetric analysis. The two benefits of this compound, facile synthesis at ambient pressure and relatively low cost elements, make it a potential candidate to replace other conventional hard and super-hard materials in cutting and machining applications. Therefore, WB_4 and mixtures of WB_4 with $Re_xW_{1-x}B_2$, which contain only a small amount of the secondary dispersed solid solution phase, may have potential for use in cutting, forming, and drilling or wherever high hardness and wear resistance is a challenge.

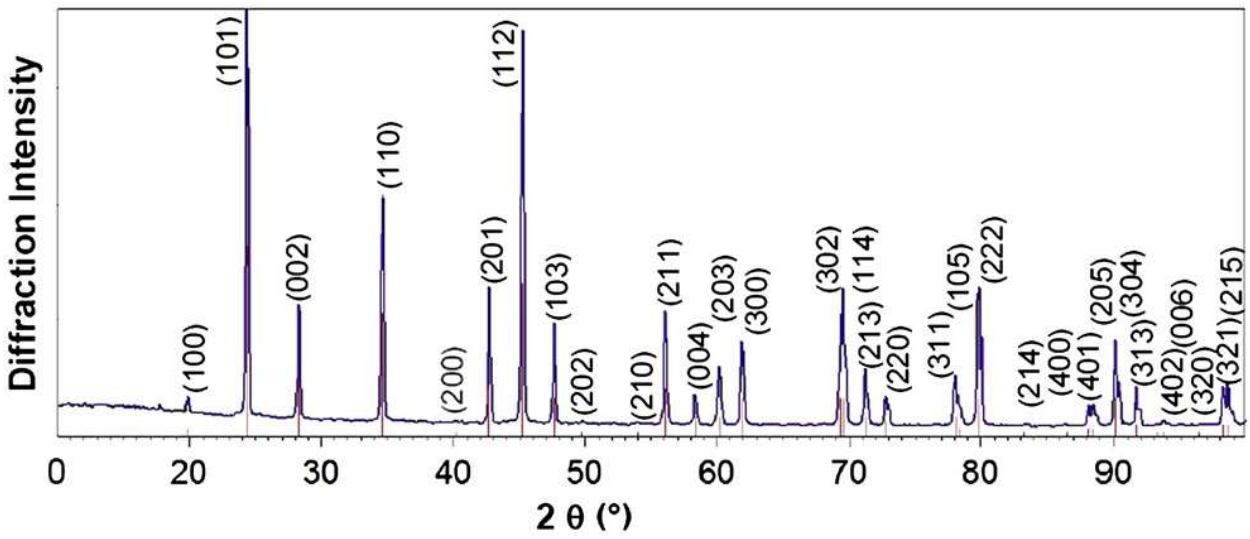

Figure 3.1: X-ray diffraction pattern of tungsten tetraboride (WB_4) synthesized via arc melting. The stick pattern given below is from the Joint Committee on Powder Diffraction Standards (ref. code: 00-019-1373) for WB_4. The corresponding Miller Index is given above each peak.

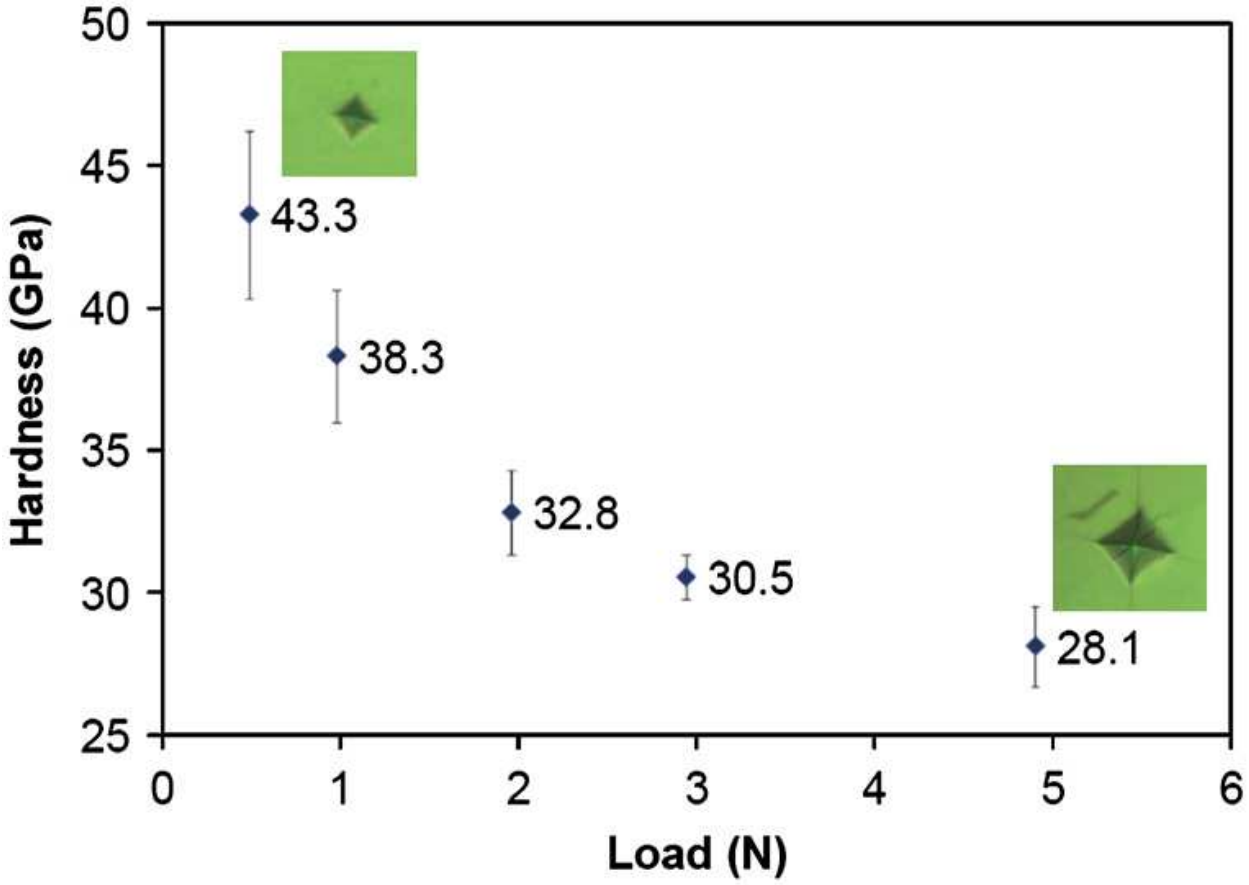

Figure 3.2: Vickers micro-indentation hardness of tungsten tetraboride under loads ranging from 0.49 N (low load) to 4.9 N (high load). The corresponding hardness values range from 43.3 GPa to 28.1 GPa at low and high loads, respectively, indicating a clear indentation size effect (ISE). Typical optical images of the impressions made at high and low loads are shown.

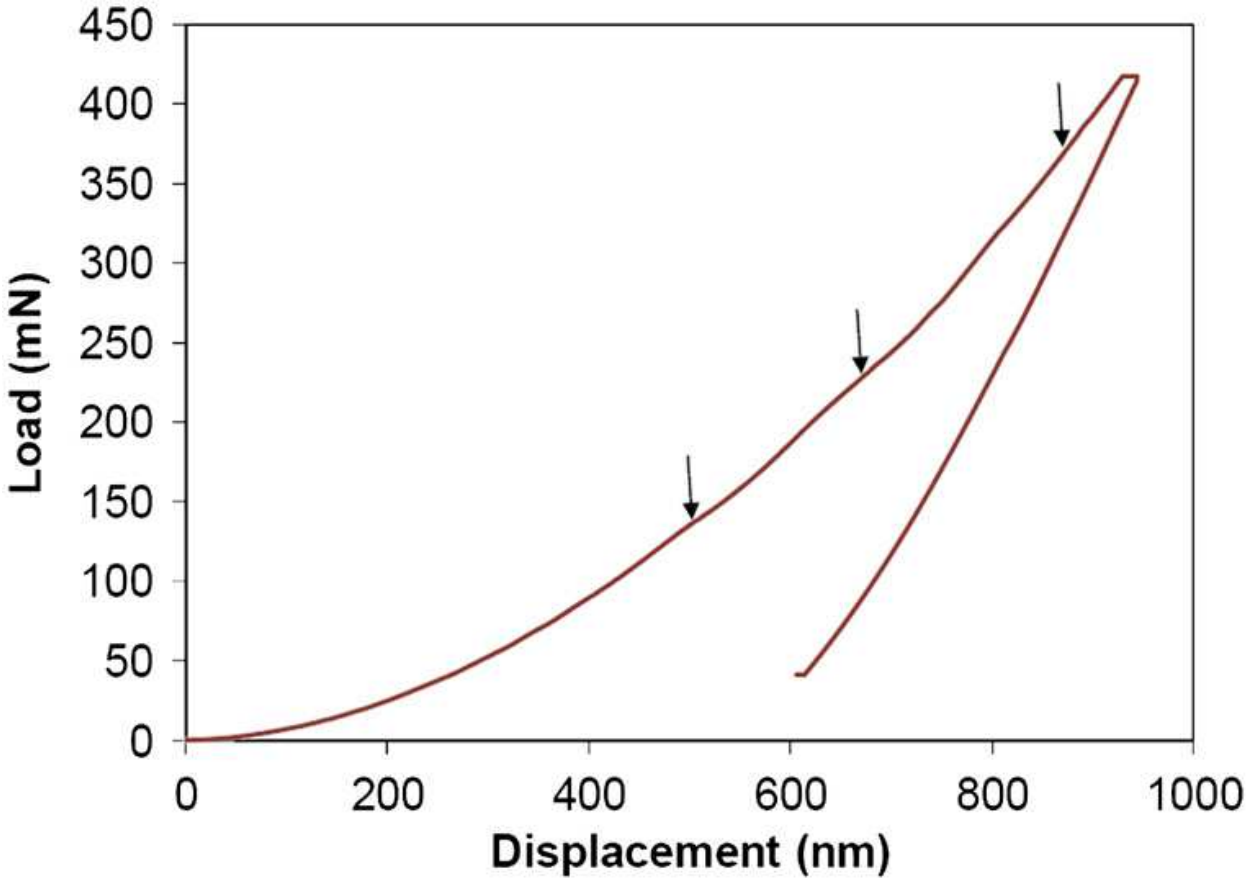

Figure 3.3: A typical load-displacement plot obtained from nano-indentation on a tungsten tetraboride ingot. From the loading and unloading curves, nano-indentation hardness values of 40.4 GPa and 36.1 GPa are calculated at indentation depths of 250 nm and 1,000 nm, respectively. The corresponding Young's modulus is approximately 553 GPa. The depth of penetration of the indenter is 1,000 nm. The arrows show the locations of small pop-in events that may be due to a burst of dislocations, cracking or elastic-plastic deformation transitions.

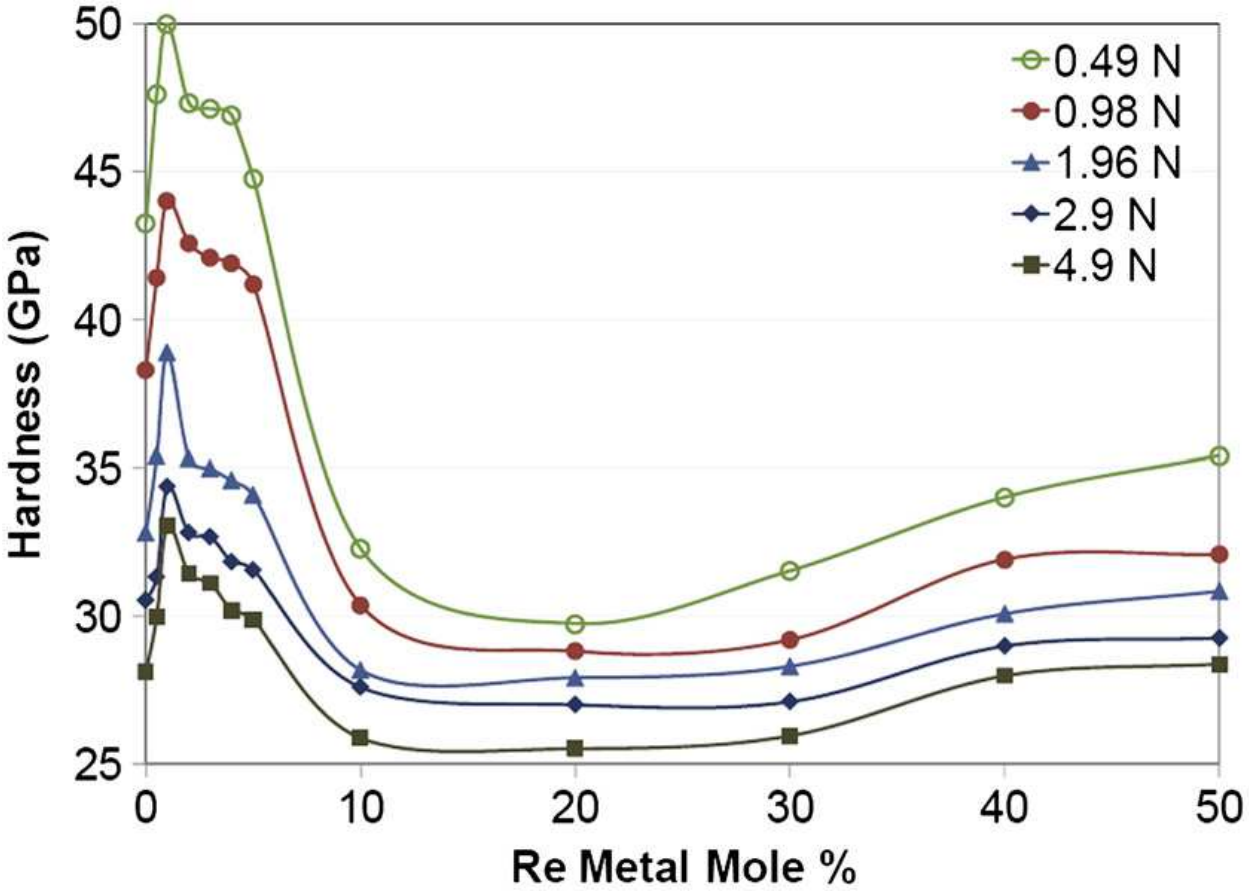

Figure 3.4: Micro-indentation hardness data for tungsten/rhenium boride samples as a function of rhenium content. Data were collected for samples with Re additions of 0.0, 0.5, 1.0, 2.0, 3.0, 4.0, 5.0, 10.0, 20.0, 30.0, 40.0, and 50.0 at.%. The low-load hardness increases from 43.3 GPa for WB 4 to a maximum of approximately 50 GPa at 1 at.% Re, decreases to a minimum of 29 GPa at 20 at.% Re and then increases again up to 34 at.% Re. Similar trends are observed for all of the loads (0.49 N–4.9 N).

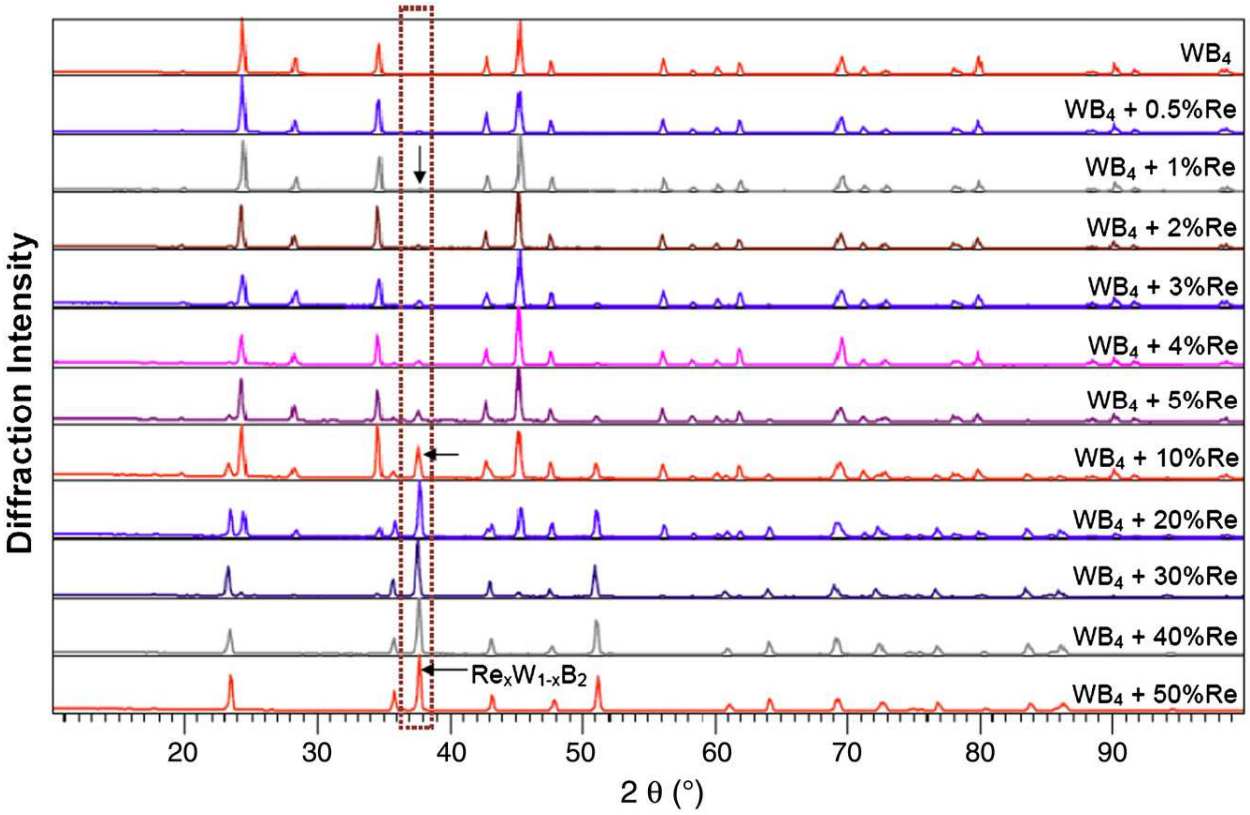

Figure 3.5: X-ray diffraction patterns for tungsten tetraboride (top pattern) and various Re additions (0.5 –50.0 at.%). The rectangle and arrows are to guide the eyes, showing the appearance of drastic changes in the intensity of the major peak of the $Re_xW_{1-x}B_2$ solid solution phase (bottom pattern). These changes help to explain the changes in hardness observed in **Figure 3.4**.

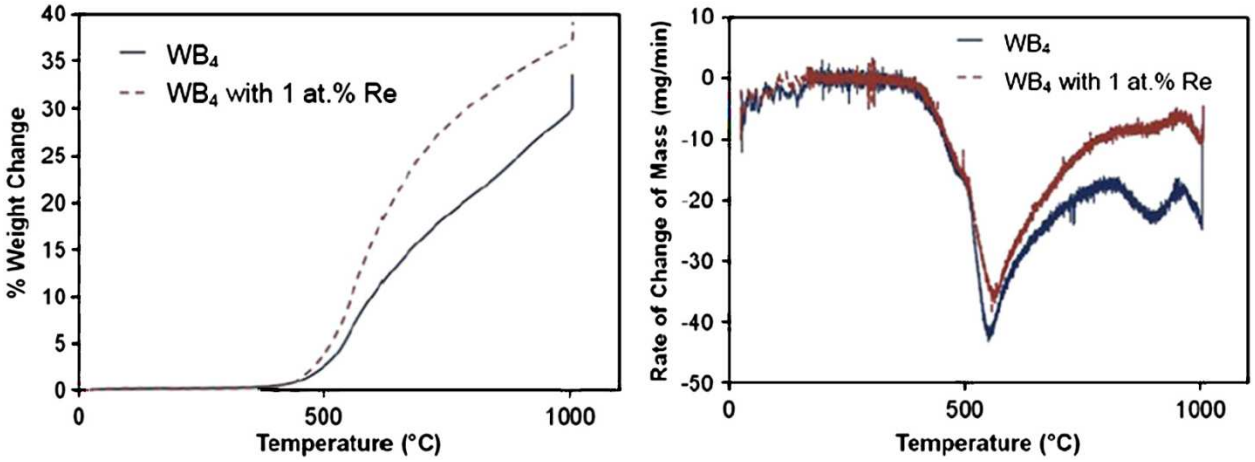

Figure 3.6: Thermal stability of tungsten tetraboride (WB_4) and WB_4 + $Re_xW_{1-x}B_2$ (containing 1 at.% Re) as measured by thermal gravimetric analysis (left). The corresponding DTG curves (right). These curves indicate that both materials are thermally stable up to 400°C in air. The weight gain of about 30 – 40% for both samples above 400°C can be mainly attributed to the oxidation of tungsten to WO_3.

Chapter 4

Behavior under High Pressure

Introduction

Broadly, two approaches are used to design and synthesize materials with high hardness. A first approach is to imitate natural diamond by combining light first-row elements (B, C, N, or O) to produce materials that maintain short bonds with high covalency, such as *c*-BN[171], B_6O[172], and BC_2N[173]. A second route is to start with elemental metals that are intrinsically incompressible, but not hard, and to attempt to improve their hardness by incorporating light elements into the metal structure to simultaneously optimize covalent bonding and valence-electron density.[103] This class, which generally contains late, transition metal borides, carbides, nitrides, and oxides contains many candidate hard materials.[169,174–176] This has been the approach we have taken in the creation of super-hard borides.[158]

For example, by adding boron to Os, which has alone only a hardness of 3.9 GPa, Cumberland *et alia*[51] introduced covalent bonds to its lattice, while maintaining the extremely high bulk modulus found in the native metal. The presence of these covalent bonds in OsB_2 resulted in a hardness of 21.6 GPa under an applied load of 0.49 N, without substantially reducing the bulk modulus (365–395 GPa).[51,150] However, although this hardness value is relatively high, it is far from falling within the "super-hard" category.[177] One reason for this is that the OsB_2 structure contains double Os layers, alternating with covalent B layers. The weak Os-Os metallic bonds within the layers likely reduce the resistance of OsB_2 to large shear deformations in the easy-slip direction, which is parallel to the layers.[177] This may be contrasted, for instance, with ReB_2. The ReB_2 structure consists of alternating single layers of hexagonally packed Re and puckered interconnected hexagonal rings of boron. Without the double metal layers that reduced

the hardness for OsB_2, this material exhibits a much higher hardness of 48 ± 5.6 GPa under an applied load of 0.49 N.[52] One might expect this trend to continue with similarly hexagonal borides containing even higher concentrations of boron (and thus greater covalency and bond-directionality).

When Gu *et alia*[157] synthesized WB_4, they reported hardness values as high as 46.2 GPa, and found a bulk modulus of 304 ± 10 GPa through fitting the second-order Birch-Murnaghan equation of state (EOS). Furthermore, with an exceptionally high first derivative $\boldsymbol{K_{0T}}$ of 15.3 ± 5.7, they obtained an extremely low value of the zero-pressure bulk modulus ($\boldsymbol{K_0}$) of 200 ± 40 GPa using the third-order Birch-Murnaghan EOS. Unfortunately, it is difficult to effectively evaluate the lattice behavior of WB_4, especially under extreme conditions, from this work, given the lack of synthetic and procedural details provided.

In parallel, Wang *et alia*[164] have predicted a hardness of between 41.1 – 42.2 GPa and a bulk modulus of 292.7 – 324.3 GPa for WB_4 from theory. Further, they calculated a low shear modulus of 103.6 – 181.6 GPa. More recently, Liu *et alia*[178] studied the high-pressure behavior of WB_4, synthesized using a hot press under a pressure of 50.8 GPa, using silicone oil as the pressure medium. The authors obtained values ranging from 256 to 342 GPa, depending on the EOS and the pressure range. Changing the pressure range can have a significant effect with silicone oil, because this pressure medium has a hydrostatic limit of 8 GPa[179] and develops a deviatoric stress of 1 GPa at pressures as low as 10 GPa.[180] Non-hydrostaticity can result in strongly biased determination of elastic properties and also can result in diffraction peak broadening and loss of resolution that may mask small changes in the lattice parameters which may indicate structural transitions. Thus, we aimed to examine the lattice behavior of WB_4 under better controlled and more hydrostatic conditions, with a goal of resolving these conflicts in the value of bulk modulus.

As discussed in chapter 5, we have found that highly crystalline WB_4 may be successfully synthesized via the arc melting technique and its high hardness was confirmed using both micro-indentation and nano-indentation, obtaining hardness values of 43.3 ± 2.9 GPa and 40.4 GPa, respectively.[181] In this chapter, high-pressure X-ray diffraction results are also presented for this compound and will be compared to previous experimental and theoretical work.

In order to clarify the elastic moduli of WB_4 with higher accuracy and to further examine the lattice distortions of WB_4 under elevated pressure, we have undertaken a more complete experimental study of the pressure-dependent compression behavior of WB_4 using synchrotron-based angle-dispersive X-ray diffraction in the diamond anvil cell. It is now widely recognized that hydrostaticity is the key to obtaining reliable values of bulk modulus and its pressure derivatives, particularly for fairly incompressible materials. We have thus used neon as a pressure transmitting medium because it offers good quasi-hydrostatic conditions to at least 50 GPa.[179] In addition, we have performed a similar set of experiments on ReB_2 to 63 GPa, allowing us to compare the behavior of these two model transition metal borides. The example of ReB_2 provides a good cross-comparison because of the close proximity of Re to W in the periodic table, the similar valence electron densities of these two materials (ReB_2: 0.477 $e^- Å^{-3}$; WB_4: 0.485 $e^- Å^{-3}$), the similar indentation hardness values measured for these materials (48.0 ± 5.6 GPa and 43.3 ± 2.9 GPa for ReB_2[52] and WB_4[181], respectively), and their related structures (both with space group $P6_3/mmc$).

Materials and Methods

Powders of pure tungsten (99.9994%, JMC Puratronic, U.S.A.) and amorphous boron (99+%, Strem Chemicals, USA) were mixed together in the molar ratio of 1 : 12 and pressed into a pellet by means of an hydraulic (Model 3851, Carver, USA) press under 10 000 pounds of force. The excess boron is needed

to ensure the thermodynamic stability of the WB_4 structure based on the binary phase diagram of the tungsten–boron system.[154,156] The pellets were then placed in an arc-melting furnace under high-purity argon at ambient pressure and fused by application of an AC current of >70 A. The resulting ingots were then crushed to form a fine powder using a hardened steel mortar and pestle. The rhenium diboride sample was produced in a two-step process that involved first synthesizing ReB_2 powder and then sintering the powder into an ingot. The detailed description of the process can be found elsewhere.[145]

The purity of the powdered borides was confirmed by powder X-ray diffraction (XRD) and energy-dispersive X-ray spectroscopy (EDS). XRD patterns were collected on an X'Pert Pro™ X-ray powder diffraction system (PANalytical, Netherlands; **Figure 4.1**). EDS was performed using a JSM-6700F field-emission scanning electron microscopy (JEOL Ltd., Japan) equipped with an energy-dispersive X-ray spectroscopy detector (EDAX™, EDAX, Inc. U.S.A.) using an ultrathin window.

Two sets of high-pressure experiments were performed. In the first set of experiments, The compressibility of WB_4 was measured using high-pressure X-ray diffraction in a Diacell diamond anvil cell with neon gas as the pressure medium. Diffraction patterns were collected for the powder samples from ambient pressure to 30 GPa. The data were fit using a finite strain equation of state (**Equation (4.1)** and **Equation (4.2)**) to calculate the zero-pressure bulk modulus (K_0).

$$P = 3f(1+2f)^{5/2}K_O[1 - 2\xi f + \cdots] \qquad \textbf{Equation (4.1)}$$

Where

$$f = \frac{1}{2}\left[\left(\frac{V}{V_O}\right)^{-2/3} - 1\right] \qquad \textbf{Equation (4.2)}$$

Equation (4.1) can be used to analyze the equation of state data using Birch's $\boldsymbol{F}$ versus $\boldsymbol{f}$ correlation.[182,183] The normalized pressure,

$$F = \frac{P}{[3f(1+2f)^{5/2}]} \qquad \textbf{Equation (4.3)}$$

which can be determined experimentally, is a polynomial in *f* according to **Equation (4.2):**

$$F(f) = K_O(1 - 2\xi f + \cdots) \qquad \textbf{Equation (4.4)}$$

Thus, the intercept of an $\boldsymbol{f}$ versus $\boldsymbol{F}$ plot yields $\boldsymbol{K_0}$, which is a second-order fit to the finite strain equation of state.

The second set of experiments were carried out both for WB_4 and for ReB_2 using a symmetric diamond anvil cell equipped with 300-μm diamond culets using a pre-indented rhenium gasket with a 150-μm diameter sample chamber. A 50-μm diameter powder sample was loaded into the cell, supported by a piece of platinum foil (5 μm thick, 99.95%, Alfa-Aesar, USA), which was used as an internal pressure calibrant. A 10-μm ruby chip was placed next to the sample as an external pressure calibrant. To ensure a quasi-hydrostatic sample environment, neon gas was loaded into the cell using the Consortium for Materials Properties Research in Earth Sciences (COMPRES) and GeoSoilEnvi-roCARS (GSECARS) gas-loading system.[184] The pressure-volume data from these experiments were fit using the third-order finite strain Birch-Murnaghan equation of state (Equation (4.5)) to infer the room-pressure isothermal bulk modulus ($\boldsymbol{K_{0T}}$) and its first derivative with respect to pressure ($\boldsymbol{K_{0T}'}$). The third-order equation shown below reduces to the second-order equation when $\boldsymbol{K_{0T}'}$ is equal to 4.

$$P = \frac{\frac{3}{2}K_O\left[\left(\frac{V}{V_0}\right)^{-7/3} - \left(\frac{V}{V_0}\right)^{-5/3}\right]}{\left\{1 - \left(\frac{3}{4}\right)(4 - K_0')\left[\left(\frac{V}{V_0}\right)^{-2/3} - 1\right]\right\}}$$ **Equation (4.5)**

High-pressure angle-dispersive X-ray diffraction experiments were performed on Beamline 12.2.2 at the Advanced Light Source (ALS, Lawrence Berkeley National Laboratory) and 16-BM-D of the High Pressure Collaborative Access Team (HPCAT) sector of the Advanced Photon Source (APS) with X-ray beam sizes of approximately 10×10 μm^2 and 5×15 μm^2, respectively. Image plate detectors were used at both beamlines. The distance and orientation of the detector were calibrated using LaB_6 and CeO_2 standards, respectively. Pressure was determined using ruby fluorescence. A secondary pressure calibration was performed by referencing the measured lattice parameter of the internal standard platinum (Pt) to its pressure-volume EOS. X-ray diffraction patterns of WB_4 and ReB_2 were collected up to pressures of 58.4 and 63 GPa, respectively.

Results

At ambient temperature and pressure, X-ray diffraction studies of WB_4 reveal a hexagonal structure with the lattice parameters a = 5.1945 ± 0.0013 Å, c = 6.3311 ± 0.0030 Å, and V_0 = 147.94 ± 0.15 $Å^3$ and axial ratio c/a = 1.2188 ± 0.0006 (**Figure 4.1**). Representative high-pressure diffraction patterns for WB_4 are shown in **Figure 4.3**. The two-dimensional diffraction patterns were integrated using the program FIT2D[185] to yield one-dimensional plots of X-ray intensity as a function of d-spacing. All patterns were indexed to the hexagonal phase, and there were no signs of phase trans-formations. The sample remained in the hexagonal phase up to the highest pressure of 58.4 GPa, at which point the lattice parameters were a = 4.949 ± 0.013 Å and c = 5.984 ± 0.027 Å, and V_0 = 126.9 ± 1.30 $Å^3$. Similarly, ReB_2 was also shown to be stable in the hexagonal phase to 63 GPa.

The hydrostatic compressibility data obtained from the first set of experiments is plotted in **Figure 4.2**. This study of the compressibility of WB4 under hydrostatic pressure resulted in a zero-pressure bulk modulus, K_0, of 339 ± 3 GPa obtained using a second-order finite strain equation of state fit. This value is close to theoretically predicted values (292.7 – 324.3 GPa) and about 11% higher than the bulk modulus of 304 GPa previously reported for this material. [157,164] The theoretical and experimental bulk modulus values both exceed 185 – 224 GPa for pure boron[186] and 308 GPa for pure tungsten[46].

Figure 4.4 shows the normalized unit cell volume of WB_4 as a function of pressure, under both compression (filled circles) and decompression (open circles). **Figure 4.5** shows the normalized compressibility of both the *a*- and *c*-lattice parameters of WB_4. Up to ≈40 GPa, both the *a*- and *c*-lattice constants show a gentle decrease upon compression, with the *a*-axis appearing slightly more compressible than the *c*-axis. However, at ≈42 GPa, the *c*-axis appears to suddenly undergo a softening, becoming significantly more compressible than the *a*-axis. The *a*-axis does not show any change in behavior. This structural change is reversible, with the *c*-lattice constant recovering its original strain values upon decompression. This structural change has not been observed in other studies and emphasizes the need for high-quality data.

Because of this anomalous behavior in the *c*-direction, fits to the Birch-Murnaghan EOS were performed at pressures lower than 42 GPa. The calculated zero-pressure bulk modulus, $\boldsymbol{K_0}$, using a second-order Birch-Murnaghan EOS is 317 ± 3 GPa. Using a third-order Birch-Murnaghan EOS, we obtain values of $\boldsymbol{K_0}$ = 367 ± 11 GPa and $\boldsymbol{K_{0T}}$ = 0.9 ± 0.6. Using only data obtained on compression results, we calculate $\boldsymbol{K_0}$ = 326 ± 3 GPa (second-order Birch-Murnaghan EOS) and $\boldsymbol{K_0}$ = 369 ± 9 GPa with $\boldsymbol{K_{0T}}$ = 1.2 ± 0.5 (third-order Birch-Murnaghan EOS). The second-order values are slightly lower than our previous study of WB_4, which presented a bulk modulus of 339 ± 3 GPa obtained using a second-order finite strain EOS.[17] The inferred values of $\boldsymbol{K_0}$ and $\boldsymbol{(\mathrm{d}K/\mathrm{d}P)_0}$ are strongly correlated, however, with an inverse relationship. For

the WB_4 data up to 40 GPa, the pairs (K_0, K_{0T}) = (326, 4) and (369, 1.2) are statistically indistinguishable. The trade-offs between the two parameters are plotted in **Figure 4.7**, which shows contours for the sum of the deviations from the fits as a function of varying K_0 and K_{0T} . The trade-off between K_0 and K_{0T} produces a change in bulk modulus of −12 GPa for every 1 of K_{0T} WB_4. This relationship is sufficient to explain the variation in previous studies, including the exceptional low-bulk modulus in Gu's results.[157]

Figure 4.4 also shows the compression and decompression behavior of ReB_2 up to 63 GPa. Second-order Birch-Murnaghan equation fitting to the ReB_2 data gives an ambient bulk modulus of K_0 = 344 ± 1 GPa, with a similar trade-off between K_0 and $(dK/dP)_0$ (**Figure 4.7**). The measured bulk modulus is slightly lower than the previously reported bulk modulus of 360 GPa, also obtained using second-order Birch-Murnaghan EOS fits to pressure-dependent X-ray diffraction,[52] but both values fall in the range of 317 – 383 GPa, previously reported from resonant ultrasound spectroscopy (RUS) experiments (**Table 4.1**).[114,116,145–147,187] Fitting the third-order Birch-Murnaghan EOS gives K_0 = 340 ± 5 GPa with K_{0T} = 4.2 ± 0.2. Compressibility along different crystallographic axes in hexagonal ReB_2 is illustrated in **Figure 4.6**. Importantly, close examination of *a*- and *c*-lattice constants shows no evidence of lattice softening in either direction. Comparison of **Figure 4.5** and **Figure 4.6** also clearly emphasizes that WB_4 shows much more isotropic bonding than ReB_2 with much more similar compressibility in *a*- and *c*-directions.

Discussion

At the point of the structural change at 42 GPa, the WB_4 diffraction pattern remains the same, with no evidence of peak broadening or splitting (**Figure 4.3**). Thus, there is no evidence for a first-order phase transition. Additionally, the compression behavior is reversible upon release of pressure. Because this transition pressure for WB_4 (42 GPa) appears far from the hydrostatic limit of the pressure medium (≈15

GPa),[179] it is unlikely that deviation from hydrostaticity is responsible for this observation. Additionally, if deviatoric stresses were affecting the measured X-ray strains, the axial geometry of the X-ray in the diamond anvil cell combined with the gasket direction would predict the opposite observation—that lattice planes should appear less compressible, not more compressible, as the medium becomes less hydrostatic. As a result, it appears that the abrupt change in *c/a* ratio observed at 42 GPa is a real structural change of the system; specifically, a second-order phase transition.

To make a more direct comparison between the high-pressure behavior of WB_4 and ReB_2, we examined their *c/a* ratios normalized to each other at ambient pressure. Because the unit cells are not the same in these two materials, the absolute *c/a* ratios are rather different (1.2188 for WB_4 and 2.5786 for ReB_2; **Figure 4.8**). Normalization is thus required to compare the fairly small changes observed here. Up to ≈40 GPa, both materials show a linear increase in their *c/a* ratio of similar magnitude. However, this increase continues for ReB_2 while there is a discontinuous change in slope for the *c/a* ratio at ≈42 GPa for WB_4. As shown in **Figure 4.5**, this *c/a* ratio drop can be almost solely accounted for by the anomalous compression behavior of the *c*-axis.

This structural change may be mechanical or may be electronic in nature. Electronic band structure calculations has been reported on ReB_2 without any evidence for transitions up to 90 GPa,[188] but less is known for WB_4. Although transitions based on changes in optimal atomic positions or bond orientation may seem to be the likely explanation for the observed transitions, other anomalous compression phenomena have been documented experimentally[189–192] and theoretically[193–201] when distortion of the electronic band structure results in a topological singularity of the Fermi surface. Those are known as electronic topological transitions (ETTs) or Lifshitz transitions.[202] The anomaly has mostly been found in hexagonal-close-packed (hcp) metals, including Zn,[189–192] Cd,[189] and Os,[48,203] and intermetallic compounds such as $AuIn_2$[200,201] or $Cd_{0.8}Hg_{0.2}$[204]. However, these transitions are highly controversial

because of their subtle nature and because of difficulties in their direct experimental detection at high pressures. The magnitude of the anomalies observed in the compression data associated with ETTs is usually small, as opposed to the significant softening observed in WB_4. In addition, most of the discontinuities associated with electronic phase transition occur below 20 GPa (e.g., calculated to be 7 and 14 GPa for Zn[198]; observed at 2.7 GPa for $AuIn_2$[200,201]). Moreover, ETTs do not necessarily affect only one lattice direction and usually result in a decrease in compressibility after the anomaly. Although the possibility of an ETT in WB_4 at high pressure is intriguing, the data do not fit the standard profile for these transitions, and thus it seems likely that the observed bond softening in WB_4 does not arise from this kind of singularity but is instead due to changes in optimal bonding at high pressure.

Lacking the observation of peak splitting and/or a new phase in the X-ray diffraction data, we assign this anomaly to a structurally induced second-order phase transition. The intersection of the two regions defines the transition pressure at 42 GPa. Furthermore, **Figure 4.8** reveals that although the *c/a* compression behavior is reversible, the *c/a* ratio does not fully recover its compression value until the pressure is decreased to less than 20 GPa. Such hysteresis further indicates that the softening is mechanical, rather than electronic in origin.

In order to understand this decompression behavior, the nature of the second-order phase transition of WB_4, and the lack of similar pressure-induced lattice-axis softening in ReB_2 and OsB_2, it is essential to consider the crystal structures of both ReB_2 and WB_4 (**Figure 4.9a** and **Figure 4.9b**). The crystal structure of ReB_2 (**Figure 4.9a**) is characterized by alternating layers of metal atoms and boron atoms. The boron atoms are condensed into six-membered rings in a chair-like conformation. The Re atoms are arranged in an hcp layer with B atoms occupying all tetrahedral voids; this enlarges the lattice by about 40%. A strong anisotropy has been found in the hexagonal structure (**Figure 4.6**), with the *c*-axis much less compressible than the *a*-axis. This can be explained by the directional electronic repulsion between

the boron and transition metal atoms aligned along the *c*-axis. This repulsion reduces the pressure-induced compression in the *c*-direction. Because the layers are not highly constrained in the *a*-*b* direction, continuous structural optimization upon compression results in smooth and continuous changes in the *c*-axis lattice constant up to 63 GPa.

The most widely cited structure of WB_4 was originally assigned by Romans and Krug in 1966,[154] which consists of alternating hexagonal layers of boron and tungsten atoms (**Figure 4.9b**). In contrast with the ReB_2 structure (**Figure 4.9a**), however, these planar B layers are propped up by B-B bonds aligned along the *c*-axis. This could make the *c* direction more compressible (pure B is more compressible than ReB_2) and less flexible. We hypothesize that because of the more constrained bonding in the WB_4 structure, high-pressure bond optimization within the ambient-pressure structure may be difficult, and a second-order phase transition could be required to optimize the bonding at high pressure. This would not be the case for the less constrained ReB_2 structure, which shows no signs of phase transitions up to 63 GPa. Upon decompression, the structural distortion is recovered, but rather incomplete at a low pressure, as is typical for pressure-induced phase transitions.

Because the primary interest in both ReB_2 and WB_4 is for applications as hard materials, the structural insights gained by examining lattice behavior under high-pressure conditions may be used to establish design parameters for developing new super-hard materials. In order for a solid to have a high hardness, it must possess sufficient structural integrity that can survive large shear strains without collapse.[205] A strongly covalently bonded three-dimensional and isotropic network may ensure high intrinsic hardness of a material, as seen in diamond and *c*-BN.[162] In WB_4, the presence of strong covalent B-B bonds in the *c*-axis apparently adds three-dimensional rigidity to the structure, which could reduce the chances of shear deformation or the creation and motion of the dislocations. At the same time, this three-

dimensional boron bonding could create a more isotropic bonding environment that can potentially withstand larger shear strains.

Moreover, high-pressure X-ray absorption spectroscopy on ReB_2 has shown flattening of the boron layers with increasing hydrostatic pressures.[206] Such flattening should facilitate slip-ping of the layers in the *a-b* plane and further reduce the hardness under load. Therefore, it may be that WB_4 possesses a higher resistance to shear strain and less dislocation activity compared to ReB_2 because of its three-dimensional, almost isotropic covalently bonded network. Although WB_4 is more compressible than ReB_2, it is intrinsically as hard, if not harder, than ReB_2. While the pressure-induced bond softening observed here is not a cause of this increased hardness; it is likely that the structural change observed in WB_4, but not in ReB_2, and the comparatively high hardness of WB_4 both stem from the increased stiffness of WB_4 that arises from the three-dimensional boron network.

Many attempts have been made to correlate hardness with other physical properties for a wide range of hard materials, especially bulk modulus and shear modulus.[27,46,51,52,102,103,147,148,207–214] Shear modulus is generally a much better predictor of hardness than bulk modulus.[46,102,148,207–210] We thus present here a calculated shear modulus of WB_4, obtained from the bulk modulus and an estimated Poisson's ratio using an isotropic model. We begin the estimation by assuming WB_4 has little elastic anisotropy, as demonstrated in OsB_2[114] and ReB_2,[116] so that an isotropic model can be applied. Because the Poisson's ratio of WB_4 has not yet been experimentally measured, the recently reported value of 0.1958 for ReB_2 from resonant ultrasound spectroscopy is used.[146] An isotropic model is then applied to estimate the shear modulus and the Young's modulus based on the measured bulk modulus and estimated Poisson's ratio of WB_4. The calculated shear and Young's modulus values are compared with first-principles calculations and nano-indentation data in **Table 4.1**. The measured bulk modulus (326 GPa) is in excellent agreement with the first-principles calculations based on the LDA method (324 GPa)[164] and

falls between Gu *et al.*[157] and our previous X-ray diffraction data.[181] Our shear modulus derived from the isotropic model is 249 GPa, comparable with the measured shear modulus of ReB_2 (223 – 276 GPa)[145,187] and nearly twice the value reported from theoretical calculations (104 – 129 GPa).[164] Although many assumptions went into calculating this shear modulus, the high value seems reasonable given the similar hardness values of ReB_2 and WB_4 and the known correlation between shear modulus and hardness. Finally, the Young's modulus calculated from the bulk modulus in a similar manner to the shear modulus is 595 GPa, which is only slightly higher than the value of 553.8 GPa derived from nano-indentation measurements[181] but lower than the measured Young's modulus of ReB_2 (642 – 671 GPa).[147]

Conclusions

WB_4 and ReB_2 were studied using synchrotron X-ray diffraction under quasi-hydrostatic conditions up to 58.4 and 63 GPa, respectively. In contrast to ReB_2, we found an anomalous lattice softening of the *c*-axis in WB_4 during compression, which was partially reversible during decompression. The anomaly was assigned to a second-order phase transition and may be due to pressure-induced structural rearrangements that are required because of the more rigid nature of the WB_4 network, compared with ReB_2. We believe that the three-dimensional, almost isotropic, rigid covalently boron network in WB_4 is responsible for both the observed structural change in WB_4 and its high intrinsic hardness. In addition, based on our measured bulk modulus and an estimated Poisson's ratio, a high shear modulus of 249 GPa was estimated for WB_4 using an isotropic model.

By examining the behavior of super-hard materials like WB_4 under extreme conditions such as highly elevated pressures, we begin to understand the structural change that take place in these strongly bonded solids. In this way, we build up a knowledge base so that future iterations of ultra-

incompressible super-hard materials can be produced by design, rather than by the trial-and-error process that we are often forced to employ.

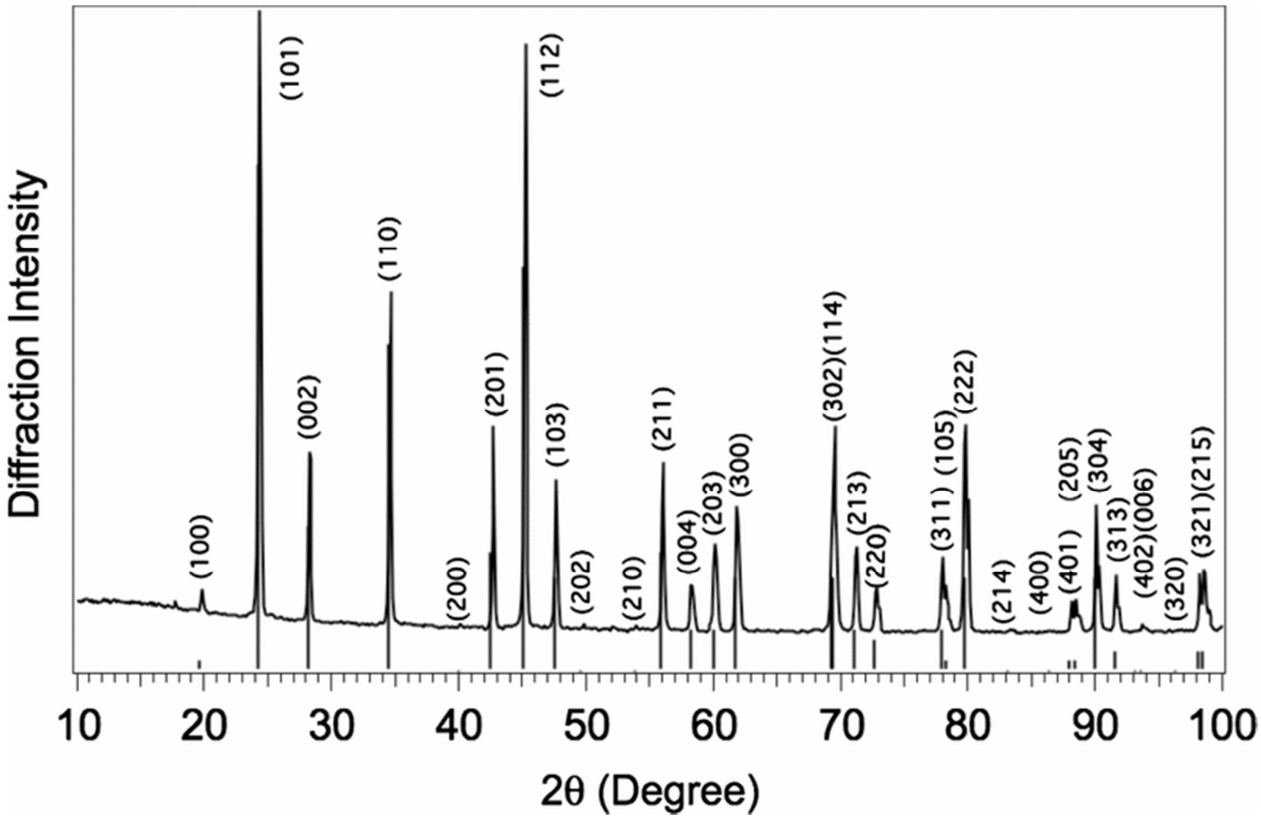

Figure 4.1: Labeled x-ray diffraction pattern for powder tungsten tetraboride (WB_4) at ambient pressure (x-ray wavelength λ=1.54 Å). The vertical bars indicate previously determined lattice spacing for WB_4 (Joint Committee on Powder Diffraction Standards, Ref. code: 00-019-1373; Ref. 13). The corresponding Miller index is given above each peak. The material used in this work is thus shown to be highly crystalline and phase pure.

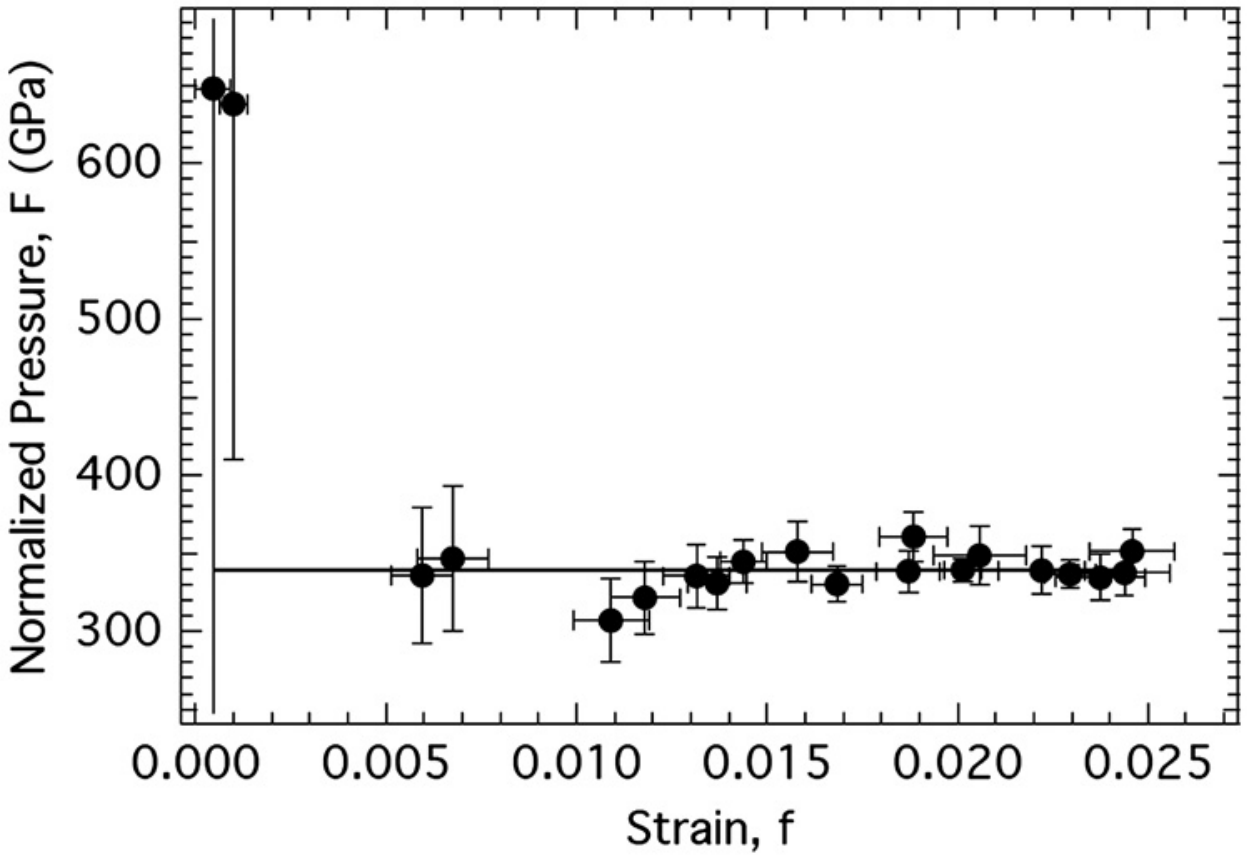

Figure 4.2: Hydrostatic compression data of WB_4 plotted as normalized pressure (***F***) as a function of finite strain (***f***). The straight line is a second-order fit of the finite strain equation of state (K_0' = 4), which gives a zero-pressure bulk modulus of 339 ± 3 GPa (**Equation (4.1)** and **Equation (4.2)**).

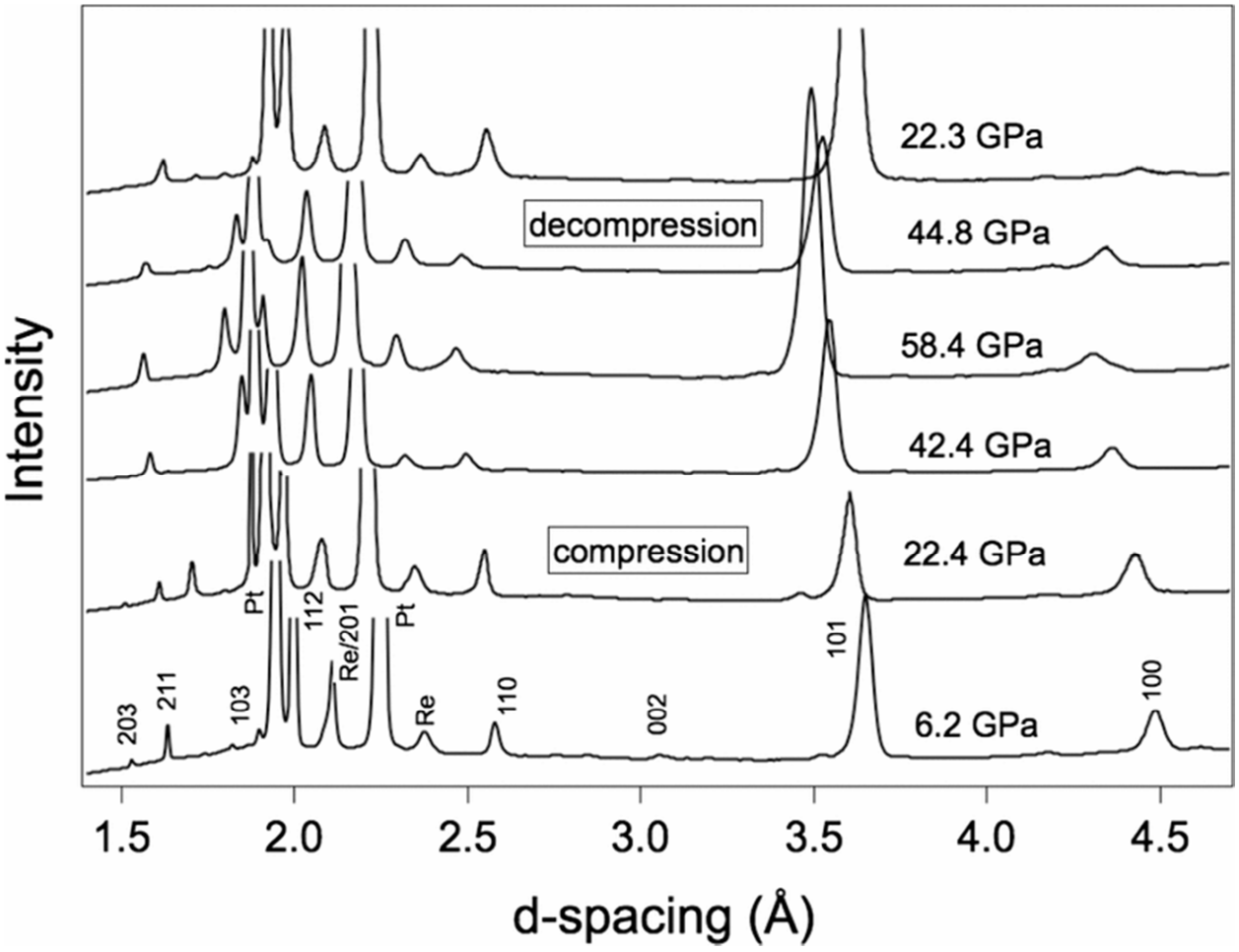

Figure 4.3: Representative angle dispersive X-ray diffraction patterns for WB_4 as a function of increasing and decreasing pressure. The Re peaks are from the gasket due to incomplete filtering of the tails of the X-ray beam. No changes in peak patterns that would be indicative of a change in symmetry are observed under pressures up to 58.4 GPa.

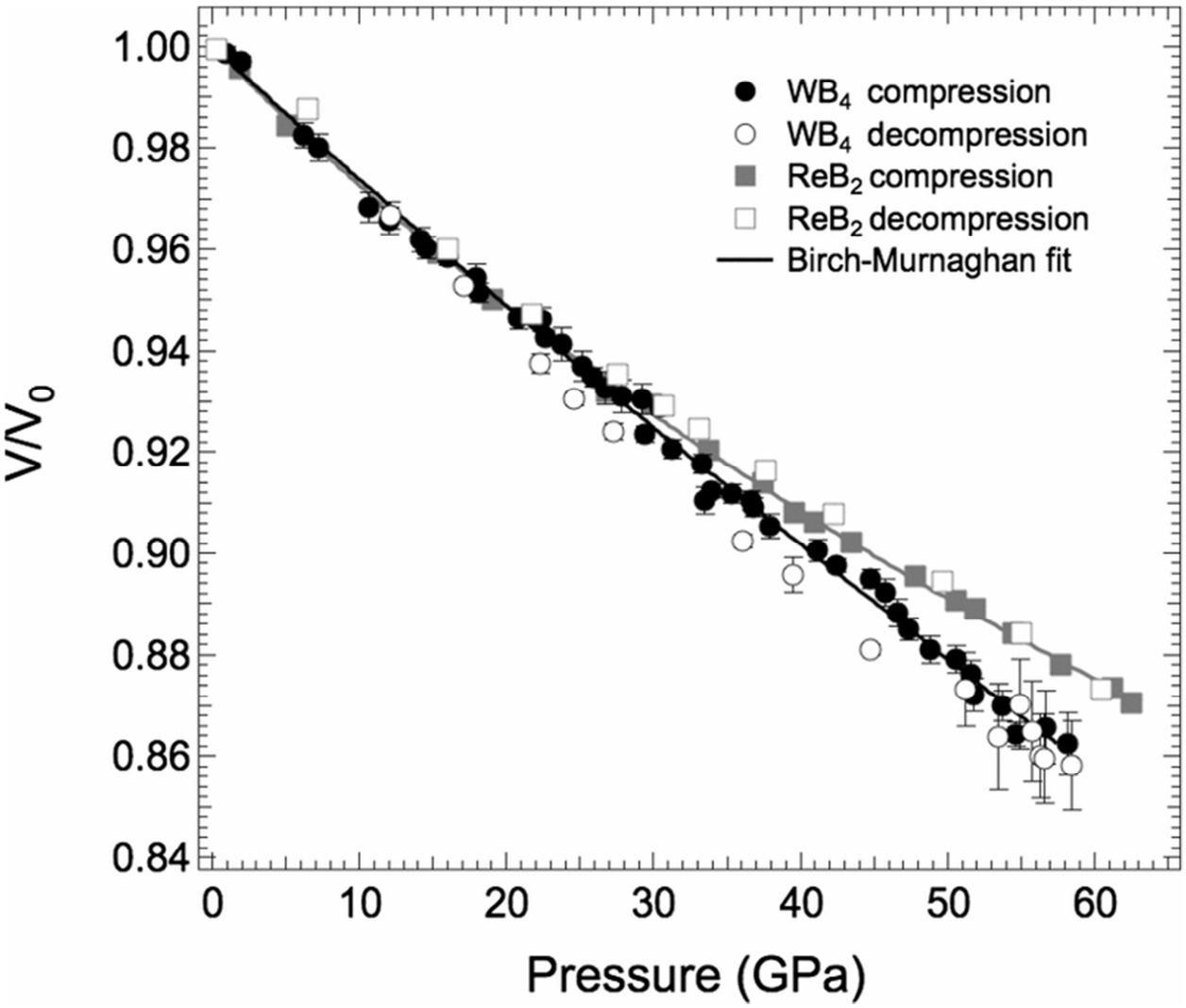

Figure 4.4: Measured fractional unit cell volume of WB_4 and ReB_2 plotted as a function of pressure. Black solid circle: compression of WB_4; black open circle: decompression of WB_4; gray solid square: compression of ReB_2; gray open square: decompression of ReB_2; black solid line: a Birch-Murnaghan fit to the compression data of WB_4; and gray solid line: a Birch-Murnaghan fit to the compression data of ReB_2. Error bars that are smaller than the size of the symbol have been omitted. While WB_4 is more compressible than ReB_2 under high pressures, below 30 GPa the data are quite comparable.

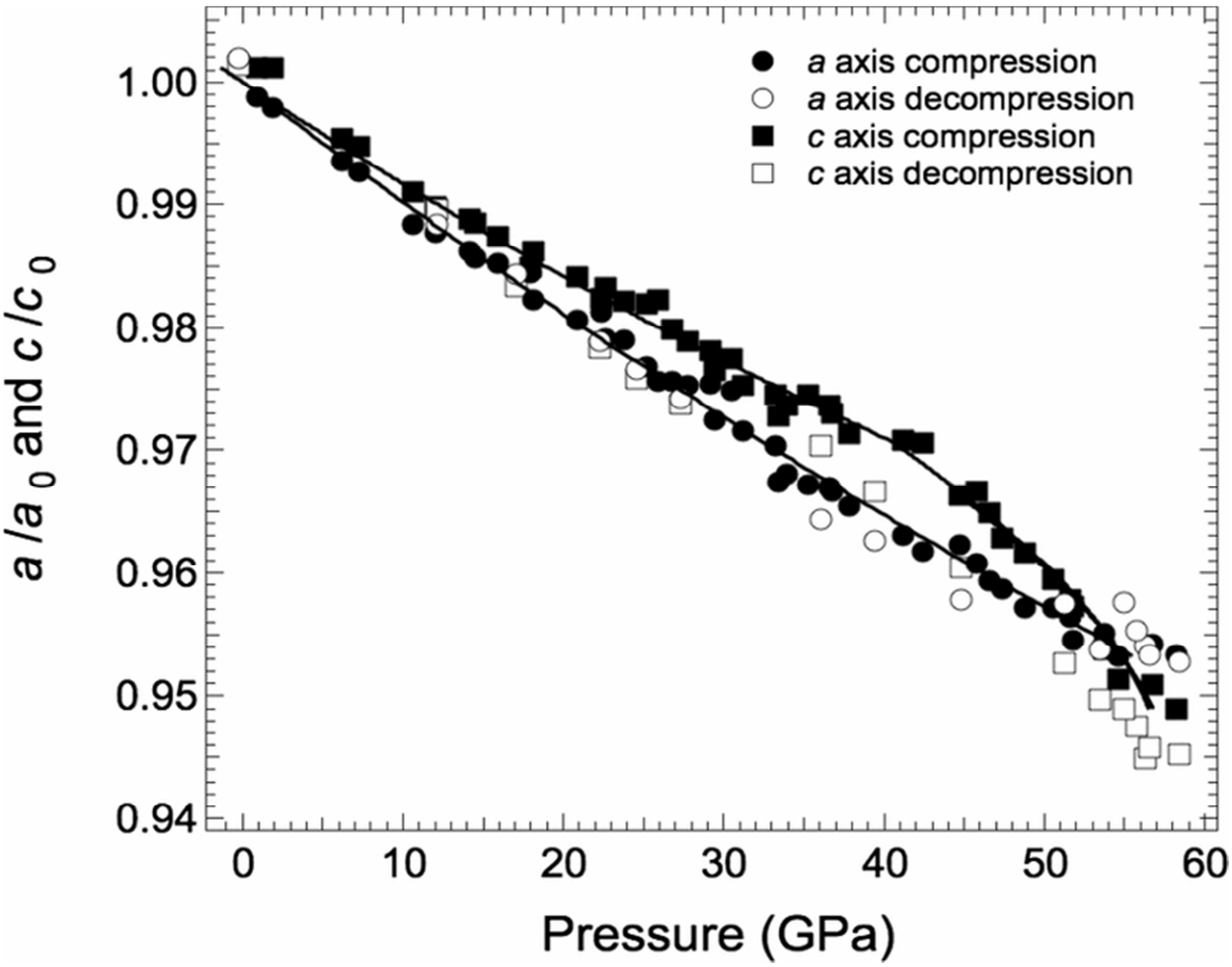

Figure 4.5: WB_4 fractional lattice parameters plotted as a function of pressure. Black solid circles: compression data for the *a*-lattice constant; black open circle: decompression data for the *a*-lattice constant; black solid squares: compression data for the *c*-lattice constant; black open square: decompression for the *c*-lattice constant; and solid lines: fits to the Birch-Murnaghan EOS. The error bars when not shown are smaller than the symbol. At ≈42 GPa during compression, the *c*-lattice constant undergoes a softening and becomes more compressible than the *a*-lattice constant. The *a*-lattice constant does not exhibit this abrupt change. Decompression data reveal that this structural change is reversible but with some hysteresis.

Table 4.1: Comparison of the Theoretical Calculations and Experimental Results for the Bulk Modulus K_0 (GPa) and their First Derivative K_{0T}, Shear Modulus *G* (GPa), Young's Modulus *E* (GPa), and Poisson's Ratio *v* of WB_4 and ReB_2 Found in the Literature and Presented in this Study

Material			K_0	K_{0T}	G	E	ν
ReB_2	Cal.	Wang (LDA)[a,114]	359		313	696	0.22
		Wang (GGA)[a, 114]	344		304	642	0.21
		Hao *et al*. (LDA)[116]	369.2		294.9	698.7	0.1846
		Hao et al. (GGA)[116]	354.5		289.4	682.5	0.1791
	Expt.	Chung *et al*. (X-ray)[52,147]	360[b]	4		712	
		Levine *et al*. (RUS)[145]	383[c]		273	661	0.21
		Koehler *et al*. (RUS)[187]	317[c]		276	642	0.163
		Suzuki *et al*. (RUS)[146]	367.7[c]		271.6	671.2	0.1958
		Xie *et al*[215].	344[b]	4			
			340[b]	4.2			
WB_4	Cal.	Wang *et al*. (GGA)[164]	292.7		103.6		
		Wang et al. (LDA)[164]	324.3		129.1		
	Expt.	Mohammadi *et al*. (X-ray)[181]	339[b]	4	553.8		
		Gu *et al*. (X-ray)[157]	304[b]	4			
			200[b]	15.3			
		Liu et al. (X-ray)[178]	342[b]	4			
			325[b]	5.1			
		This work	326[b]	4	249	595	
			369[b]	1.2			

[a] GGA refers to the generalized gradient approximation; LDA refers to local density approximation.
[b] Reported bulk modulus K_0 are isothermal values. Measured bulk modulus is obtained by fitting Birch-Murnaghan EOS.
[c] Reported bulk moduli are adiabatic values.

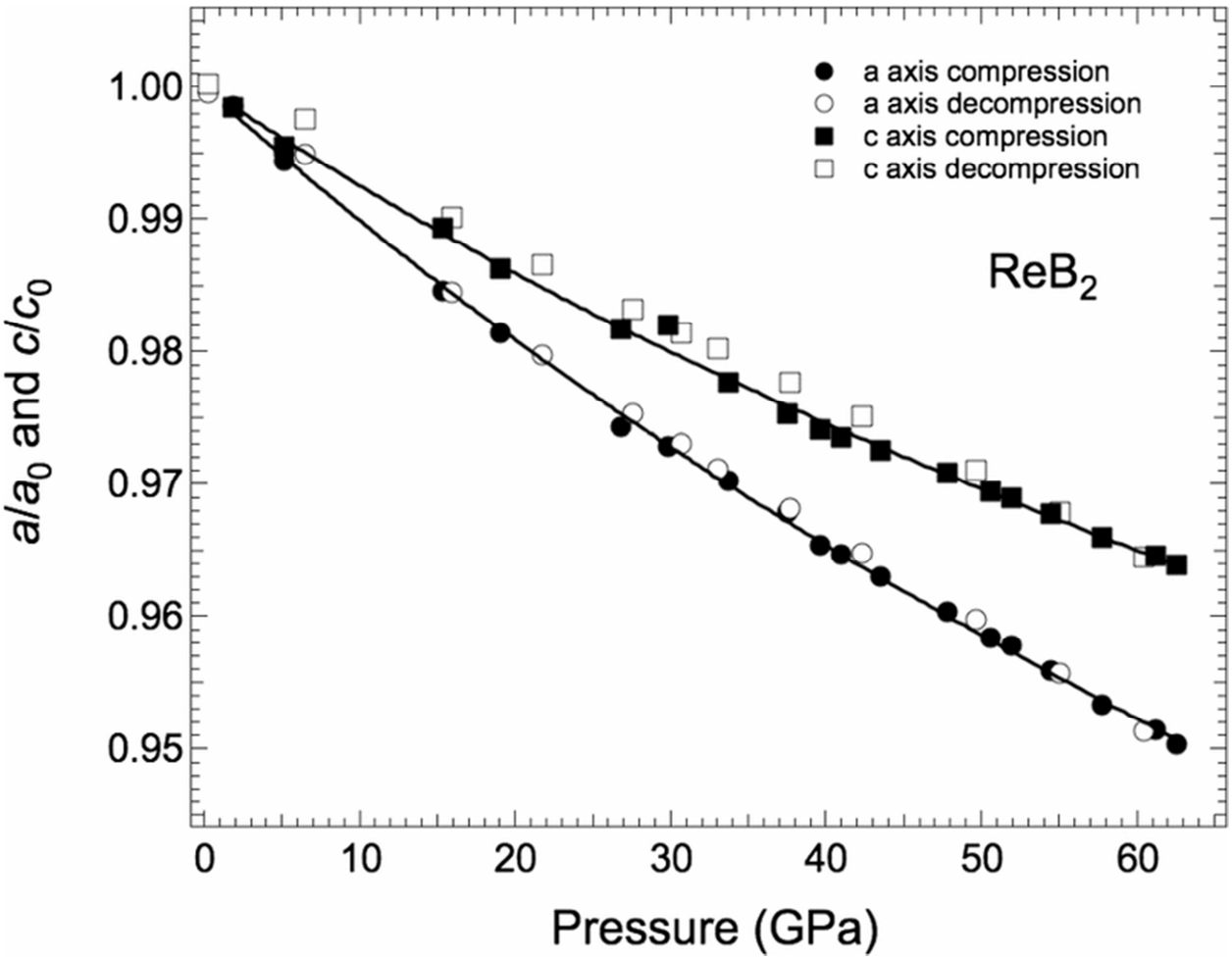

Figure 4.6: ReB_2 fractional lattice parameters plotted as a function of pressure. Black solid circles: compression data for the *a*-lattice constant; black open circle: decompression data for the *a*-lattice constant; black solid squares: compression data for the *c*-lattice constant; black open square: decompression for the *c*-lattice constant; and solid lines: fits to the Birch-Murnaghan EOS. Examination of the *a*- and *c*-lattice constants shows no evidence of lattice softening in either direction during compression.

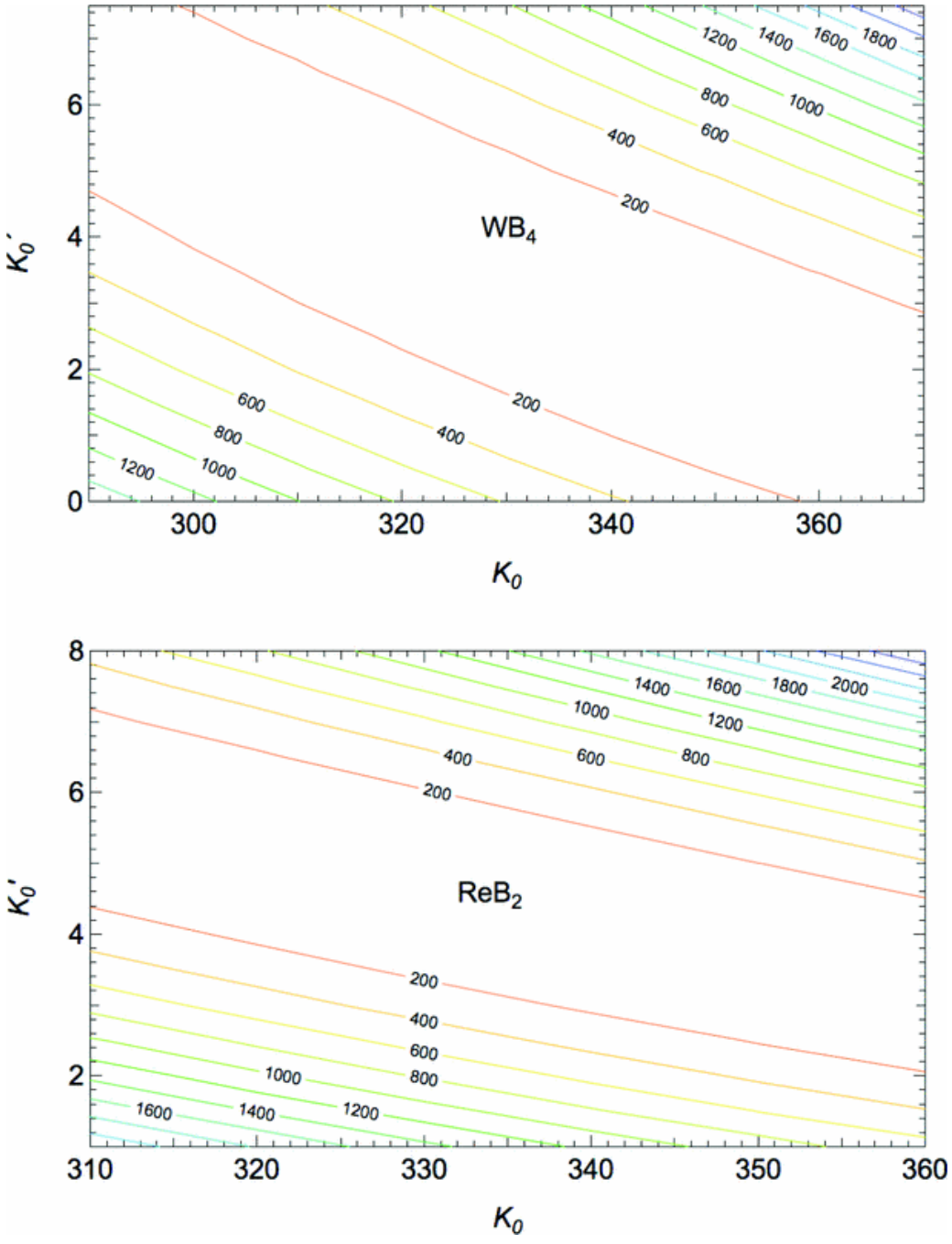

Figure 4.7: Trade-off of zero-pressure bulk modulus K_0 and its first derivative $K_{0\prime}$ for WB_4 and ReB_2. The contours are the sum of the deviations from the fits as a function of varying K_0 and $K_{0\prime}$. The inferred values of K_0 and K_0 ′ have an inverse relationship. The value obtained from second- or third-order Birch-Murnaghan EOS cannot be statistically distinguished based on this analysis.

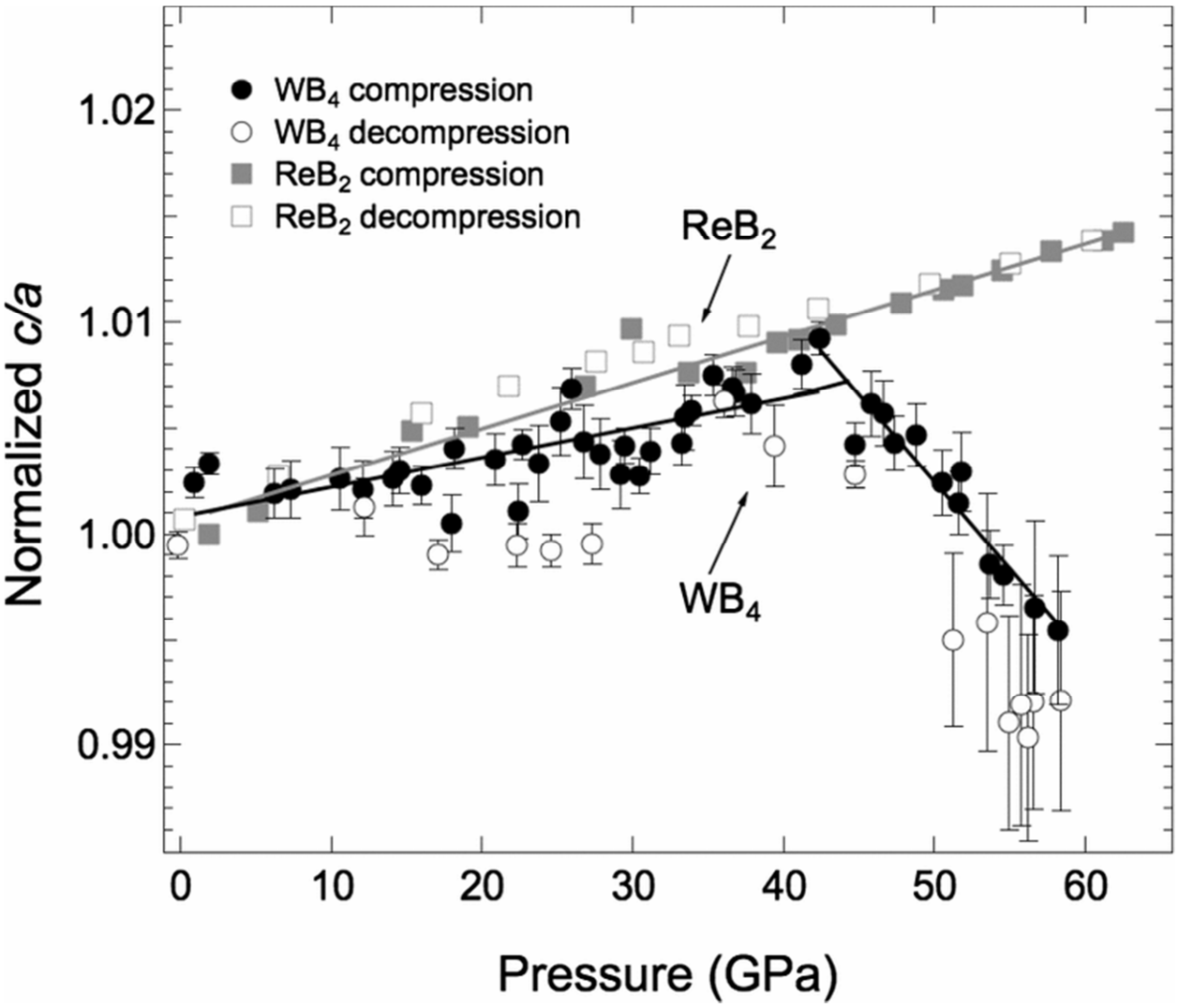

Figure 4.8: Normalized *c/a* ratio plotted as a function of pressure for WB_4 and ReB_2. Black solid circle: compression of WB_4; black open circle: decompression of WB_4; gray solid square: compression of ReB_2; gray open square: decompression of ReB_2; and solid lines: linear fits of compression data serve as a guide to the eye. WB_4 undergoes a pressure-induced second-order phase transition at ≈42 GPa. This transition is reversible with some hysteresis, suggesting a mechanical origin. In contrast, ReB_2 shows no evidence of a phase transition. The different pressure behavior can be related to difference in crystal structures between these two materials.

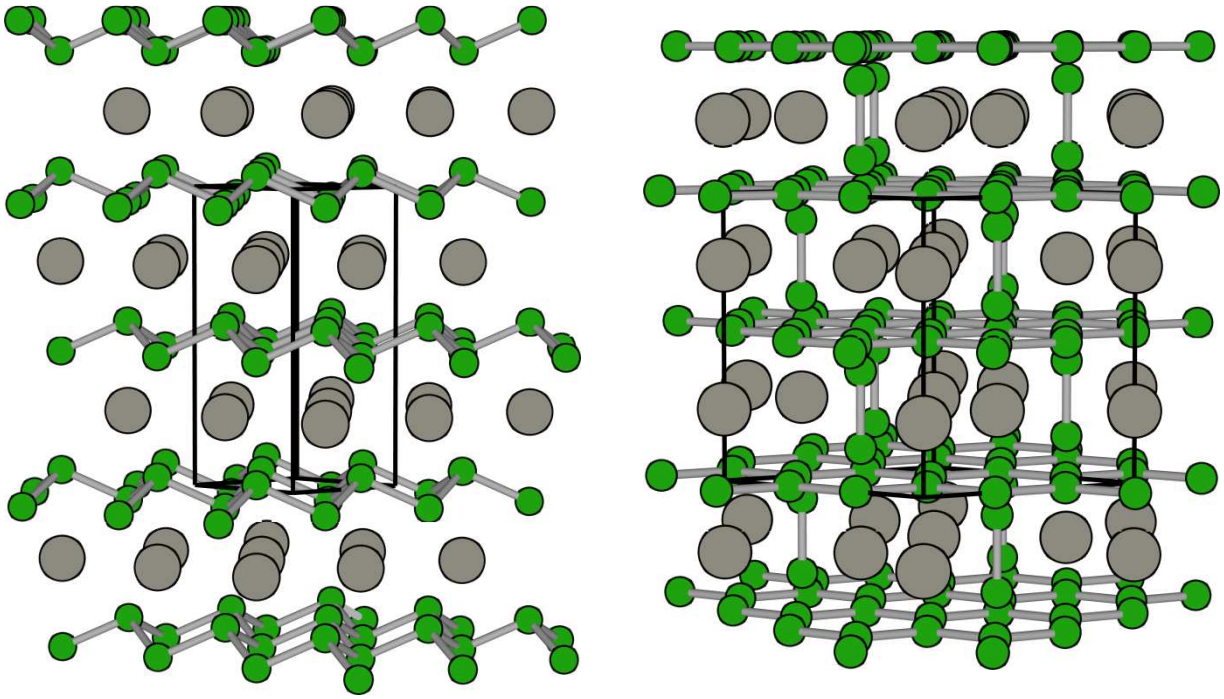

(a) **(b)**

Figure 4.9: (a) Crystal structure of ReB_2, **(b)** canonical structure of WB_4

Chapter 5

Solid Solutions of Tungsten "Tetraboride"

Introduction

In addition to dispersion hardening, which contributes an extrinsic component to the hardness and other mechanical properties, there are some other dislocation pinning mechanisms that may be used to enhance the hardness of a material if designed properly. These mechanisms include solid solution hardening, grain boundary strengthening, precipitation hardening, and strain hardening. Among these, solid solution hardening is one of the most efficient ways to increase the hardness of a material without introducing a second phase.[161] Solid solutions are established as an effective way to tune the hardness of transition metal borides, as previously observed for several compounds, including ruthenium diboride (RuB_2) when it forms solid solutions with osmium (Os).[101] A full range of solid solutions containing Os substituted for Ru in RuB_2 can be produced and they show a low-load hardness that increases linearly from ≈ 21 to 28 GPa.

To further explore possible enhancements to the hardness of WB_4, here we have added tantalum (Ta), manganese (Mn), and chromium (Cr) to form solid solutions. In this chapter, the resulting structural and hardness changes are discussed, along with an examination of possible mechanisms to explain the changes that include electronic structure changes, solid solution hardening, and dispersion hardening. Additionally, we have attempted to create even harder WB_4 solid solutions by superimposing the hardening effects of elements with different atomic size and valence electron counts in order to further intensify either dislocation-locking mechanism or electronic structure changes. We specifically examined elements with atomic radii both larger (Ta = 1.49 Å) and smaller (Mn = 1.32 or Cr = 1.30 Å) than

tungsten (W = 1.41 Å; note B = 0.78 Å), and with valence electron counts both larger (Mn, Group VII) and smaller (Ta, Group V) than tungsten (W and Cr, Group VI).[216] The bulk modulus, high-pressure stability, and thermal stability of the hardest solid solution are also reported and compared directly to WB_4.

Materials and Methods

High-purity powders of tungsten (99.95%, Strem Chemicals, U.S.A.), amorphous boron (99+%, Strem Chemicals, U.S.A.), tantalum (99.9%, ROC/RIC Corp., U.S.A.), manganese (99.9%, Fisher Scientific Co., U.S.A.), and chromium (99.9%, ROC/RIC Corp., U.S.A.) were used to systematically study the effect of compositional variations on the hardness of WB_4. The powders at each desired set of compositions, i.e. $W_{1-x}Ta_xB_4$, $W_{1-x}Mn_xB_4$, and $W_{1-x}Cr_xB_4$ (x = 0.0 − 0.5), were ground together thoroughly using an agate mortar and pestle to obtain uniform mixtures. Keeping the molar ratio of W **:** B in all mixtures constant at 1 **:** 12, different fractional ratios of tantalum, manganese, and chromium were added on a metals-basis in an attempt to make solid solutions. Excess boron is required for the synthesis of all WB_4-based compounds in order to stop the formation of soft, thermodynamically favorable impurity phases, such as tungsten diboride (WB_2).[154,156,181] Attempts at decreasing the boron concentration in relation to the total metal content or degree of solid-solubility were not investigated.

Powder mixtures were pressed into 12 mm, ≈300 mg pellets under an applied load of ≈10 000 lbs. using an hydraulic (Model 3851, Carver, U.S.A.) press. The pellets were then arc-melted under high-purity argon at ambient pressure by application of an AC current ≥70 amp. When the samples were thoroughly molten and fully homogenous, the electric arc was cut and the ingot allowed to cool naturally; the entire process taking some 2-5 min.

The as-synthesized ingots were bisected using a sinter-bonded diamond lapidary sectioning saw (South Bay Technology Inc., U.S.A.). One half of the ingot was crushed using an hardened steel mortar and pestle set into a fine powder for XRD experiments and thermal gravimetric analysis. The remaining half was mounted in epoxy using a cold-mount resin/hardener epoxy set (Allied High Tech Products Inc., U.S.A.). The epoxy mounted samples were polished against silicon carbide polishing papers of grit sizes ranging from 120 to 1200 (Allied High Tech Products Inc., U.S.A.), followed by diamond abrasive films containing diamond particles ranging from 30 to 0.5 μm (South Bay Technology Inc., U.S.A.), using a tripod polisher (South Bay Technology Inc., U.S.A.) to achieve an optically flat surface for energy-dispersive spectroscopic analysis and hardness testing.

Energy-dispersive X-ray spectroscopy (EDS) and XRD were used to verify the elemental- and phase-purity of the samples. The optically flat, mounted samples were examined for elemental composition and purity utilizing an EDAX® (EDAX, Inc., U.S.A) detector mounted on a scanning electron microscope (JEOL JSM 6700 F, Japan). Phase identification was executed on the crushed powder samples using an X'Pert Pro™ powder X-ray diffraction system (PANalytical, Netherlands) employing Cu K_α X-radiation (λ = 1.5418 Å). XRD patterns were collected from the powder samples using the following parameters: step size = 0.03°, time per step = 100.00 s, and scan speed = 0.0425°/s. The patterns were then compared to reference patterns available in the Joint Committee on Powder Diffraction Standards (JCPDS) database to determine the phases present in the samples.

After the purity and composition of the arc-melted ingots were tested, the hardness of each polished sample was measured using a MicroMet® 2103 micro-hardness tester (Buehler Ltd., U.S.A.) equipped with a pyramid diamond indenter tip. With a dwell time of 15 s, the samples were indented by the application of five different loads: 0.49 (low load), 0.98, 1.96, 2.94, 4.9 N (high load). The lengths of the diagonals of the impression marks created by the indenter on the surface of the samples were then

measured using a high-resolution Zeiss Axiotech® 100HD optical microscope (Carl Zeiss Vision GmbH, Germany) under a total magnification of 500×. The Vickers micro-indentation hardness values ($\boldsymbol{H_v}$, in GPa), under various applied loads, were calculated using **Equation (5.1) :**

$$H_v = \frac{1854.4P}{d^2} \qquad \textbf{Equation (5.1)}$$

where *P* is the applied load in Newtons (N) and *d* is the arithmetic mean of the diagonals of the indent in micrometers (μm). Each hardness datum point reported here represents the average of the indentation measurements for at least 20 randomly chosen spots on the sample at each load to ensure accurate results. The standard deviations of the mean hardness values under the applied loads of 0.49, 0.98, 1.96, 2.94, and 4.9 N are respectively within 5.60, 4.11, 3.68, 2.84, and 1.57 GPa.

The lattice elastic compressibility of the hardest phase, i.e., $W_{0.93}Ta_{0.02}Cr_{0.05}B_4$, was measured using synchrotron-based *in situ* high-pressure XRD in a Diacell diamond anvil cell. To ensure a quasi-hydrostatic sample environment, neon gas was loaded into the cell using the Consortium for Materials Properties Research in Earth Sciences (COMPRES) and GeoSoilEnviroCARS (GSECARS) gas loading system.[184] Diffraction patterns were collected for the powder samples from ambient pressure to ≈65 GPa on Beamline 12.2.2 at the Advanced Light Source at Lawrence Berkeley National Laboratory (LBNL, CA, U.S.A.) with X-ray beam size of approximately 10 × 10 μm.[215] The pressure-volume data, measured by XRD, were fit using the third-order finite strain Birch-Murnaghan equation of state (**Equation (5.2)**) to infer the room-pressure isothermal bulk modulus ($\boldsymbol{K_{0T}}$) and its first derivative with respect to pressure ($\boldsymbol{K_{0T}'}$). The third-order equation shown below reduces to the second-order equation when $\boldsymbol{K_{0T}'}$ is equal to 4.

$$P = \frac{\frac{3}{2}K_O\left[\left(\frac{V}{V_0}\right)^{-7/3} - \left(\frac{V}{V_0}\right)^{-5/3}\right]}{\left\{1 - \left(\frac{3}{4}\right)(4 - K_0')\left[\left(\frac{V}{V_0}\right)^{-2/3} - 1\right]\right\}}$$ **Equation (5.2)**

A Pyris Diamond® thermogravimetric/differential thermal analyzer module (TG-DTA, Perkin-Elmer Instruments, U.S.A.) was utilized to investigate the thermal stability of the hardest solid solution. Powder samples were heated in air to 200°C at a rate of 20°C/min and held at this temperature for 20 min to remove any moisture. The samples were then heated to 1000°C at a rate of 2°C/min and soaked at this temperature for 120 min. The samples were finally air cooled to room temperature at a rate of 5°C/min. XRD was performed on the samples after the thermal analysis experiments to identify the resulting phase(s).

Results and Discussion

EDS was used to verify the elemental purity and composition of the samples. The EDS results confirmed the desired atomic ratios of elements as well as the absence of any impurity elements in the samples. The phase purity and composition of the samples were then checked using powder XRD. The XRD patterns for the compounds $W_xTa_{1-x}B_4$, $W_xMn_{1-x}B_4$ and $W_xCr_{1-x}B_4$ (x = 0.0 − 0.5) are shown in Figure 5.1**a–c** respectively. Note that all samples contain some crystalline boron, which is unobservable using standard XRD at low scan times. The XRD patterns of the tantalum-added compounds, $W_xTa_{1-x}B_4$, are displayed in Figure 5.1**a**. These patterns show that the solubility of Ta in WB_4 (the bottom pattern) is greater than 20 at.%, above which TaB_2 appears as a second phase (JCPDS ref code: 03-065-3385). The patterns of manganese-added compounds, $W_xMn_{1-x}B_4$, are shown in Figure 5.1**b**. The solubility of manganese in WB_4 is below 20 at.%. Above 20 at.% Mn addition, MnB_4 appears as an impurity phase (JCPDS ref code: 03-065-6232). As can be seen in Figure 5.1**c**, the solubility of chromium in WB_4 appears

to be less than 10at.%. Chromium has the greatest size difference of our trial metals in comparison to tungsten, and our results indicate agreement with this fact. At and above 10 at.% Cr, two phases corresponding to CrB_2 and CrB_4 (with JCPDS ref codes of 00-034-0369 and 00-022-0208, respectively) appear simultaneously.

It should be noted that because of the rapid cooling times involved in the arc melting process, it is not possible to determine if the formation of second phases in these three series is the result of kinetic competition among the various transition metal borides or an actual thermodynamic solubility limit. The lattice parameters of the hardest WB_4 solid solutions are given in Table 5.1. It can be concluded from these data that the addition of small amounts of Ta, Mn, and Cr do not change the lattice parameters of WB_4 within the error of the measurement. Larger quantities of these elements, however, can influence the lattice parameters of WB_4, as is observed in the 20% solution of Ta ($W_{0.8}Ta_{0.2}B_4$), for example. These changes are likely due to the atomic size mismatch between tungsten and these three elements, as might be expected from Vegard's Law.[43]

Hardness measurements were undertaken after verifying the purity and composition of the samples by XRD and EDS. The Vickers hardness of each sample, as determined from micro-indentation under static loads ranging from 0.49 to 4.9 N, is shown in **Figure 5.2a–c**. Under an applied load of 0.49 N (low load) the hardness increases from 43.3 ± 2.9 GPa for pure WB_4 (x = 0.0) to a maximum of 52.8 ± 2.2 GPa with the addition of 2 at.% Ta (**Figure 5.2a**). The hardness then decreases to 43.7 ± 2.1 GPa for 5 at.% Ta followed by a broad peak between 10 and 20 at.% at about 44 GPa. Once the solubility limit is significantly exceeded, the hardness rises slightly, showing a value of 44.6 ± 3.7 GPa for a Ta concentration of 40 at.%. It is likely that the broad peak in hardness at high concentration in the two phase system stems from a fundamentally different mechanism than the hardness peak at low concentration. Similar trends are observed for the hardness under each of the other loads tested (0.98,

1.96, 2.94, and 4.9N). For the WB_4 – Mn system (**Figure 5.2b**), the trends in the Vickers hardness show some similarities to the WB_4 – Ta data. At low load (0.49 N), these data again show a peak in the hardness at a low Mn concentration (53.7 ± 1.8 GPa with the addition of 4 at.% Mn). This is followed by a decreases in hardness to 46.9 ± 3.8 GPa at 5at.% Mn addition. In contrast to Ta, Mn shows a second significant peak in the low load data between 10 and 20 at.% at ≈55 GPa. Higher loads show more of a plateau in this range, similar to the Ta data. Again, similar to the trends observed upon Ta addition, the data show a final broad hump between 30 and 40 at.% Mn addition, in the range where the sample contains a two phase mixture. The addition of Cr to WB_4 (**Figure 5.2c**) results in a trend intermediate between those of Ta and Mn. Only two peaks are observed in the plot of hardness as a function of Cr concentration, but the first peak is at higher Cr content than that observed for Ta or Mn. For example, addition of 10 at.% Cr results in an increase in hardness (at 0.49 N) from 43.3 ± 2.9 GPa for pure WB_4 to 53.5 ± 1.9 GPa. As with the other samples, a second peak in hardness is observed for Cr concentrations above the solubility limit. After dropping down to 39.4 ± 5.6 GPa at ≈20 at.% Cr, the hardness again increases to 48.0 ± 5.2 GPa at a concentration of 40 at.% Cr.

There is a general agreement among all structural models of WB_4 so-far proposed that this material is a slightly defective structural relative of the AlB_2 archetype, consisting of alternating hexagonal layers of boron and metal, with some of the metal atoms missing.[154,157,164,181,215,217] Since our EDS area mapping analyses along with XRD results (**Figure 5.1** and Table 5.1) preclude the possibility of grain boundary strengthening mechanisms within the solubility limits of these three additive elements (Ta, Mn and Cr), we postulate that the defect structure of this material may be responsible for the hardening trends observed for the solid solutions in **Figure 5.2a–c**. Located in different Groups of the Periodic Table, tantalum (Group V) and manganese (Group VII) each have a different number of valence electrons than tungsten (Group VI). At low concentrations, by sitting at the positions of missing tungsten atoms, these

elements could induce either tungsten vacancies (by adding Mn) or boron vacancies (by adding Ta) to the WB_4 structure.

These hypotheses find some support in recent calculations by Gou *et alia*, who examined the electronic and mechanical properties of defective tungsten borides by first-principle calculations.[217] They found that the presence of vacancies in the WB_4 structure is not only energetically favored, because of the significant decrease in the heat of formations compared to the vacancy-free borides, but is also electronically preferred due to the substantial reduction of the Fermi level. In addition, their calculations show that the shear modulus, which is directly related to hardness,[148] of WB_4 is increased by the presence of both tungsten and boron vacancies. These valence electron differences, together with the atomic size mismatches (Ta = 1.49, Mn = 1.32, and W = 1.41 Å),[216] might explain the first hardness increase for WB_4 solid solutions with Ta and Mn at concentrations of 2 and 4 at.%, on a metals basis, respectively.

The addition of Cr, which is in the same Group as tungsten in the Periodic Table (Group VI), to the WB_4 structure may not generate such vacancies. As a result, for Cr solid solutions with WB_4, the hardness increase at low concentrations is expected to be due only to the atomic size difference (Cr = 1.30 Å). This fact may explain the lack of a distinct peak at very low concentrations for the Cr/W solid solutions.

After filling some of the missing tungsten positions by the atoms of each of these three elements at low concentrations, it is likely that they then begin replacing tungsten atoms in other positions as the concentration increases. This could result in classical solid solution hardening, driven exclusively by atomic size mismatch. This would correspond to the second hardness increase at a maximum solubility of ≈20 at.% for Ta and Mn additions on a metals basis as well as the first hardness increase at ≈10 at.% for Cr. The observation that this peak is most significant for Cr is well justified by the fact that the size

mismatch between W and Cr is greater than the mismatch between W and Mn or Ta. The third peak in the hardness data of Ta (≈40 at.% in **Figure 5.2a**) and Mn (≈40 at.% in **Figure 5.2b**) and the second one of Cr (≈40 at.% in **Figure 5.2c**) in WB_4 may be attributed to dispersion hardening, which is an extrinsic effect due to the presence of a second phase (i.e., TaB_2, MnB_4, and CrB_2 + CrB_4 in WB_4).[22,181] Clear diffraction peaks from these second phases can be seen in **Figure 5.1a–c**.

These results motivated us to run a series of experiments in which the concentration of Ta in WB_4 was kept constant at 2 at.% on a metals basis and those of Mn or Cr were varied from 2 to 10 at.%, in an effort to combine both electronic structure and solution hardening effects. The XRD and hardness data obtained for these compounds are shown in **Figure 5.6** and Table 5.2 – Table 5.3, respectively. The XRD results (**Figure 5.6** and **Table 5.1**) confirm that, in the presence of 2 at.% Ta, the solubility of both Mn and Cr in WB_4 is limited to less than 10 at.%. Note from **Table 5.1**, however, that the lattice parameters remain almost unchanged, considering the error values, when Ta and Mn or Cr are simultaneously added to WB_4. As can be seen in **Table 5.2** and **Table 5.3**, the highest hardness values of 55.8 ± 2.3 and 57.3 ± 1.9 GPa (under a load of 0.49 N) are achieved for the concentrations $W_{0.94}Ta_{0.02}Mn_{0.04}B_4$ (**Table 5.2**) and $W_{0.93}Ta_{0.02}Cr_{0.05}B_4$ (**Table 5.3**), respectively. This hardness increase, which is also observed under other hardness loads, is likely due to the combined effects of introducing charges (by Ta and Mn), and thus vacancies, to the structure of WB_4 as well as atomic size mismatches.

Since the superposition of electronic charges imposed on the structure of WB_4 by adding 2 at.% Ta and 4 at.% Mn (in $W_{0.94}Ta_{0.02}Mn_{0.04}B_4$) is the same as that of adding 2 at.% Ta and 5 at.% Cr (in $W_{0.93}Ta_{0.02}Cr_{0.05}B_4$) but of opposite signs, these two compounds should contain similar amounts of vacancies although of different types (tungsten and boron, respectively). This could result in similar hardness values; however, the smaller size of Cr (r = 1.30 Å) compared to Mn (r = 1.32 Å)[216] along with the higher Cr concentration might be the reason for the slightly higher hardness of the $W_{0.93}Ta_{0.02}Cr_{0.05}B_4$

(57.3 GPa) solid solution in comparison to $W_{0.94}Ta_{0.02}Mn_{0.04}B_4$ (55.8 GPa). Note that the highest hardness value of 57.3 GPa, measured for the $W_{0.93}Ta_{0.02}Cr_{0.05}B_4$ solid solution, is respectively ≈16 and 24% higher than those of ReB_2 (48.0 GPa)[52] and WB_4 (43.3 GPa),[181] the hardest transition-metal borides reported to date.

Super-hard materials generally possess a high bulk modulus;[52,103,181,215] thus, the measured lattice volume as a function of pressure was used to determine the bulk modulus of $W_{0.93}Ta_{0.02}Cr_{0.05}B_4$, the solid solution showing the highest hardness. A series of representative diffraction patterns for this solid solution is shown in **Figure 5.7**. The data were collected up to 65 GPa and were fit both over the full pressure range and over only the range from 0 – 40 GPa (**Figure 5.3a**). The latter fitting was done for a fair comparison with pure WB_4, which undergoes a second-order phase transition at ≈40 GPa. The fit of the data up to 40 GPa resulted in an isothermal bulk modulus of $\boldsymbol{K_{0T}}$ = 366 ± 14 GPa with $\boldsymbol{K_{0T}'}$ = 2.6 ± 0.9. The bulk modulus and its first derivative are not independent parameters, and the bulk modulus is equal to 346 ± 3 GPa when $\boldsymbol{K_{0T}'}$ is set equal to 4. These values are comparable to the corresponding values for WB_4, determined using the same pressure range **:** $\boldsymbol{K_{0T}}$ = 369 ± 9 GPa with $\boldsymbol{K_{0T}'}$ = 1.2 ± 0.5 and $\boldsymbol{K_{0T}}$ =326 ± 3 GPa with $d\boldsymbol{K_{0T}}/dP$ set equal to 4.[181,215]

Unlike WB_4, $W_{0.93}Ta_{0.02}Cr_{0.05}B_4$ shows no signs of a lattice instability at 40 GPa. Slightly lower values of the bulk modulus were obtained over the pressure range of 0 − 65 GPa with $\boldsymbol{K_{0T}}$ = 335 ± 3 GPa from the second-order fit and $\boldsymbol{K_{0T}}$ = 350 ± 16 GPa with $\boldsymbol{K_{0T}'}$ = 3.3 ± 0.7 from the third-order fit. All these values are summarized in **Table 5.4**. The bulk modulus data suggest that this new super-hard solid solution ($W_{0.93}Ta_{0.02}Cr_{0.05}B_4$) may be slightly stiffer than pure WB_4. This result is counterintuitive, since the bulk modulus usually follows Vegard's law for solid solutions,[101] and neither Ta nor Cr borides are predicted to be significantly stiffer than WB_4. TaB_2 is reported to have an experimentally determined bulk modulus value of 341 ± 7 GPa,[218] which is very similar to WB_4. Only theoretical values are available for CrB_4, but it

is predicted to be much softer than WB_4, with a bulk modulus in the range of 265 – 275 GPa.[219] The observation of a small increase in bulk modulus based on the second-order fits for the ternary solid solution thus lends support to the idea that many of the mechanical changes in these materials are electronic in origin. In the case of bonding changes, one would not expect samples to follow Vegard's law. Note that in addition to $\boldsymbol{K_{0T}}$, the shear modulus (*G*) also has a significant contribution to hardness.[148] $\boldsymbol{K_{0T}}$ (and also *G*) can be independently constrained through ultrasonic and/or Brillouin spectroscopic measurements. This would allow for confirmation of values obtained using the third-order finite strain Birch-Murnaghan equation of state. Further examination of the high-pressure data reveals a number of other interesting trends when $W_{0.93}Ta_{0.02}Cr_{0.05}B_4$ is compared to WB_4.

First, the solid solution is mechanically more isotropic than pure WB_4. That is, the compressibility in the *a*- and *c*-directions is more similar in $W_{0.93}Ta_{0.02}Cr_{0.05}B_4$ than they are in WB_4. **Figure 5.3b** demonstrates this, showing the linear compressibility of $W_{0.93}Ta_{0.02}Cr_{0.05}B_4$ in the *a*- and *c*-directions. For WB_4, the *c*-direction is found to be 24% less compressible (i.e., stiffer) than the *a*-direction.[215] By contrast, **Figure 5.3b** indicates that $W_{0.93}Ta_{0.02}Cr_{0.05}B_4$ is less compressible in the *a*-axis than it is along the *c*-axis, though the difference is only 11%. It is unlikely that such a swap of the most compressible direction could stem from anything other than a change in electronic structure, again emphasizing that this very hard solid solution shows fundamentally altered bonding, compared to pure WB_4. Perhaps more dramatic is the comparison shown in **Figure 5.4**, which plots the *c*/*a* ratio as a function of pressure for $W_{0.93}Ta_{0.02}Cr_{0.05}B_4$ (**Figure 5.4a**) and for the parent binary solid solution $W_{0.98}Ta_{0.02}B_4$ (**Figure 5.4b**) compared with pure WB_4. WB_4 is observed to undergo a second-order phase transition at ≈42 GPa, which manifests itself as a sudden change in the *c*/*a* ratio.[215] In contrast, no significant changes in *c*/*a* ratio are observed for the solid solutions over the same pressure range. It has been hypothesized that the softening in the *c*-direction is a structural rearrangement required to re-optimize the bonding in WB_4

at high levels of compression.[215] The fact that this phase transition is not observed in the solid solutions re-emphasizes that the addition of just 2 at.% Ta to WB_4 can create a material with significantly altered bonding. Our last test involved investigation of the thermal stability of our hardest WB_4 solid solution ($W_{0.93}Ta_{0.02}Cr_{0.05}B_4$) using thermal gravimetric analysis.

The results (**Figure 5.5**) indicate that a powder of this solid solution is thermally stable in air up to ≈420 °C, which is slightly higher than the thermal stability of pure WB_4 (≈400 °C) measured under the same experimental conditions.[181] The final products of the thermal reaction in air consisted of WO_3 and Cr_2O_3 as determined by powder XRD. The thermal stability in air is a key figure of merit for hard materials, which are often used for cutting tools. In such applications, high-temperature oxidation can be a significant route to materials failure.

Conclusions

Compositional variations of WB_4 with Ta, Mn, and Cr were synthesized in an attempt to create super-hard transition metal borides with ever increasing hardness. By adding 2 at.% Ta, 4 at.% Mn, and 10 at.% Cr on a metals basis, the Vickers hardness (under an applied load of 0.49 N) of WB_4 increases from 43.3 to 52.8, 53.7, and 53.5 GPa for these three solid solutions, respectively. Significant increases in the concentration of any of these three transition metal elements switch the hardness from an intrinsic regime to an extrinsic mode, resulting from dispersion hardening, which occurs at a concentration of ≈40 at.% for all three solid solution series.

In an attempt to create even harder materials, we synthesized ternary solid solutions of WB_4 containing all three of these transition metals by keeping the concentration of Ta constant at 2 at.% on a metals basis and changing those of Mn or Cr from 2 to 10 at.%. This resulted in the formation of the hardest WB_4 solid solution, $W_{0.93}Ta_{0.02}Cr_{0.05}B_4$, with a Vickers hardness of 57.3 ± 1.9 GPa (under 0.49 N). This

material possesses a bulk modulus in the range of 335 − 366 GPa, depending on the fitting method used, as determined by *in situ* high-pressure XRD. These values are slightly higher than those obtained for pure WB_4. More importantly, the solid solution showed significantly altered bonding as evidenced by the absence of a second-order phase transition that was observed in WB_4 and more isotropic compressibility. The solid solution is also thermally stable in air up to ≈420 °C.

This work thus represents a significant step forward in the search for low-cost, easily manufactured hard materials. When ReB_2 was first shown to be super-hard at low loads, the results were heralded as a breakthrough in hard materials. At the same time, it was clear that ReB_2 would be less likely to result in a practical system because of the high cost of Re. WB_4 is a comparatively low-cost material, and the data presented here show that it can be converted to a material with significantly higher hardness than ReB_2 by the addition of small amounts of relatively low-cost elements. It is our hope that theory will be able to provide a predictive understanding of the bonding changes that occur in these solid solutions and that others will build on these results to produce solid solutions with even higher hardness. By moving from pure phases to solid solutions, we can dramatically increase the bonding in this exciting class of hard materials. Table 5.5 compares the properties of $W_{0.93}Ta_{0.02}Cr_{0.05}B_4$ with other known super-hard materials.

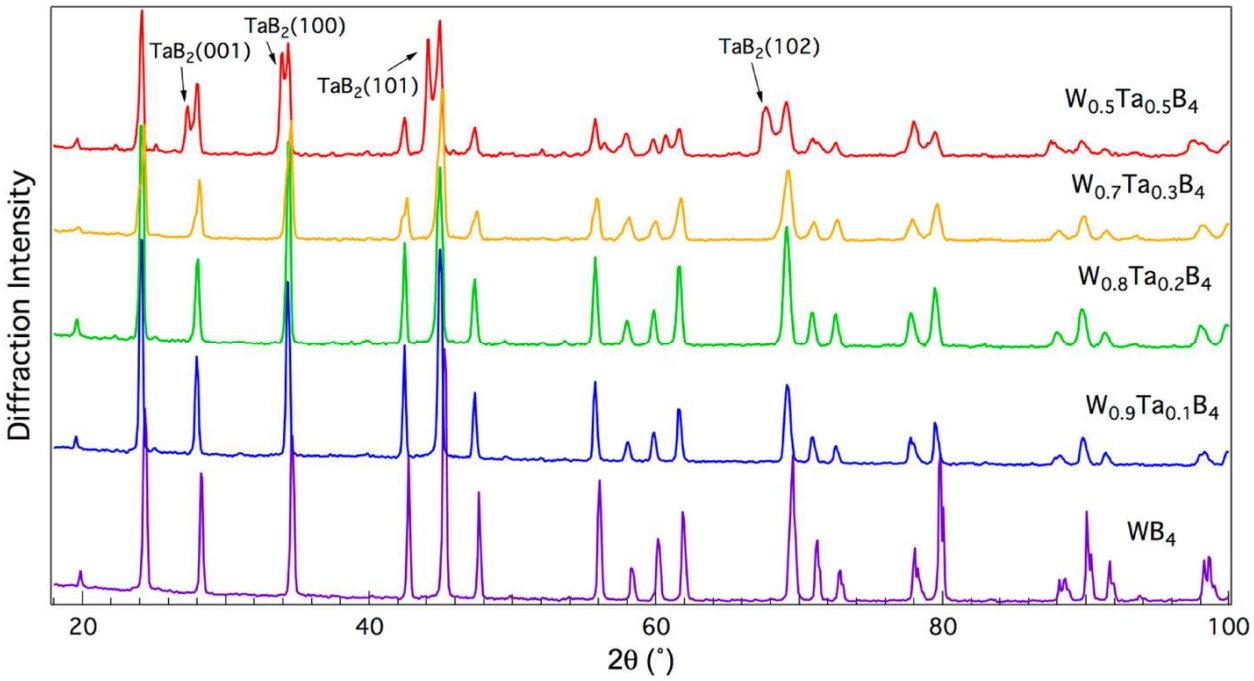
TaB2(001)
TaB2(100)
TaB2(101)
TaB2(102)
W0.5Ta0.5B4
W0.7Ta0.3B4
W0.8Ta0.2B4
W0.9Ta0.1B4
WB4
Diffraction Intensity
20
40
60
80
100
2θ (˚)

(a)

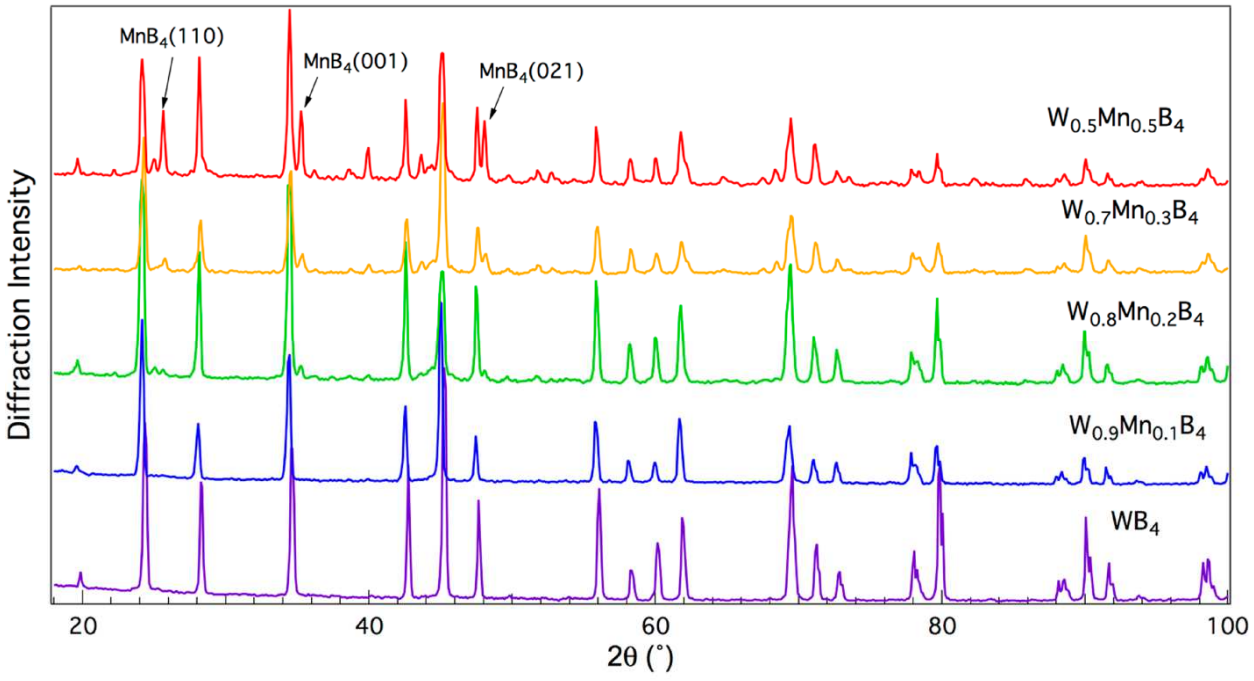
MnB4(110)
MnB4(001)
MnB4(021)
W0.5Mn0.5B4
W0.7Mn0.3B4
W0.8Mn0.2B4
W0.9Mn0.1B4
WB4
Diffraction Intensity
20
40
60
80
100
2θ (˚)

(b)

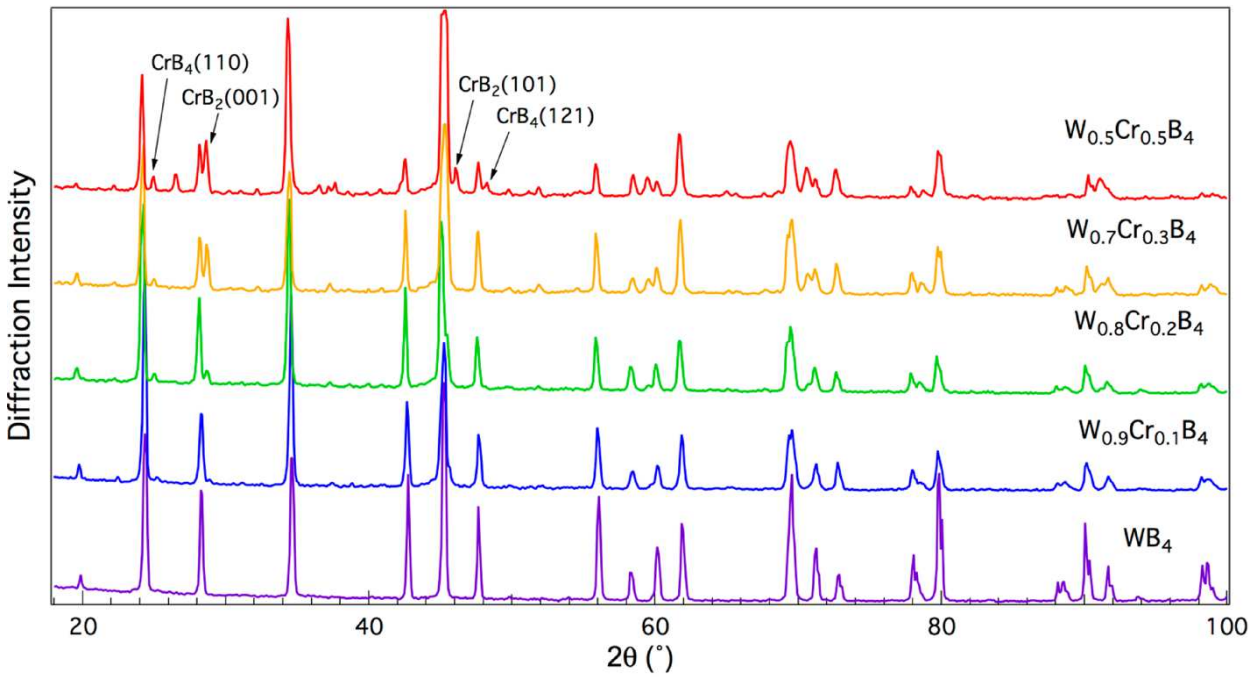

(c)

Figure 5.1: X-ray diffraction patterns of WB_4 when 0–50 at.% tantalum **(a)**, manganese **(b)**, and chromium **(c)** are added on a metals basis. The bottom pattern in each figure belongs to pure WB_4 (JCPDS ref code: 00-019-1373). Note that the solubility limit is less than 10 at.% for Cr and below 20 at.% for Mn, while the solubility of Ta in WB_4 is greater than 20 at.%. Above 20 at.% Ta, TaB_2 (JCPDS ref code : 03-065-3385) and at and above 20 at.% Mn and 10 at.% Cr, MnB_4 (JCPDS ref code : 03-065-6232) and a mixture of CrB_2 and CrB_4 (JCPDS ref codes : 00-022-0208 and 00-034-0369) appear respectively in the patterns as second phases (shown by arrows). To give the reader a clearer picture, only six patterns (0, 10, 20, 30, 40, and 50 at.% of Ta, Mn, and Cr), which are most useful to follow the structural changes, have been chosen in each series and displayed herein at higher magnification.

Table 5.1: Lattice Parameters and Selected d-Spacing for WB_4 and Some of Its Hardest Solid Solutions

Compound	a (Å)	c (Å)	V (Å^3)	d_{100} (Å)	d_{101} (Å)	d_{002} (Å)	d_{110} (Å)	d_{112} (Å)
WB_4	5.199(8)	6.338(4)	148.4	4.50316	3.67101	3.16920	2.59990	2.01006
$W_{0.98}Ta_{0.02}B_4$	5.200(5)	6.341(2)	148.5	4.50375	3.67186	3.17057	2.60024	2.01057
$W_{0.80}Ta_{0.20}B_4$	5.206(4)	6.356(5)	149.2	4.50876	3.67738	3.17781	2.60313	2.01375
$W_{0.96}Mn_{0.04}B_4$	5.200(2)	6.341(4)	148.5	4.50348	3.67174	3.17063	2.60009	2.01051
$W_{0.90}Cr_{0.10}B_4$	5.200(2)	6.340(6)	148.5	4.50348	3.67161	3.17029	2.60009	2.01042
$W_{0.96}Ta_{0.02}Mn_{0.02}B_4$	5.199(4)	6.339(1)	148.4	4.50286	3.67097	3.16953	2.59973	2.01006
$W_{0.88}Ta_{0.02}M_{n0.10}B_4$	5.199(3)	6.338(1)	148.4	4.50276	3.67072	3.16901	2.59967	2.0099
$W_{0.96}Ta_{0.02}Cr_{0.02}B_4$	5.199(1)	6.337(7)	148.4	4.50254	3.67053	3.16883	2.59954	2.0098
$W_{0.93}Ta_{0.02}Cr_{0.05}B_4$	5.199(4)	6.333(5)	148.3	4.50278	3.66983	3.16671	2.59968	2.00932
$W_{0.88}Ta_{0.02}Cr_{0.10}B_4$	5.199(7)	6.336(5)	148.4	4.50309	3.6706	3.16824	2.59986	2.0098

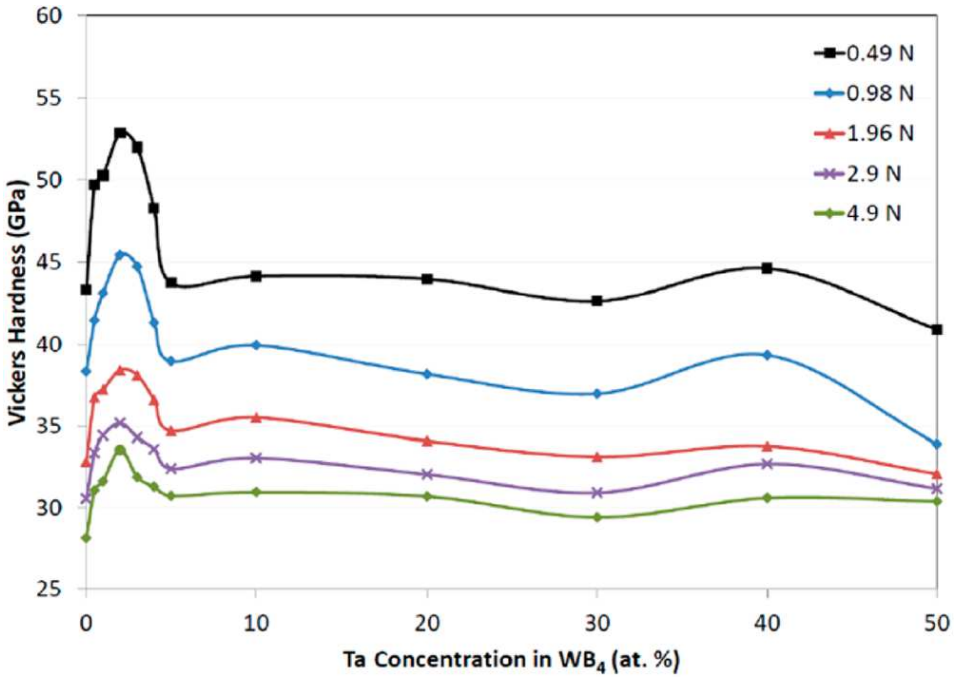
0.49 N
0.98 N
1.96 N
2.9 N
4.9 N
Vickers Hardness (GPa)
Ta Concentration in WB4 (at. %)

(a)

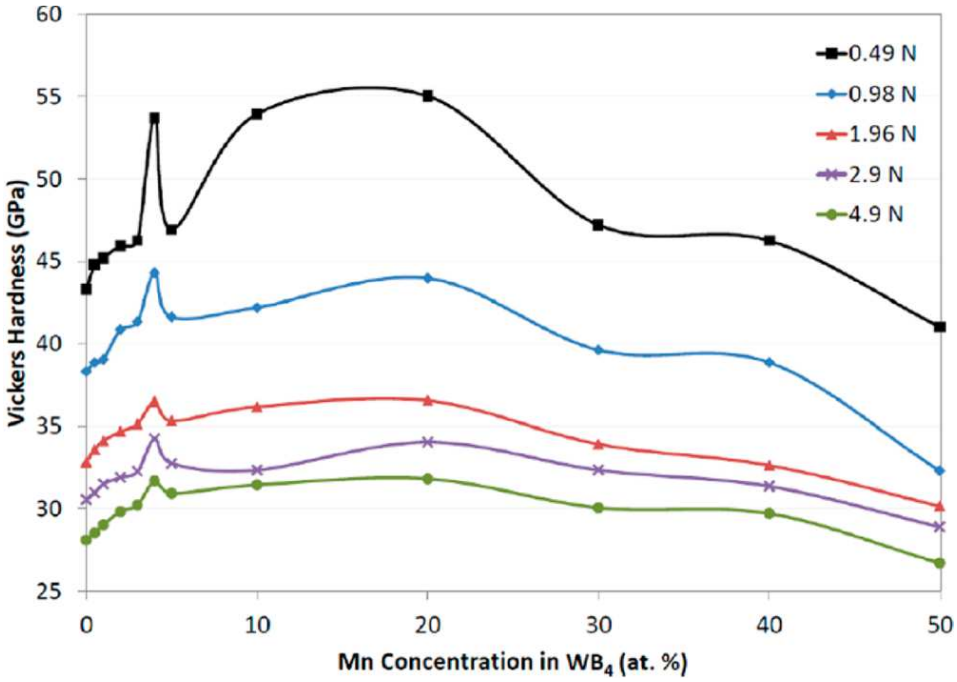
0.49 N
0.98 N
1.96 N
2.9 N
4.9 N
Vickers Hardness (GPa)
Mn Concentration in WB4 (at. %)

(b)

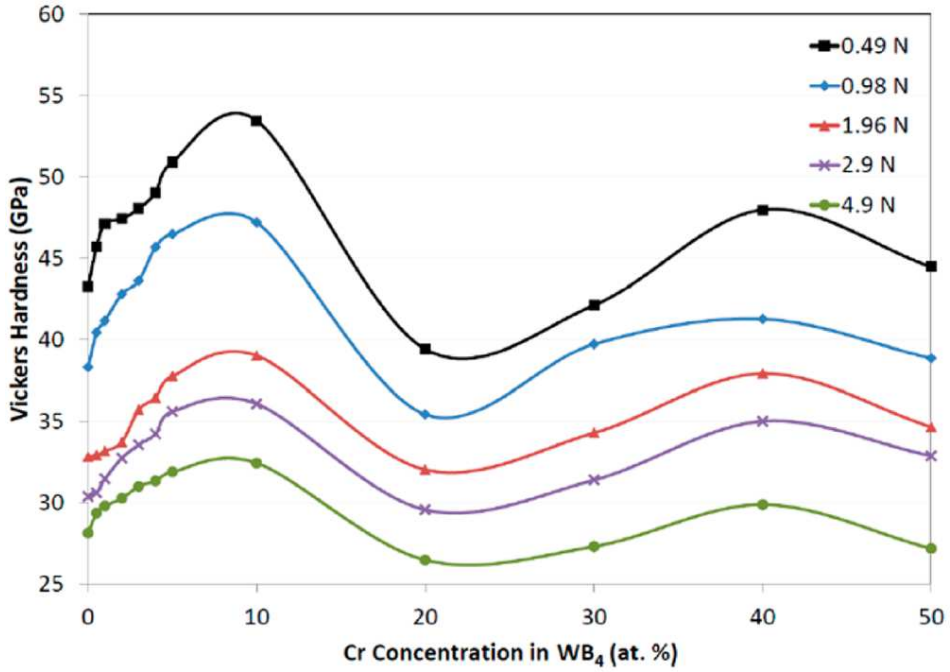

(c)

Figure 5.2: Vickers micro-indentation hardness of tungsten tetraboride solid solutions with Ta **(a)**, Mn **(b)**, and Cr **(c)** under loads ranging from 0.49 to 4.9 N (low to high loads, respectively). The concentrations were varied in WB_4 by adding 0−50 at.% Ta, Mn, and Cr on a metals basis (see Figure 5.1).

Table 5.2: Vickers Micro-indentation Hardness Data for $W_{0.98-x}Ta_{0.02}Mn_xB_4$ Solid Solutions, with x = 0.02 − 0.1, under Applied Loads Ranging From 0.49 − 4.9 N

	Applied Load (N)				
Compound	**0.49**	**0.98**	**1.96**	**2.94**	**4.9**
WB_4	43.3	38.3	32.8	30.5	28.1
$W_{0.96}Ta_{0.02}Mn_{0.02}B_4$	49.6	45.4	34.3	33.3	29.5
$W_{0.94}Ta_{0.02}Mn_{0.04}B_4$	55.8	46.7	37.0	34.8	30.9
$W_{0.88}Ta_{0.02}Mn_{0.10}B_4$	47.2	36.9	33.1	31.5	30.4

Table 5.3: Vickers Micro-indentation Hardness Data for $W_{0.98-x}Ta_{0.02}Cr_xB_4$ Solid Solutions, with x = 0.02 − 0.1, under Applied Loads Ranging From 0.49 − 4.9 N[a]

Compound	Applied Load (N)				
	0.49	**0.98**	**1.96**	**2.94**	**4.9**
WB_4	43.3	38.3	32.8	30.5	28.1
$W_{0.96}Ta_{0.02}Cr_{0.02}B_4$	46.2	39.6	33.1	31.5	29.0
$W_{0.93}Ta_{0.02}C_{r0.05}B_4$	57.3	44.1	38.2	34.8	31.7
$W_{0.88}Ta_{0.02}Cr_{0.10}B_4$	49.9	43.0	37.8	34.5	30.8

[a]Highest hardness of 57.3 GPa (at 0.49 N) was measured for the $W_{0.93}Ta_{0.02}Cr_{0.05}B_4$ solid solution.

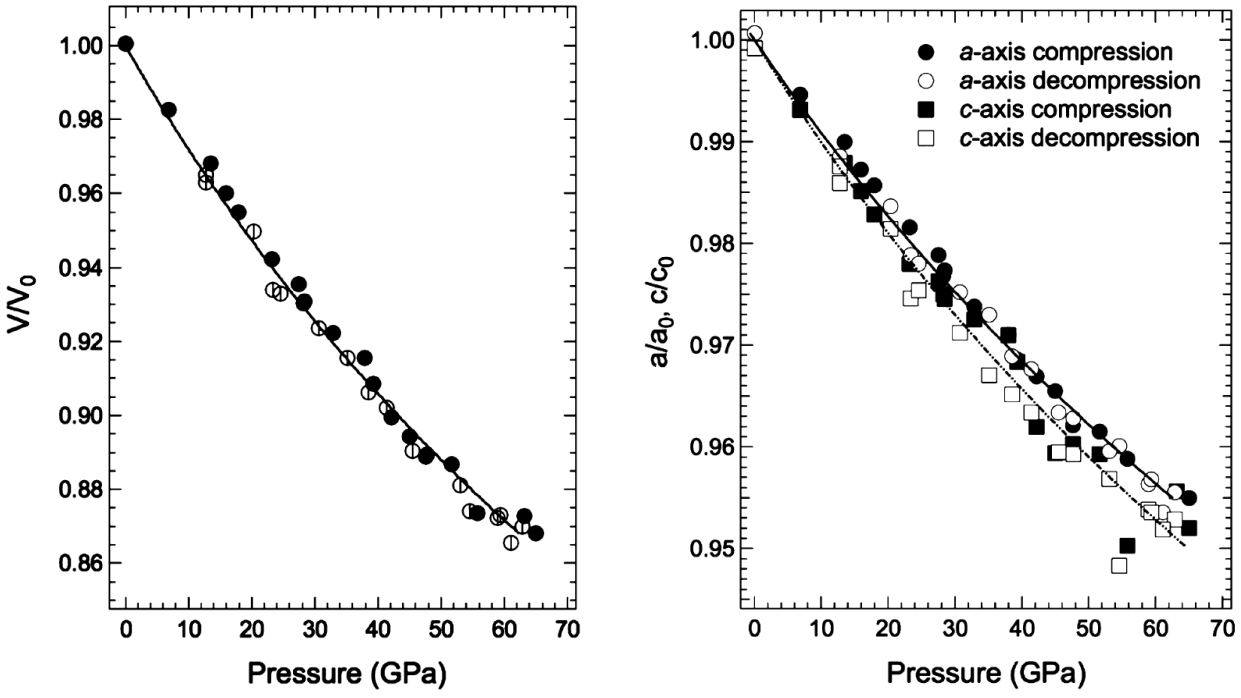

(a) **(b)**

Figure 5.3: Measured fractional unit cell volume **(a)** and fractional lattice parameters **(b)** of the hardest WB_4 solid solution, i.e., $W_{0.93}Ta_{0.02}Cr_{0.05}B_4$, plotted as a function of pressure. The data were collected using *in situ* high-pressure XRD up to 65 GPa. All the lines are Birch-Murnaghan fit to the data. Fitting the compression data to a second-order Birch-Murnaghan equation of state resulted in a zero-pressure bulk modulus of 335 GPa when its derivative with respect to pressure was set to 4. The close linear compressibilities of the *a*- and *c*-axes indicate a mechanically more isotropic structure for the hardest solid solution when compared to pure WB_4. Error bars are within the size of the symbols.

Table 5.4: Measured Isothermal Bulk Modulus (K_{0T}) and Corresponding First Derivatives (K_{0T}') of WB_4 and $W_{0.93}Ta_{0.02}Cr_{0.05}B_4$ Solid Solution Using an *in Situ* High – Pressure XRD Technique[a]

	WB_4		$W_{0.93}Ta_{0.02}Cr_{0.05}B_4$			
Pressure (GPa)	K_{0T} **(GPa)**	K_{0T}'	K_{0T} **(GPa)**		K_{0T}'	
40	326 (3)	4	346	(3)	4	
	369 (9)	1.2 (0.5)	366	(14)	2.6	(0.9)
65	–	–	335	(3)	4	
	–	–	350	(16)	3.3	(0.7)

[a]Data were fit using the second- and third- order Birch-Murnaghan equations of state up to 40 and 65 GPa. Error values are quoted in parentheses.

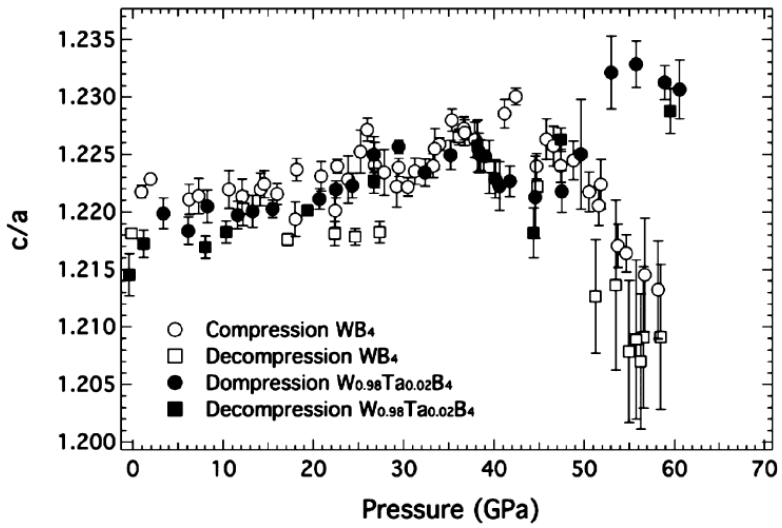

(a)

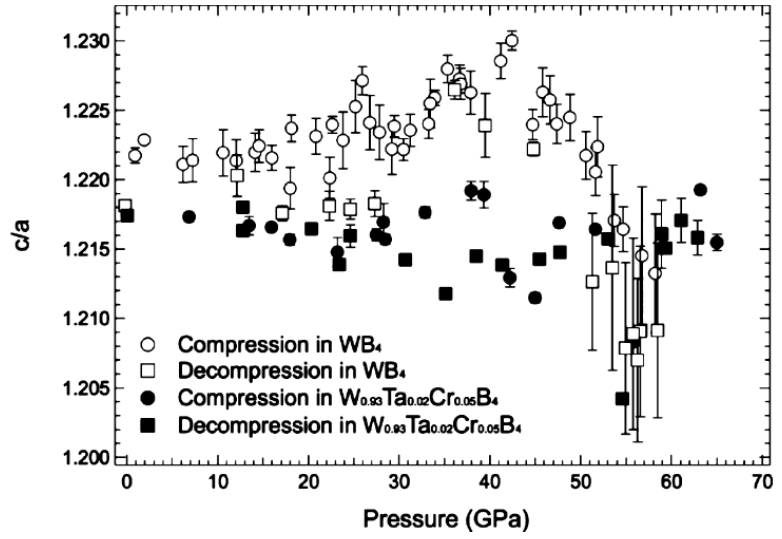

(b)

Figure 5.4: The c/a ratio plotted as a function of pressure for the $W_{0.93}Ta_{0.02}Cr_{0.05}B_4$ **(a)** and $W_{0.98}Ta_{0.02}B_4$ **(b)** solid solutions compared with pure WB_4. Solid circle (●), compression of the solid solution; solid square (■), decompression of the solid solution; open circle(○), compression of WB_4; open square (□), decompression of WB_4. WB_4 undergoes a pressure – induced second – order phase transition at ≈42GPa. In contrast, $W_{0.93}Ta_{0.02}Cr_{0.05}B_4$ and $W_{0.98}Ta_{0.02}B_4$ show no evidence of a phase transition up to the highest pressure, suggesting a significant effect of W substitution on the bonding. Error bars are within the size of the symbols.

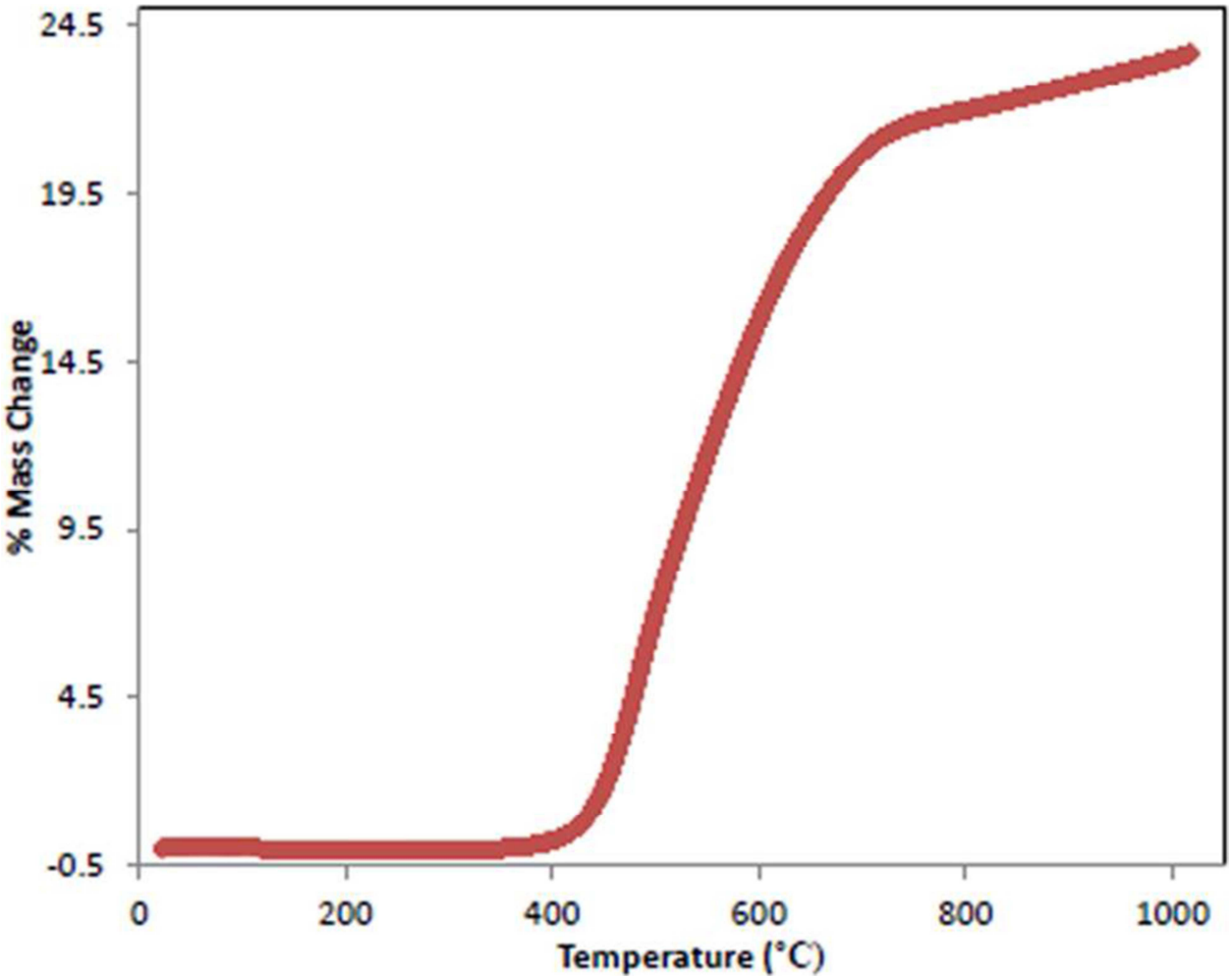

Figure 5.5: Thermal stability of the hardest tungsten tetraboride solid solution, $W_{0.93}Ta_{0.02}Cr_{0.05}B_4$, as measured by thermal gravimetric analysis. These data show that this WB_4 solid solution is thermally stable up to 420 °C in air. The weight gain of about 20 − 25% above 420°C can be attributed to the oxidation of tungsten and chromium to WO_3 and Cr_2O_3, respectively, as determined using powder XRD.

Table 5.5: Vickers Hardness (H_v), Isothermal Bulk Modulus (K_{0T}), Shear Modulus (G), and Young's Modulus (E) of Major Super-hard Materials Compared to Our Hardest Solid Solution, $W_{0.93}Ta_{0.02}Cr_{0.05}B_4$

Compound	H_v **(GPa)**	K_{0T} **(GPa)**	**G (GPa)**	**E (GPa)**
Diamond	60 – 150[46]	433 – 443[46,157]	534 – 535[46]	1142[46]
c-BN	45 – 80[46,220]	369 – 385[46,220]	409[46]	800 – 900[220]
B_6O	35[46]	200 – 208[46]	204[46]	472[221]
BC_2N	62 – 76[220]	259[222]	238[222]	980[223]
Si_3N_4	33[46]	249[46]	123[46]	280[46]
Al_2O_3	20 – 27[46,220]	246 – 252[46,157]	160 – 166[46]	403 – 44[46]
α-SiC	21 – 29[46,220]	221 – 234[46]	198 – 200[46]	457 – 466[46]
β-SiC	26 – 37[46]	210 – 227[46]	170 – 173[46]	401 – 410[46]
WC	13 – 25[220]	412 – 421[46]	269 – 280[46]	700 – 720[46]
ReB_2	30 – 48[220]	344[181]	267 – 273[158,220]	614 – 661[158,220]
WB_4	28 – 43[181]	326 (this work)	245 (theoretical)[224]	553[181]
$W_{0.93}Ta_{0.02}Cr_{0.05}B_4$	32 – 57 (this work)	335 (this work)	–	–

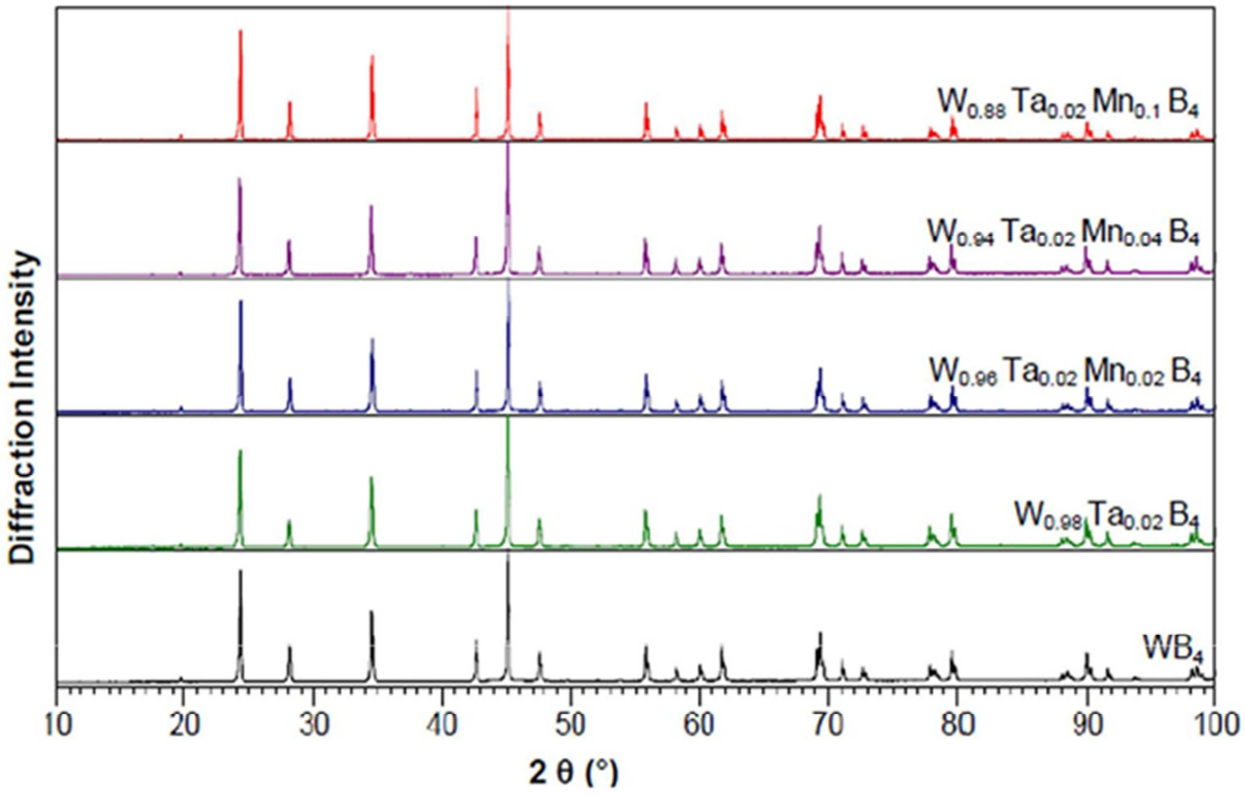

Figure 5.6: Powder X-ray diffraction patterns of WB_4 solid solutions containing a fixed concentration of Ta (2at.% on a metals basis) and concentrations of Mn (Figure 5.3**a**) and Cr (Figure 5.3**b**) varied from 2 – 10at.%. These patterns indicate that in the presence of 2 at.% Ta on a metals basis, the solubility of both Mn (**Figure 5.3a**) and Cr (**Figure 5.3b**) are limited to ≈10 at.%.

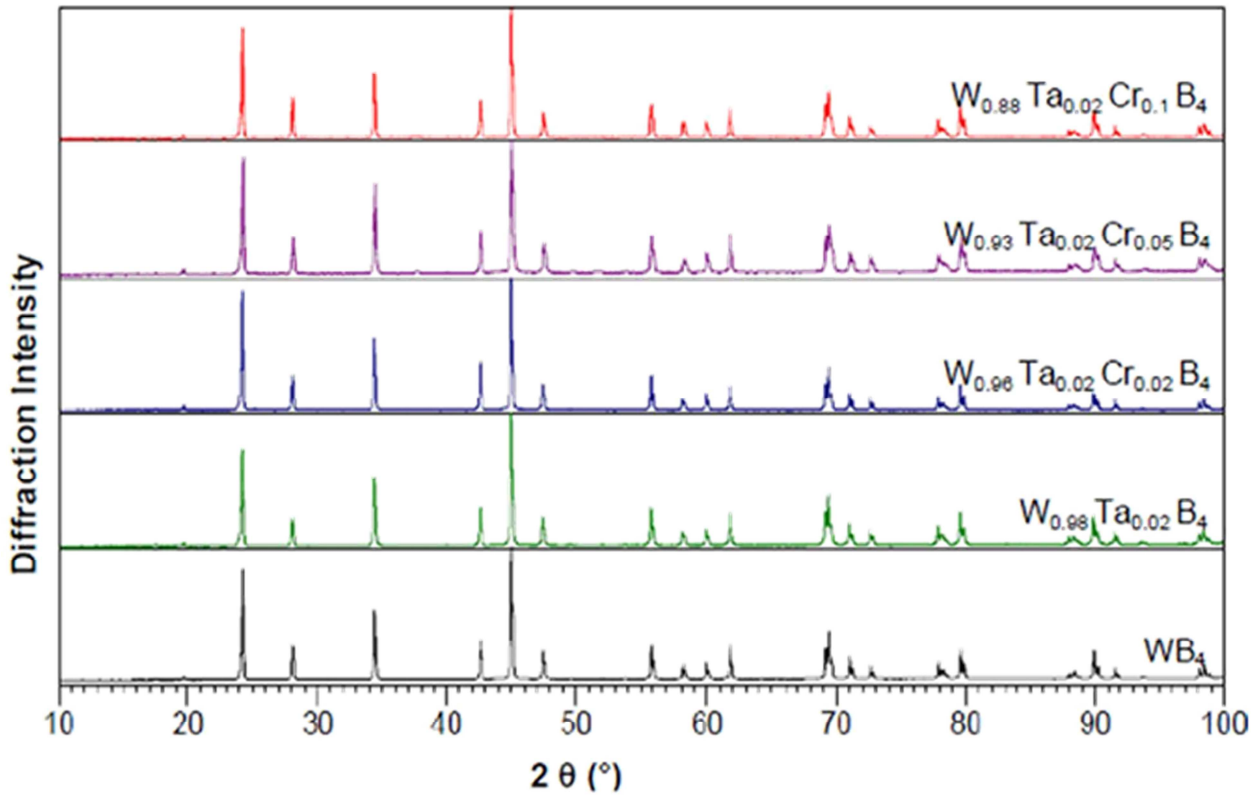

Figure 5.7: Representative X-ray diffraction patterns for $W_{0.93}Ta_{0.02}Cr_{0.05}B_4$ as a function of increasing and decreasing pressures. The Re peaks are from the gasket due to incomplete filtering of the tails of the X-ray beam.

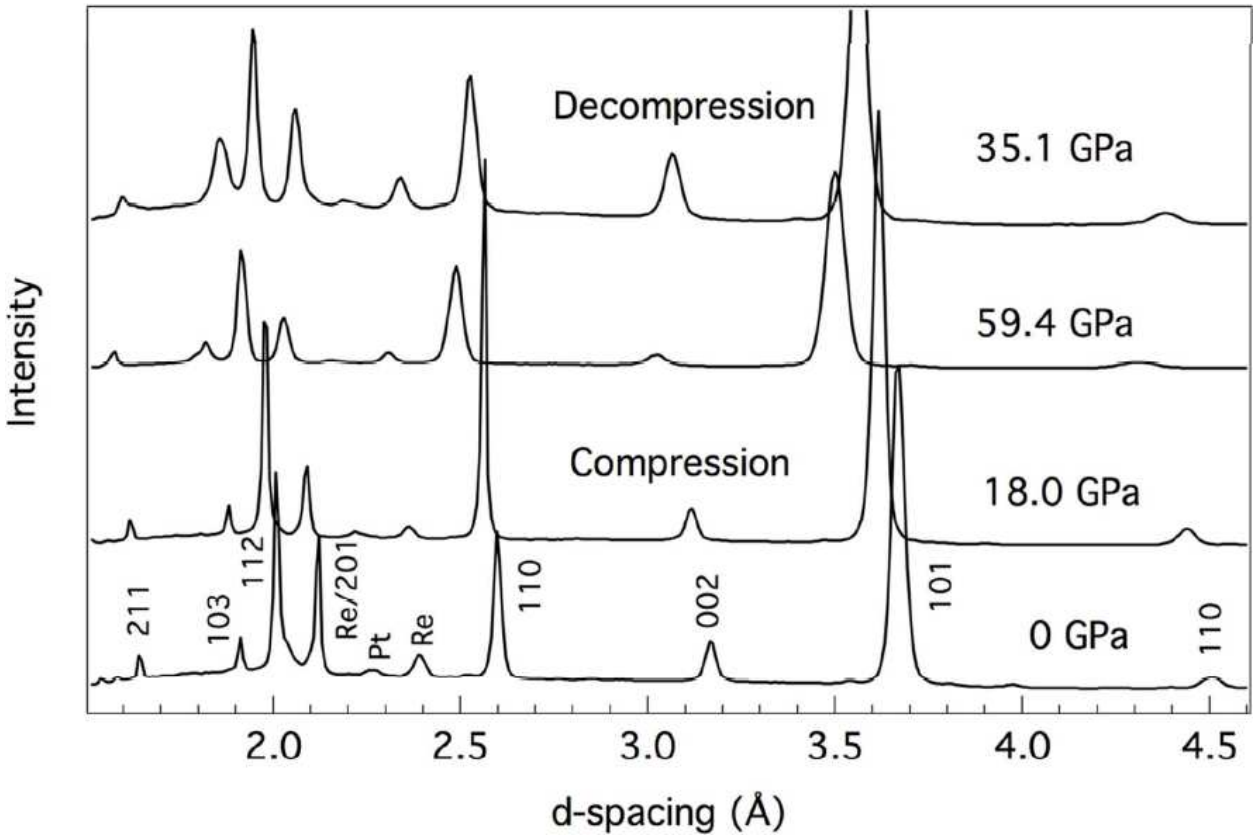

Figure 5.8: Representative X-ray diffraction patterns for $W_{0.93}Ta_{0.02}Cr_{0.05}B_4$ as a function of increasing and decreasing pressures. The Re peaks are from the gasket due to incomplete filtering of the tails of the X-ray beam.

Chapter 6

The Structure of "WB_4"

Introduction

With the increasing demand for new super-hard materials for cutting tool application, mainly due to the shortcomings of traditional tool materials such as diamond (unable to cut ferrous materials) and cubic boron nitride (very expensive), the introduction of transition metal borides as ideal candidates for this applications has recently attracted a great deal of attention. In this growing family of super-hard materials, tungsten tetraboride (WB_4) is of a specific interest due to its inexpensive nature. Although this interesting boride has demonstrated excellent mechanical properties including an extremely high Vickers hardness of ≈43 GPa (under an applied load of 0.49 N) and 40.4 GPa by nano-indentation (**Figure 6.1**), further enhancements are of significant importance – especially for tool applications. One growing method to enhance the hardness is by creating solid solutions of this compound with other transition metals. To understand the underlying mechanisms for the hardness enhancements observed in WB4, when different transition metals of various concentrations are added, and to help design new super-hard borides with tailored mechanical properties, it is crucial to know the exact crystal structure of this compound.

The precise crystal structure of the compound commonly known as "WB_4", here referred to as the highest boride of tungsten, has long been a contentious issue. Due to the similarity of its chemical formula to other higher borides (of the ThB_4 type), it was originally indexed against the tetragonal system with lattice parameters a = 6.34 Å and c = 4.50 Å when first described by Chretien and Helgorsky in 1961.[225] Goldschmidt *et al*. confirmed the existence of the phase in 1963 and refined its parameters to

a = 6.36 Å and *c* = 4.42 Å, again in a tetragonal cell.[226] Due to the lack of isolable single crystals and the crudity of powder refinement techniques used, no atomic coordinates were proposed, though it was obvious, from both the diffraction patterns and the chemical properties, that the atomic structure was quite different from that of ThB_4-type borides.

In an effort to resolve the matter, Romans and Krug re-investigated the "WB_4" system in 1965 and produced what might be called its canonical structure.[154] A lower volume (148.47 $Å^3$ vs. 180.88 $Å^3$), hexagonal unit cell with *a* = 5.200 Å *c* = 6.340 Å was chosen and a first attempt at refining the atomic coordinates made (space group *P6₃/mmc*, **Figure 6.2a**). Given the large difference in *Z*, and thus scattering power, between tungsten and boron, combined with the comparatively poor resolution of the X-ray crystallographic equipment used (non-monochromatic $Cu_{K\alpha}$ radiation), the positions of the boron atoms were inferred by chemical analogy. Thus, after assigning the tungsten sites, the only obvious remaining Wyckoff positions [*12(i)* and *4(f)*] were designated as boron sites; the resulting B-B bonding structure being justified by relation to the (later demonstrably erroneous) "W_2B_5" structure.[227] A notable consequence of this was the imposition of B-B dimers, or "dumbbells", within the tungsten layers.

Nowotny *et al*. independently re-investigated the system in 1967 using the tungsten borides isolated from eutectic melts of MB-WB_4-B (M = Ni, Rh, Pd, Pt). Finding a chemical composition of approximately $W_{1.83}B_9$ (~$WB_{4.92}$), and, perhaps indexing contaminating, X-ray lines, they assigned the highest boride to the low-symmetry trigonal group *P -3* with *a* = 5.206 Å and *c* = 3.335 Å (**Figure 6.2b**).[228] Their structure notably includes the presence of B_6 octahedra in the tungsten vacancy positions and provides allowance for fractional occupancy of one of the tungsten sites.

Perhaps the definitive attempt at an experimental solution of the full structure (including boron positions) for "WB_4", using modern least-squares refinement and Fourier difference map techniques,

was published in 1973 by Lundström and Rosenberg who, seeking to minimize the scattering power mismatch between metal and boron, worked primarily with the hypothetically isomorphic molybdenum phase commonly denoted "$Mo_{1-x}B_3$" ($x \approx 0.20$) (**Figure 6.2c**).[229] While the partial occupancy of a metal position was re-affirmed in their work, the possibility of boron atoms filling vacancies in the structure was rejected for this model compound.

The highest boride of tungsten has recently attracted renewed interest due to the identification of its outstanding physical and mechanical properties, particularly as a hard metal.[46,103,106,157,181,215] These properties include an exceptionally high Vickers hardness of 43.3 GPa (under a low applied load of 0.49 N) and 28.1 GPa (under a high applied load of 4.9N),[181] which compare favorably to the hardness of the stereotypical "super-hard" compound cubic boron nitride (*c*-BN) of 40 GPa[230]. Additionally, a relatively high zero-pressure bulk modulus of 326 GPa[215] (c.f. 369 – 400 GPa[231,232] for *c*-BN) has been measured. Taken together, these properties demonstrate the exceptional resistance of this compound to both plastic and elastic deformation; properties which typically correlate with very high structural rigidity and high atomic space filling.[233–235] Finally, solid solutions based on "WB_4" seem to have demonstrable enhancement in at least some of these properties.[106] However, a definitive structure would be more helpful in elucidating the basis of these effects, as well as guiding further chemical manipulation of its admixtures.

As a result, a new series of mainly computational-theoretical papers have recently appeared with the goal of identifying the structural origin of properties in WB_4.[164,217,224,236–242] Initially, these only ranged from an un-critical acceptance of the standard "WB_4" model of Romans and Krug,[164] to the cautionary (noting that "WB_4" is an unstable phase at ambient pressure).[241] Eventually it was noticed that that the structure, properties, and stability of the highest boride of tungsten were better accounted for if the B_2-dimers proposed by Romans and Krug were simply removed,[239,242] and that this model could be further

improved if some of the tungsten sites were treated as fractionally occupied.[217] Taken together, the calculations reported in these papers only further support the supposition that all of the previous structural models are incorrect.

Due to the large and often contradictory discrepancies in these proposed models, this study was undertaken with the goal of revisiting the structure of the highest boride of tungsten using the additional experimental resource of neutron diffraction in addition to X-ray diffraction. Neutron diffraction has a very high scattering cross-section for the boron-11 isotope, so it is highly complementary to X-ray diffraction, which is heavily weighted towards tungsten. By combining these two methods, we now report what we believe is the first correct structure of the highest boride of tungsten. The structure contains some elements previously reported, along with some new ones. Most importantly, the structure provides real insight into the extremely high hardness and solid solution behavior of this relatively low-cost transition metal boride.

Materials and Methods

Samples for X-ray and neutron diffraction were prepared in parallel from the same batch of reagents and using the same methodology. High-purity powders of tungsten (99.95%, Strem Chemicals, USA) and crystalline ^{11}B (99.9%, 99.2% ^{11}B enriched, Ceradyne, USA) were manually mixed without grinding in the ratio 1 **:** 12 using an agate mortar and pestle and consolidated into pellets by means of a hydraulic jack press (Carver, USA) under a pressure of ≈562 MPa. The pellets were placed on a water-cooled copper hearth, sealed inside a bell jar, and purged several times with ultra-high-purity argon followed by rough vacuum before being arc melted under one atmosphere of titanium/zirconium-gettered ultra-high-purity argon using ≈100 ampere DC current and a non-consumable tungsten cathode. The samples were crushed to sub-millimeter powders using a hardened steel mortar and pestle (Humboldt) and wet-

ground under methanol/ethylene glycol at low speed in a planetary mill (Pulverisette 5/2™, Fritsch, Germany) using stainless steel media until the majority passed through a 635 mesh (20 micron) screen (Humboldt, USA). The sieved powders were stirred for 2 hours under three successive aliquots of excess HCl to remove contaminating residue from the grinding and milling media. The sub-micron fraction of each sample was separated by repeated suspension in methanolic ammonia, the fastest settling fraction being retained. This procedure was found to minimize the contamination of foreign elements to below the detection limit of the energy dispersive X-ray spectroscopic analyzer (EDAX™, EDAX Inc., U.S.A) mounted to our SEM (JEOL JSM 6700 F, Japan).

Samples for X-ray diffraction were deposited directly from methanolic suspension onto silicon 511 "zero-background" plates. Excess sample was removed by a razor blade until nearly perfectly flat. Samples were at least 250 microns thick. Diffraction patterns were collected using the X'Pert Pro™ Bragg-Bentano geometry laboratory X-ray diffractometer (PANalytical, Netherlands), employing non-monochromated nickel filtered $Cu_{K\alpha}$ radiation (λ = 1.5418 Å), rotating sample stage, and X'Celerator position sensitive detector.

Neutron diffraction data were collected from the HIPPO (High-Pressure Preferred Orientation) beam line at LANSCE (Los Alamos Neutron Science Center, Los Alamos National Lab, Los Alamos New Mexico) through proposal number 20112198 submitted to LANL. This is a neutron time-of-flight machine using 5 banks of varyingly panels of ^{3}H-detector tubes. Due to the extremely high thermal neutron absorption cross-section of residual ^{10}B, even in our highly enriched samples, this line was selected due to its very high neutron flux, accommodation of large samples, and multiplicity of detector banks. Powdered samples on the order of 1 cm^3 in volume were loaded into vanadium foil "cans" and irradiated by water-moderated neutrons collimated to 1 cm diameter, while data were collected for a cumulative collection

time of 6 hours. This unusually long collection time was necessary due to the large absorbance of residual ^{10}B and for the sake of higher signal to noise ratio.

X-ray and neutron diffraction data were subjected to simultaneous Rietveld refinement[243] using the EXPGUI[133] front-end to the GSAS[134] Rietveld refinement software package. Primarily the data from the 150° and 90° neutron collection banks were used due to their combination of high resolution and accuracy.

Results

The X-ray diffraction pattern (**Figure 6.3a**) was readily indexed against an hexagonal unit cell in the space group *$P6_3/mmc$* having unit cell dimensions a = 5.2001 Å and c = 6.3388 Å. A few contaminating lines are noticeable and fully indexable against b-rhombohedral boron, as would be expected given the large molar excess of boron in the reaction mixture. All of these lines, with the exception of those at 11.92° 2θ (1,0,-2), 16.19° 2θ (110), 17.57° 2θ (104), and 19.09° 2θ (2,0,-1) are of the same relative magnitude (<1%) as the post-filtering, residual $Cu_{K\beta}$ lines from the tungsten-containing phase, and were thus ignored. Rietveld analysis of the tungsten boride phase against a base model consisting only of tungsten atoms and an hexagonal net of boron yielded a fractional occupancy of approximately 2/3 for the tungsten atom centered on coordinates (0, 0, 1/4). The second tungsten atom site at (1/3, 2/3, 1/4) is fully occupied. Attempts to refine these data with the incorporation of further boron atoms yielded poorer results.

The neutron diffraction data produced an exceptionally complex pattern due to the strong diffraction of the secondary β-boron phase, requiring it to be modeled simultaneously. Repeated subsequent attempts at refinement the 'boron-deficient' model of the tungsten boride against the neutron powder diffraction data made it immediately obvious, however, that it could not fully account for the observed

relative peak intensities. Therefore, the model was compared against Fourier difference maps (**Figure 6.4**), which revealed significant unaccounted-for diffraction density at approximately (0.24, 0.12, 1/4) and (0.26, 0.13, 1/4). A boron atom inserted into either of these positions refined to (0.24, 0.12, 1/4) with an occupancy of approximately 1/3. The resulting model accounts well for the observed X-ray and neutron diffraction intensities (**Figure 6.3**).

The final structure at which we arrived, having a stoichiometry of approximately $WB_{4.2}$, is presented in **Figure 6.5**. This analysis leads us to conclude that an array of trigonal boron is randomly distributed between this site and the position of a crystallographically identifiable, partially occupied tungsten site. This arrangement, exactly within bonding distance of the hexagonal boron nets, gives rise to a subset of slightly distorted cuboctahedra distributed between tungsten planes, averaging about two for every three unit cells. The "void" space in this structure is thus very small, leading strong evidence to the presumption of bonding between boron layers.

Unfortunately, the extreme complexity, relatively low resolution, and many overlapping peaks in the diffraction data precluded the determination of reliable anisotropic Debye-Waller factors. Reasonable isotropic factors were, however, readily obtainable. The complete crystallographic data for this analysis are presented in **Table 6.1**.

Discussion

The structural ambiguity of the highest boride of tungsten stems primarily from the difficulties surrounding the Rietveld analysis of X-ray crystallographic data for a compound consisting of both very electron poor (boron, Z = 5) and very electron rich (tungsten, Z = 74) elements. Although the ratio of boron to tungsten is large, it is not so large that its core electron contribution to the diffraction pattern strongly influences the structure factor. This situation is exacerbated by three further issues: 1) the

imprecision with which the compound's stoichiometry is known, 2) the apparently necessary presence of excess *β*-boron and 3) the lack of suitable mono-crystals for single-crystal diffraction.

Our laboratory has found electric arc-melting to be a simple and convenient means of synthesizing large-grained samples of metal borides. This process thus-far appears to be the most reliable means of producing high-quality boride samples, and has the additional advantage of producing highly-crystalline compounds directly from the elements in a fraction of the time of more traditional furnace or hot-pressing methods. Given the low synthetic parameter-space of the arc-melting technique, only a relatively simple set of experiments is needed to determine the optimal stoichiometric ratios to produce a single boride phase. For the case of the highest boride of tungsten this, unfortunately, necessitates the use of the eutectic mixture containing a substantial excess of boron (≈1 **:** 12) in the powder precursors. Stoichiometries below this ratio tend to produce mixtures of three or more related tungsten boride phases. Thus, the guarantee of the production of only the highest tungsten boride phase was deemed of more importance than the elimination of the excess reagent.

The very large contrast of the diffraction contribution of the two elements can be significantly decreased by means of neutron diffraction. Though the ratio of X-ray diffraction cross-sections for tungsten and boron is large, the diffraction cross-section for thermal neutrons is of similar magnitude between the two. Therefore, by simultaneous refinement of the powder patterns for both techniques, it becomes possible to distinguish between several possible structures proposed (among other candidates). This approach is not dissimilar to that previously taken by Lundström and Rosenberg who used the (assumed) iso-structural compound $Mo_{1-x}B_3$ as a model. In the case of the molybdenum compound, the lower fraction of metal electrons was used to enhance the overall contribution of boron to the X-ray diffraction structure factor. We find our method superior in that no assumptions need be taken and the structure is determined for the native compound.

The primary complicating circumstance of this procedure, however, is again the presence of a secondary phase. The excess boron crystallizes exclusively as the *β*-rhombohedral phase, without apparent dissolution of entrained tungsten, and crystalline grains are found throughout arc melted ingots (**Figure 6.6**). Unfortunately, the extreme chemical inertness and mechanical robustness of crystalline boron precludes its post-synthetic separation from the boride phase, necessitating the simultaneous refinement of both. While the *β*-boron produces only trivial interference with the X-ray diffraction pattern, its presence poses a much more formidable challenge for the analysis of the neutron diffraction data, where its many intense diffraction peaks heavily overlap those of the tungsten phase. Further complicating the matter is the imprecision with which the structure of *β*-boron is known, presumably due to a large amount of structural disorder in the interstices between icosahedra.

By analysis of our results, it should be apparent that the tetragonal structure proposed by Chretien and Helgorsky[244] is merely a re-indexed super-cell of the hexagonal phase, with their *c* parameter corresponding to half of the face diagonal in the *a*-*b* plane. These previous results may thus be considered as compatible with ours but otherwise dismissed.

The structure expounded by Romans and Krug[154] deserves, however, some special attention as it serves as an instructive, if cautionary, example of incomplete data being relatively unquestioningly accepted in the scientific literature. It is explicitly stated in their work that their conjectural B_2 dimer units were placed, *ad hoc*, in order to fulfill their calculated stoichiometry (derived from microprobe analysis). At no point was this final structure subject to refinement or further analysis, nor could it have been given the crudity of the diffraction pattern and the lack of modern computational tools. Indeed, the presence of boron dimers as a crystallographic entity is exceptionally rare, with only a few such examples available in the scientific literature. The nearest example seemingly being the compound $IrB_{1.5}$ where-in there is apparent dimerization of boron in what can be imagined as a Peierls-type distortion of the well-known

boron chain structural motif. Aside from this, B_2 would appear to be present much more prevalently only in the gas phase and in specific cases as inclusions in super-saturated, boron-doped compounds such as diamond (where it is detected spectroscopically and not crystallographically). The conjectured B_2 dimers would furthermore contradict the relatively firmly established rule described by Kiessling that, with increasing boron content, the structural motifs of boron atoms go from isolated atoms, to chains, to nets, to polyhedra (or portions thereof).[245] Nevertheless, this structure has been cited, usually without qualification, no fewer than some 35 times in the literature on "WB_4", and quite frequently in the past five years.

We have found no evidence supporting the *P-3* trigonal structure proposed by Nowotny *et al*. Inspection of our X-ray diffractographs and comparison to the spectra presented in their work, it is our conclusion that they mis-assigned the highest intensity *β*-boron peak to the boride pattern (observable in our data at 17.56° 2θ in **Figure 6.3a**). Using our data, we can readily replicate this reduction in symmetry of the unit cell, thus accounting for the discrepancy.

Of the previous work on this subject, the most thoroughly refined structural proposal (that of Lundström and Rosenberg) is also the most similar to ours, though lacking the substitutional/interstitial boron, and thus also the resulting polyhedral arrangement. However, we call in to question the supposition of equivalence of the highest borides of molybdenum and tungsten. This point would seem especially worthy criticism given the well-known similarity, but consequential difference, between the structure of Mo_2B_4 and W_2B_4.[76] Intriguing, however, is their discussion (and subsequent dismissal) of peaks in Fourier map corresponding to approximately 17% boron occupancy of the Wyckoff *6(h)* site. Had they further refined their structure with such sites occupied, they may very well have arrived at a similar result as we have proposed here, (though with slightly different fractional occupancies.

Given the chosen *P6$_3$/mmc* unit cell, there are three crystallographic positions [Wyckoff *2(b)*, *2(c)*, and *2(d)*] that may be occupied by tungsten atoms. One of these positions [Wyckoff *2(d)*] is completely unoccupied, and thus one-third of the tungsten atoms are systematically absent, leaving 'voids' in the structure. Furthermore, the Wyckoff position *2(b)* is only fractionally occupied (≈2/3) with substitutional 'triangles' of boron partially occupying the interstitial space between these vacancies and the vacant *2(d)* site, thus filling the Wyckoff *6(h)* position fractionally (≈1/3). The crystallographic stoichiometry of the highest boride of tungsten is approximately $WB_{4.2}$.

The structure may therefore be imagined a highly defective version of the P6/mmc (AlB_2-type) WB_2 structure. Indeed, if all of the possible tungsten sites were fully occupied, a structure with nearly idealized W-W and B-B distances would result. Instead, however, the absent tungsten sites appear to give rise to the opportunistic formation of slightly distorted cuboctahedral boron cages. This finding is especially satisfying in light of the stoichiometric position of $WB_{4.2}$ between that of the MB_2-type compounds, which contain exclusively boron 'nets', and those of other MB_x ($x > 2$) phases such as YB_{12}.The motifs of these higher boride phases are increasingly dominated by polyhedral sub-units. Indeed, this analogy is especially apparent when a somewhat fictional representation this tungsten boride (where *all 6(h)* sites are shown occupied) is compared against the cubic packing of YB_{12}, as in

Figure 6.7. In fact, the only primary distinctions between these two structure types are that: (1) $WB_{4.2}$ is hexagonal, while most dodecaborides are cubic; (2) the occurrence of cuboctahedra in MB_{12} structures is one per metal atom, whereas it is one for every four metal atoms in $WB_{4.2}$; and (3) the cuboctahedra of $WB_{4.2}$ are randomly distributed. These differences can be rationalized by noting that the formation of dodecaborides containing well-ordered cuboctahedra depends strongly on the radius of the metal atom with Y (1.80 Å)[246] and Zr (1.60 Å)[246] being, respectively, the largest and smallest metal

forming them under ambient pressure.[247] In comparison, the radius of W is only 1.39 Å[246], which is too small to accommodate one cuboctahedral cage per metal atom.

Indeed, in our model not all of the *6(h)* sites are occupied by boron, nor are all of the *2(b)* sites vacant of tungsten. Instead, vacancies and (necessarily) concomitant occupancies of these sites appear to follow a random distribution. According to our Rietveld results, the occupancy of the tungsten in Wyckoff *2(b)* approachesy exactly 2/3 and that of boron of in Wyckoff *6(h)* approaches exactly 1/3. If this is the case, each unit cell contains, on average, one boron 'trimer' to replace each tungsten absence. If the cuboctahedra are so arranged as to lead to maximal spacing, no two cuboctahedra would ever coincidentally occupy any part of the same unit cell, leading to a minimum of lattice strain. There is, however, a possibility of these occupancies being somewhat variable in spacing, particularly as a function of the excess boron used to drive the formation of the higher boride phase, though we believe the values proposed here represent an upper limit for the binary system. This hypothesis is currently subject to further investigation.

Finally, as has been mentioned previously, $WB_{4.2}$ is capable of hosting an apparently wide range of solute atoms, and these solute atoms can have a profound effect on hardness. Having an accurate model of $WB_{4.2}$ gives us invaluable insight toward understanding these phenomena and more directly predicting means of manipulating the crystal chemistry of this compound. For a low volume, high symmetry, binary compound, the unit cell of $WB_{4.2}$ contains an unusually large number of unique crystallographic sites. By carefully tailoring a solid solution scheme, it may be possible to specifically select guest atoms to replace only the fully occupied tungsten site, only the partially occupied site, or both. It may, furthermore, be possible to introduce other metals or heteroatoms at the vacant *2(d)* position, replacing the cuboctahedra with metal atoms or, conversely, enhancing the frequency and regularity with which they occur.[106] Research into these types of structural manipulations is currently

underway in our laboratory using experimental methods, but the existence of an accurate crystal structure for $WB_{4.2}$ should spur the design of new, super-hard solid solution using computational methods.

Conclusions

The structure of the highest boride of tungsten, previously denominated "WB_4", has been refined from X-ray and neutron powder diffraction data. Contrary to some previous predictions from theoretical calculations, there is strong evidence for the presence of interstitial arrangements of boron atoms and polyhedral bonding. Here, we present a new structural model for this compound, placing particular emphasis on its intermediary relationship to MB_2 and MB_{12} type boride polymorphs. Borides have recently drawn considerable attention due to their exceptionally high hardness and this information may prove invaluable for the rational design of new materials.

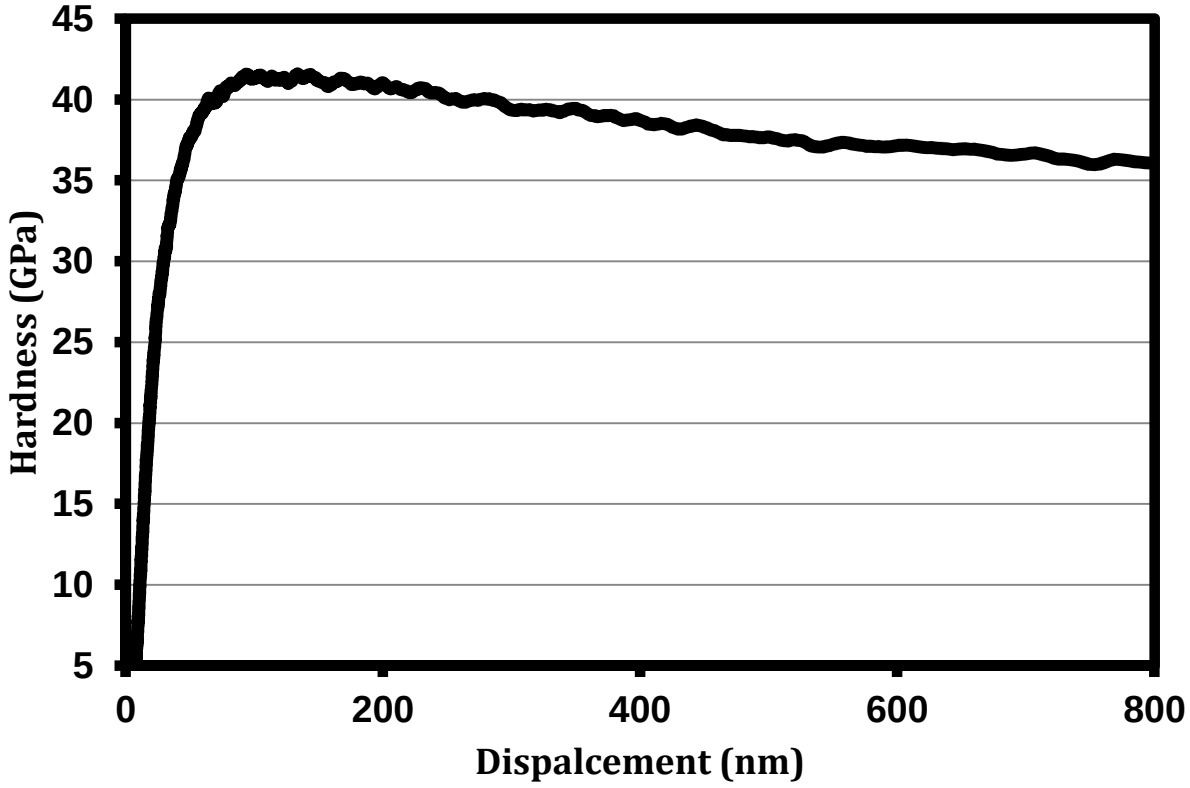

Figure 6.1: Nano-indentation data for WB4 indicating super-hardness (hardness above 40 GPa) from ≈50 nm displacement to ≈250 nm.

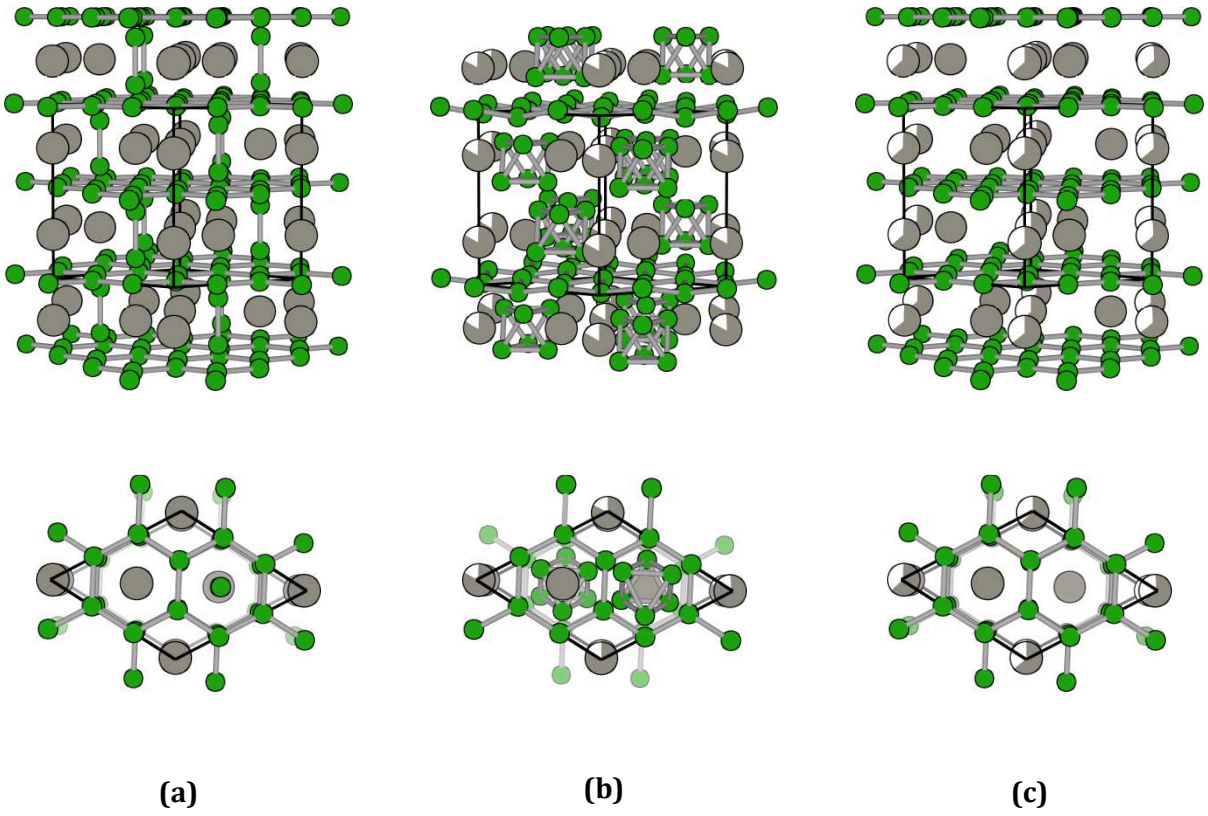

Figure 6.2: Comparison of the variously proposed structures of WB_4. **(a)** The structure of "WB_4" after Romans and Krug, **(b)** The structure of "$W_{1.83}B_9$" according to Nowotny *et al.* and **(c)** The structure of "$W_{1-x}B_3$" following Lundström and Rosenberg. Green spheres represent boron atoms and grey spheres represent tungsten atoms. Partial occupancy is indicated by partial sphere-filling. Bonds are shown to clarify the spatial arrangement only.

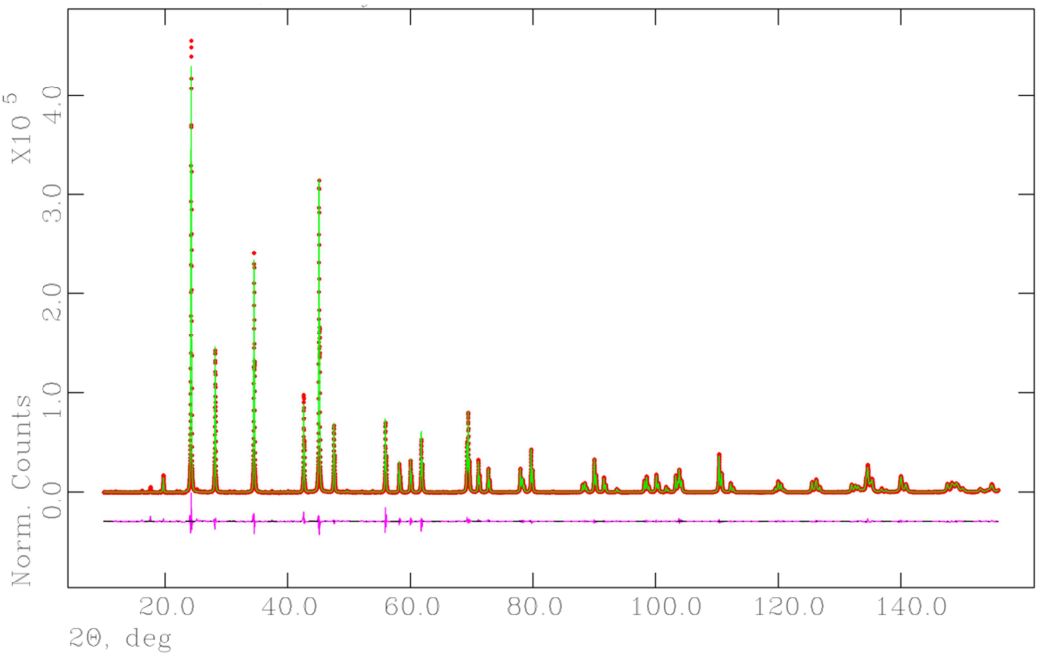

(a)

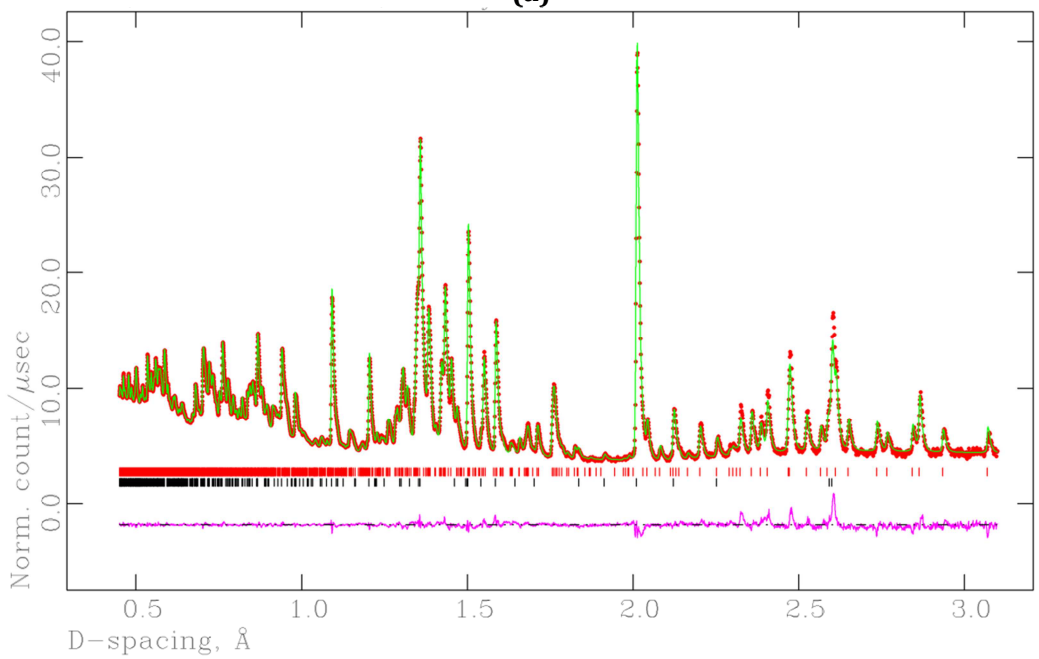

(b)

Figure 6.3: (a) X-ray and **(b)** neutron powder diffraction patterns for the highest boride of tungsten. Red points indicate observed data, the green line represents the fit against the final model. The difference between the two is shown beneath (magenta line). The background has been subtracted for clarity.

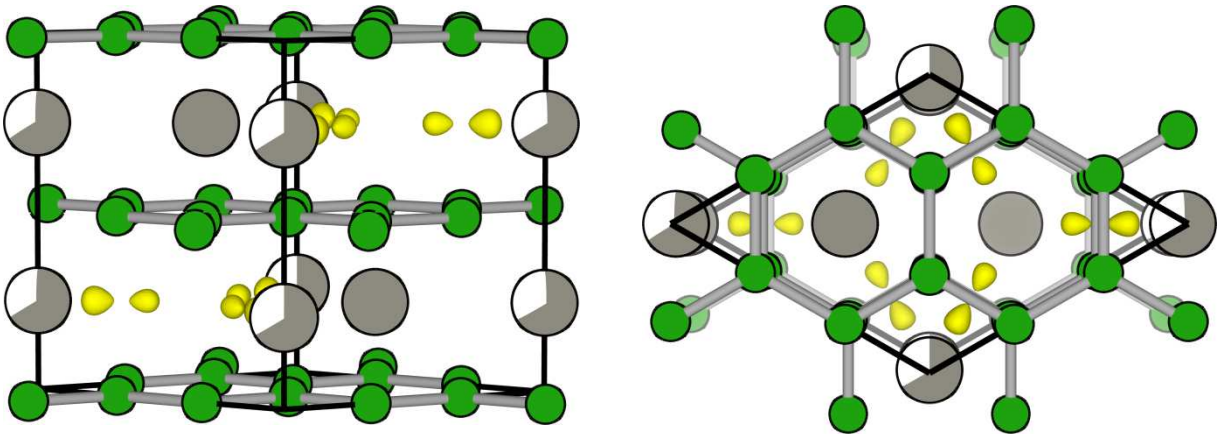

Figure 6.4: 3-dimentional Fourier difference map (yellow) from the neutron refinement overlaid on the boron-deficient model structure lacking interstitial boron. Green spheres represent boron atoms and grey spheres represent tungsten atoms.

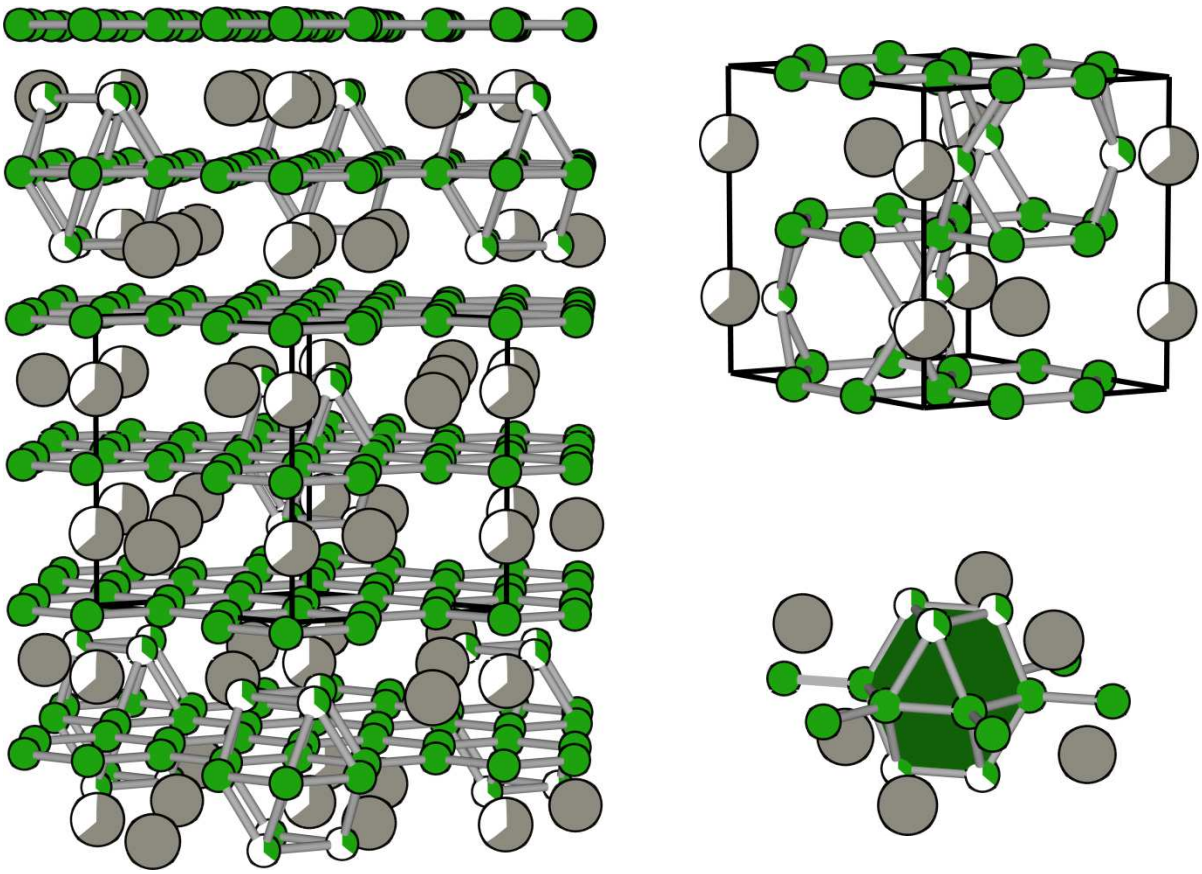

Figure 6.5: The proposed structure of the highest boride of tungsten.

Table 6.1: Relevant Crystallographic Data for the Highest Boride of Tungsten

Atom	Wyckoff	X-coordinate	Y-coordinate	Z -coordinate	Occupancy	U_{iso}
W1	*2(b)*	0.00000	0.00000	0.25000	0.6683	0.00122
W2	*2(c)*	0.33333	0.66667	0.25000	1.0000	0.00152
B1	*12(i)*	0.33100	0.00000	0.00000	1.0000	0.00293
B2	*6(h)*	0.23934	0.11967	0.25000	0.3317	0.00244

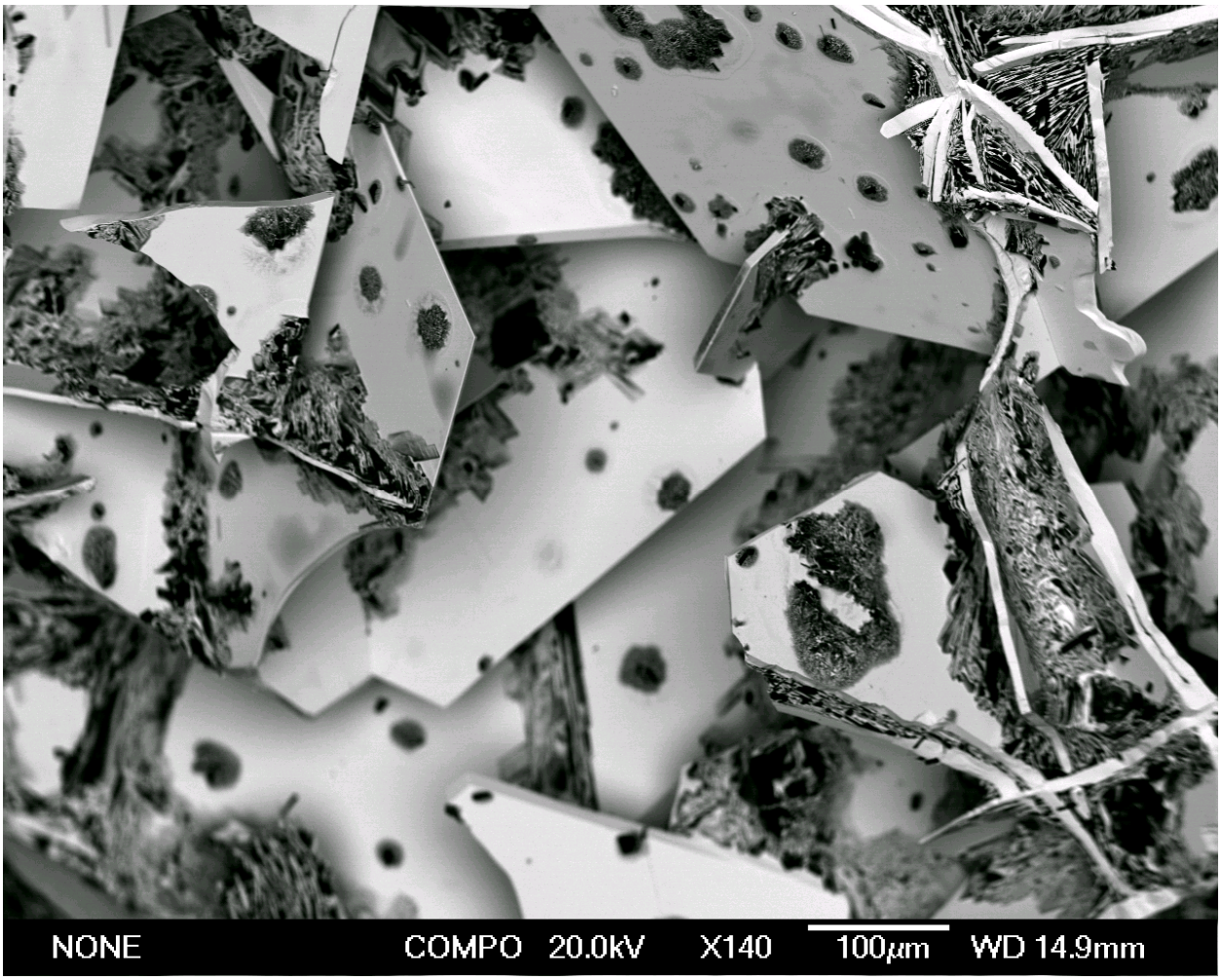

Figure 6.6: Backscattered electron SEM image of a fractured ingot of an arc-melted sample in the ratio W **:** B of 1 **:** 12. Light regions are the tungsten-containing phase.

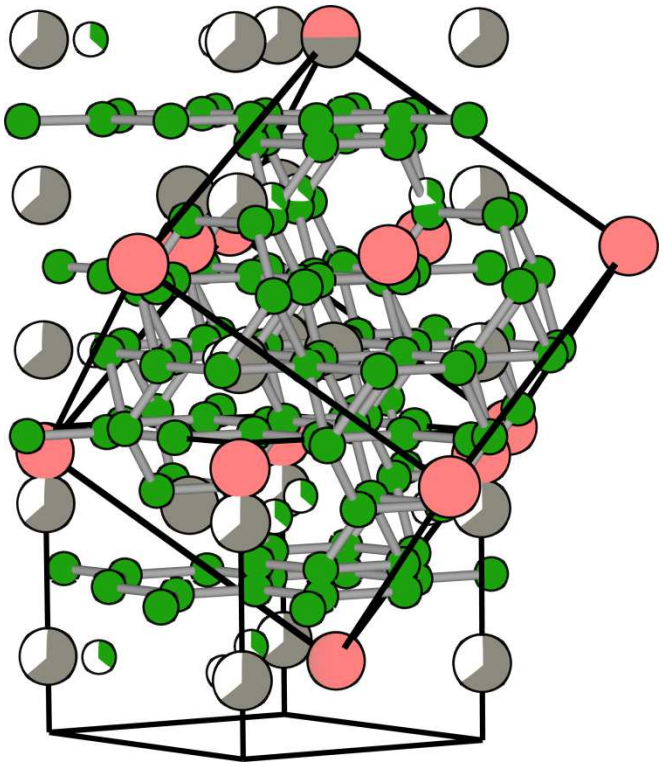

Figure 6.7: Overlay of the UB_{12} structure type on $WB_{4.2}$ showing a close similarity.

Chapter 7

Conclusions

A New Generation of Solid Solutions

Over the past several years we have increasingly focused on the synthesis and properties of tungsten tetraboride and its derivatives.[40,42,248] As mentioned above, the hardness and mechanical properties of WB_4 may be generally enhanced by the formation of solid solutions with neighboring elements (e.g. Cr and Mo, from Group 6 or Ta and Mn from Groups 5 and 7). These solid solutions are universally harder than pure WB_4 and demonstrate significantly different high pressure behavior.[42] A reasonable next goal might be to use chemical methods to more thoroughly understand and control the mechanism(s) causing these changes.

Having an accurate model of WB_4 gives us invaluable insight toward understanding and manipulating the mechanical properties of this compound. Due in part to the partial occupancy of W atoms (Chapter 6), WB_4 is able to accommodate a wide variety of guest atoms. This information might be used to 'tune' the properties of WB_4 with elements having varying valence electron counts and/or atomic sizes. By carefully tailoring a solid solution scheme, guest atoms may replace only the fully occupied tungsten site, only the partially occupied site, or both. It should ideally be possible to demonstrate control over this doping. Furthermore, it may even be possible to undertake the design of new ternary and quaternary compounds based on WB_4 by either replacing the cuboctahedra with metal atoms or, conversely, enhancing the frequency and regularity with which they occur. There are a large number of solute atoms available for this scheme. Here, we will focus our discussion on only a few, particularly

those that are not immediate neighbors of tungsten such as: Ti, Zr, and Hf from Group 4; Fe, Ru and Os from Group 8; and Sc and Y from Group 3.

Structural Stabilization and Manipulation

WB_4 is most readily synthesized from eutectic melts using a large excess of boron (WB_{12}). While this ensures that all of the tungsten precipitates as WB_4, the voluminous, co-formed, *β*-boron complicates subsequent measurements, wastes material, and cannot be feasibly separated *ex-situ* by chemical or mechanical means. Thus, a good first target would be to increase the phase purity, volume fraction, and thus overall mechanical properties of WB_4 by using our structural knowledge to reduce or eliminate the need for excess boron *in-situ*.

Some possible approaches to this follow two general, but related, routes: **(A)** phase stabilization by the formation of select solid solutions, and **(B)** controlled nucleation using a small amount of a lattice-matching phase. The first might be invoked by analogy to the well-known formation of yttria-stabilized cubic zirconia, where yttrium ions partially replace zirconium to hold the oxygen/vacancy lattice in place.[249] Thus, the unique structural elements of WB_4 might be "encouraged" by the addition of secondary metal additives, preventing phase transformation to lower borides. Metals that are known to form or dissolve well in structures containing boron cuboctahedra would be a good place to start in this regard. These are: the rare earth elements of the f-block, as well as scandium, yttrium, and zirconium. Further, by this route one might also anticipate the exciting possibility of the discovery of new, structurally-related, ternary compounds.

Encouraging Polyhedral Boron: Thermodynamic Consideration

Given that WB_4 is a defect structure based on the common AlB_2 iso-type, this might explain its propensity to transform to similarly structured borides under low chemical pressure of boron. However, due to its sub-lattice of systematic tungsten absences, and the co-occupancy of boron cuboctahedra at tungsten positions, a direct analogy can be drawn to the dodecaborides (MB_{12}) of the UB_{12} structure-type. There are only three distinctions between them: (1) WB_4 is hexagonal, while most dodecaborides are cubic; (2) the occurrence of cuboctahedra in MB_{12} structures is one per metal atom whereas it is one for every four metal atoms in WB_4; and (3) the cuboctahedra of WB_4 are randomly distributed. These differences can be rationalized by noting that the formation of dodecaborides containing well-ordered cuboctahedra depends strongly on the radius of the metal atom with Y (1.80 Å)[246] and Zr (1.60 Å)[246] being, respectively, the largest and smallest metal forming them under ambient pressure.[247] In comparison, the radius of W is only 1.39 Å[246]. The dissolution, therefore, of small amounts of larger elements should slightly expand the lattice of WB_4 such that it is thermodynamically easier for the boron cuboctahedra to 'fit' into the structure, which is already known to partially accommodate them. Similar physical rational has already been used to synthesize metastable HfB_{12}.[250] It might be reasonable to first attempt this using the late transition metal Zr and subsequently with the rare-earths (starting with Y) to investigate the extent to which size-mismatch can be accommodated.

Carrying this substitutional chemistry to extremes, it might be further anticipated that the occurrence of polyhedral boron with greater frequency and regularity might lead to 'super-stoichiometric' WB_4 and/or ternary analogues. Indeed, deformations of the MB_{12} structure type are already known, such as $Zr_{1-x}Sc_xB_{12}$; a rhombohedral modification of the "NaCl" dodecaboride structure.[251] Rhombohedral deformations tend to stretch the *c/a* ratio (1:1) of cubic systems toward the 1.63:1 ratio of hexagonal structures, in some cases being an intermediate in phase transformations. With some success in the

dissolution of large metals in WB_4, more 'dodecaboride-like' structural motifs may arise. In this case, the occurrence of cuboctahedra, and therefore the degree of inter-layer bonding, should be enhanced. The maximum super-stoichiometric composition we calculate to be achievable while maintaining a hexagonal parent structure, is approximately MB_9, although UB_{12}-like tungsten-containing ternaries are an interesting possibility.

Lattice Growth by 'Seeding': Kinetic Consideration

When considering only its stacking sequence, WB_4 can be thought of as a layered structure and like many such structures it shows pronounced differences in growth kinetics along its two crystallographic axes. SEM images in Chapter 6 above reveal the plate-like morphology that results from this. We consider this phenomenon to be exacerbated by two factors: a limited number of nucleation sites, and poor stacking in the *c*-direction. It is no coincidence that many hexagonal borides have very similar *a*-axis lattice parameters, while the *c*-axis varies significantly.[252,253] The direction of boron-boron bonding nets constrains the *ab*-plane significantly. It might be possible to take advantage of this regularity to control the nucleation kinetics, and to eventually manipulate the preferred growth orientation.[254,255]

As arc melting is still the most efficient means of synthesizing refractory borides, this technique may still be useful. However, by 'seeding' the melt with low concentrations (≈1-5%) of metals that form borides with higher melting points than WB_4, yet which possess similar lattice parameters in at least one direction, the nucleation of WB_4 could be encouraged by these early-solidifying crystallites. A similar approach has shown some success with metal carbides.[256] Target 'seed' borides worth trying might include TiB_2, TaB_2, and VB_2, which, furthermore, will not cause seeding of WB_2 given the vast structural differences between these borides. The relative success of this approach should be identifiable by the

degree to which excess boron may be removed from the starting compositions while maintaining phase purity, as evaluated by X-ray diffraction.

Moving Forward: Synthesis and Characterization of 'New' Borides

We have previously focused our efforts on the borides of relatively late, and thus heavy, transition metals. While this has led to the creation of a variety of extremely hard borides such as ReB_2 and WB_4, relatively lighter super-hard materials would be useful wherever they might form a structural role, such as in automobile and aerospace components. The density, and thus 'weight', of a family of borides may be reduced by two methods: either by increasing the concentration of boron and/or by substituting lighter elements (Mo, Mn, Cr, etc.) for heavier ones (Os, Re, W, etc.). Moving from transition metal diborides toward tetraborides, we have already taken steps in the first approach.

Lighter Borides

The encouraging results of our previous work on WB_4 solid solutions with Mo, Cr and Mn[42] should provoke some consideration as to how the chemical and mechanical properties might differ in the tetraborides if W is replaced entirely by these elements. Interestingly, all three of these solid-solution forming elements are also able to form their own independent tetraborides.

Both WB_4 and MoB_4 crystallize in the hexagonal system (space group: $P6_3/mmc$), with almost identical lattice parameters.[257,258] However, the atomic weight of Mo (95.96 g/mol) is almost half that of W (183.84 g/mol). It is currently unknown if the hardness of WB_4 and MoB_4 correlates with the difference between the atomic weights of W and Mo because the relative importance of valence electron density versus *total* electron density in determining hardness is still unclear. This relationship should be determined experimentally. Doing so, it may be possible to establish a hardness/structure/atomic

weight correlation trend and further compare it against CrB_4 and MnB_4. Chromium and manganese are even lighter than Mo (Cr = 51.99 and Mn = 54.94 g/mol) and their tetraborides have two different, but related, structures with MnB_4 being a monoclinic distortion (space group: *C2/m*) of the CrB_4 orthorhombic system (space group: *Immm*).

There are several theoretical studies suggesting that all of these tetraborides are super-hard. However, experimental data are scarce. For example, while no experimental data are available, to our knowledge, on the hardness of MoB_4, theoretical calculations using a generalized gradient approximation (GGA) and a local density approximation (LDA) predict hardness values between 37.3-46.2 GPa for this compound.[259–261] These predicted values are close to 43.3 GPa, the Vickers hardness we have measured for WB_4.[40] Since Mo has the same number of valence electrons as W, this might be expected in accordance with our theory of hardness in metal borides.[36] However, we have not yet had the opportunity to experimentally verify our central hypothesis (that hardness should scale directly with the number of valence electrons in iso-structural and iso-valent compounds). A study of MoB_4 may provide such an opportunity. Likewise, in the case of CrB_4 and MnB_4, several theoretical calculations have estimated the hardness of these two compounds as 27.6-48.0 GPa[262–264] and 40.0-49.9 GPa[265–267], respectively. Considering the inconsistencies among all these data and the lack of experimental data on the hardness of these two materials (there appears to be only one reference for CrB_4),[268] a comprehensive experimental study on the synthesis and characterization of these materials seems warranted.

Development of Compaction Techniques for Carbide-Competitive Borides

While the goal of our work has been primarily fundamental in nature, practical demonstrations of the usefulness of super-hard metals in cutting tools remain to be seen, but must be pursued if this work is to

have lasting value. WC-based tools still dominate the world of precision machining in part because the lifetime of WC tools versus their cost is superior to PCD and c-BN tools in most cases.[269] However, the economics of the situation are beginning to change. Greater social and ecological awareness has led the manufacturing industry to examine ways to reduce waste and energy consumption. One increasingly common trend in this direction is the cutting of certain metals without using coolants or lubricants (otherwise treated as waste); a process known as "hard-turning".[270] The extreme stresses and speeds used in this technique demand only the hardest current machine tools; *c*-BN and PCD.[271] As a result, it is mainly used for high value-added products such as superalloys,[272] titanium alloys[273], and the other high-strength alloys[26] of the aerospace and medical industries. In these cases, the cost of tooling is only a very small fraction of the overall cost of materials. Current super-hard tools are too expensive or otherwise unsuited for 'common' use. Thus, if the trend of 'environmentally benign' machining is to become common practice, either the hard tools need to be made cheaper, or the cheap tools made harder. We believe super-hard refractory metal borides provide a solution to both, with a potentially large economic and ecological impact.

Nevertheless, the development of usable tools from these new materials poses many challenges. We have already made significant strides toward controlling chemical composition and synthetic conditions. However, much work remains to be done to control grain sizes, densification behavior, thermal stability, and wettability toward 'cementing' binder phases. Fortunately, there is nearly 100 years of extant research manipulating another 'hard metal': WC.[24] We believe that the metallurgical behavior of our borides is similar enough to pre-existing carbides that we can use this information to help solve some of the "unknowns" standing in the way of developing new tools.

Our current synthetic approach, arc melting, produces polycrystalline ingots with large grains and yields samples only dense enough to be useful for hardness testing and simple characterization. Arc melted

ingots, therefore, will not perform well as tools due to their low fracture toughness and the presence of macroscopic voids. Learning from WC, the solution is obvious; refine the grains to be as small as possible and compact them to their maximum density. The densification may be optimized by applying synthetic techniques to borides that have already been successfully exploited for carbides, such as hot isostatic pressing (HIP) and spark plasma sintering (SPS).[274]

Two approaches toward this end might be attempted: top-down and bottom-up. For the top-down route, WB_4 produced through arc melting can be crushed to a fine powder (<10 μm) by ball milling and then pressed and sintered at elevated temperatures (1600 ºC). For the bottom-up route, phase-pure WB_4 could be produced directly during densification from the elemental powders using either HIP or SPS. Utilizing this second approach, one might anticipate greater control over crystallite size and chemical composition through the variation of parameters such as temperature, pressure, and run duration. With the first approach, however, one should have the advantage of using an already well-established synthetic technique.

One of the greatest advantages of super-hard metals over other super-hard compounds is that tools may be directly created from fully dense pellets using wire-EDM (electric discharge machining). EDM is the shaping or cutting of electrically conductive substances by facilitated ablation of the material through electric discharge (spark) between the work piece and an electrode.[275] EDM allows for efficient cutting and intricate shaping when applied to otherwise difficult-to-form hard materials, and is the method of choice for shaping WC tools. Other super-hard materials, such as *c*-BN and PCD, lack the electrical conductivity needed for EDM. As a proof-of-concept, we have already cut WB_4 ingots using this technique, highlighting this advantage of metal borides. Further work in this regard should be continued.

References

(1) M'guire, J. D. The Stone Hammer and Its Various Uses. *Am. Anthropol.* **1891**, *4*, 301–312.

(2) Gladstone, J. H. On the Transition from the Use of Copper to that of Bronze. *J. Anthropol. Inst. Gt. Britain Irel.* **1897**, *26*, 309.

(3) Hegde, K. T. M. A Model for Understanding Ancient Indian Iron Metallurgy. *Man* **1973**, *8*, 416.

(4) Sherby, O. D.; Wadsworth, J. Ancient Blacksmiths, the Iron Age, Damascus Steels, and Modern Metallurgy. *J. Mater. Process. Technol.* **2001**, *117*, 347–353.

(5) Ashton, T. S. *Iron and Steel in the Industrial Revolution*; Manchester University Press, 1968; Vol. 2.

(6) Diamond, J. M.; Ordunio, D. *Guns, Germs, and Steel*; Norton New York, 1997.

(7) Mathews, J. A. The Steel Age—1876 to 1926. *Ind. Eng. Chem.* **1926**, *18*, 913–914.

(8) Mathews, J. A. "The Electric Furnace and the Alloy Age."*Trans. Electrochem. Soc.* **1932**, *61*, 143.

(9) Rosenberg, N. Technological Change in the Machine Tool Industry, 1840-1910. *J. Econ. Hist.* **1963**, *23*, pp. 414–443.

(10) Exner, H. E. Physical and Chemical Nature of Cemented Carbides. *Int. Mater. Rev. 24*, 149–173.

(11) Ezugwu, E. O. Key Improvements in the Machining of Difficult-to-Cut Aerospace Superalloys. *Int. J. Mach. Tools Manuf.* **2005**, *45*, 1353–1367.

(12) Ortner, H. M.; Ettmayer, P.; Kolaska, H. The History of the Technological Progress of Hardmetals. *Int. J. Refract. Met. Hard Mater.* **2013**, *44*, 148–159.

(13) Allen, C.; Sheen, M.; Williams, J.; Pugsley, V. A. The Wear of Ultrafine WC–Co Hard Metals. *Wear* **2001**, *250*, 604–610.

(14) Srivatsan, T. .; Woods, R.; Petraroli, M.; Sudarshan, T. . An Investigation of the Influence of Powder Particle Size on Microstructure and Hardness of Bulk Samples of Tungsten Carbide. *Powder Technol.* **2002**, *122*, 54–60.

(15) Schubert, W. D.; Neumeister, H.; Kinger, G.; Lux, B. Hardness to Toughness Relationship of Fine-Grained WC-Co Hardmetals. *Int. J. Refract. Met. Hard Mater.* **1998**, *16*, 133–142.

(16) Schubert, W. D.; Bock, A.; Lux, B. General Aspects and Limits of Conventional Ultrafine WC Powder Manufacture and Hard Metal Production. *Int. J. Refract. Met. Hard Mater.* **1995**, *13*, 281–296.

(17) Jia, K.; Fischer, T. E.; Gallois, B. Microstructure, Hardness and Toughness of Nanostructured and Conventional WC-Co Composites. *Nanostructured Mater.* **1998**, *10*, 875–891.

(18) Lee, P. W.; Trudel, Y.; Iacocca, R.; German, R. M.; Ferguson, B. L.; Eisen, W. B.; Moyer, K. Cermets and Cemented Carbides. In *ASM Handbook, Volume 07 - Powder Metal Technologies and Applications*; Madan, D.; Sanderow, H., Eds.; ASM International: Materials Park, Ohio, 1998; pp. 922–940.

(19) Samsonov, G. V.; Voronkin, M. A. Properties of Double Carbides of Titanium and Group Va Metals. *Sov. Powder Metall. Met. Ceram.* **1976**, *15*, 296–299.

(20) Exner, H. E. Physical and Chemical Nature of Cemented Carbides. *Int. Mater. Rev.* **1979**, *24*, 149–173.

(21) Samsonov, G.; Alfintseva, R. Dispersion Strengthening of Refractory metals—A Survey. *Powder Metall. Met. Ceram.* **1972**, *2*, 98–108.

(22) Vepřek, S.; Reiprich, S. A Concept for the Design of Novel Superhard Coatings. *Thin Solid Films* **1995**, *268*, 64–71.

(23) Brookes, K. A. Half a Century of Hardmetals. *Met. Powder Rep.* **1995**, *50*, 22–28.

(24) Spriggs, G. E. A History of Fine Grained Hardmetal. *Int. J. Refract. Met. Hard Mater.* **1995**, *13*, 241–255.

(25) Heath, P. J. Developments in Applications of PCD Tooling. *J. Mater. Process. Technol.* **2001**, *116*, 31–38.

(26) Ezugwu, E. O. Key Improvements in the Machining of Difficult-to-Cut Aerospace Superalloys. *Int. J. Mach. Tools Manuf.* **2005**, *45*, 1353–1367.

(27) Sung, C.-M.; Sung, M. Carbon Nitride and Other Speculative Superhard Materials. *Mater. Chem. Phys.* **1996**, *43*, 1–18.

(28) Cook, M. .; Bossom, P. . Trends and Recent Developments in the Material Manufacture and Cutting Tool Application of Polycrystalline Diamond and Polycrystalline Cubic Boron Nitride. *Int. J. Refract. Met. Hard Mater.* **2000**, *18*, 147–152.

(29) Nabhani, F. Wear Mechanisms of Ultra-Hard Cutting Tools Materials. *J. Mater. Process. Technol.* **2001**, *115*, 402–412.

(30) König, W.; Neises, A. Wear Mechanisms of Ultrahard, Non-Metallic Cutting Materials. *Wear* **1993**, *162-164*, 12–21.

(31) Zeren, M.; Karagöz, Ş. Sintering of Polycrystalline Diamond Cutting Tools. *Mater. Des.* **2007**, *28*, 1055–1058.

(32) Komanduri, R.; Shaw, M. C. Wear of Synthetic Diamond When Grinding Ferrous Metals. *Nature* **1975**, *255*, 211–213.

(33) Heath, P. J. Developments in Applications of PCD Tooling. *J. Mater. Process. Technol.* **2001**, *116*, 31–38.

(34) Jahan, M. P.; Rahman, M.; Wong, Y. S. A Review on the Conventional and Micro-Electrodischarge Machining of Tungsten Carbide. *Int. J. Mach. Tools Manuf.* **2011**, *51*, 837–858.

(35) Gilman, J. J.; Cumberland, R. W.; Kaner, R. B. Design of Hard Crystals. *Int. J. Refract. Met. Hard Mater.* **2006**, *24*, 1–5.

(36) Kaner, R. B.; Gilman, J. J.; Tolbert, S. H. Designing Superhard Materials. *Science (80-.).* **2005**, *308*, 1268–1269.

(37) Levine, J. B.; Tolbert, S. H.; Kaner, R. B. Advancements in the Search for Superhard Ultra-Incompressible Metal Borides. *Adv. Funct. Mater.* **2009**, *19*, 3519–3533.

(38) Cumberland, R. W.; Weinberger, M. B.; Gilman, J. J.; Clark, S. M.; Tolbert, S. H.; Kaner, R. B. Osmium Diboride, An Ultra-Incompressible, Hard Material. *J. Am. Chem. Soc.* **2005**, *127*, 7264–7265.

(39) Chung, H.-Y.; Weinberger, M. B.; Levine, J. B.; Kavner, A.; Yang, J.-M.; Tolbert, S. H.; Kaner, R. B. Synthesis of Ultra-Incompressible Superhard Rhenium Diboride at Ambient Pressure. *Science (80-.).* **2007**, *316*, 436–439.

(40) Mohammadi, R.; Lech, A. T.; Xie, M.; Weaver, B. E.; Yeung, M. T.; Tolbert, S. H.; Kaner, R. B. Tungsten Tetraboride, an Inexpensive Superhard Material. *Proc. Natl. Acad. Sci.* **2011**, *108*, 10958–10962.

(41) Levine, J. B.; Nguyen, S. L.; Rasool, H. I.; Wright, J. A.; Brown, S. E.; Kaner, R. B. Preparation and Properties of Metallic, Superhard Rhenium Diboride Crystals. *J. Am. Chem. Soc.* **2008**, *130*, 16953–16958.

(42) Mohammadi, R.; Xie, M.; Lech, A. T.; Turner, C. L.; Kavner, A.; Tolbert, S. H.; Kaner, R. B. Toward Inexpensive Superhard Materials: Tungsten Tetraboride-Based Solid Solutions. *J. Am. Chem. Soc.* **2012**, *134*, 20660–20668.

(43) Vegard, L. Die Konstitution Der Mischkristalle Und Die Raumf**?**llung Der Atome. *Zeitschrift f**?**r Phys.* **1921**, *5*, 17–26.

(44) Hu, Q. M.; Kádas, K.; Hogmark, S.; Yang, R.; Johansson, B.; Vitos, L. Predicting Hardness of Covalent⁄ionic Solid Solution from First-Principles Theory. *Appl. Phys. Lett.* **2007**, *91*, 121918.

(45) Gao, F.; He, J.; Wu, E.; Liu, S.; Yu, D.; Li, D.; Zhang, S.; Tian, Y. Hardness of Covalent Crystals. *Phys. Rev. Lett.* **2003**, *91*, 15502.

(46) Brazhkin, V. V.; Lyapin, A. G.; Hemley, R. J. Harder than Diamond: Dreams and Reality. *Philos. Mag. A* **2002**, *82*, 231–253.

(47) Cynn, H.; Klepeis, J.; Yoo, C.-S.; Young, D. Osmium Has the Lowest Experimentally Determined Compressibility. *Phys. Rev. Lett.* **2002**, *88*, 135701.

(48) Occelli, F.; Farber, D.; Badro, J.; Aracne, C.; Teter, D.; Hanfland, M.; Canny, B.; Couzinet, B. Experimental Evidence for a High-Pressure Isostructural Phase Transition in Osmium. *Phys. Rev. Lett.* **2004**, *93*, 095502.

(49) Kenichi, T. Bulk Modulus of Osmium: High-Pressure Powder X-Ray Diffraction Experiments under Quasihydrostatic Conditions. *Phys. Rev. B* **2004**, *70*, 012101.

(50) Aleksandrov, I. V; Goncharov, A. F.; Zisman, A. N.; Stishov, S. M. Diamond at High Pressures: Raman Scattering of Light, Equation of State, and High-Pressure Scale. *Sov. Phys. - JETP* **1987**, *66*, 384–390.

(51) Cumberland, R. R. W.; Weinberger, M. B.; Gilman, J. J.; Clark, S. M.; Tolbert, S. H.; Kaner, R. B. Osmium Diboride, An Ultra-Incompressible, Hard Material. *J. Am. Chem. Soc.* **2005**, *127*, 7264–7265.

(52) Chung, H.-Y.; Weinberger, M. B.; Levine, J. B.; Kavner, A.; Yang, J.-M.; Tolbert, S. H.; Kaner, R. B.; Cumberland, R. W. Synthesis of Ultra-Incompressible Superhard Rhenium Diboride at Ambient Pressure. *Science (80-.).* **2007**, *316*, 436–439.

(53) Levine, J. B.; Nguyen, S. L.; Rasool, H. I.; Wright, J. A.; Brown, S. E.; Kaner, R. B. Preparation and Properties of Metallic, Superhard Rhenium Diboride Crystals. *J. Am. Chem. Soc.* **2008**, *130*, 16953–16958.

(54) Burkhardt, U. On the Electronic and Structural Properties of Aluminum Diboride Al0.9B2. *J. Solid State Chem.* **2004**, *177*, 389–394.

(55) Sevastyanova, L. G.; Gulish, O. K.; Stupnikov, V. A.; Genchel, V. K.; Kravchenko, O. V.; Bulychev, B. M.; Lunin, R. A.; Tarasov, V. P. Structure and Properties of Solid Solutions in the Mg - Al - B System. *Cent. Eur. J. Phys.* **2011**, *10*, 189–196.

(56) Portnoi, K. I.; Romashov, V. M.; Romanovich, I. V. Diagram of State of the Chromium-Boron System. *Sov. Powder Metall. Met. Ceram.* **1969**, *8*, 298–302.

(57) Hanson, B. D.; Mahning, M.; Toth, L. E. Low Temperature Heat Capacities of Transition Metal Borides. *Zeitschrift Naturforsch. Tl. A* **1971**, *26*, 739.

(58) Brasse, M.; Chioncel, L.; Kuneš, J.; Bauer, A.; Regnat, A.; Blum, C. G. F.; Wurmehl, S.; Pfleiderer, C.; Wilde, M. A.; Grundler, D. De Haas–van Alphen Effect and Fermi Surface Properties of Single-Crystal CrB2. *Phys. Rev. B* **2013**, *88*, 155138.

(59) Lugscheider, E.; Knotek, O.; Reimann, H. Das Dreistoffsystem Nickel - Chrom - Bor. *Monatshefte f*[illegible]*r Chemie* **1974**, *105*, 80–90.

(60) Okada, S.; Kudou, K.; Iizumi, K.; Kudaka, K.; Higashi, I.; Lundström, T. Single-Crystal Growth and Properties of CrB, Cr3B4, Cr2B3 and CrB2 from High-Temperature Aluminum Solutions. *J. Cryst. Growth* **1996**, *166*, 429–435.

(61) KLESNAR, H. P.; ROGL, P. Phase Relations in the Ternary Systems Rare-Earth Metal (RE)-Boron-Nitrogen, Where RE=Tb, Dy, Ho, Er, Tm, Lu, Sc, and Y. *High Temp. High Press. 22*, 453–457.

(62) Will, G.; Lehmann, V.; Buschow, K. H. J. Neutron Diffraction Investigation of Ferromagnetic TbB2. *J. Magn. Magn. Mater.* **1977**, *6*, 22–23.

(63) Will, G.; Lehmann, V.; Buschow, K. H. J. Magnetic Properties and Neutron Diffraction of TbB_2. **1978**.

(64) Castellano, R. N. Crystal Growth of TmB2 and ErB2. *Mater. Res. Bull.* **1972**, *7*, 261–265.

(65) Cannon, J. F.; Cannon, D. M.; Tracy Hall, H. High Pressure Syntheses of SmB2 and GdB12. *J. Less Common Met.* **1977**, *56*, 83–90.

(66) Kuz'ma, Y. B.; Telegus, V. S.; Marko, M. A. Phase Equilibria in the Systems Hafnium-Niobium-Boron and Tantalum-Chromium-Boron. *Sov. Powder Metall. Met. Ceram.* **1972**, *11*, 308–312.

(67) Rudy, E.; Benesovsky, F. Untersuchungen in Den Systemen: Hafnium - Bor - Stickstof Und Zirkonium - Bor - Stickstoff. *Monatshefte f*[illegible]*r Chemie* **1961**, *92*, 415–441.

(68) Post, B.; Glaser, F. W.; Moskowitz, D. Transition Metal Diborides. *Acta Metall.* **1954**, *2*, 20–25.

(69) Holleck, H. Legierungsverhalten von HfB2 Mit Uran- Und Übergangsmetalldiboriden. *J. Nucl. Mater.* **1967**, *21*, 14–20.

(70) Deligoz, E.; Ozisik, H.; Colakoglu, K.; Surucu, G.; Ciftci, Y. O. Mechanical and Phonon Properties of the Superhard LuB2, LuB4, and LuB12 Compounds. *J. Alloys Compd.* **2011**, *509*, 1711–1715.

(71) Aronsson, B.; Templeton, D. H.; Rundqvist, S.; Varde, E.; Westin, G. A Note on the Compositions and Crystal Structures of MnB2, Mn3Si, Mn5Si3, and FeSi2. *Acta Chem. Scand.* **1960**, *14*, 1414–1418.

(72) Cely, A.; Tergenius, L.-E.; Lundstrom, T. Microhardness Measurements and Phase Analytical Studies in the Mn - B System. *J. Less Common Met.* **1978**, *61*, 193–198.

(73) Klesnar, H.; Aselage, T. L.; Morosin, B.; Kwei, G. H. The Diboride Compounds of Molybdenum: MoB2−x and Mo2B5−y. *J. Alloys Compd.* **1996**, *241*, 180–186.

(74) Storms, E.; Mueller, B. Phase Relations and Thermodynamic Properties of Transition Metal Borides. I. The Molybdenum-Boron System and Elemental Boron. *J. Phys. Chem.* **1977**, *81*, 318–324.

(75) Wittmann, A.; Nowotny, H.; Boller, H. Ein Beitrag Zum Dreistoff Titan-Molybdaen-Bor. *Monatshefte f*[illegible]*r Chemie* **1960**, *91*, 608–615.

(76) Frotscher, M.; Klein, W.; Bauer, J.; Fang, C.-M.; Halet, J.-F.; Senyshyn, A.; Baehtz, C.; Albert, B. M2B5 or M2B4? A Reinvestigation of the Mo/B and W/B System. *Zeitschrift für Anorg. und Allg. Chemie* **2007**, *633*, 2626–2630.

(77) Otani, S.; Korsukova, M. .; Mitsuhashi, T. Floating Zone Growth and High-Temperature Hardness of NbB2 and TaB2 Single Crystals. *J. Cryst. Growth* **1998**, *194*, 430–433.

(78) Andersson, L.-H.; Kiessling, R.; Lindstedt, G.; Kinell, P.-O. Investigations on the Binary Systems of Boron with Chromium, Columbium, Nickel, and Thorium, Including a Discussion of the Phase "TiB" in the Titanium-Boron System. *Acta Chem. Scand.* **1950**, *4*, 160–164.

(79) Levchenko, G.; Lyashchenko, A.; Baumer, V.; Evdokimova, A.; Filippov, V.; Paderno, Y.; Shitsevalova, N. Preparation and Some Properties of ScB2 Single Crystals. *J. Solid State Chem.* **2006**, *179*, 2949–2953.

(80) Okada, S.; Kudou, K.; Higashi, I.; Lundström, T. Single Crystals of TaB, Ta5B6, Ta3B4 and TAB2, as Obtained from High-Temperature Metal Solutions, and Their Properties. *J. Cryst. Growth* **1993**, *128*, 1120–1124.

(81) Kiessling, R.; Christensen, S. Å. K.; Sillén, L. G. The Borides of Tantalum. *Acta Chem. Scand.* **1949**, *3*, 603–615.

(82) Otani, S.; Ishizawa, Y. Preparation of TiB2 Single Crystals by the Floating Zone Method. *J. Cryst. Growth* **1994**, *140*, 451–453.

(83) Higashi, I.; Takahashi, Y.; Atoda, T. Crystal Growth of Borides and Carbides of Transition Metals from Molten Aluminum Solutions. *J. Cryst. Growth* **1976**, *33*, 207–211.

(84) Bulfon, C.; Leithe-Jasper, A.; Sassik, H.; Rogl, P. Microhardness of Czochralski-Grown Single Crystals of VB2. *J. Solid State Chem.* **1997**, *133*, 113–116.

(85) Nakano, K.; Nakamura, K.; Kumashiro, Y.; Sakuma, E. Single Crystal Growth of VB2 and NbB2. *J. Cryst. Growth* **1981**, *52*, 602–608.

(86) Lukačević, I.; Gupta, S. K. Nature of Low Compressibility and Anisotropic Elasticity in YbB2. *J. Alloys Compd.* **2014**, *597*, 148–154.

(87) Veremchuk, I. V.; Chaban, N. F.; Davydov, V. N.; Kuz?ma, Y. B. 1070-K Section of the Yb - Co - B Phase Diagram. *Inorg. Mater.* **2004**, *40*, 1301–1306.

(88) Spear, K. E. Chemical Bonding in AlB2-Type Borides. *J. Less Common Met.* **1976**, *47*, 195–201.

(89) Kuz'ma, Y. B.; Lakh, V. I.; Stadnyk, B. I.; Voroshilov, Y. V. Phase Equilibria in the Systems Zr - Re - B and W - Re - B. *Sov. Powder Metall. Met. Ceram.* **1968**, *7*, 462–466.

(90) Bsenko, L.; Lundström, T. The High-Temperature Hardness of ZrB2 and HfB2. *J. Less Common Met.* **1974**, *34*, 273–278.

(91) Ozisik, H.; Deligoz, E.; Colakoglu, K.; Surucu, G. Structural and Mechanical Stability of Rare-Earth Diborides. *Chinese Phys. B* **2013**, *22*, 046202.

(92) Nishihara, Y.; Tokumoto, M.; Yamaguchi, Y.; Ogawa, S. Magneto-Volume Effect of the Interant-Electron Antiferromagnet CrB2. *J. Phys. Soc. Japan* **1987**, *56*, 1562–1567.

(93) Rieger, W.; Nowotny, H.; Benesovsky, F. Ueber Einige Komplexboride von Uebergangsmetallen. *Monatshefte f[illegible]r Chemie* **1965**, *96*, 844–851.

(94) Knyshev, E. A.; Novgorodtsev, V. M.; Plyshevski, U. S.; Kobyakov, V. A.; Stepanova, Z. G.; Svistunov, V. V.; Becketov, A. R. Synthesis of Transition Metal Borides and Their Properties. *J. Less Common Met.* **1976**, *47*, 273–278.

(95) Samsonov, G. V.; Goryachev, Y. M.; Kovenskaya, B. A.; Tel'nikov, E. Y. The Electronic Spectrum and Physical Properties of Titanium, Vanadium, and Chromium Diborides. *Sov. Phys. J.* **1972**, *15*, 809–813.

(96) Kislyi, P. S.; L'vov, S. N.; Nemchenko, V. F.; Samsonov, G. V. Physical Properties of the Boride Phases of Chromium. *Sov. Powder Metall. Met. Ceram.* **1964**, *1*, 441–443.

(97) Tao, Q.; Zhao, X.; Chen, Y.; Li, J. J.; Li, Q.; Ma, Y.; Cui, T.; Zhu, P.; Wang, X. Enhanced Vickers Hardness by Quasi-3D Boron Network in MoB2. *RSC Adv.* **2013**, *3*, 18317.

(98) Samsonov, G. V.; Stasovskaya, V. V. Correlation of Microhardness and Microbrittleness of Refractory Compounds with Their Electronic Structure. *Sov. Powder Metall. Met. Ceram.* **1966**, *5*, 989–992.

(99) *Boron and Refractory Borides*; Matkovich, V. I., Ed.; Springer Berlin Heidelberg: Berlin, Heidelberg, 1977.

(100) Mohammadi, R.; Kaner, R. B. Superhard Materials. In *Encyclopedia of Inorganic and Bioinorganic Chemistry*; Scott, R. A., Ed.; John Wiley & Sons, Ltd: Chichester, UK, 2011.

(101) Weinberger, M. B.; Levine, J. B.; Chung, H.; Cumberland, R. W.; Rasool, H. I.; Yang, J.-M.; Kaner, R. B.; Tolbert, S. H. Incompressibility and Hardness of Solid Solution Transition Metal Diborides: Os1−xRuxB2. *Chem. Mater.* **2009**, *21*, 1915–1921.

(102) Gilman, J. J.; Cumberland, R. W.; Kaner, R. B. Design of Hard Crystals. *Int. J. Refract. Met. Hard Mater.* **2006**, *24*, 1–5.

(103) Kaner, R. B.; Gilman, J. J.; Tolbert, S. H. Designing Superhard Materials. *Science (80-.).* **2005**, *308*, 1268–1269.

(104) Albert, B.; Hillebrecht, H. Boron: Elementary Challenge for Experimenters and Theoreticians. *Angew. Chemie Int. Ed.* **2009**, *48*, 8640–8668.

(105) Fehlner, T. P. Molecular Models of Solid State Metal Boride Structures. *J. Solid State Chem.* **2000**, *154*, 110–113.

(106) Mohammadi, R.; Xie, M.; Lech, A. T.; Turner, C. L.; Kavner, A.; Tolbert, S. H.; Kaner, R. B.; Tolbert, H. Toward Inexpensive Superhard Materials: Tungsten Tetraboride-Based Solid Solutions. *J. Am. Chem. Soc.* **2012**, *134*, 20660–20668.

(107) Mohammadi, R.; Lech, A. T.; Xie, M.; Weaver, B. E.; Yeung, M. T.; Tolbert, S. H.; Kaner, R. B. Tungsten Tetraboride, an Inexpensive Superhard Material. *Proc. Natl. Acad. Sci. U. S. A.* **2011**, *108*, 10958–10962.

(108) Shibuya, M.; Kawata, M.; Ohyanagi, M.; Munir, Z. A. Titanium Diboride–Tungsten Diboride Solid Solutions Formed by Induction-Field-Activated Combustion Synthesis. *J. Am. Ceram. Soc.* **2003**, *86*, 706–710.

(109) Rogl, P.; Nowotny, H.; Benesovsky, F. Komplexboride Mit ReB2-Struktur. *Monatshefte f**r Chemie* **1970**, *101*, 27–31.

(110) Rogl, P.; Nowotny, H.; Benesovsky, F. Tern  re Komplexboride in Den Dreistoffen: {Mo, W} - {Ru, Os} - B Und W - Ir - B. *Monatshefte f**r Chemie* **1970**, *101*, 850–854.

(111) Rogl, P.; Rudy, E. New Complex Borides with ReB2- and Mo2IrB2-Type Structure. *J. Solid State Chem.* **1978**, *24*, 175–181.

(112) Zeiringer, I.; Rogl, P.; Grytsiv, A.; Polt, J.; Bauer, E.; Giester, G. Crystal Structure of W1−x B3 and Phase Equilibria in the Boron-Rich Part of the Systems Mo-Rh-B and W-{Ru,Os,Rh,Ir,Ni,Pd,Pt}-B. *J. Phase Equilibria Diffus.* **2014**.

(113) Lin, F.; Wu, K.; He, J.; Sa, R.; Li, Q.; Wei, Y. Mixed-Metal Effects on Ultra-Incompressible Metal Diborides: Density Functional Computations. *Chem. Phys. Lett.* **2010**, *494*, 31–36.

(114) Wang, Y. X. Elastic and Electronic Properties of TcB2 and Superhard ReB2: First-Principles Calculations. *Appl. Phys. Lett.* **2007**, *91*, 101904.

(115) Šimůnek, A. Anisotropy of Hardness from First Principles: The Cases of ReB2 and OsB2. *Phys. Rev. B* **2009**, *80*, 060103.

(116) Hao, X.; Xu, Y.; Wu, Z.; Zhou, D.; Liu, X.; Cao, X.; Meng, J. Low-Compressibility and Hard Materials ReB2 and WB2: Prediction from First-Principles Study. *Phys. Rev. B* **2006**, *74*, 224112.

(117) Aydin, S.; Simsek, M. First-Principles Calculations of MnB2, TcB2, and ReB2 within the ReB2-Type Structure. *Phys. Rev. B* **2009**, *80*, 134107.

(118) Lazar, P.; Chen, X.-Q.; Podloucky, R. First-Principles Modeling of Hardness in Transition-Metal Diborides. *Phys. Rev. B* **2009**, *80*, 12103.

(119) Zhong, M.-M.; Kuang, X.-Y.; Wang, Z.-H.; Shao, P.; Ding, L.-P.; Huang, X.-F. Phase Stability, Physical Properties of Rhenium Diboride under High Pressure and the Effect of Metallic Bonding on Its Hardness. *J. Alloys Compd.* **2013**, *581*, 206–212.

(120) LIANG, Y.; LI, A.; ZHAO, J.; ZHANG, W. DESIGNING SUPERHARD MATERIALS BY INCORPORATING BORON INTO HEAVY TRANSITION METALS. *Mod. Phys. Lett. B* **2009**, *23*, 1281–1290.

(121) Zhou, W.; Wu, H.; Yildirim, T. Electronic, Dynamical, and Thermal Properties of Ultra-Incompressible Superhard Rhenium Diboride: A Combined First-Principles and Neutron Scattering Study. *Phys. Rev. B* **2007**, *76*, 184113.

(122) Chen, W.; Jiang, J. Z. Elastic and Electronic Properties of Low Compressible 4d Transition Metal Diborides: First Principles Calculations. *Solid State Commun.* **2010**, *150*, 2093–2096.

(123) Soto, G.; Moreno-Armenta, M. G.; Reyes-Serrato, A. Study on the Formation of Rhenium Borides by Density Functional Calculations. *Comput. Mater. Sci.* **2008**, *44*, 628–634.

(124) Zhong, M.-M.; Kuang, X.; Wang, Z.-H.; Shao, P.; Ding, L.-P.; Huang, X.-F. Phase Stability , Physical Properties , and Hardness of Transition- Metal Diborides MB2 (M = Tc , W , Re , and Os): First-Principles Investigations. *J. Phys. Chem. C* **2013**, *2*, 10643–10652.

(125) Tu, Y.; Wang, Y. First-Principles Study of the Elastic Properties of OsxW1−xB2 and RexW1−xB2 and Alloys. *Solid State Commun.* **2011**, *151*, 238–241.

(126) Tian, Y.; Xu, B.; Zhao, Z. Microscopic Theory of Hardness and Design of Novel Superhard Crystals. *Int. J. Refract. Met. Hard Mater.* **2012**, *33*, 93–106.

(127) Gao, F. M.; Gao, L. H. Microscopic Models of Hardness. *J. Superhard Mater.* **2010**, *32*, 148–166.

(128) Šimůnek, A. How to Estimate Hardness of Crystals on a Pocket Calculator. *Phys. Rev. B* **2007**, *75*, 172108.

(129) Chen, X.-Q.; Fu, C.; Krčmar, M.; Painter, G. Electronic and Structural Origin of Ultraincompressibility of 5d Transition-Metal Diborides MB2 (M=W, Re, Os). *Phys. Rev. Lett.* **2008**, *100*, 196403.

(130) Du, X. P.; Wang, Y. X. Ab Initio Study of Os0.5W0.5B2, Re0.5W0.5B2, and Os0.5Re0.5B2 with High Shear Modulus. *Phys. Status Solidi - Rapid Res. Lett.* **2009**, *3*, 106–108.

(131) Ivanovskii, A. L. Mechanical and Electronic Properties of Diborides of Transition 3d–5d Metals from First Principles: Toward Search of Novel Ultra-Incompressible and Superhard Materials. *Prog. Mater. Sci.* **2012**, *57*, 184–228.

(132) Hölzer, G.; Fritsch, M.; Deutsch, M.; Härtwig, J.; Förster, E. Kα{1,2} and Kβ{1,3} X-Ray Emission Lines of the 3d Transition Metals. *Phys. Rev. A* **1997**, *56*, 4554–4568.

(133) Toby, B. H. EXPGUI , a Graphical User Interface for GSAS. *J. Appl. Crystallogr.* **2001**, *34*, 210–213.

(134) Larson, A. C.; Von Dreele, R. B. General Structure Analysis System (GSAS). *Los Alamos Natl. Lab. Rep.* **2000**.

(135) Oliver, W. C.; Pharr, G. M. An Improved Technique for Determining Hardness and Elastic Modulus Using Load and Displacement Sensing Indentation Experiments. *J. Mater. Res.* **2011**, *7*, 1564–1583.

(136) Frotscher, M.; Hölzel, M.; Albert, B. Crystal Structures of the Metal Diborides ReB2, RuB2, and OsB2 from Neutron Powder Diffraction. *Zeitschrift für Anorg. und Allg. Chemie* **2010**, *636*, 1783–1786.

(137) Wood, R. M. The Lattice Constants of High Purity Alpha Titanium. *Proc. Phys. Soc.* **1962**, *80*, 783–786.

(138) Deligoz, E.; Colakoglu, K.; Ciftci, Y. O. Lattice Dynamical Properties of ScB2, TiB2, and VB2 Compounds. *Solid State Commun.* **2009**, *149*, 1843–1848.

(139) Swanson, H. *Standard X-Ray Diffraction Powder Patterns. Howard E. Swanson, Ruth K. Fuyat and George M. Ugrinic.*; U.S. Government printing office: Washington, 1954.

(140) Hume-Rothery, W. CXXII. Metallic Carbides and Nitrides of the Type MX. *Philos. Mag. Ser. 7* **1953**, *44*, 1154–1160.

(141) Pauling, L. Atomic Radii and Interatomic Distances in Metals. *J. Am. Chem. Soc.* **1947**, *69*, 542–553.

(142) Rundle, R. E. A New Interpretation of Interstitial Compounds–metallic Carbides, Nitrides and Oxides of Composition MX. *Acta Crystallogr.* **1948**, *1*, 180–187.

(143) Wang, J.; Wang, Y.-J. Mechanical and Electronic Properties of 5d Transition Metal Diborides MB2 (M=Re, W, Os, Ru). *J. Appl. Phys.* **2009**, *105*, 083539.

(144) Okada, S.; Kudou, K.; Lundström, T. Preparations and Some Properties of W2B, Δ -WB and WB2 Crystals from High-Temperature Metal Solutions. *Jpn. J. Appl. Phys.* **1995**, *34*, 226–231.

(145) Levine, J. B.; Betts, J. B.; Garrett, J. D.; Guo, S. Q.; Eng, J. T.; Migliori, A.; Kaner, R. B. Full Elastic Tensor of a Crystal of the Superhard Compound ReB2. *Acta Mater.* **2010**, *58*, 1530–1535.

(146) Suzuki, Y.; Levine, J. B.; Migliori, A.; Garrett, J. D.; Kaner, R. B.; Fanelli, V. R.; Betts, J. B. Rhenium Diboride's Monocrystal Elastic Constants, 308 to 5 K. *J. Acoust. Soc. Am.* **2010**, *127*, 2797–2801.

(147) Chung, H.-Y.; Weinberger, M. B.; Yang, J.-M.; Tolbert, S. H.; Kaner, R. B. Correlation between Hardness and Elastic Moduli of the Ultraincompressible Transition Metal Diborides RuB2, OsB2, and ReB2. *Appl. Phys. Lett.* **2008**, *92*, 261904.

(148) Teter, D. M. Computational Alchemy: The Search for New Superhard Materials. *MRS Bull.* **1998**, *23*, 22–27.

(149) Ivanovskii, a. L. Microhardness of Compounds of Rhenium with Boron, Carbon, and Nitrogen. *J. Superhard Mater.* **2012**, *34*, 75–80.

(150) Chung, H.-Y.; Yang, J.-M.; Tolbert, S. H.; Kaner, R. B. Anisotropic Mechanical Properties of Ultra-Incompressible, Hard Osmium Diboride. *J. Mater. Res.* **2011**, *23*, 1797–1801.

(151) Tkachev, S. N.; Levine, J. B.; Kisliuk, A.; Sokolov, A. P.; Guo, S.; Eng, J. T.; Kaner, R. B. Shear Modulus of Polycrystalline Rhenium Diboride Determined from Surface Brillouin Spectroscopy. *Adv. Mater.* **2009**, *21*, 4284–4286.

(152) Woods, H. P.; Wawner F. E., J.; Fox, B. G. B.; Wawner, F. Tungsten Diboride: Preparation and Structure. *Science (80-.).* **1966**, *151*, p. 75.

(153) Otani, S.; Ishizawa, Y. Preparation of WB2−x Single Crystals by the Floating Zone Method. *J. Cryst. Growth* **1995**, *154*, 81–84.

(154) Romans, P. a.; Krug, M. P. Composition and Crystallographic Data for the Highest Boride of Tungsten. *Acta Crystallogr.* **1966**, *20*, 313–315.

(155) Bodrova, L. G.; Koval'chenko, M. S.; Serebryakova, T. I. Preparation of Tungsten Tetraboride. *Sov. Powder Metall. Met. Ceram.* **1974**, *13*, 1–3.

(156) Itoh, H.; Matsudaira, T.; Naka, S.; Hamamoto, H.; Obayashi, M. Formation Process of Tungsten Borides by Solid State Reaction between Tungsten and Amorphous Boron. *J. Mater. Sci.* **1987**, *22*, 2811–2815.

(157) Gu, Q.; Krauss, G. Gã¼.; Steurer, W. Transition Metal Borides: Superhard versus Ultra-Incompressible. *Adv. Mater.* **2008**, *20*, 3620–3626.

(158) Levine, J. B.; Tolbert, S. H.; Kaner, R. B. Advancements in the Search for Superhard Ultra-Incompressible Metal Borides. *Adv. Funct. Mater.* **2009**, *19*, 3519–3533.

(159) Chung, H.-Y. H.-Y.; Weinberger, M. B.; Levine, J. B.; Cumberland, R. W.; Kavner, A.; Yang, J.-M. J.-M.; Tolbert, S. H.; Kaner, R. B. Response to Comment on "Synthesis of Ultra-Incompressible Superhard Rhenium Diboride at Ambient Pressure."*Science (80-.).* **2007**, *318*, 1550d–1550d.

(160) Duschanek, H.; Rogl, P. Critical Assessment and Thermodynamic Calculation of the Binary System Boron-Tungsten (B-W). *J. Phase Equilibria* **1995**, *16*, 150–161.

(161) Dieter, G. E. *Mechanical Metallurgy*; MCGRAW-HILL Higher Education, 1988; p. 751.

(162) Vepřek, S.; Veprek, S. The Search for Novel, Superhard Materials. *J. Vac. Sci. Technol. A Vacuum, Surfaces, Film.* **1999**, *17*, 2401.

(163) Jenkins, R.; Fawcett, T. G.; Smith, D. K.; Visser, J. W.; Morris, M. C.; Frevel, L. K. JCPDS — International Centre for Diffraction Data Sample Preparation Methods in X-Ray Powder Diffraction. *Powder Diffr.* **2013**, *1*, 51–63.

(164) Wang, M.; Li, Y.; Cui, T.; Ma, Y.; Zou, G. Origin of Hardness in WB4 and Its Implications for ReB4, TaB4, MoB4, TcB4, and OsB4. *Appl. Phys. Lett.* **2008**, *93*, 101905.

(165) Nix, W. D.; Gao, H. Indentation Size Effects in Crystalline Materials: A Law for Strain Gradient Plasticity. *J. Mech. Phys. Solids* **1998**, *46*, 411–425.

(166) Li, H.; Ghosh, A.; Han, Y. H.; Bradt, R. C. The Frictional Component of the Indentation Size Effect in Low Load Microhardness Testing. *J. Mater. Res.* **2011**, *8*, 1028–1032.

(167) Bull, S. J.; Page, T. F.; Yoffe, E. H. An Explanation of the Indentation Size Effect in Ceramics. *Philos. Mag. Lett.* **1989**, *59*, 281–288.

(168) Ren, X. J.; Hooper, R. M.; Griffiths, C.; Henshall, J. L. Indentation Size Effect in Ceramics: Correlation with H/E. *J. Mater. Sci. Lett.* **2003**, *22*, 1105–1106.

(169) Lee, H. C.; Gurland, J. Hardness and Deformation of Cemented Tungsten Carbide. *Mater. Sci. Eng.* **1978**, *33*, 125–133.

(170) Zhao, J.; Holland, T.; Unuvar, C.; Munir, Z. A. Sparking Plasma Sintering of Nanometric Tungsten Carbide. *Int. J. Refract. Met. Hard Mater.* **2009**, *27*, 130–139.

(171) Taniguchi, T.; Akaishi, M.; Yamaoka, S. Mechanical Properties of Polycrystalline Translucent Cubic Boron Nitride as Characterized by the Vickers Indentation Method. *J. Am. Ceram. Soc.* **1996**, *79*, 547–549.

(172) He, D.; Zhao, Y.; Daemen, L.; Qian, J.; Shen, T. D.; Zerda, T. W. Boron Suboxide: As Hard as Cubic Boron Nitride. *Appl. Phys. Lett.* **2002**, *81*, 643.

(173) Solozhenko, V. L.; Andrault, D.; Fiquet, G.; Mezouar, M.; Rubie, D. C. Synthesis of Superhard Cubic BC2N. *Appl. Phys. Lett.* **2001**, *78*, 1385.

(174) Tse, J.; Klug, D.; Uehara, K.; Li, Z.; Haines, J.; Léger, J. Elastic Properties of Potential Superhard Phases of RuO2. *Phys. Rev. B* **2000**, *61*, 10029–10034.

(175) Zerr, A.; Miehe, G.; Riedel, R. Synthesis of Cubic Zirconium and Hafnium Nitride Having Th3P4 Structure. *Nat. Mater.* **2003**, *2*, 185–189.

(176) Stone, D. S. Hardness and Elastic Modulus of TiN Based on Continuous Indentation Technique and New Correlation. *J. Vac. Sci. Technol. A Vacuum, Surfaces, Film.* **1991**, *9*, 2543.

(177) Yang, J.; Sun, H.; Chen, C. Is Osmium Diboride an Ultra-Hard Material? *J. Am. Chem. Soc.* **2008**, *130*, 7200–7201.

(178) Liu, C.; Peng, F.; Tan, N.; Liu, J.; Li, F.; Qin, J.; Wang, J.; Wang, Q.; He, D. Low-Compressibility of Tungsten Tetraboride: A High Pressure X-Ray Diffraction Study. *High Press. Res.* **2011**, *31*, 275–282.

(179) Klotz, S.; Chervin, J.-C.; Munsch, P.; Le Marchand, G. Hydrostatic Limits of 11 Pressure Transmitting Media. *J. Phys. D. Appl. Phys.* **2009**, *42*, 075413.

(180) Zhao, J.; Angel, R. J.; Ross, N. L. Effects of Deviatoric Stresses in the Diamond-Anvil Pressure Cell on Single-Crystal Samples. *J. Appl. Crystallogr.* **2010**, *43*, 743–751.

(181) Mohammadi, R.; Lech, A. T.; Xie, M.; Weaver, B. E.; Yeung, M. T.; Tolbert, S. H.; Kaner, R. B. Tungsten Tetraboride, an Inexpensive Superhard Material. *Proc. Natl. Acad. Sci.* **2011**, *108*, 10958–10962.

(182) Birch, F. Finite Strain Isotherm and Velocities for Single-Crystal and Polycrystalline NaCl at High Pressures and 300°K. *J. Geophys. Res.* **1978**, *83*, 1257.

(183) Jeanloz, R. Finite-Strain Equation of State for High-Pressure Phases. *Geophys. Res. Lett.* **1981**, *8*, 1219–1222.

(184) Rivers, M.; Prakapenka, V.; Kubo, A.; Pullins, C.; Holl, C.; Jacobsen, S. The COMPRES/GSECARS Gas-Loading System for Diamond Anvil Cells at the Advanced Photon Source. *High Press. Res.* **2008**, *28*, 273–292.

(185) Hammersley, A. P.; Svensson, S. O.; Hanfland, M.; Fitch, A. N.; Hausermann, D. Two-Dimensional Detector Software: From Real Detector to Idealised Image or Two-Theta Scan. *High Press. Res.* **1996**, *14*, 235–248.

(186) Nelmes, R.; Loveday, J.; Allan, D.; Besson, J.; Hamel, G.; Grima, P.; Hull, S. Neutron- and X-Ray-Diffraction Measurements of the Bulk Modulus of Boron. *Phys. Rev. B* **1993**, *47*, 7668–7673.

(187) Koehler, M. R.; Keppens, V.; Sales, B. C.; Jin, R.; Mandrus, D. Elastic Moduli of Superhard Rhenium Diboride. *J. Phys. D. Appl. Phys.* **2009**, *42*, 095414.

(188) Zhao, E.; Wang, J.; Meng, J.; Wu, Z. Phase Stability and Mechanical Properties of Rhenium Borides by First-Principles Calculations. *J. Comput. Chem.* **2010**, *31*, 1904–1910.

(189) Kenichi, T. Structural Study of Zn and Cd to Ultrahigh Pressures. *Phys. Rev. B* **1997**, *56*, 5170–5179.

(190) Kenichi, T. Zn under Pressure: A Singularity in the Hcp Structure at c/a=3. *Phys. Rev. Lett.* **1995**, *75*, 1807–1810.

(191) Schulte, O.; Holzapfel, W. Effect of Pressure on the Atomic Volume of Zn, Cd, and Hg up to 75 GPa. *Phys. Rev. B* **1996**, *53*, 569–580.

(192) Kenichi, T. Absence of the C/a Anomaly in Zn under High Pressure with a Helium-Pressure Medium. *Phys. Rev. B* **1999**, *60*, 6171–6174.

(193) Meenakshi, S.; Vijayakumar, V.; Godwal, B.; Sikka, S. Distorted Hcp Structure of Zinc under Pressure. *Phys. Rev. B* **1992**, *46*, 14359–14361.

(194) Godwal, B.; Meenakshi, S.; Rao, R. C/a Anomalies and Electronic Topological Transitions in Cd. *Phys. Rev. B* **1997**, *56*, 14871–14874.

(195) Novikov, D.; Katsnelson, M.; Trefilov, A.; Freeman, A.; Christensen, N.; Svane, A.; Rodriguez, C. Anisotropy of Thermal Expansion and Electronic Topological Transitions in Zn and Cd under Pressure. *Phys. Rev. B* **1999**, *59*, 4557–4560.

(196) Steinle-Neumann, G.; Stixrude, L.; Cohen, R. Absence of Lattice Strain Anomalies at the Electronic Topological Transition in Zinc at High Pressure. *Phys. Rev. B* **2001**, *63*, 054103.

(197) Godwal, B. K.; Modak, P.; Rao, R. S. On the High Pressure Electronic Topological Transitions in Zinc. *Solid State Commun.* **2003**, *125*, 401–405.

(198) Qiu, S. L.; Apostol, F.; Marcus, P. M. Structural Anomalies in Hcp Metals under Pressure: Zn and Cd. *J. Phys. Condens. Matter* **2004**, *16*, 6405–6414.

(199) Sin'ko, G. V; Smirnov, N. A. Effect of Electronic Topological Transitions on the Calculations of Some Zn and Fe Properties. *J. Phys. Condens. Matter* **2005**, *17*, 559–569.

(200) Godwal, B.; Jayaraman, A.; Meenakshi, S.; Rao, R.; Sikka, S.; Vijayakumar, V. Electronic Topological and Structural Transition in AuIn2 under Pressure. *Phys. Rev. B* **1998**, *57*, 773–776.

(201) Godwal, B. K.; Speziale, S.; Clark, S. M.; Yan, J.; Jeanloz, R. High Pressure Equation of State Studies Using Methanol–ethanol–water and Argon as Pressure Media. *J. Phys. Chem. Solids* **2010**, *71*, 1059–1064.

(202) Lifshitz, I. M.; Kaganov, M. I. Some Problems of the Electron Theory of Metals I. Classical and Quantum Mechanics Of Electrons in Metals. *Sov. Phys. Uspekhi* **1960**, *2*, 831–855.

(203) Koudela, D.; Richter, M.; Möbius, A.; Koepernik, K.; Eschrig, H. Lifshitz Transitions and Elastic Properties of Osmium under Pressure. *Phys. Rev. B* **2006**, *74*, 214103.

(204) Speziale, S.; Jeanloz, R.; Clark, S. M.; Meenakshi, S.; Vijayakumar, V.; Verma, A. K.; Rao, R. S.; Godwal, B. K. Axial Ratio Anomalies and Electronic Topological Transitions in Cd0.80Hg0.20 at High Pressures. *J. Phys. Chem. Solids* **2008**, *69*, 2325–2331.

(205) Veprek, S.; Argon, A. S.; Zhang, R. F. Design of Ultrahard Materials: Go Nano! *Philos. Mag.* **2010**, *90*, 4101–4115.

(206) Pellicer-Porres, J.; Segura, A.; Muñoz, A.; Polian, A.; Congeduti, A. Bond Length Compressibility in Hard ReB2 Investigated by X-Ray Absorption under High Pressure. *J. Phys. Condens. Matter* **2010**, *22*, 45701.

(207) Dubrovinskaia, N.; Dubrovinsky, L.; Crichton, W.; Langenhorst, F.; Richter, A. Aggregated Diamond Nanorods, the Densest and Least Compressible Form of Carbon. *Appl. Phys. Lett.* **2005**, *87*, 083106.

(208) Dubrovinskaia, N.; Dubrovinsky, L.; Solozhenko, V. L. Comment on "Synthesis of Ultra-Incompressible Superhard Rhenium Diboride at Ambient Pressure". *Science* **2007**, *318*, 1550; author reply 1550.

(209) Tse, J. S. Intrinsic Hardness of Crystalline Solids. *J. Superhard Mater.* **2010**, *32*, 177–191.

(210) Gerk, A. P. The Effect of Work-Hardening upon the Hardness of Solids: Minimum Hardness. *J. Mater. Sci.* **1977**, *12*, 735–738.

(211) Haines, J.; Léger, J. M.; Bocquillon, G. Synthesis and Design of Superhard Materials. *Annu. Rev. Mater. Res.* **2001**, *31*, 1–23.

(212) Léger, J. M.; Haines, J.; Schmidt, M.; Petitet, J. P.; Pereira, A. S.; da Jornada, J. A. H. Discovery of Hardest Known Oxide. *Nature* **1996**, *383*, 401–401.

(213) Liu, A. Y.; Cohen, M. L. Prediction of New Low Compressibility Solids. *Science* **1989**, *245*, 841–842.

(214) Oganov, A. R.; Lyakhov, A. O. Towards the Theory of Hardness of Materials. *J. Superhard Mater.* **2010**, *32*, 143–147.

(215) Xie, M.; Mohammadi, R.; Mao, Z.; Armentrout, M. M.; Kavner, A.; Kaner, R. B.; Tolbert, S. H. Exploring the High-Pressure Behavior of Superhard Tungsten Tetraboride. *Phys. Rev. B* **2012**, *85*, 64118.

(216) Egami, T.; Waseda, Y. Atomic Size Effect on the Formability of Metallic Glasses. *J. Non. Cryst. Solids* **1984**, *64*, 113–134.

(217) Gou, H.; Li, Z.; Wang, L.; Lian, J.; Wang, Y. Peculiar Structure and Tensile Strength of WB4: Nonstoichiometric Origin. *AIP Adv.* **2012**, *2*, 12171.

(218) Juarez-Arellano, E. a.; Winkler, B.; Friedrich, A.; Bayarjargal, L.; Morgenroth, W.; Kunz, M.; Milman, V. In Situ Study of the Formation of Rhenium Borides from the Elements at High-(p, T)

Conditions: Extreme Incompressibility of Re7B3 and Formation of New Phases. *Solid State Sci.* **2013**, *25*, 85–92.

(219) Gou, H.; Li, Z.; Niu, H.; Gao, F.; Zhang, J.; Ewing, R. C.; Lian, J. Unusual Rigidity and Ideal Strength of CrB4 and MnB4. *Appl. Phys. Lett.* **2012**, *100*, 111907.

(220) *Encyclopedia of Inorganic and Bioinorganic Chemistry*; Scott, R. A., Ed.; John Wiley & Sons, Ltd: Chichester, UK, 2011.

(221) Lu, Y. P.; He, D. W. Structure and Elastic Properties of Boron Suboxide at 240 GPa. *J. Appl. Phys.* **2009**, *105*, 083540.

(222) Tkachev, S.; Solozhenko, V.; Zinin, P.; Manghnani, M.; Ming, L. Elastic Moduli of the Superhard Cubic BC2N Phase by Brillouin Scattering. *Phys. Rev. B* **2003**, *68*, 52104.

(223) Solozhenko, V. L.; Dub, S. N.; Novikov, N. V. Mechanical Properties of Cubic BC2N, a New Superhard Phase. *Diam. Relat. Mater.* **2001**, *10*, 2228–2231.

(224) Zhang, R. F.; Legut, D.; Lin, Z. J.; Zhao, Y. S.; Mao, H. K.; Veprek, S. Stability and Strength of Transition-Metal Tetraborides and Triborides. *Phys. Rev. Lett.* **2012**, *108*, 255502.

(225) Chretien, A.; Helgorsky, J. On New Boride Compositions of Molybdenum and Tungsten, MoB4 and WB4. *Comptes Rendus* **1961**, *252*, 742–744.

(226) Goldschmidt, H.; Catherall, E.; Ham, W.; Oliver, D. Investigation into the Tungsten-Rich Regions of the Binary Systems Tungsten-Carbon, Tungsten-Boron, and Tungsten-Beryllium. **1963**.

(227) Kiessling, R.; Wetterholm, A.; Sillén, L. G.; Linnasalmi, A.; Laukkanen, P. The Crystal Structures of Molybdenum and Tungsten Borides. *Acta Chem. Scand.* **1947**, *1*, 893–916.

(228) Nowotny, H.; Haschke, H.; Benesovsky, F. Bor-Reiche Wolframboride. *Monatshefte für Chemie / Chem. Mon.* **1967**, *98*, 547–554.

(229) Rosenberg, I.; Lundström, T. The Crystal Structure of the Molybdenum Boride Mo1-xB3. *J. Solid State Chem.* **1973**, *6*, 299–305.

(230) Akaishi, M.; Satoh, T.; Ishii, M.; Taniguchi, T.; Yamaoka, S. Synthesis of Translucent Sintered Cubic Boron Nitride. *J. Mater. Sci. Lett.* **1993**, *12*, 1883–1885.

(231) Knittle, E.; Wentzcovitch, R. M.; Jeanloz, R.; Cohen, M. L. Experimental and Theoretical Equation of State of Cubic Boron Nitride. *Nature* **1989**, *337*, 349–352.

(232) Grimsditch, M.; Zouboulis, E. S.; Polian, A. Elastic Constants of Boron Nitride. *J. Appl. Phys.* **1994**, *76*, 832.

(233) Mukhanov, V. A.; Kurakevych, O. O.; Solozhenko, V. L. The Interrelation between Hardness and Compressibility of Substances and Their Structure and Thermodynamic Properties. *J. Superhard Mater.* **2009**, *30*, 368–378.

(234) Mukhanov, V. A.; Kurakevych, O. O.; Solozhenko, V. L. Thermodynamic Aspects of Materials' Hardness: Prediction of Novel Superhard High-Pressure Phases. *High Press. Res.* **2008**, *28*, 531–537.

(235) Zhang, Y.; Sun, H.; Chen, C. Atomistic Deformation Modes in Strong Covalent Solids. *Phys. Rev. Lett.* **2005**, *94*, 145505.

(236) Liang, Y.; Gou, Y.; Yuan, X.; Zhong, Z.; Zhang, W. Unexpectedly Hard and Highly Stable WB3 with a Noncompact Structure. *Chem. Phys. Lett.* **2013**, *580*, 48–52.

(237) Zang, C.; Sun, H.; Chen, C. Unexpectedly Low Indentation Strength of WB3 and MoB3 from First Principles. *Phys. Rev. B* **2012**, *86*, 180101.

(238) Cheng, X.; Zhang, W.; Chen, X.-Q.; Niu, H.; Liu, P.; Du, K.; Liu, G.; Li, D.; Cheng, H.-M.; Ye, H.; et al. Interstitial-Boron Solution Strengthened WB3+x. *Appl. Phys. Lett.* **2013**, *103*, 171903.

(239) Liang, Y.; Fu, Z.; Yuan, X.; Wang, S.; Zhong, Z.; Zhang, W. An Unexpected Softening from WB3 to WB4. *EPL (Europhysics Lett.* **2012**, *98*, 66004.

(240) Zhang, M.; Yan, H.; Wei, Q.; Wang, H. Universal Ground State Hexagonal Phases and Mechanical Properties of Stoichiometric Transition Metal Tetraborides: TMB4 (TM=W, Tc, and Re). *Comput. Mater. Sci.* **2013**, *68*, 371–378.

(241) Zhao, E.; Meng, J.; Ma, Y.; Wu, Z. Phase Stability and Mechanical Properties of Tungsten Borides from First Principles Calculations. *Phys. Chem. Chem. Phys.* **2010**, *12*, 13158–13165.

(242) Liang, Y.; Yuan, X.; Zhang, W. Thermodynamic Identification of Tungsten Borides. *Phys. Rev. B* **2011**, *83*, 220102.

(243) Rietveld, H. M. A Profile Refinement Method for Nuclear and Magnetic Structures. *J. Appl. Crystallogr.* **1969**, *2*, 65–71.

(244) Chretien, A.; Helgorsky, J. On New Boride Compositions of Molybdenum and Tungsten, MoB4 and WB4. *Comptes Rendus* **1961**, *252*, 742–744.

(245) Kiessling, R. The Borides of Some Transition Elements. *J. Electrochem. Soc.* **1951**, *98*, 166–170.

(246) Pauling, L. Atomic Radii and Interatomic Distances in Metals. *J. Am. Chem. Soc.* **1947**, *69*, 542–553.

(247) Placa, S. La; Binder, I.; Post, B. Binary Dodecaborides. *J. Inorg. Nucl. Chem.* **1961**, *18*, 113–117.

(248) Xie, M.; Mohammadi, R.; Mao, Z.; Armentrout, M. M.; Kavner, A.; Kaner, R. B.; Tolbert, S. H. Exploring the High-Pressure Behavior of Superhard Tungsten Tetraboride. *Phys. Rev. B* **2012**, *85*, 64118.

(249) Stapper, G.; Bernasconi, M.; Nicoloso, N.; Parrinello, M. Ab Initio Study of Structural and Electronic Properties of Yttria-Stabilized Cubic Zirconia. *Phys. Rev. B* **1999**, *59*, 797–810.

(250) Cannon, J. F.; Farnsworth, P. B. High Pressure Syntheses of ThB12 and HfB12. *J. Less Common Met.* **1983**, *92*, 359–368.

(251) Hamada, K.; Wakata, M.; Sugii, N.; Matsuura, K.; Kubo, K.; Yamauchi, H. Structural Phase Transition in the Zr1−xScxB12 System. *Phys. B Condens. Matter* **1994**, *194–196, P*, 443–444.

(252) Post, B.; Glaser, F. W.; Moskowitz, D. Transition Metal Diborides. *Acta Metall.* **1954**, *2*, 20–25.

(253) Mudgel, M.; Awana, V. P. S.; Kishan, H.; Felner, I.; Alvarez, D. G. A.; Bhalla, G. L. Superconductivity of Various Borides: The Role of Stretched c-Parameter. *J. Appl. Phys.* **2009**, *105*, 07E313.

(254) Zhang, M.-X.; Kelly, P. M. Edge-to-Edge Matching and Its Applications: Part I. Application to the Simple HCP/BCC System. *Acta Mater.* **2005**, *53*, 1073–1084.

(255) Zhang, M.-X.; Kelly, P. M. Edge-to-Edge Matching Model for Predicting Orientation Relationships and Habit Planes: The Improvements. *Scr. Mater.* **2005**, *52*, 963–968.

(256) Razavi, M.; Rahimipour, M. R.; Rajabi, A. Prenucleation Effect on Characterisations of Synthesised Nanocrystalline Tungsten Carbide via Mechanical Milling.

(257) Romans, P. A.; Krug, M. P. Composition and Crystallographic Data for the Highest Boride of Tungsten. *Acta Crystallogr.* **1966**, *20*, 313–315.

(258) Lundstrom, T.; Rosenberg, I. The Crystal Structure of the Molybdenum Boride Mo1-xB3. *J. Solid State Chem.* **1973**, *6*, 299–305.

(259) Zhang, R. F.; Legut, D.; Lin, Z. J.; Zhao, Y. S.; Mao, H. K.; Veprek, S. Stability and Strength of Transition-Metal Tetraborides and Triborides. *Phys. Rev. Lett.* **2012**, *108*, 255502.

(260) Gou, H.; Dubrovinskaia, N.; Bykova, E.; Tsirlin, A. A.; Kasinathan, D.; Schnelle, W.; Richter, A.; Merlini, M.; Hanfland, M.; Abakumov, A. M.; et al. Discovery of a Superhard Iron Tetraboride Superconductor. *Phys. Rev. Lett.* **2013**, *111*, 157002.

(261) Liang, Y.; Yuan, X.; Fu, Z.; Li, Y.; Zhong, Z. An Unusual Variation of Stability and Hardness in Molybdenum Borides. *Appl. Phys. Lett.* **2012**, *101*, 181908.

(262) Pan, Y.; Zheng, W. T.; Guan, W. M.; Zhang, K. H.; Fan, X. F. First-Principles Study on the Structure, Elastic Properties, Hardness and Electronic Structure of TMB4 (TM=Cr, Re, Ru and Os) Compounds. *J. Solid State Chem.* **2013**, *207*, 29–34.

(263) Li, B.; Sun, H.; Zang, C.; Chen, C. Fundamental Constraints on the Strength of Transition-Metal Borides: The Case of CrB4. *Phys. Rev. B* **2013**, *87*, 174106.

(264) Niu, H.; Wang, J.; Chen, X.-Q.; Li, D.; Li, Y.; Lazar, P.; Podloucky, R.; Kolmogorov, A. N. Structure, Bonding, and Possible Superhardness of CrB4. *Phys. Rev. B* **2012**, *85*, 144116.

(265) Wang, B.; Li, X.; Wang, Y. X.; Tu, Y. F. Phase Stability and Physical Properties of Manganese Borides: A First-Principles Study. *J. Phys. Chem. C* **2011**, *115*, 21429–21435.

(266) Zhao, W.-J.; Xu, B. First-Principles Calculations of MnB4, TcB4, and ReB4 with the MnB4-Type Structure. *Comput. Mater. Sci.* **2012**, *65*, 372–376.

(267) Gou, H.; Li, Z.; Niu, H.; Gao, F.; Zhang, J.; Ewing, R. C.; Lian, J. Unusual Rigidity and Ideal Strength of CrB4 and MnB4. *Appl. Phys. Lett.* **2012**, *100*, -.

(268) Knappschneider, A.; Litterscheid, C.; Dzivenko, D.; Kurzman, J. A.; Seshadri, R.; Wagner, N.; Beck, J.; Riedel, R.; Albert, B. Possible Superhardness of CrB4. *Inorg. Chem.* **2013**, *52*, 540–542.

(269) Arsecularatne, J. A.; Zhang, L. C.; Montross, C. Wear and Tool Life of Tungsten Carbide, PCBN and PCD Cutting Tools. *Int. J. Mach. Tools Manuf.* **2006**, *46*, 482–491.

(270) Gaitonde, V. N.; Karnik, S. R.; Figueira, L.; Davim, J. P. Analysis of Machinability During Hard Turning of Cold Work Tool Steel (Type: AISI D2). *Mater. Manuf. Process.* **2009**, *24*, 1373–1382.

(271) Cook, M. W.; Bossom, P. K. Trends and Recent Developments in the Material Manufacture and Cutting Tool Application of Polycrystalline Diamond and Polycrystalline Cubic Boron Nitride. *Int. J. Refract. Met. Hard Mater.* **2000**, *18*, 147–152.

(272) Ezugwu, E. O.; Wang, Z. M.; Machado, A. R. The Machinability of Nickel-Based Alloys: A Review. *J. Mater. Process. Technol.* **1998**, *86*, 1–16.

(273) Ezugwu, E. O.; Wang, Z. M. Titanium Alloys and Their Machinability: A Review. *J. Mater. Process. Technol.* **1997**, *68*, 262–274.

(274) Kim, H.-C.; Shon, I.-J.; Garay, J. E.; Munir, Z. A. Consolidation and Properties of Binderless Sub-Micron Tungsten Carbide by Field-Activated Sintering. *Int. J. Refract. Met. Hard Mater.* **2004**, *22*, 257–264.

(275) Ho, K. H.; Newman, S. T.; Rahimifard, S.; Allen, R. D. State of the Art in Wire Electrical Discharge Machining (WEDM). *Int. J. Mach. Tools Manuf.* **2004**, *44*, 1247–1259.